3D printing versus foaming of melt-derived bioactive glasses for bone regeneration

Amy Elizabeth Nommeots-Nomm

Submitted in partial fulfilment of the requirements for the degree of Doctor of Philosophy

November 2015

Department of Materials

Imperial College London

Declaration of Originality

I hereby declare that, unless appropriately referenced or acknowledged, all work presented in this thesis is my own and was carried out in the laboratories of Imperial College London or within collaboration at Diamond Light Source Harwell Campus, Didcot.

Copyright

'The copyright of this thesis rests with the author and is made available under a Creative Commons Attribution Non-Commercial No Derivatives licence. Researchers are free to copy, distribute or transmit the thesis on the condition that they attribute it, that they do not use it for commercial purposes and that they do not alter, transform or build upon it. For any reuse or redistribution, researchers must make clear to others the licence terms of this work'.

Abstract

Bioactive glasses have the ability to regenerate bone defects as they form a rapid bond with bone and their dissolution products can stimulate new bone growth. The original Bioglass® 45S5 composition (46.1 mol% SiO_2, 26.9 mol% CaO, 24.4 mol% Na_2O, and 2.6 mol% P_2O_5) is available as a clinical product in a particulate form, but surgeons require scaffolds that can act as temporary templates for bone repair. Bioglass 45S5 cannot be made into porous scaffolds while maintaining an amorphous glass structure, due to its susceptibility to crystallise during sintering. New melt-derived glass compositions have recently been developed which avoid crystallisation, enabling bioactive glasses to be made into porous constructs.

The aim of this thesis was to investigate the relationship between glass composition and scaffold production techniques. Three glasses compositions were used, ICIE16 (49.46 SiO_2, 36.27 CaO, 6.6 Na_2O, 1.07 P_2O_5 and 6.6 K_2O, in mol%), 13-93 (54.6 SiO_2, 22.1 CaO, 6.0 Na_2O, 1.7 P_2O_5, 7.9 K_2O, 7.7 MgO, in mol%) and SBP-3 (44.5 SiO_2, 17.8 CaO, 4.0 Na_2O, 4.5 P_2O_5, 4.0 K_2O, 7.5 MgO, 17.8 SrO, in mol%), each with an extended thermal processing window. These glasses were made into 3D scaffolds utilising two processing techniques: an adapted gel-cast foaming and, for the first time, robocasting. Here we present the adaption and optimisation of these techniques.

The three glass compositions, ICIE16, 13-93 and SBP-3, all have different modified network connectivities (mean number of bridging Si-O-Si bonds per silicon atom, NC') of 2.13, 2.84 and 3.01 respectively. *In vitro* and *in vivo* analysis were completed to understand how the different glass chemistry affected their bioactivity and dissolution characteristics. The composition of ICIE16 chemistry was the most similar to the original 45S5 composition was shown to promote and sustain better bone ingrowth than comparable scaffolds produced from SBP-3.

Acknowledgements

First, the serious stuff: I would like to thank my funding bodies, the Engineering and Physical Sciences Research Council (EPSRC), Department of Materials, Imperial College London for funding my studentship, access to facilities and consumables. I would also like to thank the Honourable Company of Armourers & Brasiers and Mo-Sci Corporation (Missouri, USA) for supporting me to attend conferences.

Thank-you to my collaborators, Professor Christopher Mitchell (University of Ulster for completing the *in vivo* studies, Professor Peter Lee (University of Manchester) for the 3D imaging. It has been wonderful working with you and your research groups. A special thanks to Hua Geng (Research Campus at Harwell and University of Manchester) for your patience with our X-ray microtomography data.

To my supervisors, Professor Julian Jones, and Professor Eduardo Saiz. Julian thank you for putting up with me! Your guidance, smiley emoji's and advice have been instrumental in me completing. Eduardo, your laugh is incredible, I hope one day to master such an infectious chuckle, thank you for allowing me to join the CASC family, and your support these last few months.

Richard Sweenie, (Richieroo) for running overnight scans, magic tricks and concern, you've been fantastic. And finally Gowsh, thank you for being my big brother in the lab, simultaneous consoler, counsellor and cheerleader you really have been my saving grace.

Muffin, G, Louise, Fra, Prince Ali and Justin my goodness you have given me the best time! Friendship, lab dance-offs, weird questions and Katy Perry passion, thanks for making this experience so SO wonderful. My glass siblings Anu, and Dimitri, your wise words, high temperature finesse, proof reading excellence, and tea breaks, I could not have done it without you. The extended JRJ crew, my Badminton Buddies, the BioBoners, the CASC kids, my

Conference Partners in Crime and finally the Wilsonia Subbies particularly Hannah and Marissa: As a friend once told me, ‘timing is everything’, it has been a delight to have spent my time with you.

Last but not least, Family Nomm, this is as much my work, as it is your encouragement, love and support; I thank you.

TABLE OF CONTENTS

DECLARATION OF ORIGINALITY I

COPYRIGHT II

ABSTRACT III

ACKNOWLEDGEMENTS IV

TABLE OF CONTENTS VI

List of Figures: X

List of Equations: XVI

List of Tables: XVII

List of Abbreviations: XIX

1 INTRODUCTION 21

Thesis road map 24

2 LITERATURE REVIEW 25

2.1 UNDERSTANDING BIOACTIVE GLASSES 25

2.1.1 Glass theories 26

2.1.2 Stimulating bone growth 28

2.1.3 Theoretical predictions of the bioactivity of glasses 29

2.2 BIOACTIVE COMPOSITIONS 32

2.2.1 Dissolution behaviour 34

2.2.2 Driving forces for sintering 44

2.3 SCAFFOLD MANUFACTURING METHODS 46

2.3.1 Foam replica process 46

2.3.2 Gel-cast foaming 49

2.3.3 Selective laser sintering 50

2.3.4 Robocasting 51

2.3.5 Mechanical properties: can bone be matched? 56

2.4 TESTING BIOACTIVE PERFORMANCE 60

2.4.1 In vitro testing 61

2.4.2 In vivo studies 64

2.5 AIMS AND OBJECTIVES 67
3 METHODOLOGY 68
3.1 GLASS MAKING 68
3.2 GLASS GRINDING 70
3.3 CHARACTERISATION TECHNIQUES 70
3.3.1 Glass composition characterisation 70
3.3.2 Particle size analysis 72
3.3.3 Zeta potential 72
3.3.4 X-ray diffraction 73
3.3.5 Thermal analysis 74
3.3.6 Scanning electron microscopy 75
3.3.7 Mercury porosimetry 77
3.3.8 Fourier transform infrared spectroscopy 79
3.3.9 Compression testing 79
3.3.10 Helium pyconometry and percentage porosity 80
3.3.11 Rheology 81
3.3.12 X-ray microtomography 81
4 GEL-CASTING: 84
4.1 INTRODUCTION 84
4.2 MATERIALS AND METHODS 84
4.2.1 Protocol 84
4.3 OPTIMISATION OF GEL-CAST FOAMING OF ICIE16 85
4.3.1 Varying surfactant concentration 85
4.3.2 The effect of surfactant concentration on mechanical properties 91
4.3.3 Sintering conditions 92
4.4 OPTIMISATION OF GEL-CAST FOAMING OF 13-93 98
4.4.1 Varying surfactant concentration 98
4.4.2 Sintering analysis 99
4.5 OPTIMISATION OF GEL-CAST FOAMING OF SBP-3 100
4.6 MECHANICAL TESTING 103
4.6.1 Gel-cast scaffolds mechanical properties 104
4.7 CONCLUSIONS 107

5 BIOACTIVE PERFORMANCE OF GEL-CAST FOAMED SCAFFOLDS 111

5.1 INTRODUCTION 111

5.2 METHODOLOGY 111

5.2.1 SBF preparation 111

5.2.2 Dissolution protocol for bioactive glass scaffolds 112

5.2.3 Ion concentration profiles 113

5.2.4 Surface analysis 113

5.3 *SBF* TESTING RESULTS 114

5.3.1 pH change 114

5.3.2 ICP-OES results 116

5.3.3 Surface analysis 125

5.3.4 Conclusions of the dissolution study 131

5.4 *IN VIVO* TESTING 131

5.4.1 Methodology 132

5.4.2 Results 133

5.4.3 Conclusions 135

6 3D PRINTING.....137

6.1 INTRODUCTION 137

6.2 FINDING A SUITABLE INK: DESIGN CRITERIA 137

6.2.1 Ethyl cellulose 138

6.2.2 Pluronic F-127 139

6.2.3 Ink Comparison 139

6.2.4 Conclusions on carrier selection 141

6.3 NOZZLE SHAPE 141

6.4 PLURONIC F-127 INK RHEOLOGY 144

6.4.1 Understanding Pluronic F-127 144

6.4.2 Herschel-Bulkley model 148

6.4.3 The effects of particle loading on gelation temperature 150

6.4.4 The effects of particle loading on viscosity 151

6.4.5 The effects of particle loading on mechanical properties of inks 154

6.5 SIMULATING PRINTING 157

6.5.1 The effect of particle size 158

6.5.2 The effect of printing speed 164

6.6 PROCESS OPTIMISATION 167

6.6.1 Ink formulation 167

6.6.2 Green bodies 170

6.6.3 Sintering robocast scaffolds 171

6.6.4 Reducing strut porosity 174

6.6.5 Drying 176

6.7 COMPARISONS OF ROBOCAST SCAFFOLDS MANUFACTURED FROM 3 GLASS COMPOSITIONS 179

6.7.1 Shrinkage 179

6.7.2 Does glass chemistry affect rheology? 180

6.7.3 Compression testing 181

6.8 SCAFFOLD COMPARISON: ROBOCASTING VERSES GEL-CAST FOAMING 183

6.9 CONCLUSIONS 184

7 CONCLUSIONS 186

8 FURTHER WORK 189

9 REFERENCES 190

List of Figures:

Figure 2.1: The effect of temperature on enthalpy of glass forming melts, adapted from reference [20]. 25
Figure 2.2: Schematic of the different roles ions can play within a glass network. 27
Figure 2.3: Compositional map showing the relationship between CaO, Na_2O and SiO_2 where P_2O_5 was held constant at 6 wt %, after [42]. Region A: bioactive and bond to bone, b) glasses which also bond to soft tissue, c) highly reactive glasses, and d) glasses which do not dissolve. 32
Figure 2.4 An overview of biological responses to ionic dissolution products of bioactive glasses, adapted from reference [46] 34
Figure 2.5: Schematic of a differential scanning calorimetry plot for a glass material showing the concept of a thermal processing sintering window. 45
Figure 2.6: example of a hollow strut formed, highlighted by the arrow, during the foam replica processing, reproduced with permission from Hoppe *et al.*[71] 48
Figure 2.7: Schematic of robocasting set-up adapted from Dellinger et al. [132] 52
Figure 2.8: Example of robocast 13-93 scaffolds reproduced with permission from reference [135] 53
Figure 2.9: A schematic of the structure of human bone adapted from Rho *et al.* [148] 57
Figure 2.10: Summary of current literature of scaffolds manufactured of 13-93 via various processing methods *grey areas denotes reported strengths of cortical bone and cancellous bone reported in Table 2.4 59
Figure 2.11: Schematic of the testing procedures options and variables to understanding bioactivity of bioactive materials 60
Figure 2.12: Summary of SBF testing results from Deliormanlı *et al.* [52] a) weight loss, b) pH change, and c) compressive strength variation with time and d) SEM image of precipitation after 60 days in SBF. 63

Figure 3.1: Schematic of X-ray diffraction 73
Figure 3.2: a schematic of an atom, where the shells from outside inwards are M, L, K, and the filled circle is the nucleus. The orange arrow represents the Lα transition, green the Kα and blue arrow is the Kβ transition. 77
Figure 4.1: Schematic of the adapted gel casting process 85
Figure 4.2: Schematic of surfactants forming micelles within an aqueous system 87
Figure 4.3: Variation in scaffold volume with increasing surfactant concentration, measured after freeze drying..... 88
Figure 4.4: SEM images (100x magnification) of scaffolds sintered with varying surfactant concentration, (a) 0.1 ml, (b) 0.2 ml, (c) 0.3 ml, (d) 0.4 ml, (e) 0.5 ml, (f) 0.6 ml. 89
Figure 4.5: Interconnect size distributions obtained from mercury porosimetry, for samples with 0.1, 0.2 and 0.6 ml of surfactant. 89
Figure 4.6: Scaffold porosity and modal interconnect diameter post sintering as a function of surfactant concentration..... 91
Figure 4.7: The effect of surfactant concentration on compressive strength. Porosity percentages are marked for reference above..... 92
Figure 4.8: Schematic of the sintering cycle used for ICIE16 foam scaffolds. . 93
Figure 4.9: TGA analysis of an ICIE16 green body. 94
Figure 4.10: Sintering of scaffolds for 1 h at the following temperatures (a) 680°C, (b) 690°C, (c) 700°C and (d) 710°C, the second column are higher magnification images, the white circles highlight pit formation upon the surface. 95
Figure 4.11: XRD patterns collected from scaffolds sintered at 690° for 1, 1.5, 2 and 5 h. Grey dotted lines highlight the formation of crystalline peaks at 2 h. The crystalline phases present are $Na_{4.24}Ca_{3.8}$ (Si_6O_{18}) and $Ca_2Si_4Ca_3(PO_4)_2$ (reference codes 01-078-1650 and 00-049-1674 respectively). 96
Figure 4.12: ICIE16 gel-cast scaffolds sintered at 690°C for 1.5 h. 97

Figure 4.13: SEM images of 13-93 scaffolds foamed at the following surfactant concentrations (a) 0.2 ml, (b) 0.3 ml, (c) 0.4 ml, (d) 0.5 ml, (e) 0.6 ml. 98
Figure 4.14: Post sintering XRD analysis of 13-93 scaffolds when sintered for 1 h at 700°C. 100
Figure 4.15: Topography of 13-93 gel-cast scaffolds post process optimisation. 100
Figure 4.16: SEM micrographs of SBP-3 gel cast foam scaffolds sintered under different conditions (a) 690°C for 5 h, (b) 700°C for 3 h, (c) 700°C for 5 h, (d) 705°C for 5 h. 101
Figure 4.17: XRD patterns collected for SBP-3 after sintering at various times and temperatures. 102
Figure 4.18: Example stress strain curves for ICIE16 scaffolds with percentage porosities stated. 103
Figure 4.19: Compressive strength of gel-cast scaffolds of ICIE16, SBP-3, and 13-93 compositions and their associate percentage porosity. 105
Figure 4.20: SEM images of ICIE16, SBP-3 and 13-93 gel cast foam scaffolds post sintering 106
Figure 5.1: pH change across 500 h immersion in SBF for scaffolds made by gel-cast foaming from 13-93, SBP-3 and ICIE16 compositions. 114
Figure 5.2: Silica dissolution profiles for 13-93, ICIE16 and SBP-3 gel cast foam scaffolds in SBF up to 500 h. 117
Figure 5.3: Calcium dissolution profiles in SBF following immersion of gel-cast foams of 13-93, ICIE16 and SBP-3 compositions, up to 500 h. 118
Figure 5.4: Phosphorous content in SBF after immersion of gel-cast foam scaffolds made from 13-93, ICIE16 and SBP-3 bioactive glass compositions, up to 500 h. 120
Figure 5.5: Potassium dissolution profiles in SBF containing gel-cast foam bioactive glass scaffolds of 13-93, ICIE16 and SBP-3 composition up to 500 h. 122

Figure 5.6: Magnesium dissolution from gel-cast foam scaffolds of the SBP-3 and 13-93 bioactive glass compositions over 500 h in SBF..... 123
Figure 5.7: Strontium dissolution from gel-cast foam scaffolds of the SBP-3 bioactive glass composition over 500 h in SBF. 124
Figure 5.8: FTIR spectra collected from gel-cast foam scaffolds of three glass compositions at after 0, 72 h, 1 week and 4 weeks immersion in SBF. 125
Figure 5.9: XRD patterns collected from gel-cast foam scaffolds of three glass compositions at after 0, 72 h, 1 week and 4 weeks immersion in SBF. Dotted grey lines represent the peaks for HCA reference (ICSD 01-084-199)..... 126
Figure 5.10: SEM images collected of scaffold surface of ICIE16, 13-93 and SBP-3 at various time points up to 4 weeks of SBF testing. 128
Figure 5.11: EDS spectra collected from the SEM images (insets) of surfaces of the three bioactive glasses, after 4 weeks in SBF. Dotted lines mark the corresponding K_{α} energies for each element..... 130
Figure 5.12: XMT evaluation of bone regeneration in rabbits femur condyle defect (a, b) implanted with ICIE16 and SBP-3 scaffold (c,d,e,f) at 7 weeks, (g,h,I,j) at 12 weeks post-operation. A reticulated trabecular bone is observed at 7 weeks followed by growth and development of bone. The morphology of the cortical region restored its pattern at 12 weeks post-operation. Image and analysis provide by Hua Geng. 134
Figure 6.1: DSC/TGA data of ethyl cellulous and Pluronic F-127 inks. 141
Figure 6.2: Compression testing aparatus to mimic the force dynamics during robocasting..... 142
Figure 6.3: Compression testing of tips with diameters of 610 μm with needle and conical profiles. 143
Figure 6.4: Rheological properties of Pluronic F-127 at various wt%: viscosity as a function of shear rate,..... 145
Figure 6.5: Rheological properties of Pluronic F-127: modulus as a function of temperature. 146

Figure 6.6: Oscillation sweep for a solution of 25 wt% F127 at 25°C, which is above its gelation temperature. 147
Figure 6.7: Rheometry data for 20–45 vol% of ICIE16 mixed with 25 wt% F127 fitted to the Herschel–Bulkley Model. 149
Figure 6.8: Relationship between the gelation temperature of 25 wt% of Pluronic F–127 loaded with 0–45 vol% of ICIE16 or 13–93 particles, the values are derived from oscillation sweeps shown in Figure 6.6 151
Figure 6.9: The influence of particle size on viscosity, values taken from the equivalent viscosity at a shear rate of 50 s^{-1}. 152
Figure 6.10: a) Yield point and b) Modulus at yield point as a function of vol% glass for inks of ICIE16, SBP–3 and 13–93 in solutions of 25 wt% F–127, tested at 25°C. 156
Figure 6.11: An example of the compression data created from ink testing: stabilisation force and time were compared and contrast between different ink concentrations, glass compositions and nozzle sizes. 157
Figure 6.12: Data collected via compression testing to simulate the force and time needed to reach stabilisation of ink at various ink compositions through nozzles diameters of 200, 250, 410 and 580 μm. The bars represent force, and the points represent time. Wt% refers to the concentration of Pluronic in solution, before the vol% of glass was added. 158
Figure 6.13: (a) Particle size distribution of ICIE16 when milled via jet and ball milling; SEM images of (b) jet milled glass; (c) ball milled glass. 162
Figure 6.14: The effects of particle size on the force and time needed to reach stabilisation during simulated robocasting via compression testing of inks. .. 163
Figure 6.15: The effect of printing speed on stabilisation and force required to stabilise an ink, made of 25 wt% Pluronic with 40 vol% of ICIE16, through a 250 μm nozzle. 165
Figure 6.16: Force as a function of time for inks that contained air bubbles (blue) or by printing with nozzle blockages (green). 168

Figure 6.17: Issues associated with air bubbles induced during mixing and syringe transfer on robocast scaffolds. A) air bubbles coagulating within the ink after it has been stored in a fridge for 24 h; B) a fracture surface of a scaffold strut containing air bubbles..... 169
Figure 6.18: SEM images of z, and x,y struts of 13-93, ICIE16 and SBP-3 robocast green bodies 3D printed in inks of 30 wt% of Pluronic F-127 and 47.5 vol% of glass. The bottom row shows cross sections of the struts at higher magnification. 171
Figure 6.19: 3D printed ICIE16 scaffolds sintered with and without a dwell period for binder removal. (a-c) single step 1 h at 690 °C, (d-f) initial dwell at 500°C for 1 h followed by 690°C for 1 h. 172
Figure 6.20: Typical stress-strain curves for ICIE16 scaffolds of similar porosity, printed with 47.5 vol% of glass and 30wt% pluronic, sintered using different protocols. 173
Figure 6.21: SEM images of fracture surfaces of struts, (a) and (d) ICIE16, (b) and (e) SBP-3 and (c) and (f) 13-93..... 174
Figure 6.22: XRD patterns of ICIE16, SBP-3 and 13-93 glasses, post-sintering, with changing particle size due to the different grinding methods..... 176
Figure 6.23: XMT image of ICIE16 scaffold with inherent cracking within the struts. Image provided by Xiaomeng Shi..... 176
Figure 6.24: Photograph of sintered scaffolds after drying in different environments. From left to right: printed into oil, air dried, water bath, ethanol. 177
Figure 6.25: SEM images of the effects of different drying protocols on sintered ICIE16 scaffolds. 178
Figure 6.26: Summary of compression testing results of comparable scaffold printed hrough 410 and 610 μm diameter nozzles from ICIE16, SBP-3 and 13-93, porosity of the scaffolds is marked in % within the bars..... 181
Figure 6.27: XMT images (provided by Xiaomeng Shi) of equivalent robocast and gel-cast scaffolds..... 183

List of Equations:

3.1 Network connectivity equation 29
3.2 Modified network connectivity equation 30
4.1 Vectors of Bragg's Law 73
4.2 Bragg's Law 73
4.3 Using Bragg's Law to calculate Miller indices and atomic spacing of crystal 73
4.4 Washburn equation for mercury porosimetry 76
4.5 Calculation of pore distribution via mercury porosimetry 76
4.6 The measure of stress and strain via compression testing 78
4.7 Measure of porosity skeletal density 78
4.8 Skeletal density skeletal density 78
4.9 Measure of loss and storage modulus via rheometry 80
6.1 Equivalent printing velocity 138
6.2 Herschel-Bulkley model 143
6.3 Kreiger-Dougherty model 148

List of Tables:

Table 2.1: Examples of commonly used bioactive glasses within literature [10, 15, 29, 32]. 31
Table 2.2: summary of different groups robocasting glass and ink combinations 55
Table 2.3: Comparison between the compressive strength of Fu *et al.* [135] and Liu *et al.* [37] using 13-93. 56
Table 2.4: Summary of the mechanical properties of human cortical and cancellous bone 57
Table 2.5: Ionic Concentration of Simulated Body Fluid and Human Body Plasma all in mM [162] 61
Table 3.1: Summary of the glasses used within this project and their chemistry's in mol%. 68
Table 3.2: calculations used to batch up 150 g of ICIE16 69
Table 3.3: Summary of the melting profile used for ICIE16, SBP-3 and 13-93 69
Table 4.1: Summary of modal interconnect values from mercury porosimetry Figure 4.5 90
Table 4.2: Mercury porosimetry data for 13-93 at surfactant concentrations between 0.2-0.6 ml. 99
Table 4.3: Mechanical properties of ICIE16, SBP-3 and 13-93 manufactured and sintered to their optimised process 105
Table 5.1: Reagents used for preparing SBF solution. 112
Table 5.2: Glass compositions, including the ratios of network formers to modifiers within the compositions, all in mol% 116
Table 5.3: Summary of the porosity and dimensions of the samples used within the rabbit in vivo study 132
Table 6.1: Ethyl cellulose ink composition defined by Deliormanlı *et al.* [52] and adapted for use with ICIE16 139
Table 6.2: Summary of the variation in yield and storage modulus with Pluronic F-127 concentration between 20-30 wt%, all measured at 25°C. 148

Table 6.3: The Herschel-Bulkley Model parameters obtained from the gradients and intercepts of Figure 6.7. 150
Table 6.4: Summarising the abilities of glasses to mix at various volume fractions of powder in a solution of 25wt % of Pluronic F-127. 154
Table 6.5: % increases in time and force required for extrusion, collected via compression testing through a 410µm nozzle from Figure 6.12. 159
Table 6.6: Particle size of ball milled glasses used within the printing inks all in µm. 160
Table 6.7: ICIE16 particle size and distribution when produced via jet and ball milling, all in µm. 161
Table 6.8: Analysis of the time taken to reach stabilisation at different extrusion speeds 165
Table 6.9: Tabulated summary of sintering outcomes 173
Table 6.10: Particle size data of ICIE16, SBP-3 and 13-93 glasses when ground via ball or jet milling, all errors were below ± 0.3 µm. 175
Table 6.11: Variation in porosity and compressive strength with drying protocol. 178
Table 6.12: Shrinkage of printed scaffolds in x, y and z dimensions. 179
Table 6.13. Zeta potential results for the three glasses in water. 180
Table 6.14: Comparison of compressive strengths of ICIE16 scaffolds printed with a 410 µm nozzle diameter compared with published literature. 182
Table 6.15: Robocast scaffolds compared with adapted gel-cast foams rom ICIE16 with comparable pore interconnects. 183

List of Abbreviations:

ALP	Alkaline phosphatase
ATR	Attenuated reflectance
BO	Bridging oxygens
BMP-2	Bone morphogenetic protein-2
CMC	Carboxymethyl cellulose
DMEN	Dulbecco's Modified Eagle's Medium
DSC	Differential scanning calolrimetry
EPSRC	Engineering and Physical Sciences Research Council
EDS	Energy dispersive spectroscopy
FTIR	Fourier transform infrared spectroscopy
FDA	Food and Drug Administration
HA	Hydroxyapatite
HCA	Hydroxcarbonate apatite
HIF-1α	Hypoxia-inducible factor
ICP-OES	Induced coupled plasma- optical emission spectroscopy
ISO	International Standards Organisation
MAS-NMR	Magic angle spinning nuclear magnetic resonance
MIP	Mercury porosimetry
MSC	Mesenchymal stem cell
NC	Network connectivity
NC'	Modified network connectivity

NBO	Non-bridging oxygens
PEG	Poly(ethylene glycol)
PEO	Poly(ethylene oxide)
PTFE	Polytetrafluoroethylene
PRP	Platelet rich plasma
PPO	Poly(propylene oxide)
PVA	Polyvinyl alcohol
SEM	Scanning electron microscopy
SBF	Simulated body fluid
T_c	Glass crystallisation temperature
T_g	Glass transition temperature
T_m	Glass melting temperature
TGA	Thermogravimetric analysis
TGF-β	Transforming growth factor-β
VEGF	Vascular endothelial growth factor
XMT	X-ray tomography
XRD	X-ray diffraction
XRF	X-ray fluorescence

1 INTRODUCTION

In 1969 Larry Hench invented Bioglass®. Bioglass, or 45S5, was the first artificial material to form a chemical bond with bone [1]. Not only did the glass bond, the strength of the bond formed was greater than that of the bone itself. Bioglass has been shown to up-regulate seven families of genes in bone forming cells, osteoblasts, a phenomenon termed osteoinduction [2]. Here, the term osteoinduction is used to mean stimulation of progenitor cells to differentiate into osteogenic cells to produce new bone, even away from an implant/bone interface.

The 45S5 Bioglass composition was 46.1 mol% SiO_2, 26.9 mol% CaO, 24.4 mol% Na_2O, and 2.6 mol% P_2O_5. Since its invention, 45S5 has been used to aid bone regeneration in more than a million operations in jaw and orthopaedic repairs [3].

To date, bioactive glasses in particulate form have gained success in various commercial products. By being mixed with a viscous media, such as blood, the particles allow ease of use by enabling it to be packed into a defect or wound site. PerioGlas® was the first particulate Bioglass commercially available and is now sold by NovaBone Products LLC (Alachau, FL) in 35 countries. It has a particle size between 90-710 μm and is used to regenerate the jaw, beneath teeth, to permit anchoring of titanium implants or reinsertion of a tooth. The first successful product available from an alternative composition was BonAlive (S53P4) 53.8 mol% SiO_2, 21.8 mol% CaO, 22.7 mol% Na_2O, 1.7 mol% P_2O_5. It has a granule size between 1-4 mm and has been successfully used in various clinical trials for bone defects between 1- 30 cm^3 [4].

Surgeons tend to mix bioactive glass particles with blood to form a putty to ease use *in vivo*. Although this creates a malleable format it also allows a high variability in samples due to differences in ratio of glass to blood. NovaBone

acted on this market need by releasing a NovaBone® putty, which is 69% Bioglass held within a glycerine binder. Its performance was compared with powder compaction in a 10 mm diameter defect in the spine of a sheep. The defect filled with putty yielded 22% more bone ingrowth than the particulate equivalent after 6 weeks of implantation [5]. There are two hypotheses as to why this occurred. One is that the packing within the putty, being of lower density than the particles alone, when pushed into the defect, allowed more bone to grow between the particles. Another hypothesis is that the pH environment produced by the putty creates a more favourable environment than the neat powder itself.

The variation in results seen between glass in it raw powder form and use as a putty have led to investigations regarding the ideal form that the glass should be supplied in. The *in vivo* success of the NovaBone putty has steered researchers to investigate the concept of temporary scaffold templates, mirroring the gaps created within the putty by forming a construct with open porosity to steer cell growth enhancing vascularised bone development.

Scaffolds can be produced by sintering glass particles. The problem is that the original Bioglass composition, 45S5, has a very narrow sintering window (Section 2.2.2) of less than 100°C [6], therefore it is difficult to produce 3D structures which remain amorphous post-sintering. If the sintering process is not tightly controlled, then a glass-ceramic is formed [7].

Bioglass's bioactivity is due to its controlled release of ions into the surrounding environment, which stimulate osteoinduction, and also result in the precipitation of hydroxycarbonate apatite (HCA) upon the surface of the material. This HCA layer is similar to bone mineral and is thought to interact with collagen fibrils from the host tissue enabling a bond to form between the glass and the bone itself. If the glass crystallises, this reaction is altered and consequently the bioactivity is reduced [8]. Filho *et al.* [9] showed that formation of the HCA took 12 h longer when the samples were crystallised,

compared with amorphous 45S5. Partial crystallisation could lead to inhomogeneity within the material and preferential degradation of certain phases or ions altering local pH rises [10–14] .

Due to the clinical need, and subsequent potential success of a material that induces osteoinduction, researchers have investigated various glass compositions to gain comparable bioactive performance but with an enhanced sintering widow [6, 15–18]. By having a larger thermal processing window, sintering, without the formation of a crystalline phase, could be achieved. This would enable the formation of solid constructs while maintaining the bioactivity of the glass.

An optimal scaffold should mechanically and structurally replicate the extracellular matrix of human bone [4, 19], e.g. a three dimensional scaffold that can interact with the body, acting as a template for cells to grow through, and biodegrade at the rate of natural repair. Jones *et al.* [4, 19] suggested that the ideal scaffold would meet the following criteria:

- The surface should promote cell adhesion and absorption of biological metabolites;
- Osteoprogenitor cells should be influenced by the material to enable guided cell differentiation and proliferation;
- The scaffold should be absorbed at the same rate as the host tissue repairs, creating mechanical continuity;
- Degradation products produced by the dissolution/absorption process should be non-toxic and easily excreted by the body;
- The scaffold should be able to be manufactured into complex shapes which can be tailored to the defect of the individual.
- The device must have the potential to be produced commercially in high volumes to the required International Standards Organisation (ISO) and the Food and Drug Administration (FDA) standards [19].

A variety of methods and materials have been developed to manufacture scaffolds suitable for bone ingrowth, but to date none meet all of the above requirements. Either they have not had the desired level of bioactivity, or their mechanical properties have fallen short of the required target. The aim of this work is to investigate new combinations of processing methods and glass compositions to see if these problems can be addressed.

Thesis road map

Chapter 2 discusses the wider context of the research field and the surrounding literature. The analysis techniques and methodologies used are summarised in Chapter 3. Three bioactive glass compositions were studied, linking all three results chapters. Chapter 4 focusses on the adapted gel-casting foaming process and optimising its protocol for use with each glass composition. Chapter 5 aims to evaluate the gel-cast scaffolds bioactivity, to compare and contrast the glass compositions, their topography and their resulting ability to act as scaffolds for bone repair. Chapter 6 utilises a second manufacturing method, robocasting, and aims to optimise the processing parameters for the glass compositions chosen. Chapter 7 and 8 conclude the work completed and discuss the further work opportunities.

2 LITERATURE REVIEW

2.1 UNDERSTANDING BIOACTIVE GLASSES

A glass can be described as an amorphous brittle solid without long range order. It is formed by supercooling a molten composition so quickly that a periodical structure does not have time to form. This process can be described schematically by Figure 2.1 [20].

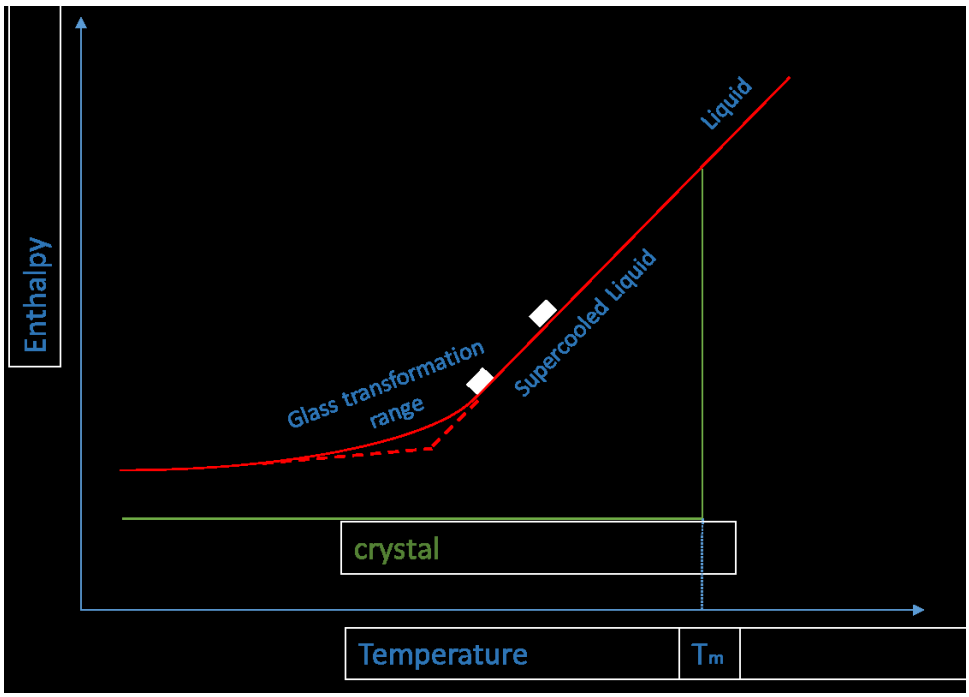


Figure 2.1: The effect of temperature on enthalpy of glass forming melts, adapted from reference [20].

As temperature reduces within the melt, the viscosity of the glass increases. When the viscosity becomes too great, atoms are no longer able to rearrange themselves, therefore the enthalpy of the system deviates from equilibrium. Eventually the viscosity of the liquid becomes so great that it is independent of temperature, and the atomic arrangement becomes fixed. The temperature range, where the enthalpy is between that of an equilibrium liquid and a frozen solid is known as the glass transformation region, and is dependent upon the kinetics of the particular system, which are altered by experimental factors,

such as cooling rate and composition. Within this region falls the glass transition temperature of the glass (T_g), deemed as the start of the glass transformation range. On reheating, after cooling, if enough energy is supplied to a glass, for example thermal energy for sintering, then the atoms can have enough energy to rearrange into a crystalline structure (the temperature for the onset of crystallisation) [20, 21].

2.1.1 Glass theories

Many attempts have been made to model glasses and their properties. The two most common models used are Zachariasen's random network theory and inorganic polymer theory [20].

Zachariasen's theory was put forward in the early 1930s. He suggested a theory relating glass structure to their properties. He categorised cations into 3 groups as to their effects on glass formation and the subsequent structure formed. He suggested that glasses are formed by a network former, which forms the backbone of the structure. In Bioglass, this is silica, forming Si–O–Si bridging bonds. When other components are added to the glass they disrupt the continuity of the network. These additives are known as network modifiers [22]. The addition of network modifiers result in the formation of non-bridging oxygen bonds, which disrupt the continuity of the network. A third category was also defined termed intermediate ions. Intermediates are a group which when added to a network can act as either network formers or modifiers, however, they cannot form a glass network on their own. This can be described schematically by Figure 2.2 [23].

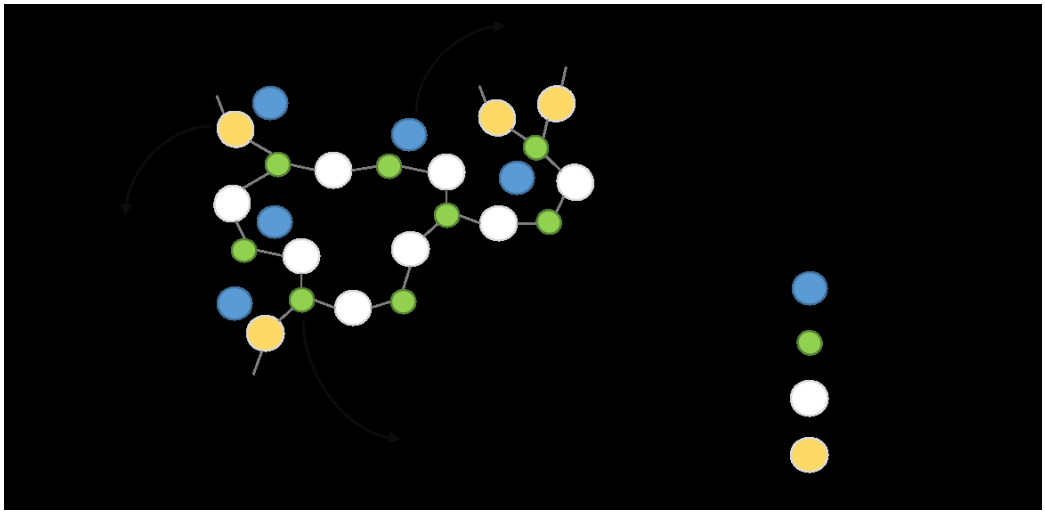


Figure 2.2: Schematic of the different roles ions can play within a glass network.

Holliday's [24] inorganic polymer theory describes the connectivity of glasses by comparing them to polymeric systems. One method of relating polymers to their properties is via their crosslink density. Holliday suggests that silicate glasses can be thought of as inorganic polymers of oxygen atoms crosslinked by silicon, suggesting that glasses can have continuous three dimensional networks of finite molar mass instead of discontinuous linear chains. The crosslink density of a glass can be defined as the average number of crosslink bonds greater than 2 for elements other than oxygen in the glass backbone. In bioactive glass this can be silicon or phosphorus. At a crosslink density of 0, the network changes between a linear polymer to a three dimensional network. A continuous silica network would have a cross link density of 2. The crosslink density of a glass can be used to predict various properties such as; surface reactivity, solubility, and expansion coefficient [25–27].

When a glass is made up of multiple components, the glass structure is modified. If a glass is pure silica then it is made up of tetrahedral silica bonded by bridging oxygen (BO) ions. When another constituent is added, the structure is modified, and some of the oxygen atoms which were previously bonded to silicon atoms are no longer bonded and become non-bridging oxygen atoms (NBO). The number of non-bridging oxygens is important as it alters the form

of the network, and creates heterogeneity. A silicate tetrahedron bonded to other tetrahedral by the maximum of four bridging oxygen bonds would be a Q^4 unit. Silicon atoms can be bonded to one (Q^3) or up to four (Q^0) non-bridging oxygens, altering the dissolution rate and mechanical properties of the glass. The number of bridging oxygen bonds can be quantified by Q^n, via solid state magic angle spinning nuclear magnetic resonance (MAS NMR), where n is the number of bridging oxygens in a silica tetrahedron [22, 28].

2.1.2 Stimulating bone growth

Stimulation of bone growth by Bioglass is thought to be a two stage process: first hydroxycarbonate apatite (HCA) is formed via dissolution and precipitation, then the HCA layer then interacts with the damaged collagen fibrils to form a bond with the bone. The dissolution products created from the glass also stimulate cells throughout the process. HCA formation is well understood and is thought to form in 5 stages, similar to those of conventional glass corrosion mechanisms [4]:

1. Rapid cation exchange, e.g. of Na^+ and/or Ca^{2+} in the glass, with H^+ from solution, creating silanol bonds (Si–OH) on the glass surface. This creates an increase in the local pH and a silica-rich region forms near the glass surface. (phosphate is also released within this first stage if it is in the glass composition);

2. High local pH leads to attack of the silica glass network by OH^-, breaking Si–O–Si bonds. Soluble silica is lost in the form of $Si(OH)_4$ to the solution, leaving more Si–OH (silanols) at the glass–solution interface;

3. Condensation of Si–OH groups near the glass surface in the silica-rich layer;

4. Ca^{2+} and PO^{3-}_4 groups migrate from solution and from the bulk glass to the surface to the silica-rich layer, forming a film rich in amorphous $CaO–P_2O_5$;

5. Incorporation of hydroxyls and carbonate from solution and crystallisation of the $CaO–P_2O_5$ film to HCA [4, 28].

One HCA has formed, the formation and interaction of the collagen fibrils is less well understood. The biological response of the body, which involves protein interaction, cell differentiation through to mineralisation is complex and consequently difficult to predict and study. There is also a lack of understanding in the roles of osteoclasts within the system, and whether they break down the silica network of the glass or just the HCA layer. This leads to questions regarding what surface chemistry and topography would create the perfect scaffold [4].

2.1.3 Theoretical predictions of the bioactivity of glasses

Within Bioglass, silica acts as a network former. Sodium and calcium act as modifiers within the glass system. Calcium is critical for the formation of HCA, and sodium is used to reduce the melting temperature of the glass and improve its viscosity for processing ease. It was initially thought that phosphorus acted as a modifier within the glass network.

One method to compare bioactivity of glasses suggested by Hill *et al.*, which is a refinement of Holliday's previous work [24, 25], is the network connectivity model. It can be defined as (where all values are in mol%):

$$NC = 2 + \frac{\mathrm{BO} - \mathrm{NBO}}{G} \qquad 2.1$$

BO represents the total mol% of oxides that can form bridging oxygen bonds, NBO is the total mol% of oxides that form non-bridging oxygen bonds and G is the total mol% of glass forming units within the system. This model is similar to that of Holliday's [24] inorganic polymer theory in that it estimates the quantity of disconnects within the system. A network connectivity of 2 directly corresponds to a crosslink density of 0, which is classed as the point where a linear polymer forms a three dimensional network [25]. Network connectivity is an average measure of the amount of disruption within the glass network, therefore there will always be some error in its calculation [22, 28].

Bioglass has a network connectivity of 1.9 according to Equation 2.1. Research has shown that glasses with a network connectivity higher than 2.4, have limited capability to form apatite upon their surface, and consequently are not likely to be bioactive [25, 26]. The higher the connectivity of the network the less bioactive a glass becomes, as the network is more condensed reducing dissolution of ions which stimulate the bioactive affect. By disrupting the network, by adding network modifying cations such as calcium or sodium, the network connectivity is reduced by increasing the number of non-bridging oxygens, therefore, increasing its bioactivity [22, 28]. However, these results were not based on *in vivo* data.

Since the publication of this theory in 1996, ^{31}P NMR has shown that phosphorus forms its own orthophosphate phase instead of acting as a network modifier as previously assumed [15, 26, 29-31]. The size of this phase separation is suggested to be submicron, due to the glasses optical transparency proving the lack of light scatter and X-ray diffraction properties of the materials. Phosphorus reduces the melting temperature but can also decrease the local pH at the implantation site.

Bioactive glass degradation *in vitro* controls its ability to form HCA at the surface and consequent formation of a chemical bond with bone. When Hench *et al.* [23] presented the initial Bioglass composition, 45S5, no theories were presented to quantify the level of bioactivity. Since Hench's 45S5 Bioglass composition, various glass compositions have been formulated and there is a need for a quantitative model to compare and predict their bioactivity.

Therefore, the equation has been modified, as shown in equation 2.2. In the modified equation P-O-P bonds are counted as bridging oxygens instead of non-bridging oxygens. Bioglass has a network connectivity of 1.9 or a modified network connectivity (NC') of 2.11 [22, 28]. All values are mol% and M_2^1O and $M^{II}O$ are mono- and divalent modifier oxides within the glass.

$$NC' = \frac{4(SiO_2) - 2(M_2^1O + M^{II}O) + 6(P_2O_5)}{SiO_2} \qquad 2.2$$

The network connectivity prediction of bioactivity is limited by various factors. It assumes that a glass is homogeneous, whereas in reality this is not correct; for example submicron phase separation can occur and some cations can have bonding preferences to certain species. It assumes that each ion behaves either 100% as a network modifier or former, so it does not take into account network intermediates. It also assumes that, once a bridging oxygen is broken and replaced with a non-bridging oxygen, the bond disappears, in actual fact it depends on the replacing ion and its characteristics. Hill *et al.* [25] reported that certain bonds within the glass network change between covalent to a more ionic nature depending on their valency of the substitution. However, the model does give a suggestion of how the bioactivities of different glasses can be compared with one another [25].

Table 2.1: Examples of commonly used bioactive glasses within literature [10, 15, 29, 32].

all mol. %	SiO_2	CaO	Na_2O	P_2O_5	K_2O	MgO	B_2O_3	SrO	NC'
45S5	46.13	26.91	24.35	2.6					2.11
13-93	54.6	22.1	6.0	1.7	7.9	7.7			3.01
13-93B3		22.1	6.0	1.7	7.9	7.7	54.6		3.01
BonAlive (S53P4)	53.9	21.8	22.7	1.7					2.54
6P53B	51.9	19	9.8	2.5	1.8	15			3.31
ICIE16	49.46	36.27	6.6	1.07	6.6				2.13
SBP-3	44.5	17.8	4	4.5	4	7.5		17.8	2.84

Table 2.1 summarises commonly used bioactive glass compositions from literature, and their modified network connectivity. Some of these glasses, such as 45S5, ICIE16, and S53P5 support the network connectivity measure of bioactivity [6, 15, 29, 33]. However, there are some that do not, such as 13-93 and 6P53B. 13-93 [34-37] is a well-documented glass, due to its good thermal processing window, which allows it to stay amorphous post-sintering. It

has a modified network connectivity of 3.01 which suggests it should not be bioactive. Simulated body fluid (SBF) testing, which is a test for HCA formation (Section 2.4.1), where a controlled volume of material is left in a solution that has similar ionic content to human body plasma [38, 39], showed that 13-93 formed HCA within 7 days, according to X-ray diffraction (XRD) [40, 41]. It also performed well *in vivo*, with one histology study showing that in scaffolds with 50% porosity and orientated pores, gave bone infiltration and remodelling of 46 vol% of a bone defect by 24 weeks [37]. This therefore, contradicts the presented theory that its modified network connectivity is too high to result in bioactivity. This highlights the complexity of the glass system and how difficult it is to predict a glasses performance, and therefore design a new bioactive glass, based on molar ratios alone.

2.2 BIOACTIVE COMPOSITIONS

Hench *et al.* [10] reports upon glasses made up of SiO_2, Na_2O, CaO and P_2O_5. SiO_2, Na_2O, CaO compositions were varied to create a ternary diagram keeping P_2O_5 at 6 wt%, as shown in Figure 2.3. However, published data to support the creation of the diagram is limited.

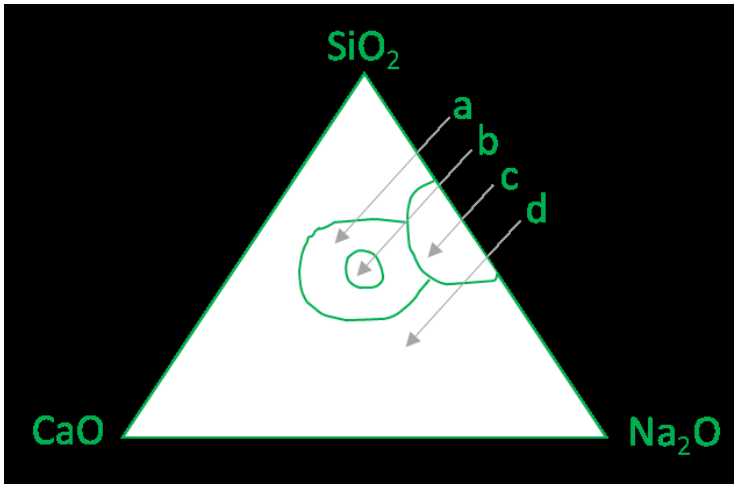


Figure 2.3: Compositional map showing the relationship between CaO, Na_2O and SiO_2 where P_2O_5 was held constant at 6 wt %, after [42]. Region A: bioactive and bond to bone, b) glasses which also bond to soft tissue, c) highly reactive glasses, and d) glasses which do not dissolve.

Compositions in region A are reported to be bioactive and fully bond to bone; region labelled B is a sub category formed within A, in which some glasses have been shown to form bonds with soft tissue. Glasses with compositions within region C are thought to degrade too quickly, e.g. within 10–30 days from implantation, due to too low a network connectivity. The boundary between A and C is dependent upon the ratio of surface area to solution [10] [42]. Glasses in region D do not dissolve and act as inert materials due to their high network connectivity and low concentrations of modifiers reducing dissolution. This is reported to be when silica concentrations are greater than 60 mol%, however there is limited date to support this. Materials which do not dissolve can elicit a defensive response within the body leading to encapsulation by fibrous tissue. Figure 2.3 suggests that the balance between elements within the glass greatly affects their performance, a slight change can alter a glass from bonding to bone to being completely inert [4].

Since the discovery of the original 45S5 composition, researchers have investigated the effect of other elements on dissolution behaviour and bone formation; these include borate, magnesium, potassium, strontium and silver (Section 2.1.3). Small changes in composition have a had a dramatic effect on the glass network [4, 26].

The number of different elements added to the composition needs to be carefully considered. The ratios of the elements within the glass control its bioactivity by affecting the network connectivity, dissolution characteristics, mechanical properties and the sintering window therefore, it has to be tightly controlled [10]. The more elements that are added, the more complex the system becomes and mixed alkali effects can occur. The mixed alkali affect describes the non-linear affect that multiple alkali ion additions can have on a glasses thermal and mechanical properties, due to their mobility within the network. Tylkowski *et al.* [43] completed a systematic study of alkali additions of sodium, lithium and potassium into the 45S5 network. The ionic additions

altered the packing within the network, which created unexpected non-linear property changes, such as increased sintering window, increased hardness and Young's modulus.

2.2.1 Dissolution behaviour

The dissolution characteristics of a glass and the speed at which it dissolves is associated with its chemistry, through ionic additions as its consequent network connectivity. In general, the higher the number of network modifiers, the more disrupted the forming network becomes therefore, the greater the dissolution [44, 45]. However, glass chemistry alone does not define dissolution, it is associated with a variety of other bulk material, topographical, and surface effects. This can be described schematically by Figure 2.4, adapted from Hoppe *et al.* [46].

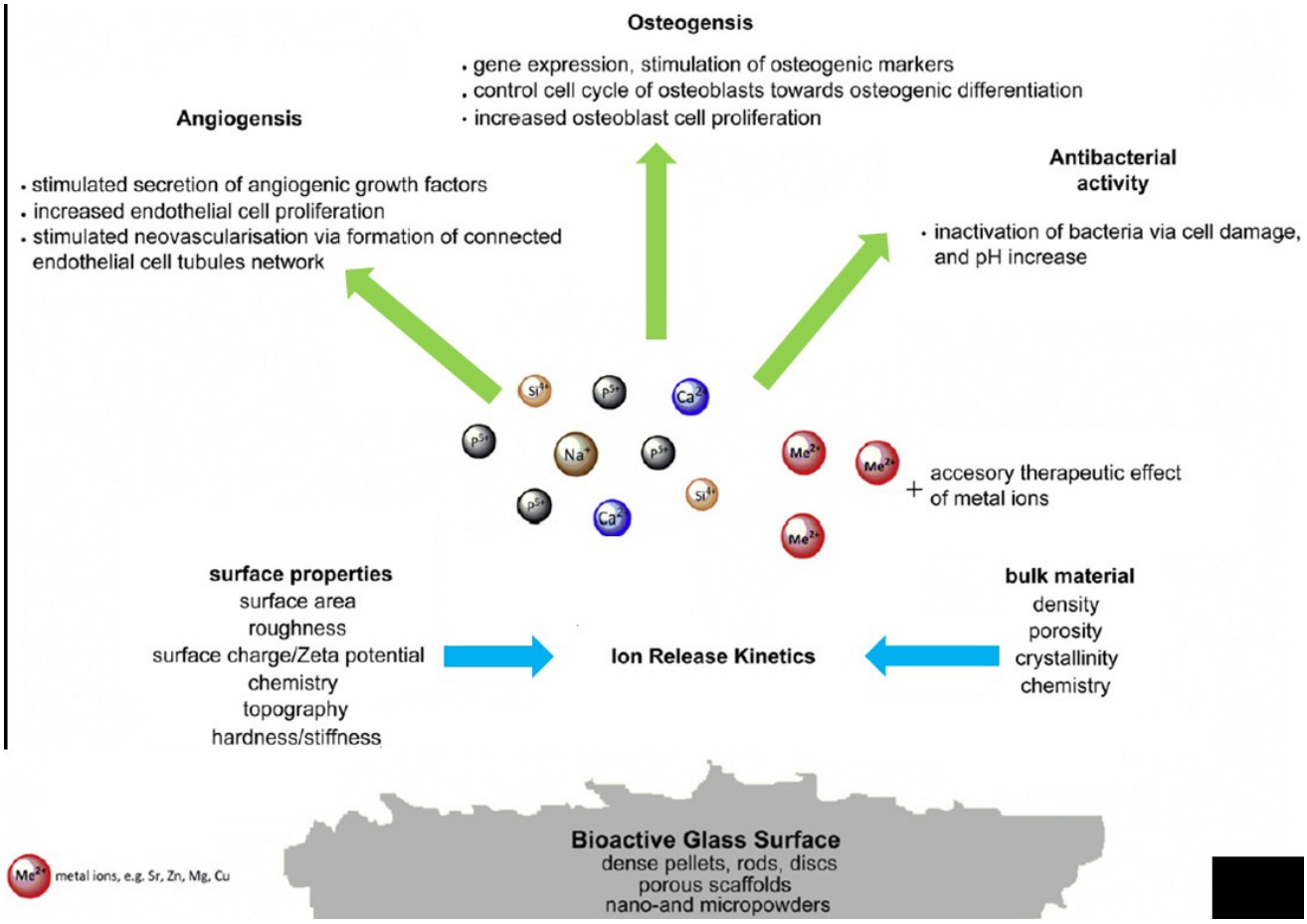


Figure 2.4 An overview of biological responses to ionic dissolution products of bioactive glasses, adapted from reference [46]

The biological response is dependent on the surface and bulk properties of the material and the environment in which it is in [46]. Osteogenesis, angiogenesis (blood vessel formation) and antibacterial responses are composition dependent and can be tailored by including various ionic additions. Dissolution behaviour can be investigated within the laboratory by SBF testing, cell culture studies and *in vivo* testing, discussed in Section 2.4. All of these test methods can be used to help predict the behaviour within the human body.

Over recent years many different elements have been added into silica, phosphate and borate based glasses and their effects *in vivo* and *in vitro* investigated. Doping of glasses with therapeutic ions has gained momentum in recent years, pushing the boundaries of applications for bioactive glasses. This is due to their low cost, controllability, and availability compared with the additions of growth factors [47–49]. The behaviour of ionic additions, their effects, and performance are discussed:

Boron

Bioactive glass implants can remain present after many years within the body due to the silica backbone degrading very slowly [50]. This has led to substituting borate for silica as the primary network former to increase dissolution rates [51–59]. It is thought that the boron dissolves into boric acid $B(OH)_3$ reducing the local pH. Research has reported that boric acid can greatly influence ribonucleic acid synthesis and is thought to have subsequent positive effects on the angiogenesis pathways, including vascular endothelial growth factor [46, 60].

Rahaman *et al.* showed that borate substitution resulted in up to 10 times faster glass dissolution and HCA conversion when compared with the silicate equivalent *in vivo* in both wound and bone healing studies [61, 62]. These tests were completed by substituting boron with silica in 13–93 glass. 13–93 has a very high modified network connectivity of 3.01, as previously discussed, consequently making it the most slowly degrading glass used in bone

regeneration experiments. The comparison of borate doped 13-93 and 45S5 by Liu *et al*. [56] showed that the borate glasses did degrade faster, and form amorphous calcium phosphate quicker, but that its conversion to crystalline HCA was slower than that of silica 45S5. This suggests that borate glasses may be most suitable for applications where fast dissolution is imperative such as wound and soft tissue repair [59].

Cobalt

An issue associated with bioactive glass scaffolds for bone repair is the need for the formation and supply of blood vessels. To be able to achieve regrowth of the host tissue throughout the scaffold, the scaffold needs to form an energy and waste stream by recruiting blood vessels.

The first approach to solve this was to look at scaffold design in terms of porosity and tortuosity [54]. Secondly, studies looked at the influence and effect of preconditioning with growth factors [63]. The most recent approach to improve blood vessel formation and propagation is to incorporate ions into the glass structure that can stimulate their growth, e.g. cobalt. Cobalt ions can mimic a state of ischemia or hypoxia which can stimulate angiogenesis. The body responds by increasing blood vessel formation. Cobalt, as Co^{2+}, has been shown to act as a chemical inducer of the hypoxia-inducible factor (HIF)-1α pathway. In normal oxygen environments (HIF)-1α is continually made and degraded. If (HIF)-1α can be stabilised it can be combined with (HIF)-1β forming HIF-1 which then up-regulates a number of genes associated with hypoxia response, mesenchymal stem cell (MSC) survival, extracellular matrix remodelling and angiogenesis [64]. Therefore, cobalt has started to be incorporated into glass compositions for bone and wound repair [65-70].

Cobalt acts as an intermediate, both disrupting and modifying the glass network and also taking a forming role [65, 68], [71]. Hoppe *et al.* [71] completed an experimental analysis of cobalt substitution into 13-93, showing that by adding

cobalt, the glass transition temperature of the glass reduces due to replacement of Si–O bonds with weaker Co–O bonds within the glass backbone.

One concern regarding the use of cobalt is its toxicity. Current literature has mainly focused on low concentrations substitutions, with a maximum of 10 mol%, with most studies focusing upon compositional series between 0–5 mol% of CoO [64, 69, 70]. One study used mesoporous sol–gel bioactive scaffolds and investigated the effects of mol% cobalt substitution on vascular endothelial growth factor (VEGF) levels. It showed that low amounts of cobalt (<5 mol%) was not cytotoxic. However, they did not test glasses with greater than 5 mol%. Due to the meoporous nature of these glasses, which created much higher specific surface area, their local short term dissolution would be much higher than their melt derived equivalents. Therefore, transferring these results to comparable melt derived compositions may yield different results. The glasses containing cobalt substitution for calcium significantly enhanced VEGF secretion and HIF–1α stabilisation. Confirming the hypothesis that this could be a way to increase blood vessel formation [69].

Lee *et al.* [70] manufactured melt derived phosphate–sodium–titanium–cobalt glasses, of composition $(P_2O_5)_{45}(Na_2O)_{20}(TiO_2)_5(CaO)_{30-x}(CoO)_x$ where x is = 0, 5, 10, and 15 mol). They report increased VEGF secretion from osteoblastic MG63 cells, when exposed to glass discs at 1, 3 and 7 days. VEGF response was greatest for glass 5 mol% CoO, but this study also showed that phosphate glasses alone, with no cobalt substitution, also enhanced VEGF compared with the control of tissue culture plastic. The results raise questions regarding what is the key ion that is enhancing (HIF)–1α stabilisation. In this composition multi–ion dissolution may be influencing the change or positive effects could be solely due to the cobalt release. These studies are interesting and important for bioactive glass understanding. VEGF is key in angiogenesis so up regulating and controlling its production would enable greater and better vascularised bone formation [72].

Magnesium

Magnesium's role within the glass network is currently debated within literature. A study by Watts *et al.* [30] investigated a range of glass compositions (49.5 SiO_2, 1.1 P_2O_5, (23(1−*x*))CaO, 26.4 Na_2O, *x*MgO all mol%) substituting calcium for magnesium between 0–23 mol%. ^{29}Si magic angle spinning nuclear magnetic resonance (MAS–NMR) showed that with increasing magnesium addition, a shoulder in the silica peak appeared suggesting magnesium enters the network as both a former, as MgO_4, and a modifier as Mg^{2+}. Their study suggested that within their compositional range 14% of the total magnesium within the system acted as a network former, the remaining 86% as a modifier. This hypothesis was supported by the decrease in the onset of the glass transition (T_g) temperature and T_g itself. The paper continues to hypothesise that magnesia will only behave like this when the silica network is highly disrupted, and that in general Si–O–Si bonds are energetically favourable to form over Mg–O–Si bonds. Due to the mixed reports in literature [30, 73] about magnesium behaviour within the network it does suggest that magnesium's behaviour is composition dependent and related to the level of silica disruption. Magnesium additions are also beneficial as they create an increased sintering window by raising the crystallisation temperature [30].

In terms of biological influence, Mg^{2+} has been shown to play a critical role in bone remodelling and skeletal development. Studies completed in bioceramics show that by adding magnesium to alumina in orthopaedic implants improved integration of cells and enhanced gene expression of extracellular matrix proteins [74]. However, magnesium inclusion within bioactive glasses retards apatite formation during bioactivity (SBF) testing [75–77]. Whether this is due to its effects upon the network and consequent release rate rather than the magnesium ions itself is unknown.

Strontium

Strontium has been shown to be an effective treatment for osteoporosis, and is currently commercially available as the drug Strontium Ranelate [78]. It is understood that SrO release into the body affects the replication of pre-osteoblastic cells, while reducing the function of osteoclasts [79, 80]. A study by Autefage *et al.* on strontium substituted 45S5 showed that strontium had a global effect on human MSCs, up regulating the isoprenoid pathway. The work also showed BMP-2 was upregulated by the presents of strontium, which may result in MSCs progressing towards the osteoblastic lineage in response to strontium exposure [81]. Santocildes-Romero *et al.* also studied strontium substituted 45S5 at 0, 50 and 100 mol%. They used real time reverse-transcription quantitative polymerase chain reaction to study the effect of the glasses on specific osteogenic genes on rat mesenchymal stromal cells. The glasses upregulated all six genes associated with osteogenic differentiation: runt-related transcription factor-2, alkaline phosphatase, collagen type Iα chain, osteocalcin, BMP-2, and osteopontin. Their work also showed that strontium doped glasses produced greater enhancement of alkaline phosphatase and osteocalcin, compared with the calcium rich 45S5 [82].

Strontium is known to act as a network modifier within the glass network. It is commonly substituted for calcium within bioactive glass compositions due to their similar ionic radius, 1.16 Å verses 0.94 Å [83-86]. If the substitution is done on a weight basis then due to strontium's greater ionic radius, less ions are included compared to calcium [33, 79, 84]. This results in a more polymerised network and consequently reduces dissolution rates. This can be avoided if substitution is done on a mol%. Weight based substitutions have shown that strontium's size difference results in a more condensed network with increasing substitution, resulting in changes in mechanical properties, glass transition temperature and dissolution rate [87, 88].

Work by Fredholm *et al.* [33, 84] showed that in SBF testing strontium for calcium substitution enhanced HCA formation, by substituting into the HCA lattice. Their conclusions from XRD, FTIR and MAS-NMR analysis were that the glass with complete strontium substitution for calcium gave faster and greater HCA formation by 8 h. XRD and FTIR are non-quantitative techniques unless precise standards are formulated therefore, so this conclusion may be debated. Massera *et al.* [83, 85] found contradictory results regarding HCA formation in strontium substituted glass S53P4 (53.8 SiO_2, 21.9 Na_2O, 21.8 CaO,1.7 P_2O_5) with between 0 and 100 mol% substitution for calcium. In SBF, the thickness of HCA formed within a two week period for strontium containing glass was less than a strontium-free control. However, in cell culture media (DMEM with 10% fetal bovine serum and 100 U μg^{-1} penicillin streptomycin) the inverse was seen. Their study also showed strontium presence lead to enhanced fibroblast growth and proliferation compared to the strontium-free calcium alternative.

Potassium

Potassium incorporation into bioactive glasses has primarily been to manipulate the thermal processing of the glass rather than for a therapeutic effect. It acts a network modifier, breaking up the glass network reducing mechanical properties, melting temperature and increasing dissolution characteristics. Work by Salam *et al.* [39] showed that substituting potassium for sodium resulted in more thermal energy needed for crystallisation to occur by increasing disorder within the system, due to the mixed alkali affect [43]. This substitution came at the expense of bioactivity, with an apatite layer forming faster in potassium free glasses [89].

Zinc

Zinc ion incorporation into bioactive glasses has been shown to have multi-functional response. Zinc has been shown to have an anti-inflammatory effects, by reducing the secretion of tumour necrosis factor (TNF-α) and interleukin-1, and can stimulate bone formation by activation of protein synthesis by

osteoblasts [46, 73, 90–95]. Studies have shown correlation between concentration of zinc and increased alkaline phosphatase (ALP) activity, as well as angiogenic stimulation including VEGF [92, 95, 96].

In most research zinc ions were substituted for calcium as both are thought to behave as network modifiers within the glass network. A study by Jaroch *et al.* [97] used molar ratios of calcium and zinc of 1.5, 3.5 and 6.5. Their *in vitro* testing showed retarded HCA formation compared with calcium glasses. They hypothesised that zinc substitution slowed the rate of HCA formation and inhibited the transformation from an amorphous to crystalline structure. This theory has been supported by various other studies with substitutions varying up to 10 mol% [98, 99]. This could be due to the lack of calcium available within solution to allow transformation at the same rate as comparable calcium compositions, or due to zinc also taking a network forming role.

Silver

Silver is known to have good antimicrobial properties, therefore silver doped bioactive glasses have been investigated for dental, degradable sutures, and bone applications [12, 100–104]. The antibacterial properties of silver ions are thought to be associated with their high surface to volume ratio due to their small ionic radius. This allows the ions to interact with the bacterial membranes resulting in cell fluids leaking from the membrane and consequent cell death. This effect is not unique to bacteria, in high concentrations silver can also cause eukaryotic cell cytotoxicity [105, 106]. Silver incorporation into bioactive glass has been approached by many processing techniques including melt and sol–gel processing. However, the favoured method is to introduce silver ions only at the surface of the material so that the antibacterial release is directly at point of need. Silver is monovalent, so when substituted into glasses for other elements which are divalent it reduces the number of non–bridging oxygens within the system. This results in a more connected silica network giving reduced ion release in bioactivity testing [73, 107].

One approach by Clupper *et al.* [12] to manufacture silver doped 45S5 bioactive glass scaffolds utilised the tape casting process to form 3D constructs. Then subjected the scaffolds to a silver nitrate solution in ethanol between 0.01–0.1 M for 18 h. The glasses were then heated to 800°C to allow the silver ions to infiltrate the network as modifiers. The glasses released non-toxic concentrations of silver measured via Inductively Coupled Plasma Optical Emission Spectrometer (ICP–OES), which was tailorable by varying the molar concentration of soaking solution used suggesting this method could be an approach for antibacterial use *in vivo*.

A study by Newby *et al.* [102] took this concept further by manufacturing 45S5 scaffolds by the foam replica method and doping them with silver via molten salt ion exchange. Their results showed that with increasing silver concentration the less human periodontal ligament stromal cell survived. This highlights how challenging it is to tailor the concentration of therapeutic ion release to achieve the antimicrobial goal without inducing cytotoxicity. The limitation of these studies are that they fail to quantify the concentration of silver that has entered the glass network, so precise glass compositions are unknown.

Copper

During angiogenesis, copper is found in human endothelial cells. Initial analysis showed that copper depletion impedes angiogenesis in a wide variety of cell types [108]. It is reported to enhance angiogenesis by stabilising the hypoxia-inducible factor (HIF-1α) expression, which, as with cobalt, mimics hypoxia, resulting in the differentiation and recruitment of cells and blood vessel formation through the body's automated response. The use of copper ions to stimulate angiogenesis in wound healing is thought to speed up the body's response by stimulating proangiogenic factors such as transforming growth factor-β (TGF-β) and VEGF [47, 109–113].

Copper is thought to act a network modifier within the glass system. Stahli *et al.* [114] showed that 45S5 containing copper gave release rates consistent with other modifier ions.

Applications of copper containing bioactive glasses have been focussed upon wound healing applications and have therefore used fast degrading glasses like 45S5 or borate glasses in high surface area formats. One study by Zhao *et al.* [112] used a borate equivalent of 13–93 containing 0–3 wt% copper, formed into microfibers via a melt spinning technique. Their study showed that their glasses promoted VEGF and simulated angiogenic genes of the fibroblasts in *in vitro* testing of human umbilical vein endothelial cells and fibroblasts. They continued to test the materials *in vivo* in a 2 cm full thickness wound in 2 year old male Sprague–Dawley rats. The glasses with the highest copper doping, 3 wt%, had a significant angiogenesis response when compared with undoped fibres.

A study by Hu *et al.* [111] suggested that human fibroblasts were not influenced by copper ions alone, suggesting that a more complex mechanism is taking place due to the overall ion dissolution, not just the copper, which supports fibroblast proliferation.

Dosage questions raised by the effects of high quantities of boron and copper in rat kidneys have been assessed by Lin *et al.* [115]. Their data showed minor kidney degradation in all animals tested after four weeks, but no chronic histopathological changes were seen. The paper debated whether the kidney changes seen were within the normal range for the animal type at the euthanasia age. This paper is limited as no reference is made to a control within the study. Copper cytotoxicity has also been addressed by various studies and it is thought in the wider context that high levels of copper results in free radical species generation which can result in neurodegenerative diseases [114, 116, 117]. Studies doping bioactive glasses with up to 10 mol% of copper have shown conflicting results in literature regarding their cytotoxicity,

however, most studies have not fully quantified their glass compositions post manufacture so the actual copper concentrations may be different from their estimates [111, 114, 117–120].

Conclusions on glass compositional effects on bioactivity

Comparing and understanding ionic additions within bioactive glasses is complicated. The range of elements that can be chosen, and the possibility of unexpected property and dissolution affects created is difficult to predict. It is also difficult to determine the specific effects of an individual ions dissolution on a system or cells even in a series of glasses as changing one element cannot be done discretely without altering the concentration of another within the system. Due to the mixed alkali affect and composition depend variables especially where elements act as intermediates can make translating literature conclusions about ionic behaviours to other systems problematic.

Another issue with comparing literature data from *in vitro* and *in vivo* testing is the lack of continuity within testing methods. Different approaches to testing, and the varying formats that glass products can form result in a huge spectrum of concentrations of material being tested. As bioactive glasses dissolution is dependent upon the surface area of material available, drawing conclusions or comparing available literature is challenging.

2.2.2 Driving forces for sintering

The thermal behaviour of glasses can be studied via Differential scanning calorimetry (DSC), which can yield information of T_g, glass crystallisation onset (T_c onset) and melting temperature (T_m), Figure 2.5. T_g can be described as the temperature at which the glass has enough energy to flow like a viscous fluid. T_c onset is the temperature at above which the glass has enough energy to start forming crystal phases within its structure [20].

To be able to form a mechanically strong glass scaffold, the glass particles need to be sintered (fusion of particles), which required heating above T_g. As

the glass particles are heated a liquid phase forms at the points of contact, the two liquids mix and on cooling form one continuous glass network. For this to occur there must be a mechanism for material transport and a supply of energy that is great enough to activate and sustain the transportation mechanism.

Sintering needs to be optimised for the particle size and composition used so that strong constructs are formed which remain amorphous. Glass is in a metastable state, so once heated above its T_g the atoms begin to rearrange. If a glass is held at an elevated temperature for long enough, the atoms will rearrange into a crystalline form to reduce the overall energy of the system. The limitation of 45S5 Bioglass is that its sintering window (Figure 2.5), the temperature difference between T_g and $T_{C\ onset}$, is approximately 100°C, which this makes it very difficult to manufacture 3D scaffolds without crystallisation taking place, which can reduce the glasses bioactivity. This has resulted in new ionic additions and compositions being designed which allow enhanced sintering capability while remaining bioactive, such as 13-93 [10-14].

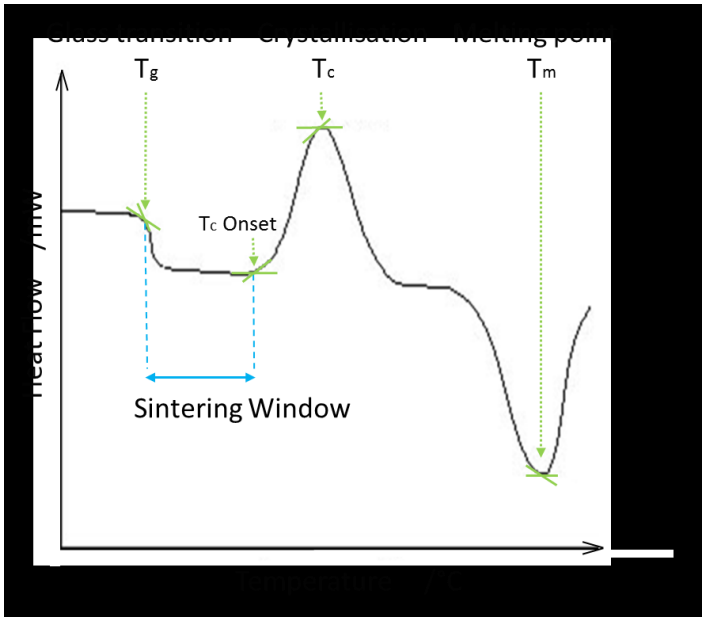


Figure 2.5: Schematic of a differential scanning calorimetry plot for a glass material showing the concept of a thermal processing sintering window.

There are many methods of sintering which all use different sources to create the energy needed for mass transport to take place: Conventional sintering [6,

41, 55, 121], spark plasma sintering [100, 122, 123] and laser sintering [40, 124-127] have all been used with bioactive glasses.

Conventional sintering is the most commonly used sintering method due to its ease, wide availability and control. Conventional sintering uses an electric resistance furnace to heat samples to the required temperature, this method heats samples from the outside in and can create non-uniform distribution depending on the heating elements and size of the furnace used.

2.3 SCAFFOLD MANUFACTURING METHODS

Since the concept of manufacturing bioactive glasses into 3D scaffolds has evolved, many groups using many different glass composition and numerous processing methods have taken on the challenge. The diversity of the processing methods used results in a wide variety of macro and micro topographies, porosities, and consequent strengths.

In recent years 3D printing has grown rapidly. 3D printing encompasses a whole genre of automated manufacturing techniques, including ink jet printing, selective laser sintering, freeze extrusion fabrication, robocasting, laser melting, and stereolithography. Many of these processes have been adapted for use with bioactive glasses. Due to the breadth of this field only the two most common 3D printing methods that used for bioactive glasses (robocasting and selective laser sintering) will be discussed.

2.3.1 Foam replica process

The foam replica process employs a polymeric foam to act as a template for a glass slurry. The foam is infiltrated with a stable suspension, and then dried. A heating programme is then used to remove the polymer foam and sinter the particles to form a sintered interconnected porous material. The mechanical properties of the material produced via this technique depends on the particle packing within the foam prior to burnout, which is controlled by the stability and concentration of the suspension used.

The first to achieve this was Fu *et al.* [34] who used the foam replication process with the 13-93 glass composition (54.6 mol% SiO_2, 22.1 mol% CaO, 6.0 mol% Na_2O, 7.7 mol% MgO, 7.9 mol% K_2O,1.7 mol% P_2O_5) with a particle size of 2 μm in an aqueous suspension. The scaffolds met many of the requirements for bone regeneration, previously discussed in section 1, with reported porosity of 85 ± 2%, interconnected pores between 100-500 μm, and compressive strengths of 11 ± 1 MPa. These values are similar to those of human trabecular bone and outperform other glass-ceramic foams reported in literature at the time [34]. This was due to their optimisation of glass loading within the slurry. Their particle size distribution allowed for good particle packing within the system enhancing sintering. Combining this with the sintering window provided by the 13-93 composition that allowed viscous flow without crystallisation during sintering, led to the formation of dense struts with limited distortion of the foam morphology.

A limitation of the foam replica process is that excess slurry can become trapped inside the sacrificial polymer foam after infiltration, which can be difficult to remove prior to burnout and sintering. It has to be squeezed out and if excess slurry remains, the structure will be heterogeneous with a porosity gradient being formed. Even with optimum processing, the foam replica method can leave struts with hollow centres which reduce the mechanical properties and performance of the scaffolds, as highlighted by the arrow in Figure 2.6.

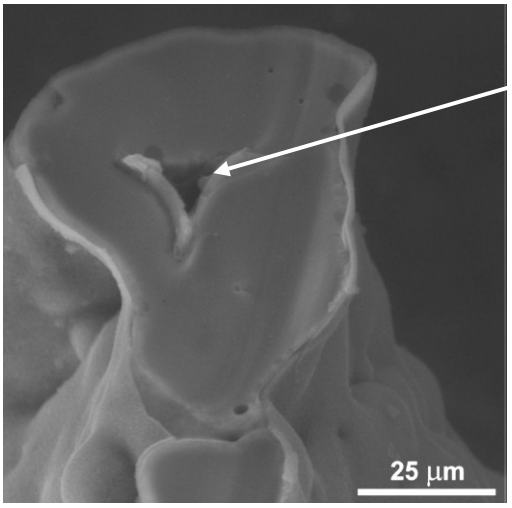


Figure 2.6: example of a hollow strut formed, highlighted by the arrow, during the foam replica processing, reproduced with permission from Hoppe et al.[71]

Gu *et al.* [128] completed *in vivo* and *in vitro* studies using 13-93B1 glass (6% Na_2O, 8% K_2O, 8% MgO, 22% CaO, 18% B_2O_3, 36% SiO_2, 2% P_2O_5 all in mol%) with the foam replica process. Their scaffolds had a porosity of 78%, with an average pore size of 500 µm, and compressive strength of 5.1 ± 1.7 MPa, half of that of their silicate equivalents. They were shown to nucleate HCA within 30 days in SBF, however concerns due to the dissolution of boron *in vivo* and the possibility of cytotoxic effects in high concentrations remain. Two osseous defect models were used in this study to assess the performance of the 13-93B1, a non-critical sized defect in a rabbit femoral head and a critical sized defect in the radius bone. The scaffolds were inserted without pre-treatment, but were loaded with and without platelet rich plasma (PRP) at the time of insertion. The scaffolds which were loaded with PRP were more successful than those without, however, they did not quantified the differences.

The use of PRP in pre-treatment is much debated in literature. Some studies suggest it advantageous (even though not quantified) to use PRP due to the inherent growth factors such as β1, and VEGF enhance the scaffold's osteoinductive properties [128]. However, PRP has a limited shelf-life, and stability, therefore its success in this area is dependent upon finding a suitable source.

2.3.2 Gel-cast foaming

Sepulveda *et al.* [129] first used gel-cast foaming to create porous ceramics. Rather than using a foam template, as used within the foam replica process, the ceramic slurry was foamed under vigorous agitation with the aid of a surfactant. The process used *in situ* polymerisation of an organic monomer, such as methacrylamide, to form a gel and stabilise the foam. The polymer was then burnt out during the sintering cycle.

Wu *et al.* [6] adapted this gel-casting process to manufacture scaffolds using the composition ICIE16 (49.46% SiO_2, 36.27% CaO, 6.6% Na_2O, 1.07% P_2O_5 and 6.6% K_2O, in mol%). This process was based upon *in situ* polymerisation of acrylamide by using a cross-linker (N,N'-methylene bisacrylamide), surfactant (Triton X-100), initiator (ammonium persulfate solution), and a catalyst (tetramethylethylene diamine).

The purpose of this study was to create a manufacturing process tailored to bioactive glasses that could produce scaffolds with a foam morphology and improved mechanical strength compared to the foam replica method by avoiding creation of hollow struts. ICIE16 was used as it was thought it would have improved bioactivity over 13-93, due to its similar network connectivity to Bioglass (45S5), while having an extended sintering window of approximately 200 °C; 100°C greater than that of Bioglass.

ICIE16 has not been widely used, it was first presented by Elgayar *et al.* in 2004 [15]. The majority of studies focus on the original Bioglass composition, or 13-93. SBF testing of ICIE16 showed that amorphous calcium phosphate formed within 8 h and it crystallised HCA formed within 3 days, which was much faster than the 13-93 results previously reported by Fu *et al.* of 7 days [34]. This could be a result of ICIE16 lower network connectivity (previously discussed) suggesting that is it more susceptible to ion exchange and dissolution which are the first stages of HCA formation.

The scaffolds produced by Wu *et al.* [6] had porosities of 79%, with modal pore diameters of 379 μm and compressive strength of 1.9 MPa. These values were a factor of 10 lower than those reported by Fu *et al.* [34] of foam replica scaffolds manufactured from 13-93. These could be due to a variety of different reasons, the difference in sinterability between the two glasses used, the difference in the manufacturing methods resulting in similar porosity but differences in pore formation and interconnect size.

If gel-cast scaffolds were to become commercial products the processing method must be scaled up for mass manufacture. Wu *et al.* [6] process relies on the foam being loaded into a mould seconds prior to gelation, approximately a 2 second window. When trying to upscale to mass manufacture the point between forming a stable foam and cross linking may not be great enough to reliably create high volumes of samples.

Another issue with the gel-casting process suggested was the formation of potassium sodium sulphate due to the reagents used. Although it is stated by Wu *et al.* [6] that sulphur is non-toxic and the quantity is unlikely to provoke a response, its removal from the processing method would still be beneficial.

These issues led to Tang [130] developing a gelatin-based adaptation of the gel-casting processing method which avoided these issues stated previously. The process moved from a polymerisation based gelation process to a thermally controlled process. His work reported the ability to manufacture scaffolds of another glass compositions, SBP-3 (see Table 2.1), with porosities and strengths within the range of cancellous bone. One aim of this thesis was to investigate the parameters in this new process and optimise it for ICIE16 and 13-93 compositions.

2.3.3 Selective laser sintering

Selective laser sintering is a layer-by-layer '3D printing' technique to manufacture green bodies. Particles are commonly mixed with a thermoplastic

binder after which, a laser locally heats the binder, forming mechanically stable green bodies. The powder bed drops and another layer of particulate is selectively bound. Unbound particles are removed and the green body is sintered. As with any 3D printing technique, its advantages are that complex or challenging geometries can be manufactured. However, it is limited by the accuracy of the laser, the size of construct, the detail of the features that can be formed, and the ability to completely burn out the binder without leaving residual porosity [127].

One study by Velez *et al.* [127] manufactured scaffolds of 13–93 glass, with particles of sizes up to 75 μm, using stearic acid as a binding agent. The scaffold with 50% porosity had strengths of 40 ± 10 MPa post-sintering. Work by Kolan *et al.* [40] reported mechanical properties within the same range as Velez *et al.* [127] of 41 MPa for 50% porosity. Their work looked at optimising the process by reducing the binder concentration and particle size, and increasing the laser power to increase processing speed. However, the time to produce scaffolds compared with competing 3D printing techniques, such as robocasting was still much longer.

2.3.4 Robocasting

Robocasting is another '3D printing' method being used to manufacture porous scaffolds from bioactive glasses. Originally developed in 1998 by Cesarano *et al.* [131], it can be described as a solution based extrusion process controlled by a computer aided design programme. A schematic of the set-up is shown in Figure 2.7 [132].

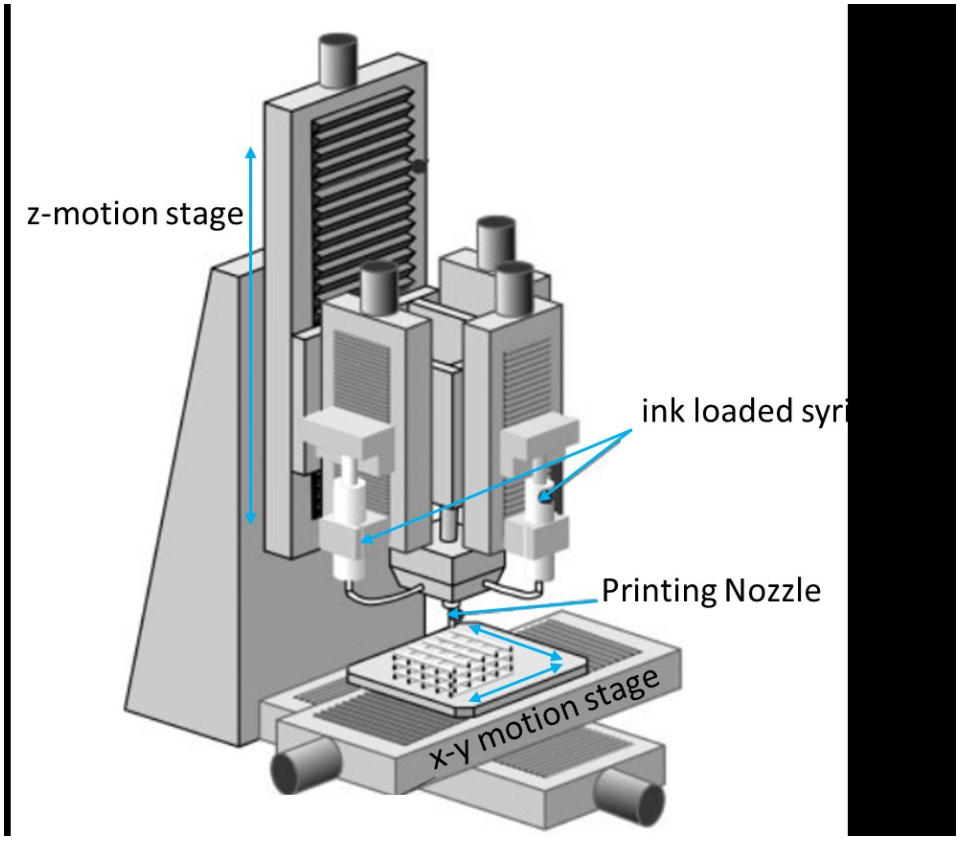


Figure 2.7: Schematic of robocasting set-up adapted from Dellinger et al. [132]

An example of a robocast scaffold is shown in Figure 2.8. Robocasting is the most commonly used 3D printing technique for bioactive glasses. This is for a number of reasons: the speed of fabrication; the ease at which inks can be produced; and the capability of machines. This enables the printing of inks with high glass loading, which produce scaffolds with low strut porosity, enhancing their mechanical properties. Robocasting also has the potential to create bespoke implants for patients with tailored geometries and pore distributions [34, 37, 133–138].

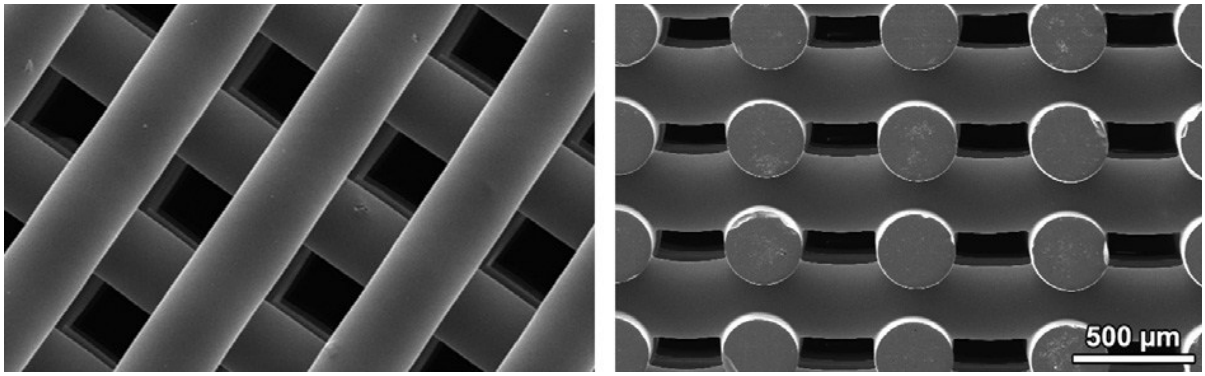


Figure 2.8: Example of robocast 13-93 scaffolds reproduced with permission from reference [135]

The robocasting technique relies on the formulation of glass loaded inks which can be extruded through fine diameter nozzles. The first development of this technique relied on manipulating the interparticle forces within particle loaded suspensions to create inks with the correct rheological properties for printing [139]. Now binder 'inks' are formulated with the correct rheological properties to act as a carrier of the particles which bind them together prior to sintering. An ideal ink would exhibit the following properties:

- Be easily mixed, forming a homogeneous ink without air bubbles or agglomerated particles;
- Incorporate high percentage volumes of glass powders to obtain dense struts for complete sintering, while maintaining a printable viscosity;
- Binder burn-out temperature needs to be below the glass transition temperature of the glass composition being printed;
- Rheological properties must be pseudoplastic, to be able to flow under the stresses implemented during the extrusion process, but once it has been extruded and the stress removed remain in its printed structure;
- The yield strength and storage modulus need to be great enough to withstand the compressive stress of multiple layers being laid down;
- Be of non-aqueous based chemistry to limit premature ion dissolution and reactions.

The first robocasting paper published for bone applications was by Franco *et al.* [140] using calcium phosphate and Pluronic F-127 surfactant as a carrier ink. Pluronic F-127 is a block co-polymer surfactant with thermally reversing rheological behaviour, made up of poly(ethylene oxide)-poly(propylene oxide)-poly(ethyleneoxide) tri-blocks (PEO-PPO-PEO) ($HO(C_2H_4O)_a(C_3H_6O)_b(C_2H_4O)_c$).

Pluronic F-127 can form a stable suspension when dissolved in water via steric repulsions of -OH groups by forming Van der Waals and hydrogen bonds with particles. At low temperatures it forms a low viscosity solution due to the absorption of water, allowing the polymer chains to slide across each other. Above its gelation temperature, the polymer chains can rearrange themselves to form micelle aggregates due to the absorption of water within the system becoming energetically unfavourable. The release of water molecules and the reduction of hydrogen bonding between the water and the -OH groups of the hydrophobic PPO segment results in the formation of a viscous gel, which is strong enough to be able to support multiple layers printed upon one another. At all temperatures it behaves pseudoplastically, reducing viscosity when subject to increasing force, enabling it to meet many of the requirements for a ink for robocasting [135, 140-143].

Using hydrogels, like F-127, as polymeric binders moves away from traditional surface chemistry, interparticle viscosity relationships and allows printing to be utilised for a much wider selection of materials. Since Franco's [140] work and the increased availability of robocasting technology other groups have looked at utilising this processing method with different ink chemistries and glass compositions, as summarised in Table 2.2 [37, 52, 137, 144]. Table 2.2 shows the range of inks that are currently used with various glass compositions. When manufacturing via robocasting, the ink chemistry in tandem with the particle size distribution and packing has a huge effect on the quality of the green body produced. The particle size and distribution of the glass needs to be tightly controlled to achieve a printable ink. The average particle size used in literature

is between 1–5 μm, enabling extrusion through nozzles as fine as 30 μm [140]. Due to bioactive glasses degradability in water, a particle size of this distribution is usually achieved by attrition milling in ethanol. A wide particle distribution allows the formulation of higher glass loaded inks by allowing rearrangement and slippage of particles during printing [140, 145].

Table 2.2: summary of different groups robocasting glass and ink combinations

**not amorphous post sintering **values not reported therefore, measured using imageJ from the published SEM images available*

Glass used	Max glass loading /Volume %	Ink chemistry and (dispersant)	Strut Size /μm	Pore Size /μm	Porosity /%	Compressive strengths /MPa
6P53B [133]	30	F–127 (water)	100	500	60	136 ± 22
13–93B3	45	Ethyl cellulose/ PEG (ethanol)	300 ± 20	420 ± 30	48 ± 3	65 ± 11
13–93 [52]						142 ± 20
13–93 [37]	40	F–127 (water)	330	300	47	86.9 ± 9
45S5 [137, 144]*	45	Carboxymethyl cellulose (water)	250–300**	Not available	63 ± 3	13 ± 1

Fu *et al.* [135] and Liu *et al.* [37] both robocast 13–93 particles between 1–2 μm using F–127 as their ink binder. Table 2.3 shows the versatility of the scaffold pore sizes, porosities, and strengths that can be achieved via this technique. As expected with increasing porosity given by increasing pore size compressive strength decreases.

The homogeneity of the ink, particle packing, sintering process, strut size and spacing all contribute to the scaffolds overall mechanical properties. As shown by Table 2.2 and Table 2.3 the strengths that can be achieved via robocasting were much higher compared with other discussed manufacturing techniques. This is due to the periodically arranged structure with layered struts, compared

with the random porosity created by foaming processing. Strength values are in the range of cortical instead of cancellous bone [146, 147].

Table 2.3: Comparison between the compressive strength of Fu et al. [135] and Liu et al. [37] using 13-93.

Authors	Compressive Strength /MPa	Pore Size /μm	Porosity /%
Fu *et al.[135]*	136 ± 22	500	60
	74 ± 13	750	70
	40 ± 7	1000	80
Liu *et al.[37]*	86 ± 9	300	47

2.3.5 Mechanical properties: can bone be matched?

Human bone is a complex composite made up of different layers. This can be described schematically by Figure 2.9. Cancellous bone is the inner spongy layer which initial scaffolds were modelled upon, cortical bone is the much denser outer layer which has much greater mechanical properties [148].

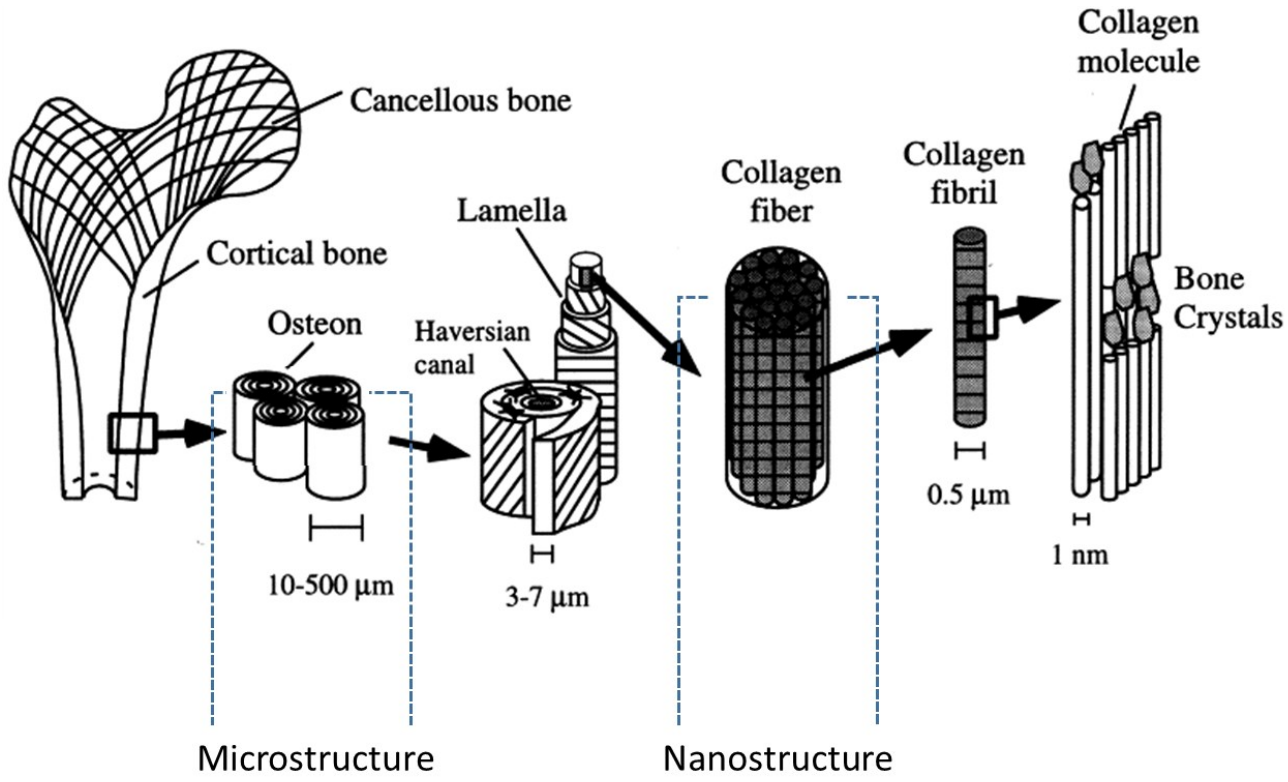


Figure 2.9: A schematic of the structure of human bone adapted from Rho et al. [148]

Table 2.4 summaries the mechanical properties of bone reported [146, 147, 149–152]. One of the complexities of designing scaffolds for bone repair from bioactive glasses is trying to match and maintain these properties during dissolution.

Table 2.4: Summary of the mechanical properties of human cortical and cancellous bone

	Compressive strength /MPa	Flexural strength /MPa	Tensile strength /MPa	Fracture toughness /MPa $m^{1/2}$	Modulus /GPa	Porosity /%
Cortical Bone [146, 147, 149–151]	100–150	135–193	50–151	2–12	10–20	5–10
Cancellous bone [147, 151, 152]	2–12	10–20	1–5	0.1–5	0.1–0.8	50–90

A review paper published by Fu *et al.* [151] reflected upon the current processing methods of various bioactive glass compositions and their mechanical properties. The issues associated with comparing mechanical property data published in literature is the variation in samples dimensions used and their mechanical testing protocols. As glasses are brittle materials and their mechanical performances are based upon critical flaws, sample dimension is key in their performance. Some sample test specimens have been tested at a third of their *in vivo* test size, which may give them an exaggerated mechanical strength value [21].

13-93 is one of the most commonly used glasses, and scaffolds have been made using the majority of commonly used processing methods; therefore, it acts as a useful benchmark for comparison. Figure 2.10 summarises the compressive strength values from current literature for scaffolds manufactured from 13-93 [34, 36, 40, 41, 121, 153-156], with reference to the values of cortical and cancellous bone stated in Table 2.4.

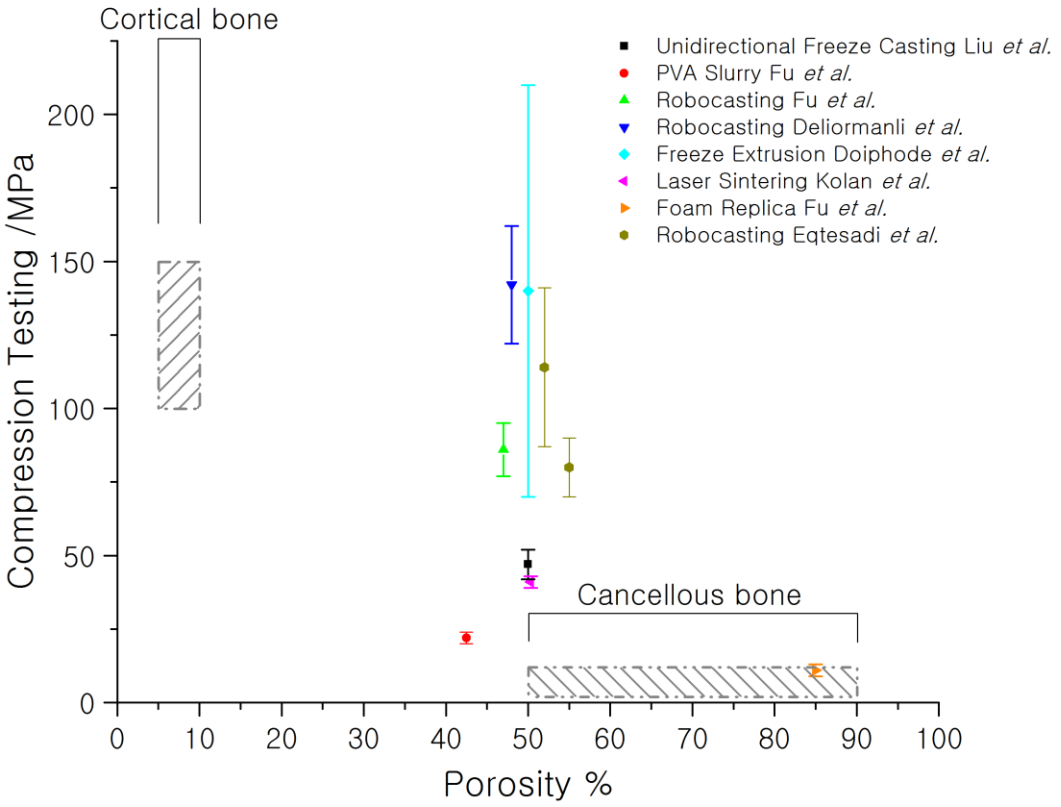


*Figure 2.10: Summary of current literature of scaffolds manufactured of 13-93 via various processing methods * grey areas denotes reported strengths of cortical bone and cancellous bone reported in Table 2.4*

Figure 2.10 summarises the compressive strength values reported for scaffolds manufactured from 13-93. The majority of scaffolds have porosities around 50% which is at the lower range of cancellous bone. Scaffolds manufactured via robocasting had the highest compressive strength values due to the controlled formulation of ordered struts available from this processing method which can sustain much greater load than randomly orientated porosity [52, 135].

As shown by Figure 2.10, only one set of scaffolds manufactured by Fu *et al.* [34] via the foam replica method met the required values for either bone type. The problem with compression testing is that the bone is actually subject to cyclic loading within the body, not a single compressive force that this test simulates. Also the nature of bioactive glass scaffolds is that they degrade over

time inducing their bioactive response, therefore, it is preferable to have a higher initial strength which reduces to the range of cancellous bone with dissolution, rather than meeting it initially and reducing to below it during dissolution.

2.4 TESTING BIOACTIVE PERFORMANCE

Testing of bioactive materials is a multistage process, to gain entry into the commercial market FDA and ISO approval is required. To gain this various testing methods need to be completed to prove material safety, as described schematically by Figure 2.11.

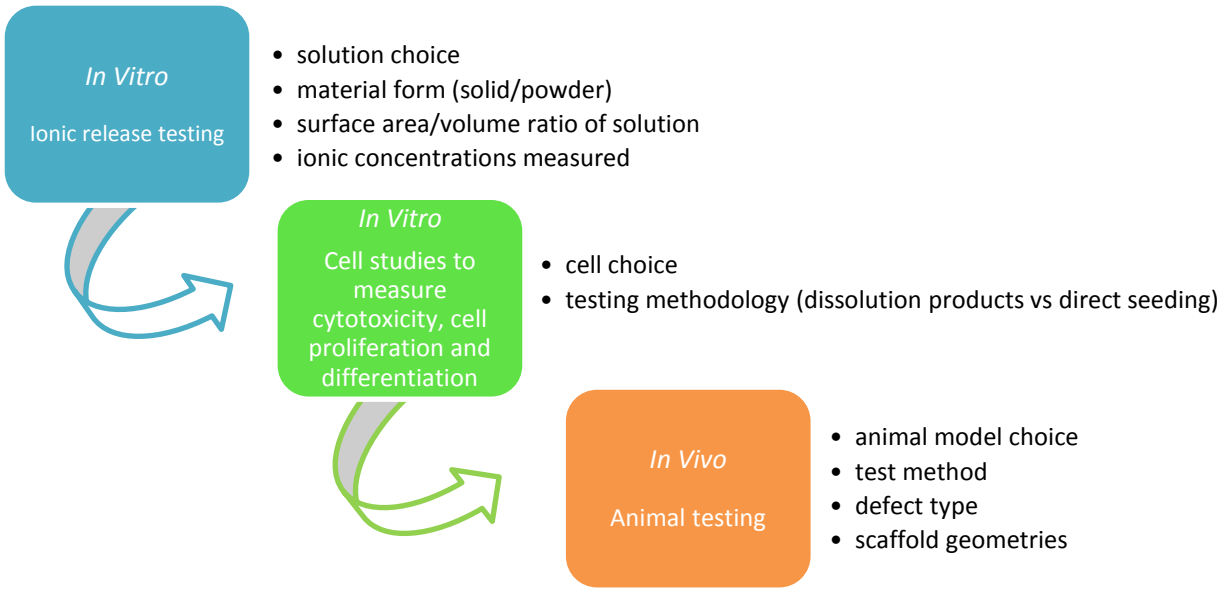


Figure 2.11: Schematic of the testing procedures options and variables to understanding bioactivity of bioactive materials

Figure 2.11 aims to convey the breadth and variety of studies and their variables that can be completed when studying a bioactive materials performance. Ionic release testing and cell studies can be completed to reduce the number of unnecessary and inappropriate animal tests on potentially toxic materials. However, due to the limitations of these tests methods only looking at individual systems in isolation, it is difficult to gain an understanding of how a material will perform *in vivo*.

2.4.1 *In vitro* testing

Dissolution testing

Bioactive glasses degrade over time in solutions releasing ions into their local environment. Within literature there is a huge variety of approaches to test this experimentally with studies varying; testing solution, sample to solution ratio, incubation environment and analysis method [32–34, 38, 48, 72, 98, 99, 112, 157–161]. Understanding the ionic release rate and quantities, and how ions can affect each other can give an indication as to how they may release and precipitate *in vivo*. The most commonly used solution for bioactive glass testing is SBF.

Table 2.5: Ionic Concentration of Simulated Body Fluid and Human Body Plasma all in mM [162]

Ion	Human Body Plasma /mM	Simulated Body Fluid /mM
Na^+	142.0	142.0
k^+	5.0	5.0
Mg^{2+}	1.5	1.5
Ca^{2+}	2.5	2.5
Cl^-	103.0	103.0
HCO^-_3	27.0	4.2
HPO^{2-}_4	1.0	0.5
SO^{2-}_4	1.0	0.5

SBF solution is intended to simulate the ionic environment of human body plasma, its composition is summarised in Table 2.5. When completing SBF testing the protocol is to keep samples in a dynamic environment at 37°C with a pH of 7.4; then at various time points remove and replace solution for ionic testing conducted via ICP–OES.

A positive result from an SBF test would be the precipitation of HCA upon the surface of the test material. Due to the highly saturated ionic concentrations in SBF the additions of ionic degradation products from bioactive glasses can create precipitation of a phosphate–calcium rich phase. This can be measured post testing via SEM or XRD or by measuring a simultaneous drop in calcium and phosphorus via ICP–OES.

Work by Deliormanli *et al*. [52] is summarised in Figure 2.12. Here they investigated both the mass and mechanical degradation rate of robocast scaffolds manufactured from 13–93 and 13–93B3 in SBF over 80 days. Instead of doing ionic release, via ICP–OES, they only studied pH change. 13–93 is a well characterised glass however, studying ionic dissolution gives a greater understanding of precipitation rates, and is characteristic of their particular scaffolds tested as relative surface area has a huge effect. There results show a drop in compressive strength with dissolution in scaffolds made of both compositions. The higher stability of 13–93 compared with 13–93B is evident by the greater weight loss seen in the 13–93B samples tested. Interestingly, the drop in compressive strength is similar, even though 13–93B lost nearly 50% more weight throughout the study. The SEM image of 13–93 shown in Figure 2.12 is an example of HCA precipitation upon a bioactive glass surface [52]. The borate substituted equivalent precipitate had a noticeably different morphology, but they did not specify or quantify the change.

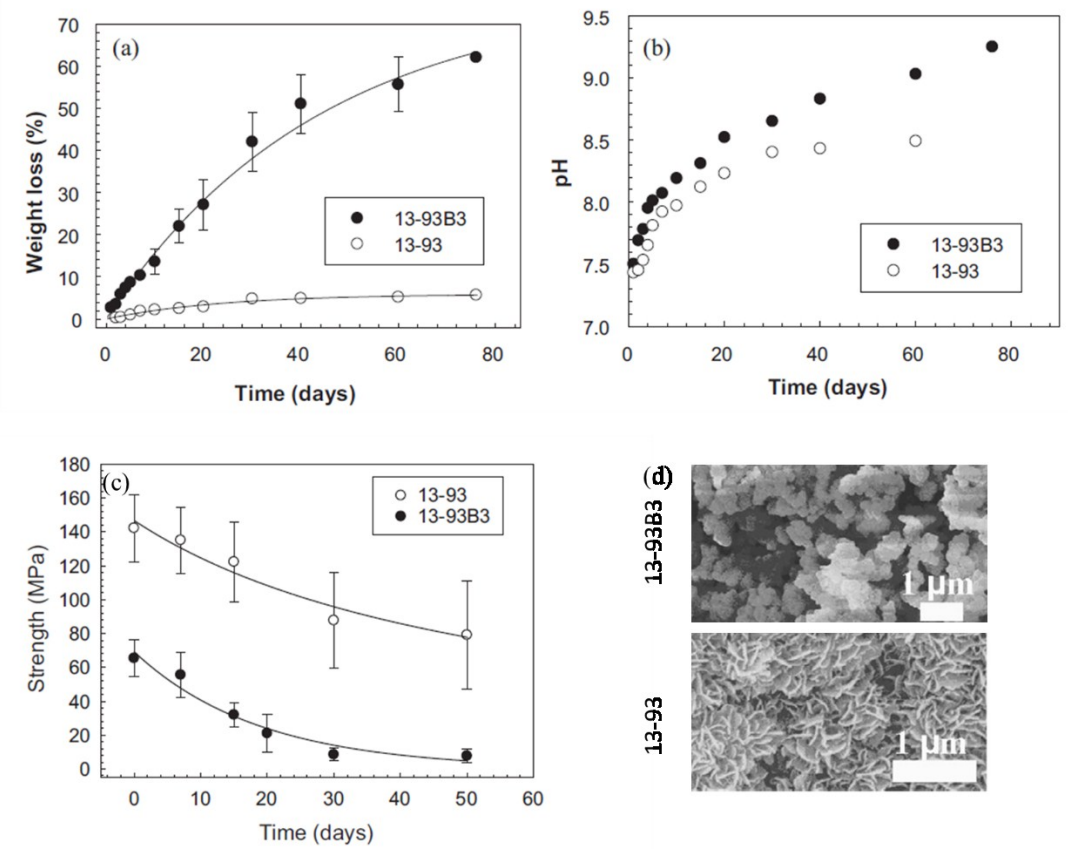


Figure 2.12: Summary of SBF testing results from Deliormanlı et al. [52] a) weight loss, b) pH change, and c) compressive strength variation with time and d) SEM image of precipitation after 60 days in SBF.

This highlights one of the opportunities presented by the capability of 3D printing. Due to their highly reproducible and repeatable structures, enabling the production of very similar scaffolds from various compositions, a greater insight can be gained from studying printed scaffolds *in vivo* and *in vitro* when compared with other manufacturing techniques which exhibit more topographical variation [37, 52, 133].

Literature has mixed reviews regarding the reliability of SBF testing for predicting *in vivo* results and the optimum solution and testing procedure. Many reviews [38, 157, 162–165] question what the correct approach is. Solution stability is a common issue raised, as the ionic concentrations within the solution are high, slight changes can tip the balance and initiate precipitation regardless of a materials bioactivity. A round robin study conducted by various institutions is summarised by Macon *et al.* [38]. They compare the current ISO

standard, which fixes surface area to volume of solution, with a fixed mass approach. Their paper puts forward a protocol which aims to reduce the variability currently seen within literature. This protocol was adopted herein.

2.4.2 *In vivo* studies

To be able to introduce bioactive glasses into the commercial market, *in vivo* tests must be completed to gain FDA approval and meet ISO standards. As with *in vitro* testing, the variety of approaches seen within literature is vast. To date, *in vivo* studies of bioactive glass scaffolds have been completed in a range of animals, including goats [166], sheep [130], rabbits [161, 167, 168] and predominately rats [34, 41, 49, 54, 55, 121, 156, 169].

A review by Pearce *et al.* [170] discusses the various complications when choosing an animal model for bone repair. They highlight that the key considerations are:

- Difference in bone morphology;
- Animal specific bone regrowth rate, and how it relates to human bone;
- Size of defect (critical or not);
- How defect is inflicted—the associated physiological effects of blunt or induced trauma;
- Fixation method;
- Location of defect;
- Loading of defect during healing;
- Number of defects per animal;
- Number of subjects;
- Cost of study.

Added to this list is the complication of scaffold design, with variability in porosity, pore interconnects, x, y, and z geometries as well as surface area all contribute to the different results that have been reported. Due to the complexity and variation of human bone and defect type compared to animal

models it makes it difficult to draw conclusions and extrapolate potential bone healing performances *in vivo* to the human context [170–172].

Three of the most relevant, and interesting, *in vivo* studies to this work are discussed below, all of the tests use Sprague–Dawley rats with different defect sizes, and all defects were induced via sharp incisions.

Liu *et al.* [49] studied the effect of pre–conditioning 13–93 robocast scaffolds. Their hypothesis was that preconditioning with bone morphogenetic protein–2 (BMP–2) would speed up the conversion to HCA and improve the performance.

All the scaffolds tested had 50% porosity, and were either preconditioned with phosphate solution or BMP–2 for 1, 3 or 6 days and placed in a 4.6 mm calvarial diameter defect. Liu *et al.* [49] evaluated the effects on bone ingrowth by histomophometric analysis. Their results showed scaffolds without pre–conditioning had a bone ingrowth of 32%, pre–conditioning in phosphate solution between 1– 6 days enhanced bone formation to between 46–57%. The same preconditioning protocol but with added BMP–2 increased bone infiltration to 61–65%. Their study concluded pre–conditioning had a positive effect on bone ingrowth—but the length of time of preconditioning did not have a significant effect between the time points tested. However, all BMP–2 conditioned samples gave a positive significant difference compared to the non–preconditioned control.

Other work by Liu *et al.* [37] investigated robocast 13–93 scaffolds with 47% porosity and how their mechanical properties varied with *in vitro* and *in vivo* testing. The compressive strengths of the scaffolds reduced from 86 ± 9 MPa, to 58 ± 5 MPa after 2 weeks in SBF and to 35 ± 4 MPa after the same time *in vivo*. At the 12 week point, the *in vivo* strength reduced to 16 ± 4 MPa, while within SBF it has relatively stable, reducing to 52 ± 10 MPa. Similar reductions were seen in the elastic modulus measurements. A reduction in strength is to be expected due to the glass dissolution over time. As dissolution starts it

increases the porosity of the scaffolds therefore, reducing its mechanical properties. It is suggested that the *in vivo* reduction in mechanical properties was greater than *in vitro* due to greater glass dissolution and faster conversion of the glass into HCA, although this statement has not been quantified experimentally within the study.

What was most interesting about their work was their conclusion regarding the type of mechanical responses seen by the scaffolds. Their study concluded that throughout SBF testing, the scaffolds showed a brittle mechanical response when tested, whereas *in vivo* the response changed from brittle to elasto-plastic within 2-4 weeks of implantation. This again highlights the difference and limitations of *in vitro* studies at predicting *in vivo* performance. The change in failure mechanism would be due to the attachment of proteins and cells through the dissolution *in vivo*, forming more of a glass-biological composite, than a brittle glass, which would not occur in SBF testing alone.

Deliormanli *et al*. [54] robocast scaffolds of 13-93B3, varying x, y pore widths to 300, 600, 900 μm, while holding the z spacing constant at 300 μm. This varied the porosity between 45, 53, and 60 % respectively. They compared histology and SEM to evaluate tissue growth and blood vessel infiltration with a robocast 13-93 scaffold with a 300 μm pore width and 45% porosity. Each rat had 4 subcutaneous sites in the dorsum, two above the shoulders, two in the back legs. Their study showed that pore size had little effect on tissue infiltration or angiogenesis by their final 4 week time point. However, with pore size change also comes porosity and surface area alterations so it is difficult to understand the results independently of each other. This paper also raises questions about the effects of porosity, and the orientation of pores at the defect sites if x, y and z are not equal. If the scaffolds had been orientated differently within the defect site, alternative conclusions may have been drawn.

The complexity of predicting bioactivity and potential performance *in vivo* or within a human model is complex. However, key studies are pulling out valid

conclusions, which enhance our knowledge of the subject area and bioactive glass performance.

2.5 AIMS AND OBJECTIVES

The aim of this study was to understand the relationship between glass composition and morphology of bioactive glass scaffolds and their effect on bioactivity. To do this, three glasses, ICIE16, SBP-3 and 13-93, were processed into porous scaffolds via two manufacturing processes. The objectives were to:

1. Investigate the process variables for the adapted gel-cast foaming process for ICIE16, SBP-3 and 13-93 and optimise the process for bone scaffolds;
2. Investigate the process variables for robocating of ICIE16, SBP-3 and 13-93 and optimise the process for bone scaffolds;
3. Produce foam and 3D printed scaffolds with straight pore channels, with pores of the same interconnect diameter/width, to enable investigation of the effect of tortuosity on bone ingrowth *in vivo*.

3 METHODOLOGY

3.1 GLASS MAKING

All glasses used throughout this project were made via melt quenching using high purity silica (SiO_2) (High Purity, Prince Minerals, Stoke-on-Trent), phosphate (P_2O_5) and the carbonate equivalent of the modifying oxides required, all reagents were purchased from Sigma Aldrich UK at < 96% purity unless otherwise stated. The three glasses used within this project chemistry is stated in mol% in Table 3.1. For simplicity the following procedure describes manufacture of ICIE16, the same protocol was applied to manufacture SBP-3 and 13-93.

Table 3.1: Summary of the glasses used within this project and their chemistry's in mol%.

Oxide	ICIE16	13-93	SBP-3
SiO_2	49.46	54.60	44.50
CaO	36.60	22.40	17.80
Na_2O	6.60	6.00	4.00
P_2O_5	1.07	1.70	4.50
K_2O	6.60	7.90	4.00
MgO		7.70	7.50
SrO			17.80

ICIE16 (49.46% SiO_2, 36.27% CaO, 6.6% Na_2O, 1.07% P_2O_5 and 6.6% K_2O, in mol%) was batched up according to Table 3.2. When the glass is molten the following reactions occur:

$CaCO_3 \rightarrow CaO + CO_2$

$Na_2CO_3 \rightarrow Na_2O + CO_2$

$K_2CO_3 \rightarrow K_2O + CO_2$

These reactions reduce the final weight of the glass produced. Table 3.2 shows the calculation used to batch up 150 g of glass.

Table 3.2: calculations used to batch up 150 g of ICIE16

Oxides	mol. /%	RMM	Reagent used	RMM of reagent	Bulk Factor	Mass of precursor /g
SiO_2	49.46	60.08	SiO_2	60.08	1.00	72.03
CaO	36.27	56.08	$CaCO_3$	100.09	1.78	87.99
Na_2O	6.6	61.98	Na_2CO_3	105.99	1.71	16.96
P_2O_5	1.07	141.94	P_2O_5	141.94	1.00	3.68
K_2O	6.6	94.2	K_2CO_3	138.21	1.47	22.11
						202.77

The powders were mixed for 2 h using a Wheaton Small Roller until homogenous. The powder was then transferred into a 95 wt% platinum 5 wt% gold crucible and placed into a furnace at 1400°C for 2 h. The melt was then quenched into deionised water, forming coarse frit. The frit was collected and dried at 100°C. A summary of the melting parameters for SBP-3, ICIE16 and 13-93 are summarised in Table 3.3.

Table 3.3: Summary of the melting profile used for ICIE16, SBP-3 and 13-93

Glass Composition	Temperature /°C
ICIE16	1400
SBP-3	1350
13-93	1400

3.2 GLASS GRINDING

Three grinding methods were used throughout this project, ball, planetary, and jet milling.

Ball mill

The powder was then ground for 6 minutes at 500 rpm using Fritsch Premium Line 7 ball mill, using 80 ml grinding bowls with nine 15 mm tempered steel balls.

Planetary ball mill

Retsch PM 100 Planetary Ball Mill, with 500 ml zirconia cup, was used. Powders were ground both wet and dry. Dry grinding used 10 mm zirconia balls for 1 hour at 420 RPM reversing direction every 5 minutes. Wet grinding used 0.5 kg of 2 mm zirconia balls with a ratio of 20 g of glass to 60 ml of anhydrous ethanol.

Jet mill

A Picojet 40AFG Hosokawa Alpine jet mill with a gas pressure of 5 PSI, with a classifier speed between 5000- 8000, was used. All internal parts were ceramic lined to limit contamination and abrasion during use.

Sieving

The ground powder was then sieved to <32 μm using a Russell Finex compact sieve shaker with ultrasonic deblinder. Any oversized particles were then collected, reground and sieved using the same procedure.

3.3 CHARACTERISATION TECHNIQUES

3.3.1 Glass composition characterisation

Glass compositional accuracy was analysed via X-ray fluorescence (XRF) and acid digestion using ICP-OES; all glasses were within 0.5 mol%.

Acid digestion

ICP-OES is a method of measuring the elemental concentration within a solution. Small volumes of solution are sprayed into an argon plasma where the atoms within the solution are ionised. This process leads to a release of light specific to the ionised element. Quantitative data is collected by formulating calibration curves of light intensity versus concentration of the element of interest. Multiple elements can be analysed simultaneously, as long as the wavelengths of light do not overlap.

Within this project ICP-OES was used to measure the dissolution profile of ions released into solution during bioactive testing, and used to measure the chemical composition of glass formulations via acid digestion.

For acid digestion, 100 mg of glass to 400 mg lithium metaborate were mixed and added to a platinum crucible, the mixture was then heated to 1200°C for 30 minutes. The glass was then dissolved under sonication in a known concentration of nitric acid and then analysed via ICP-OES.

X-ray fluorescence

When a sample is irradiated with X-rays, a variety of interactions can take place. In XRF the sample is irradiated and the X-ray fluorescence radiation emitted is collected and analysed. These energies are characteristic discrete wavelengths dependent upon the elements present within the sample. Qualitative analysis can be completed by studying the energy of the wavelengths emitted, which can be made quantitative by measuring their intensities and comparing it within known standards. The limitations of this technique is that light elements are difficult to analyse due to the low intensities of the fluorescence emitted. Low intensity energies can easily be absorbed by surrounding matter and consequently fail to reach the detector for analysis.

XRF was completed using a PANalytical Epsilon3^{XLE} 30 kV 0.250 mA samples were analysed in powder form, all ball milled and sieved under the same

conditions to less than 32 μm. Samples were analysed in both air and helium, as helium improves the measurements of lighter atoms.

3.3.2 Particle size analysis

Particle size analysis was completed using the Malvern Mastersizer 2000. This technique uses laser diffraction to measure the variation in the intensity of scattered light created by different particle sizes. The particles are dispersed into a liquid medium which is then passed through a pump to a glass analysis cell. As the particles travel through the cell they scatter the light of the laser; smaller particles scattering light at a greater angle than the larger ones. The intensity of the light scattered, and the scattering pattern formed is then analysed using Mie theory to calculate the size of the particles. Mie theory relies on the optical properties of the solution used and the particles tested. The size of the particles are then reported as the diameter of a volume equivalent sphere [173].

To form stable suspensions suitable for measurement, glass powders were dispersed in water using a sonicator, and ethylene glycol was added to aid dispersion. Refractive index values used were glass: 1.54 water: 1.33 ethylene glycol: 1.44. Due to the grinding method used, and the brittle nature of the glass, the particles measured were not spherical. Therefore, the scattering pattern produced was dependent upon which face passed through the laser, and aspect ratio was not taken into account. To make the data consistent 20 repeats were completed and the data averaged to reduce the level of error created [173].

3.3.3 Zeta potential

Glass powders were made into stable suspensions in water dispersed with ethylene glycol. 1 ml of suspension was inserted into a Malvern Zen 3600 Zetasizer (Zetasizer Nano): disposable folded capillary cell. Each sample was

subjected to 14 scans and repeated 3 times, and the results averaged. Refractive index values used were the same as stated in 3.3.2.

3.3.4 X-ray diffraction

XRD uses monochromatic X-rays to determine crystalline phases within a material. Diffraction occurs when a wave interacts with a regularly spaced lattice, if the spacing of the lattice is of similar magnitude to the wavelength of the X-rays. X-rays are used when investigating crystallographic structures due to the wavelength of an X-ray being similar to the atomic spacing of many materials; this allows diffraction to occur forming constructive and deconstructive interference of the X-rays. This can be described schematically by Figure 3.1.

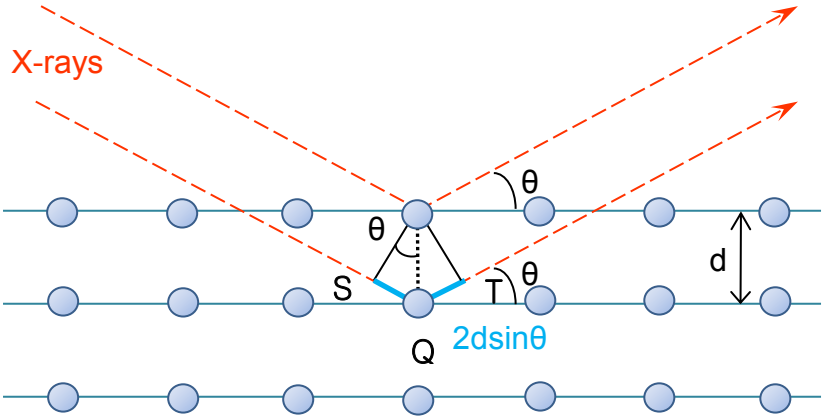


Figure 3.1: Schematic of X-ray diffraction

The distribution of constructive and deconstructive interference is specific to the lattice parameter of a material and gives rise to a characteristic diffraction pattern. By using Figure 3.1, equation 3.1, Braggs law can be derived [174, 175]. For diffraction to occur, Bragg's law (equation 3.2) must be satisfied when 'n' is any integer, λ is the wavlength, d is the interatomic spacing, and θ is the diffraction angle.

$$n\lambda = \overline{SQ} + \overline{QT} \qquad 3.1$$

$$n\lambda = 2d \sin\theta \qquad 3.2$$

Braggs law is only satisfied when the diffracted waves are in phase, allowing 'n' to be an integer. Bragg's law can be used for calculating the atomic spacing 'd' by equation 3.3 . Where 'D' is related to the miller indicies 'h' 'k' and 'l' (for strucutres with cubic symmetry) where 'a' is the lattice parameter [174, 175].

$$d_{hkl} = \frac{a}{\sqrt{(h^2 + k^2 + l^2)}} \qquad 3.3$$

Glasses were ground into a fine powder prior to analysis, the powders were then mounted onto a single crystal silica substrate with a zero background, and whose diffraction peak is above the range of interest. The spectra were collected using a Bruker D2 PHASER desktop X-ray diffractometer with a step size of 0.0345°, 10 seconds per step, measuring between 5 and 80 degrees 2θ. The radiation source was Ni filtered CuKα.

3.3.5 Thermal analysis

Thermogravimetric analysis (TGA) was used to understand the thermal degradation of the organic content of both the gel-cast and 3D printed scaffolds. DSC (Differential Scanning Calolimetry) was used to analyse T_g and T_c onset of the glasses used at their specific particle size. Simultaneous TGA-DSC consists of a sample head containing two platinum crucibles, one containing the sample and one containing a reference. The sample is heated through a set temperature profile and the change in mass is measured as a function of temperature; while simultaneously measuring the difference in temperature between the sample and the reference material. The reference material must exhibit no change in thermal properties during the experiment or react with the chosen testing gas. If a difference in temperature between the sample and the reference occurs, then it is due to a change in the physical properties of the sample. For example an exothermic reaction is indicative of crystallisation and an endotherm is associated with melting.

50 mg of sample (either glass, binder or a combination) was placed in a platinum crucible. Analysis was completed in continuously flowing air up to 1200°C at a heating rate of 10 °C min^{-1} using a NETZSCH STA 449C Dual Thermogravimetric Analysis–Differential Scanning Calorimeter. The reference sample used was alumina. Calibration scans were run of both empty crucibles and just the reference sample to reduce error.

3.3.6 Scanning electron microscopy

SEM uses a high energy beam of electrons within a vacuum to collect data about a conductive sample. The sample surface is bombarded with electrons and the electrons that are emitted are detected and used to determine information about its topography and composition [176].

There are two types of electrons that can be collected: secondary and backscattered. Secondary electrons are electrons which are close to the surface and are loosely bound to their nucleus, which become excited by the electron beam. They are low energy electrons that undergo elastic and inelastic collisions as they reach the surface of the material. Due to the low energy of these electrons they are sensitive to the distance travelled from initial excitation to release from the materials surface making them highly sensitive to the sample topography. This enables them to be used to provide detailed images about the samples surface. The contrast created is dependent upon the distance travelled to the detector therefore, surfaces closer to the detector will appear brighter than those further away [176].

Backscattered electrons are high energy electrons and are produced by elastic collisions from the incident beam. The number of backscattered electrons produced is dependent upon the atomic number of the material in question. Backscattered electrons can be collected to provide compositional data of the sample, and atomic number contrast [176].

Low magnification images of the scaffolds topography were collected using the JEOL JSM 5610 LV with a working distance of 10–12 mm. Samples were mounted onto conductive stubs using carbon tape sputter coated in gold using an Emitech K550 for two minutes at 25 mA. Due to the porous nature of the scaffolds one side was painted with silver to increase the conductivity of the samples. Images were taken using a voltage of 5 kV to reduce charging of the samples.

High magnification images were collected using the LEO Gemini 1525 FEGSEM, samples were sputter coated in chromium (Emitech K550) for two minutes at 20 mA. A voltage of 5 kV was used with a working distance of 5–10 mm.

Energy dispersive spectroscopy

Energy dispersive spectroscopy (EDS) uses X-rays to complete compositional analysis of a materials surface, and can be conducted within the SEM. When the electrons hit the target sample, approximately 99% of the electrons are scattered, and 1% hit an electron in one of the outer shells of an atom of the target materials [174, 175]. If the fired electron makes contact with an electron in the 'K' shell of the target material and the electron is knocked out of the orbit. An electron from the atoms 'L' shell moves to take its place. When an electron moves from 'L' to 'K' it loses energy, (due the electron shells surrounding an atom having different energy levels) this energy is given off as an X-ray photon (Kα radiation). An electron could also be replaced by an electron from the 'M' shell, when an electron moves from 'M' to 'K' there is a higher energy change therefore a shorter wavelength of radiation is produced called Kβ.



Figure 3.2: a schematic of an atom, where the shells from outside inwards are M, L, K, and the filled circle is the nucleus. The orange arrow represents the Lα transition, green the Kα and blue arrow is the Kβ transition.

These X-rays can be collected and give a characteristic spectrum of the elements present within the material. The atomic number of the atoms of the target materials affects the level of Kα and Kβ radiation produced; it is usually in the ratio 5:1 respectively. Due to this ratio and the low percentage of interactions where X-rays are produced, this method of analysis for chemical investigation is very inefficient, and can take a long time to collect an accurate set of data [174, 175]. To complete EDS the following parameters were used on the LEO Gemini 1525 FEGSEM, samples were sputter coated in chromium for two minutes at 30 mA, a voltage of 20 kV was used with a working distance of 5-10 mm. Analysis was completed using Inca software (Oxford Instruments, UK).

3.3.7 Mercury porosimetry

Mercury porosimetry (MIP) uses pressure to infiltrate porous materials to gain information about its pores such as modal pore interconnect diameter and its distribution. Macropores with diameters of ~14 -250 μm can be analysed via low pressure MIP, and mesopores and nanopores of 3 nm – 14 μm can be investigated by high pressure MIP [177].

A sample is placed within a glass cell under vacuum. The sample is then infiltrated with mercury under pressure. Mercury is a non-wetting liquid therefore, the pressure to overcome the liquid surface tension and consequent pore size can be calculated by balancing the opposing forces. This is done by using the Washburn equation as stated in equation 3.4, where r_1 and r_2 are

curved interface in which is measures the pressure difference, r_{pore} is the corresponding pore size, γ is the surface tension of mercury (taken as 480 nM/m) and θ is the contact angle between the material studied and mercury (approximated at 140°).

$$\Delta P = \gamma \left(\frac{1}{r_1} + \frac{1}{r_2} \right) = \frac{2\gamma \cos \theta}{r_{pore}} \qquad 3.4$$

The raw data is plotted as an intrusion–extrusion curve of cumulative volume vs pressure. From this pore size distribution can be calculated by the pore volume per unit interval of pore diameter using equation 3.5.

$$D_v(r) = \frac{P}{r} \frac{dV}{dP} \qquad 3.5$$

This can be plotted as –dV/d(logd) as a function of pore diameter, which allows median, mode, and mean pore diameters to be determined about the sample tested. The limitations of this method are that it measures the largest entrance into the pore (i.e the interconnect diameter), not actual pore size; as the interconnect size dictates the pressure needed to infiltrate the pore. It also assumes that all the pores are cylindrical. These factors therefore need to be taken into account when studying the data collected [177].

MIP was carried out using a Quantachrome Poremaster 33 machine equipped with both high and low pressure functionality and fitted to a Thermo Renaissance 2005 ARL–LS vacuum pump. Due to the size of the interconnects within these scaffolds, only low pressure analysis was used. Sample volumes were recorded and their masses inputted into the software, cylinders of approximately 1 cm^3 were used and five repeats were done of each sample set tested. The samples were left to vacuum for 30 minutes prior to infiltration, the cells were then filled with mercury under nitrogen gas (pressure 340 kPa) and the pressure was recorded. The raw data were analysed using PoreMaster for windows 8.1 software.

3.3.8 Fourier transform infrared spectroscopy

Fourier transform infrared spectroscopy (FTIR) allows the formulation of a spectrum, which is characteristic of the covalent bonds present within a material. A beam of light of various frequencies interacts with the sample, which excites and vibrates the covalent bonds containing dipole moments, and the detector measures the intensity of light post-interaction. A Fourier transform is carried out upon the interferogram collected, to measure the amount of light absorbed at each wavelength. This data set can be collected in reflected, absorbed, or transmitted mode. The amount of energy absorbed by the bonds is dependent upon the bond present and therefore creates a characteristic spectrum. FTIR has been used to analyse the glasses within this project pre and post bioactivity testing, to see if any changes have occurred. All samples were ground into a fine powder prior to testing and spectra was measured between 450–4000 cm^{-1} at a resolution of 2 cm^{-1} and averaged over 64 scans. Data was collected using a Scientific Nicolet iS10 Spectrometer operating in attenuated reflectance (ATR) mode.

3.3.9 Compression testing

Ten samples of each scaffold were compression tested to obtain the compressive strength and compression moduli. The results were averaged and standard deviations calculated. Gel cast samples were cut into cubes prior to sintering, and ground post sinter to cubes with dimensions of 6 mm. 3D printed scaffolds were printed into the required dimension, allowing for shrinkage post sintering, so that the final volume was 6 x 6 x 6 mm^3. Samples were carefully prepared to ensure that all sides were flat and parallel. The samples were compressed using a Zwick/Roell z2.5 at a strain rate of 1 $mm.min^{-1}$. Force exerted was recorded as a function of distance moved by the compression plates, and test time. From these values, stress and strain were calculated and plotted using equations 3.6 . Where ΔL is the distance moved by the compression heads during testing, and L_0 is the original length.

$$Strain: \varepsilon = \frac{\Delta L}{L_0} \qquad Stress: \sigma = \frac{force}{apparent\ cross\ sectional\ area} \qquad 3.6$$

3.3.10 Helium pyconometry and percentage porosity

To be able to understand the effects of processing on scaffold formation and to compare mechanical properties between samples the porosity needs to be calculated. Percentage porosity can be measured using the following equation:

$$\%\ Porosity = \left(1 - \frac{bulk\ density}{skeletal\ density}\right) \text{x } 100 \qquad 3.7$$

Bulk density calculations of scaffolds were determined by mass and dimensional measurements. True density was measured using a Quantachrome Ultrapycnometer 1000 Helium pycometry.

Helium pycnometry can be used to accurately measure the true (skeletal) density of solids and powders. It calculates a more accurate volume measure by filling a cell containing a sample with helium gas the helium will infiltrate any pore greater than a single helium atom (≈1 Å). It compares this with the known measure of the cells volume without the sample calculated by the ideal gas law (PV = nRT). The skeletal density can then be measured using equation 3.8.

$$skeletal\ density = \frac{mass\ sample}{skeletal\ volume} \qquad 3.8$$

Cell volumes were calibrated using a steel ball of known volume, calibration was completed between each sample. The samples were weighed and inserted into the cell and 20 runs were taken to obtain an average value of skeletal volume. Experiments were kept at a static temperature of 25 °C. Three samples of each composition were tested to determine a mean skeletal density and standard deviation.

3.3.11 Rheology

Rheological studies were completed using a TA Instruments Discovery HR-1 rheometer fitted with a 40 mm parallel plate geometry, a solvent trap to prevent drying and a Peltier plate for temperature control. Solutions were prepared and pipetted between the two plates, the geometer was then closed to a 1 mm gap and the excess material extruded was removed. Care was taken to ensure the solutions were free from air bubbles, and that homogenous fill was achieved between the two plates prior to testing.

Three tests were completed:

- Oscillation temperature sweep: 0–35°C ramp rate 5 °C/minute at constant 0.5 % strain;
- Flow tests: all tests were conducted at 25 °C, 30 second pre-test temperature soak, shear rate logarithmic sweep between 5–500 s^{-1};
- Oscillation amplitude sweeps: logarithmic stress sweep between 0.02–200 Hz, at a frequency of 1 Hz [178] at 25°C with 30 s pre-test temperature soak.

For oscillation amplitude sweeps, the phase lag, δ, between peak applied shear stress and peak shear strain was determined automatically by the equipment's software over 10 oscillations. The storage and loss moduli, G' and G'', were also calculated by the software using equations 3.9. Where τ is the shear stress, and γ is shear rate.

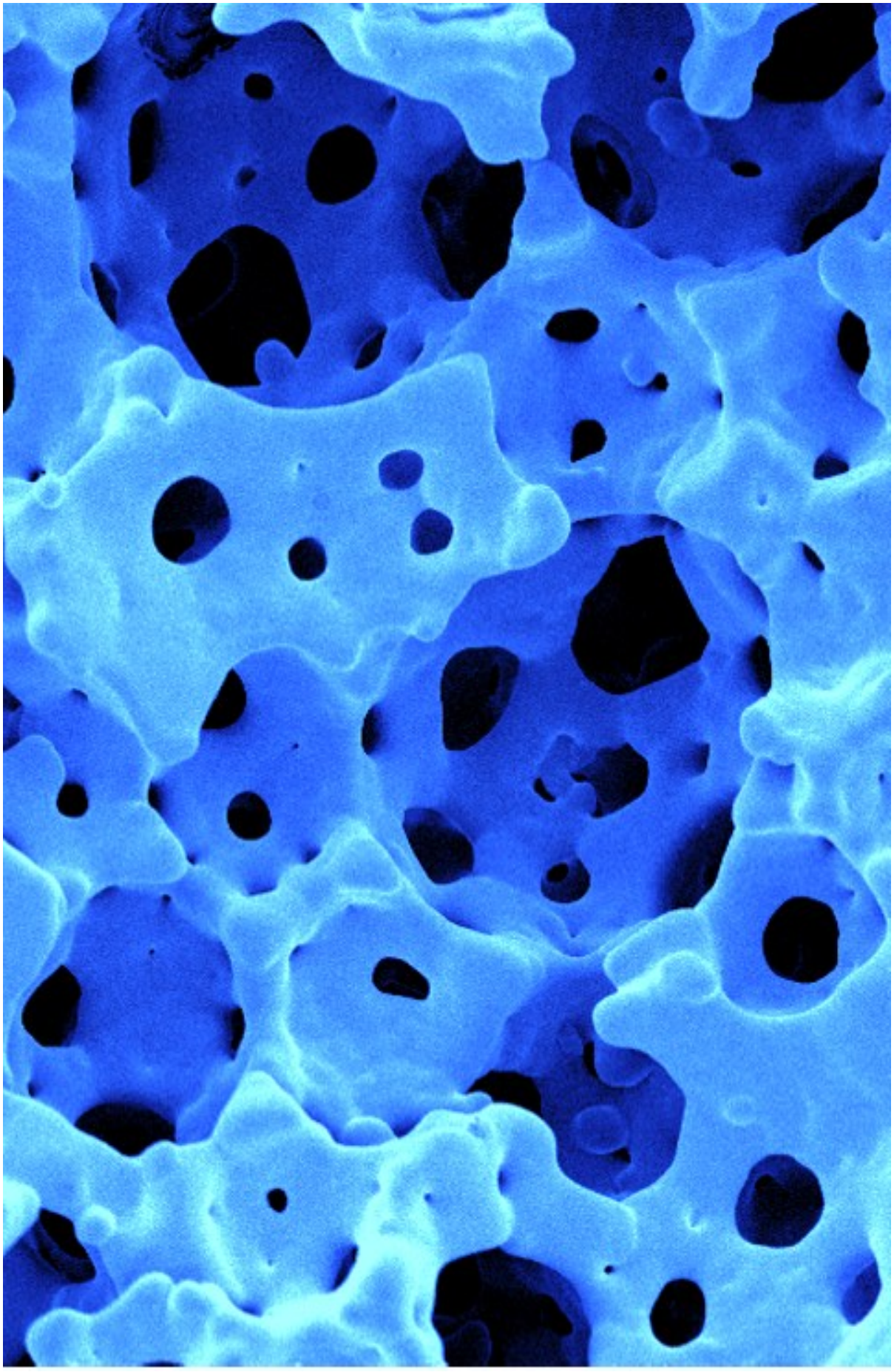
$$G' = \frac{\tau_{max}}{\gamma_{max}} \cos\delta \qquad G'' = \frac{\tau_{max}}{\gamma_{max}} \sin\delta \qquad 3.9$$

3.3.12 X-ray microtomography

X-ray tomography (XMT) is a powerful non-destructive 3D imagining techniques that utilises x-rays to form radiographs which can be reconstructed to produce a 3D generations of the sample. The resolution of the images

formed is dependent upon the sample size and the strength of the X-ray Beam used.

The scanning was completed in collaboration with Professor Peter Lee's group at the Diamond Manchester collaboration at Harwell, Oxfordshire. The Analysis was completed by Hua Geng, using a Pheonix Nanotom (GE Measurement & Control, Wunstorf, Germany) under the following processing conditions: accelerating voltage of 70 kV, current 140 uA, pixel size 9.5 μm, number of pixels 1989x1989, Number of projections 1000, Exposure time 2000 ms. 3D image analysis methods developed in-house were applied to quantify the pore and interconnect diameter size distributions [63, 179].



4 GEL-CASTING:

4.1 INTRODUCTION

The starting point of this work was to determine if the adapted gel-casting process, developed by Tang [130], could be optimised to produce suitable scaffolds for bone repair from alternative bioactive glass compositions.

4.2 MATERIALS AND METHODS

Three glass compositions, ICIE16, 13-93 and SBP-3, were pilot-tested for use in the adapted gel-casting process. All three glasses were manufactured via melt quenching, then ball milled and sieved to a particle size of less than 32 μm as described in Section 3.2.

4.2.1 Protocol

The first gel-casting process developed for bioactive glass scaffolds was developed by Wu *et al.* [6] and has been further adapted by Tang [130]. The main changes in processing method between their work, is the change from an *in situ* polymerisation gelation process to a thermally controlled one using gelatin. The gelatin procedure was adapted by Tang [130] for the glass composition SBP-3 (44.5 SiO_2, 4.5 P_2O_5, 17.8 CaO, 17.8 SrO, 7.5 MgO, 4 Na_2O, 4 K_2O, mol%) bioactive glass.

The adapted gel-casting protocol was to dissolve 1 g of gelatin into 20 ml of water at 30 °C. 25 g of pre-ground glass powder was then added to form a slurry. An optimised quantity of Triton X-100 surfactant was added and the solution is vigorously agitated (Kenwood Chef hand mixer, UK) [130].

Once a stable foam was achieved, after approximately 2 minutes, the beaker was transferred to an ice bath where it is left for 8 minutes. The scaffolds were then frozen for twenty minutes in a -20°C freezer. By running hot water over the outside of the beaker, the scaffolds were removed and transferred to a -80°C

freezer. After two hours, they were placed in a CoolSafe 100-4 freeze-drier fitted to a Vacuubrand RZ6 vacuum pump, operating at −110°C with an ultimate total vacuum of 1 × 10^{-2} mbar for 2 days until dry. This process is described schematically by Figure 4.1.

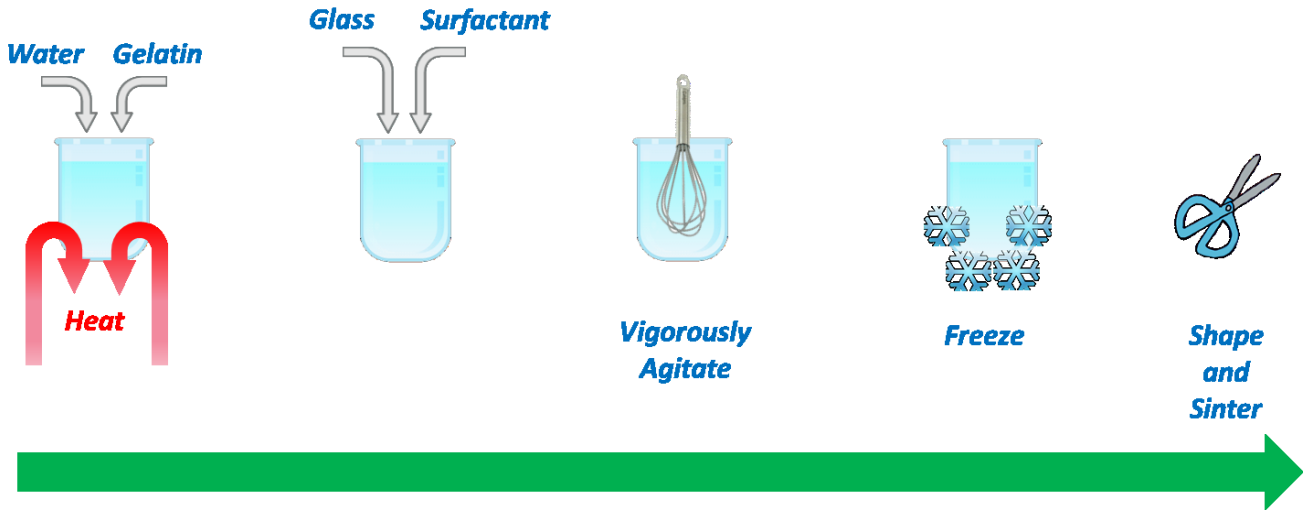


Figure 4.1: Schematic of the adapted gel casting process

This thesis reports on studies that aimed to optimise and adapt the process to make comparable amorphous bioactive glass scaffolds of other glass compositions. Scaffolds were characterised by pre and post sinter porosity, mercury porosimetry, compression testing, XRD and SEM (methods described in Section 3.3)

4.3 OPTIMISATION OF GEL-CAST FOAMING OF ICIE16

4.3.1 Varying surfactant concentration

Surfactant was used to stabilise the bubbles formed by the mechanical agitation during the foaming process. Surfactants have hydrophobic and a hydrophilic parts, which enable them to absorb onto liquid-gas interfaces. Triton X-100 ($C_{14}H_{22}O(C_2H_4O)_n$) was used, which is a common non-ionic surfactant, formed of an aromatic hydrocarbon lipophilic and a hydrophilic polyethylene oxide chain, and is soluble in water at 25 °C. The hydrophilic end of the surfactant molecule has affinity to the water in the slurry and the

hydrophobic end remains in the air. This enables the surfactant to reduce the surface tension of the air/water interface, enabling the formation of a stable foam for a limited time [129]. However, the stability of the foam also depends on the viscosity of the slurry. During foaming, the agitation allows air to be drawn into the suspension. For a liquid to foam, the surfactant and slurry must form a membrane around the air bubble. The membrane that is formed must be able to create an elastic force, which counterbalances the applied stresses from mixing, which act locally thinning and stretching the membrane [180]. If these forces become too high the bubbles will burst. Their tendency to do either is dependent upon a variety of factors such as the elastic behaviour of the membrane, electrostatic repulsion, van der Waals forces, surfactant efficiency and the viscosity of the suspension [129].

The experimental parameter that affects the ability of the bubbles to stay within the suspension is the surfactant efficiency within the slurry. An effective surfactant will efficiently reduce the surface tension, creating temporarily stable bubbles by forming new surfaces and establishing the required stabilisation forces. Once enough surfactant molecules are acting at the gas liquid interfaces, the foam becomes stable, resulting in no further volume increase of the suspension. The relationship between the formation of new bubbles via agitation is equalled by the disintegration of previously formed bubbles [129].

To make the foam architecture permanent, samples are frozen and freeze dried to produce mechanically stable green bodies prior to sintering. During gelation, or in this case freezing, if the surface tension becomes too great the membranes rupture creating interconnects between the previously discreet pores. If the surfactant concentration is appropriate and well distributed the bubbles, and consequent pores, should be homogenous throughout the structure and on gelling rupture should occur forming uniform interconnects between them. For scaffolds suitable for bone ingrowth, open cell foams are required and it is these interconnects which are vital as they allow blood

vessels and cells to propagate throughout the scaffold forming an energy supply and waste stream.

To optimise this processing method for use with ICIE16, Triton X-100 additions to the slurry were investigated between 0.1-0.6 ml. When using less than 0.1 ml of surfactant, the slurry did not foam. At 0.1 ml surfactant, very few bubbles were formed within the solution and the scaffolds produced had the lowest porosity, of 16 %. At 0.2 ml of surfactant, the foam volume after freeze drying, increased by 60% and a foamed construct was formed. As the surfactant concentration increased, the foam volume also increased until a critical value of surfactant was reached at 0.3 ml. It is know that above a critical concentration of surfactant within a system surfactant efficiency reduces and micelles start to form [129]. A micelle is where the surfactant clusters together with the hydrophilic heads forming an outer ring with the hydrophobic tails inside, as shown schematically in Figure 4.2. Micelle formation uses up the excess surfactant within the system making them counterproductive creating a competing mechanism with bubble formation.

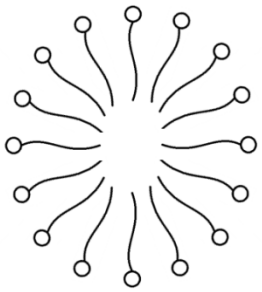


Figure 4.2: Schematic of surfactants forming micelles within an aqueous system

As surfactant concentration was increased, the green body foam volume produced (Figure 4.3) increased up until 0.4 ml of surfactant was added. This suggests that above 0.3 ml the efficiency of the surfactant within the system reduced and micelles were forming in addition to pores.

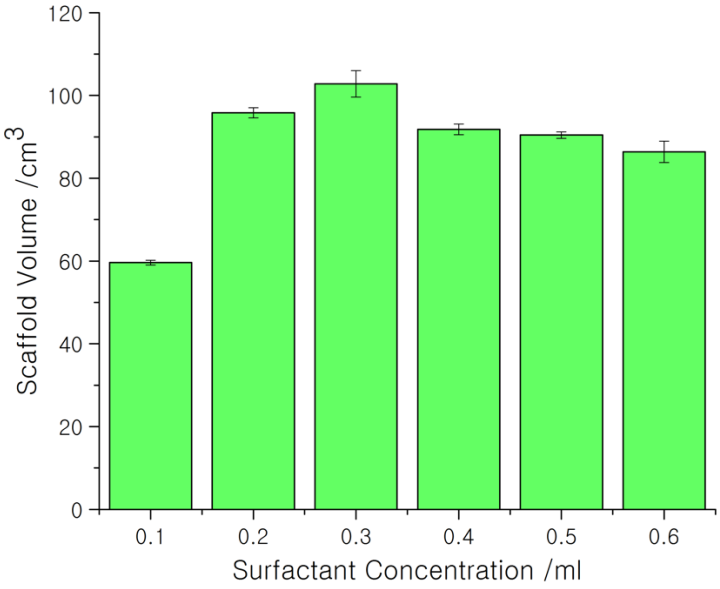


Figure 4.3: Variation in scaffold volume with increasing surfactant concentration, measured after freeze drying.

All scaffolds were sintered under the same conditions (discussed in 4.3.3), and analysed via SEM as shown in Figure 4.4. As suggested by the volume changes seen during processing, the scaffold with 0.1 ml of surfactant did not form pores or interconnects suggesting that there was not enough surfactant to maintain a foamed structure during agitation (Figure 4.4a). This was confirmed by mercury porosimetry measurements (Figure 4.5). Using up to 0.4 ml of surfactant addition led to the formation of a foamed structure with spherical pores and interconnect development (Figure 4.4b–d). Above this, the pore shape became distorted, less spherical and homogenous (Figure 4.4e, and f).

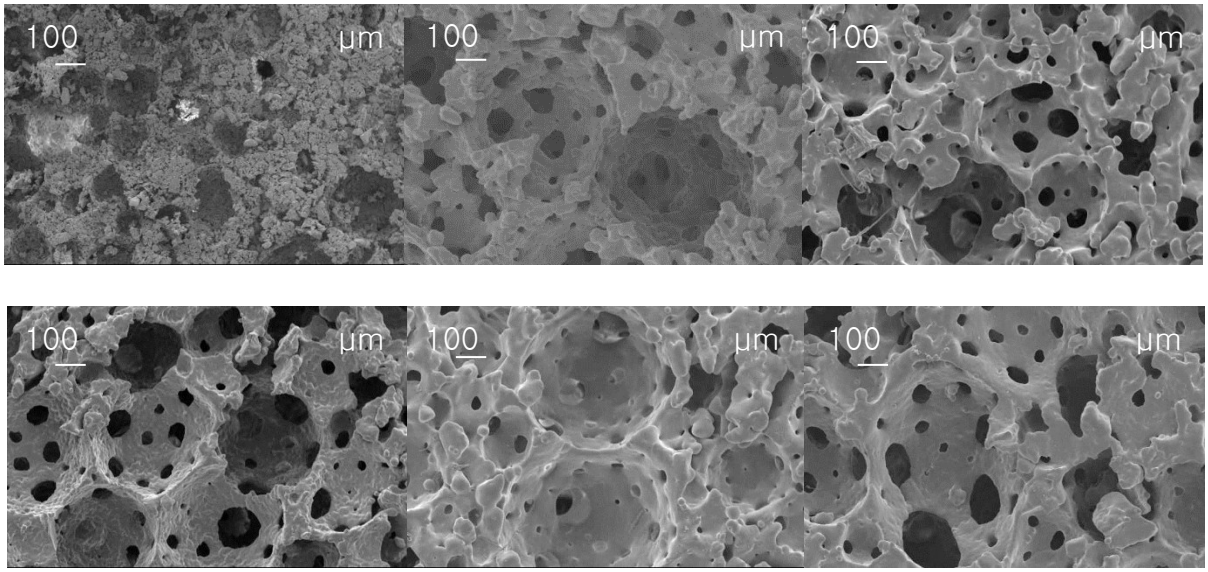


Figure 4.4: SEM images (100 magnification) of scaffolds sintered with varying surfactant concentration, (a) 0.1 ml, (b) 0.2 ml, (c) 0.3 ml, (d) 0.4 ml, (e) 0.5 ml, (f) 0.6 ml.

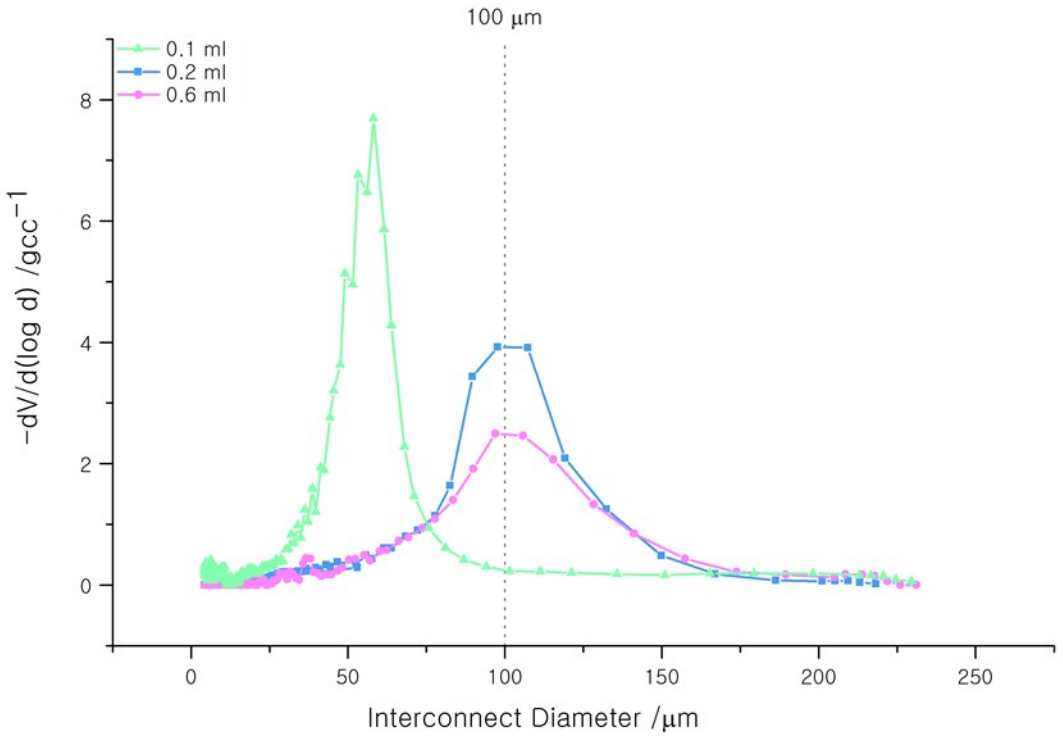


Figure 4.5: Interconnect size distributions obtained from mercury porosimetry, for samples with 0.1, 0.2 and 0.6 ml of surfactant.

Table 4.1: Summary of modal interconnect values from mercury porosimetry Figure 4.5

Surfactant Concentration /ml	Modal Interconnect Diameter /µm
0.1	61.0 ± 2.7
0.2	100.0 ± 3.4
0.6	97.6 ± 0.8

The modal interconnect diameter, determined by mercury porosimetry is summarised in Figure 4.5 and Table 4.1. For scaffolds with surfactant concentration of 0.2 and 0.6 ml, their modal interconnect diameter was 100.0 ± 3.4 µm and 97.6 ± 0.8 µm respectively. It is thought that an interconnect size of 100 µm is suitable for blood vessel growth and penetration. By analysing the SEM images in Figure 4.4 in tandem with the mercury results (Figure 4.5), increasing surfactant concentration only altered the pore geometry and not the number or size of interconnects. This was expected as the pore interconnects formed by the pores rupturing during gelation, which is dependent upon surface tension within the system.

Another consideration, when designing scaffolds for bone repair, is their percentage porosity (Figure 4.6). At 0.1 ml of surfactant, the porosity of the scaffold was 40 ± 0.8 %, due to the low concentration of surfactant being unable to sustain a foamed architecture. As surfactant levels increased from 0.2 to 0.6 ml, the porosity and interconnect diameter remained relatively stable, ranging between 65–70 % and 82–100 µm respectively.

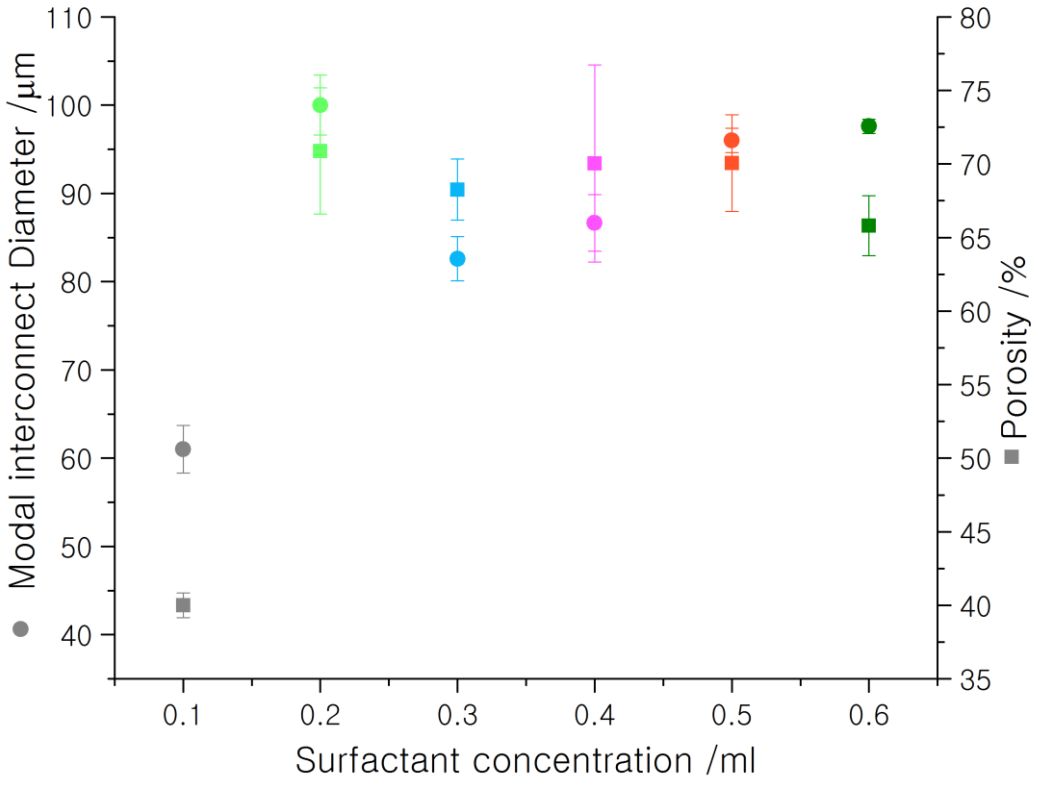


Figure 4.6: Scaffold porosity and modal interconnect diameter post sintering as a function of surfactant concentration.

4.3.2 The effect of surfactant concentration on mechanical properties

Compression testing was completed on samples of different surfactant concentrations. The results are summarised in reference to their porosity in Figure 4.7. The scaffolds made with 0.1 ml of surfactant, which had the lowest porosity (53%), had the highest compressive strength of 9.9 ± 1.5 MPa. As surfactant concentration and porosity increased from 53–79 %, compressive strength reduced from 9.9 ± 1.5 MPa to 2 ± 0.2 MPa, as expected. 0.3 ml surfactant was deemed to be the most suitable surfactant concentration, giving a high level of surfactant efficiency, combined with suitable porosity of 66 %, interconnect diameter of 83 µm and good compressive strength, 6 ± 0.9 MPa.

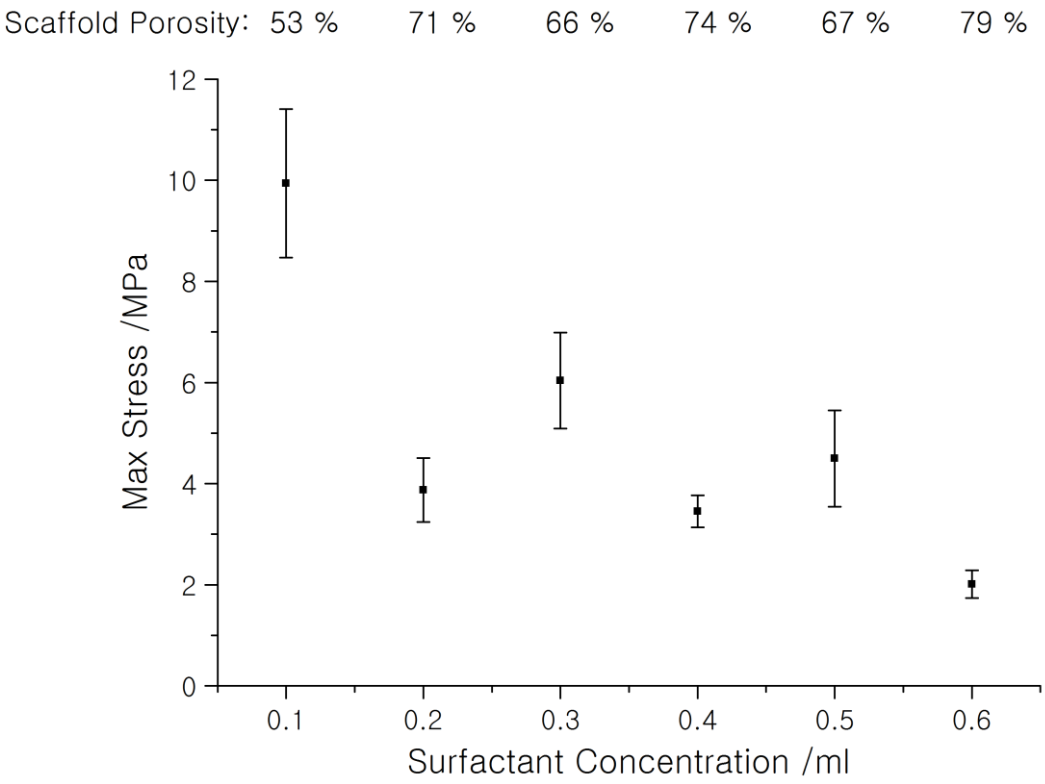


Figure 4.7: The effect of surfactant concentration on compressive strength. Porosity percentages are marked for reference above.

4.3.3 Sintering conditions

Sinterability is affected by many process variables, such as: particle size, particle packing (controlled by glass loading within the slurry), temperature ramp rate and dwell time. Variation in particle size affects the Gibbs free energy, therefore it alters the activation energy and driving force needed for sintering to take place [21]. Smaller particles have higher specific surface area and therefore sintering occurs more rapidly than larger particles of the same glass composition. When working with porous bioactive glass scaffolds, sintering needs to be optimised to maximise mechanical properties while maintaining the amorphous structure of the glass and the porous topography. Crystallisation of glasses is often surface nucleating, therefore a higher specific surface area also promotes crystallisation, effectively lowering $T_{c\ onset}$.

Bioactive glasses are known to react in aqueous environments; this reaction is key to their bioactivity. Reactions are known to release ions into the local solution and alter the surface chemistry. The gel-cast foaming method uses water to form the slurry and enable the surfactant to work. Therefore, premature reactions could take place during processing, which could premature effects its sintering ability. Previous work by Wu *et al.* [6] suggested that sintering ICIE16 into porous scaffolds processed at a temperature between 680-700°C was optimum. As discussed, many different factors effect crystallisation in glasses therefore, this temperature range was taken as a guideline and was optimised for this specific particle size and possible processing reactions.

Once green bodies were produced by the adapted gel-casting process, the scaffolds were sintered using a two part cycle described by Figure 4.8. The preliminary dwell at 500°C was used to burn out the gelatin, which acts as a binder for the particles. The higher dwell period (at 680-710°C), which was above the glasses transition temperature, was used to sinter the particles to form the porous construct.

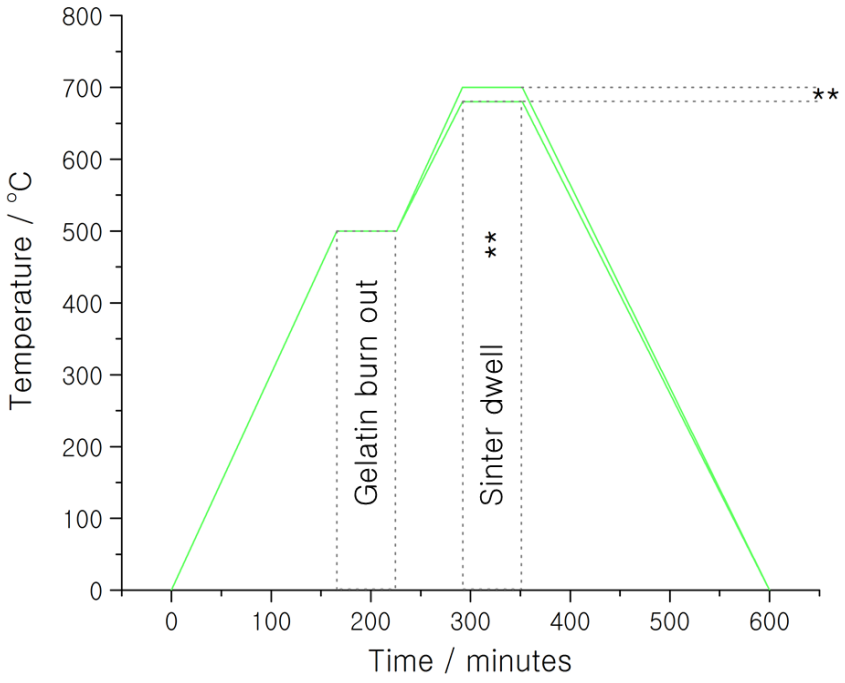


Figure 4.8: Schematic of the sintering cycle used for ICIE16 foam scaffolds.

Thermal gravimetric analysis (TGA) on a pre-sintered scaffold showed that gelatin burned out between 200-500°C (Figure 4.9). Therefore, scaffolds were held for 1 h at 500°C to burn out the gelatin. If the scaffolds were not sintered using this two-step approach or without enough oxygen available within the furnace it resulted in incomplete burn out of the gelatin showed by a black scaffold post sintering.

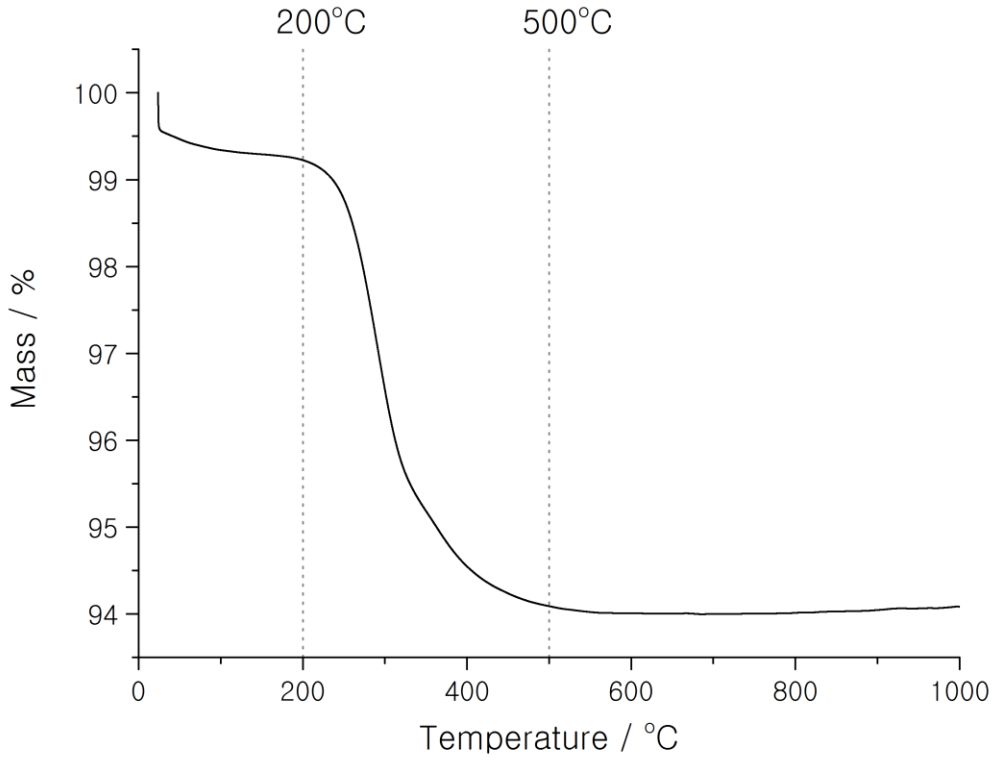


Figure 4.9: TGA analysis of an ICIE16 green body.

Ideally, the scaffold would sinter so that it was no longer possible to see discrete particles within the surface of the foamed struts, while maintaining an amorphous structure, and without allowing too much viscous flow that the scaffolds shape becomes distorted. For ICIE16, sintering was initially completed at 680, 690, 700 and 710°C with a 1 h hold time. Figure 4.10 summarises the SEM images collected of the scaffolds after the various sintering temperatures.

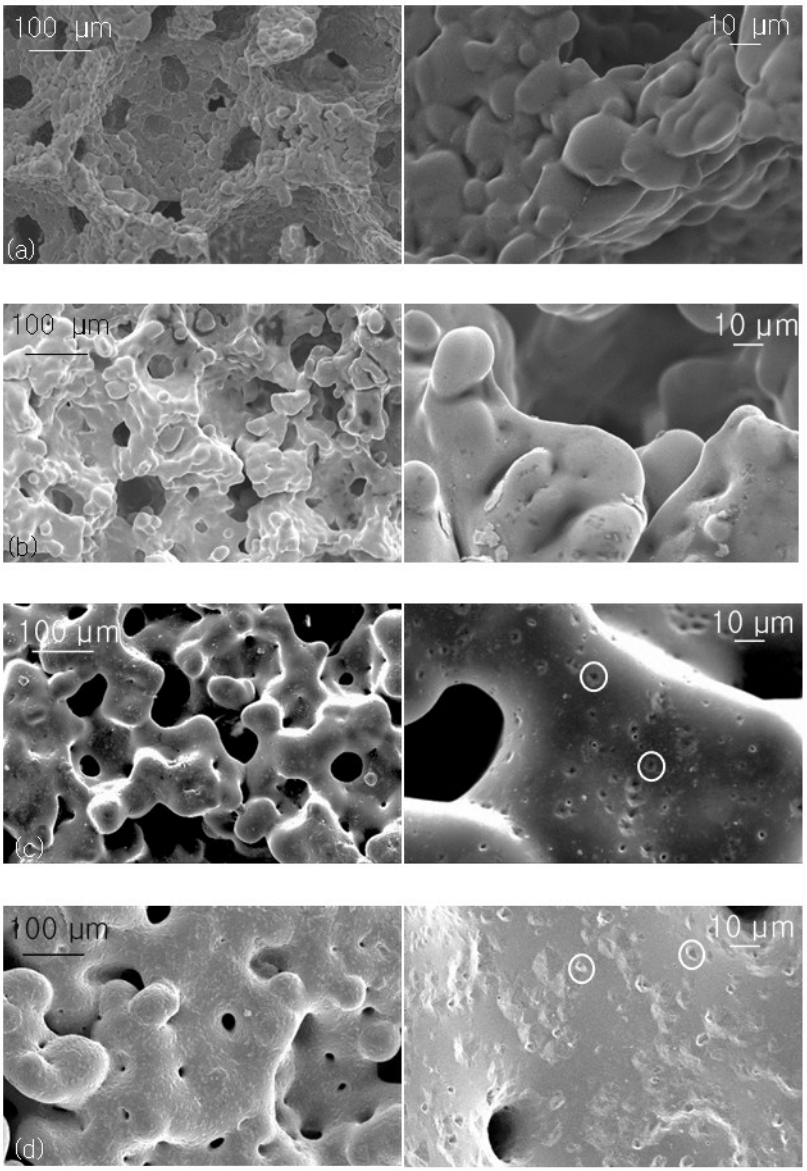


Figure 4.10: Sintering of scaffolds for 1 h at the following temperatures (a) 680°C, (b) 690°C, (c) 700°C and (d) 710°C, the second column are higher magnification images, the white circles highlight pit formation upon the surface.

After sintering at 680°C and 690°C, discrete particles were seen within the scaffold surface (Figure 4.10). This suggests that not enough energy was supplied to allow complete viscous flow of the particles resulting in incomplete sintering. The presence of visible particles upon the surface of the scaffold results in a reduction in the mechanical properties as they can act as crack nucleation sites within the material. After sintering at 700 and 710°C, the scaffold surfaces became more uniform, suggesting greater flow of the glass

and improved sintering. However, as highlighted within Figure 4.10, pits started to form upon the surface, the number of which increased with temperature. Bioactive glass compositions have a tendency to crystallise, this is known to be a surface activated process therefore, these pits could be the early formation of a crystalline phase.

Sintering at 690°C was the highest temperature that could be used without pits forming upon the glass surface, however at a 60 minute dwell time particles could still be seen within scaffold surface. Therefore, to improve the sintering of the scaffolds, increased dwell times were investigated between 1 and 5 h.

XRD was used to determine if the scaffolds remained amorphous post sintering. An amorphous glass XRD result would be a broad halo, as shown by the blue pattern in Figure 4.11. As crystallinity occurs within the sample the XRD trace would change to discrete peaks as diffraction occurs at characteristic angles of 2θ. As shown by Figure 4.11, with increasing hold time at 690 °C, the number of crystalline phases present within the scaffolds increased.

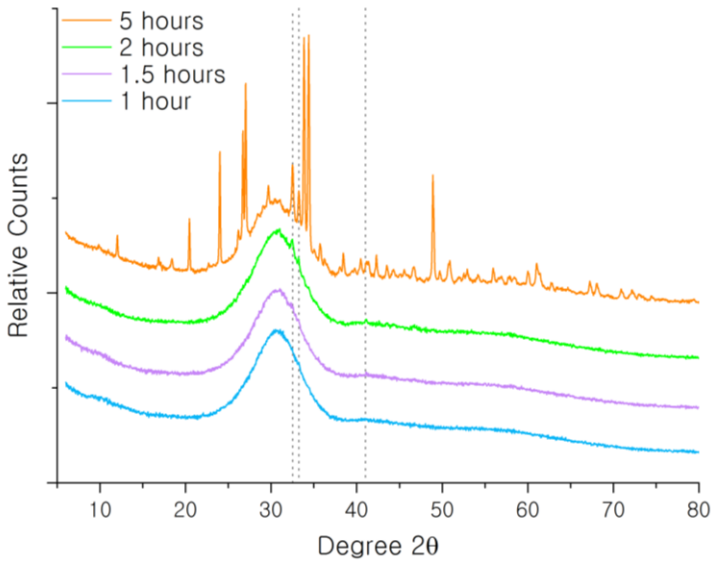


Figure 4.11: XRD patterns collected from scaffolds sintered at 690° for 1, 1.5, 2 and 5 h. Grey dotted lines highlight the formation of crystalline peaks at 2 h. The crystalline phases present are $Na_{4.24}Ca_{3.8}$ (Si_6O_{18}) and $Ca_2Si_4Ca_3(PO_4)_2$ (reference codes 01-078-1650 and 00-049-1674 respectively).

Sintering for 1 and 1.5 h at 690°C gave an amorphous scaffold. When the time was increased to 2 h there was a change in the shape of the amorphous halo with slight peaks at 32.5, 33 and 41 °2Θ. As the length of time at 690°C was increased to 5 h, the level of crystallinity seen within the sample increased. At 5 h the peaks matched two crystal formations: $Na_{4.24}Ca_{3.8}(Si_6O_{18})$ and $Ca_2Si_4Ca_3(PO_4)_2$ (reference codes 01-078-1650 and 00-049-1674 respectively). The diffraction peaks for $Na_{4.24}Ca_{3.8}$ (Si_6O_{18}) are at 32.5, 33 and 41 °2Θ, matching the peaks seen at 2 h, suggesting that this phase formed first, and then after an extended time at temperature $Ca_2Si_4Ca_3(PO_4)_2$ formed.

Due to the inverse relationship between bioactivity and crystallisation of bioactivity glasses it was deemed that a 1.5 h hold at 690°C was the optimum sintering profile, as it enabled viscous flow of particles while maintaining an amorphous structure. Figure 4.12 shows the topography of the final optimised scaffold.

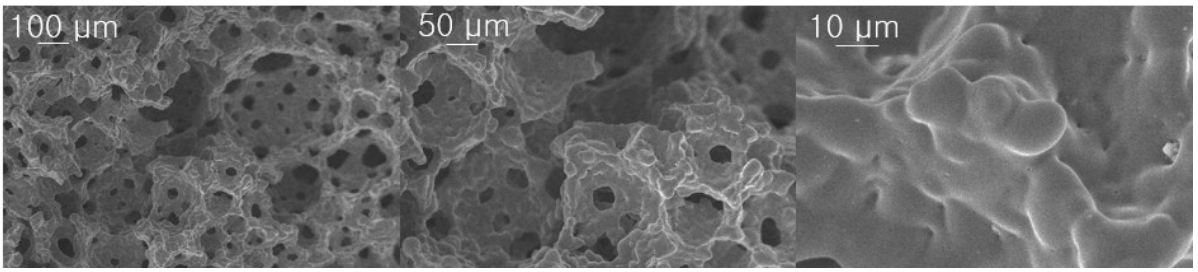


Figure 4.12: ICIE16 gel-cast scaffolds sintered at 690°C for 1.5 h.

4.4 OPTIMISATION OF GEL-CAST FOAMING OF 13-93

4.4.1 Varying surfactant concentration

The effect of surfactant concentration on scaffolds manufactured from glass composition 13-93 was then investigated. As it was known (Section 4.3.1) that 0.1 ml of surfactant was not enough to form a porous scaffold, surfactant additions between 0.2 and 0.6 ml were investigated.

Figure 4.13 shows that with increasing surfactant concentration, the pores became more distorted but the number and diameter of interconnects stayed constant, as seen previously with the ICIE16 scaffolds. When MIP analysis was completed (Table 4.2), it showed that the model interconnect size was similar for all surfactant concentrations, as with the ICIE16 results.

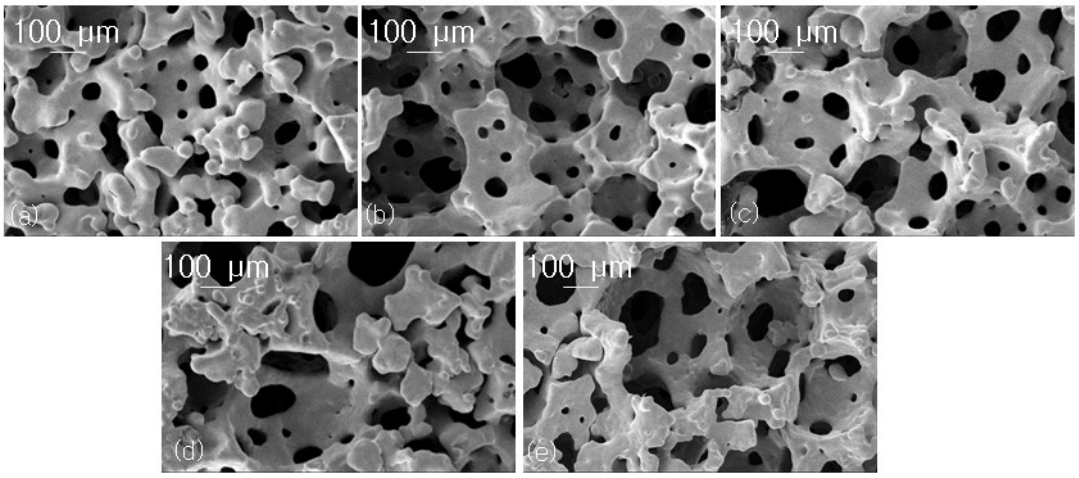


Figure 4.13: SEM images of 13-93 scaffolds foamed at the following surfactant concentrations (a) 0.2 ml, (b) 0.3 ml, (c) 0.4 ml, (d) 0.5 ml, (e) 0.6 ml.

Table 4.2: Mercury porosimetry data for 13-93 at surfactant concentrations between 0.2-0.6 ml.

Surfactant Concentration /ml	Modal Interconnect /μm
0.2	131.9 ± 5.3
0.3	135.1 ± 8.4
0.4	132.4 ± 9.3
0.5	126.4 ± 6.2
0.6	119.1 ± 13.2

4.4.2 Sintering analysis

Scaffolds of 13-93 were sintered using the same two step approached described previously in 4.3.3 with dwell at 500°C for 1 h to burn out the gelatin. Literature suggests that for a similar particle size sintering for 1 h at 700°C was the optimum sintering procedure [34, 37, 127]. Using this regime produced scaffolds with smooth surfaces which remained amorphous post processing (Figure 4.14), while maintaining the green bodies macro topography. Figure 4.15 shows the topography of the final optimised scaffold.

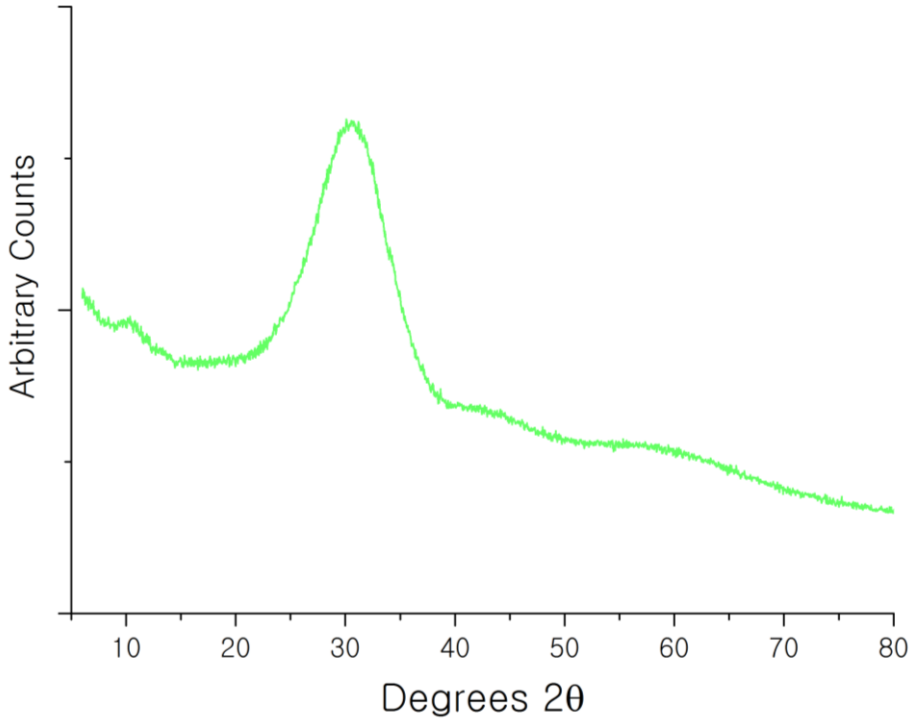


Figure 4.14: Post sintering XRD analysis of 13-93 scaffolds when sintered for 1 h at 700°C.

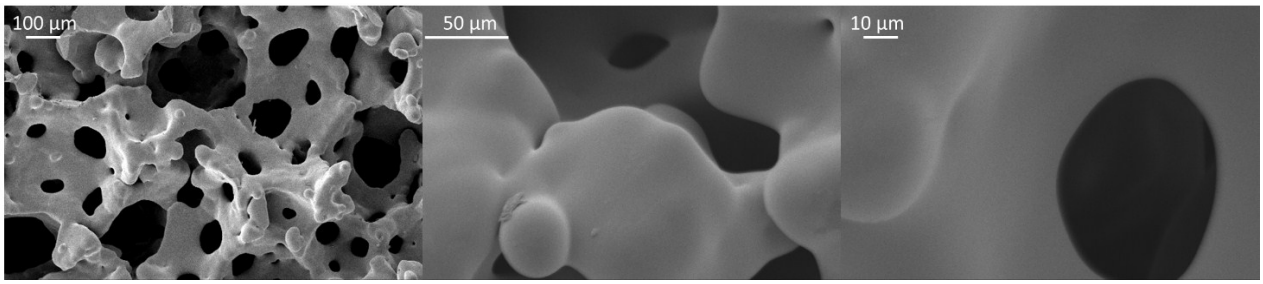


Figure 4.15: Topography of 13-93 gel-cast scaffolds post process optimisation.

4.5 OPTIMISATION OF GEL-CAST FOAMING OF SBP-3

The use of SBP-3 composition using this processing method was originally adopted by Tang *et al.* [130] however, due to the use of a different particle size, re-evaluation was needed. Sintering optimisation was evaluated by XRD and SEM after sintering at various temperatures and times. Initially samples were sintered at 690°C for 5 h, 700°C for 3 h, 700°C for 5 h, and 705°C for 5 h as shown in Figure 4.16.

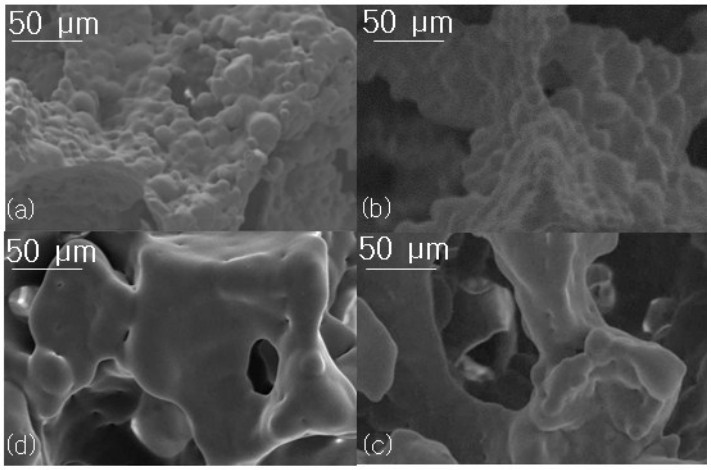


Figure 4.16: SEM micrographs of SBP-3 gel cast foam scaffolds sintered under different conditions (a) 690°C for 5 h, (b) 700°C for 3 h, (c) 700°C for 5 h, (d) 705°C for 5 h.

Figure 4.16 summaries the SEM images collected after sintering. The times required for sintering were much longer than that of the other glass compositions. This could be due to the added strontium within the composition increasing the glass transition temperature [83, 84]. Even at a hold time of 5 h the scaffold surfaces produced were not as homogenous as those of ICIE16 or 13-93.

XRD was used to analyse the structure of the glass after sintering (Figure 4.17). Even after the shortest and lowest temperature sintering profile, 5 h at 690°C, a crystallisation peak appeared at 31° 2Θ. This is interesting as it is discussed widely within literature that adding multiple components to glasses increases their thermal processing window enabling improved sintering without crystallisation [43, 89, 181]. SBP-3, especially at this particle distribution, does not seem to follow this trend. This may be due to the low silica content. As only one small peak appeared within the XRD trace, its structure cannot be defined. When sintering scaffolds from glass powders, a compromise needs to be met between viscous flow of particles to form a continuous phase, changes of the scaffold morphology, mechanical properties and crystallisation. It was not possible to sinter SBP-3 without having this single crystalline peak form,

consequently it was decided that 700°C for 5 h was optimum as there was cohesion of particles with low crystallisation.

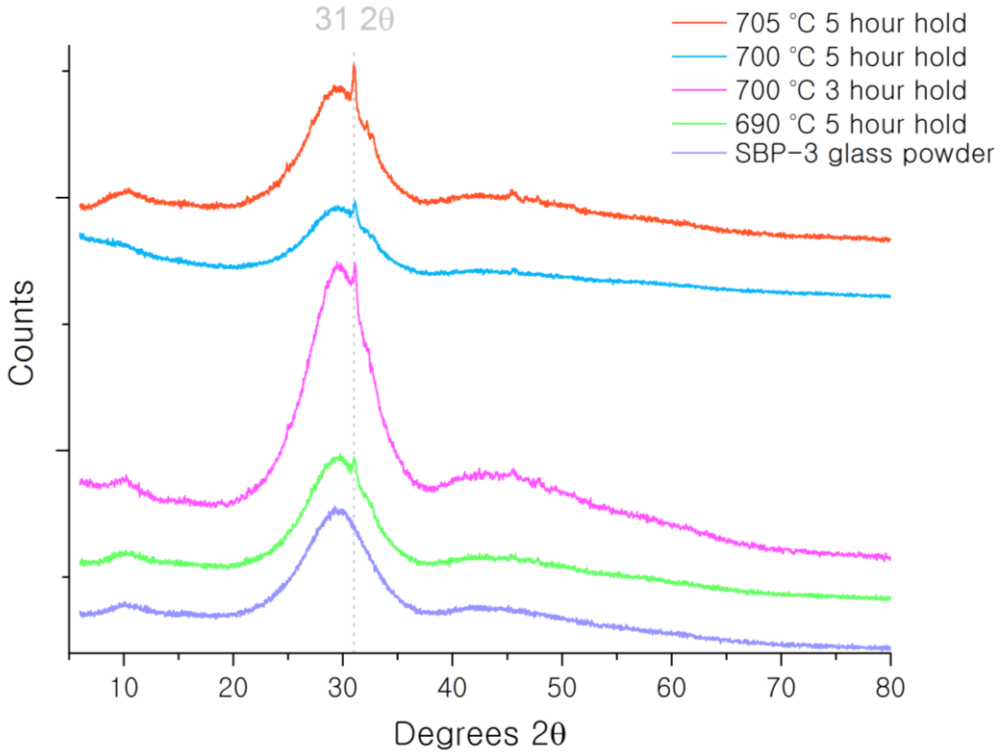


Figure 4.17: XRD patterns collected for SBP-3 after sintering at various times and temperatures.

4.6 MECHANICAL TESTING

Scaffolds in their green body form were cut into cubes for compression testing with dimensions of 1 cm, then sintered using their specific temperature profile. A typical stress strain curve for the foams are shown in Figure 4.18. As expected with a brittle material the sample was not subject to plastic deformation, only deforming elastically before failure resulting in limited strain before failure. The scaffolds had multiple strut failures throughout loading within the elastic region, maintaining a minimum level of force until complete scaffold collapse. This loading profile is due to the random nature of the foams morphology.

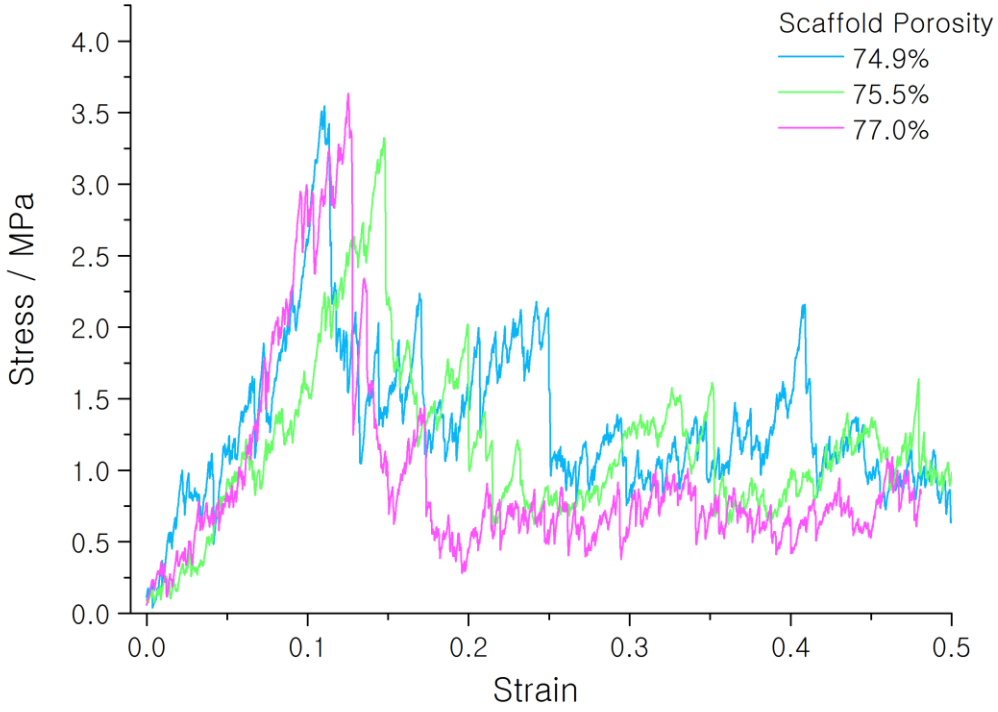


Figure 4.18: Example stress strain curves for ICIE16 scaffolds with percentage porosities stated.

This stress–strain profile highlights the limitations of bioactive glass scaffolds for loaded bone repair. Although the bioactive properties elicit an excellent

biological response, their inability to take load, and their failure mechanism makes them unsuitable for the cyclic loading behaviour of the body.

4.6.1 Gel-cast scaffolds mechanical properties

Scaffolds of the three glass compositions were produced using their optimised processing protocols to produce samples with similar porosities between 75-77 %. Their mechanical properties were compared via compression testing. The results are summarised in Figure 4.19 and Table 4.3. Compressive strengths for all glass compositions were within the range of 2-12 MPa, which is the range for cancellous bone [182].

Mechanical properties of these glasses were affected by many factors. Due to the random pore morphology of the scaffolds, the amount of material in the direction of the loading force was not equivalent between samples, therefore variation was seen between samples tested. Between the scaffolds there was also a 25 μm variation in modal interconnect diameter, ICIE16 being the smallest and 13-93 the greatest. All of the glasses used had different sintering windows, due to their specific glass compositions. A key criterion was to keep the glasses amorphous post sintering; this resulted in the amount of sintering achieved, even though optimised for each composition, differing between glass composition and the consequent scaffolds produced.

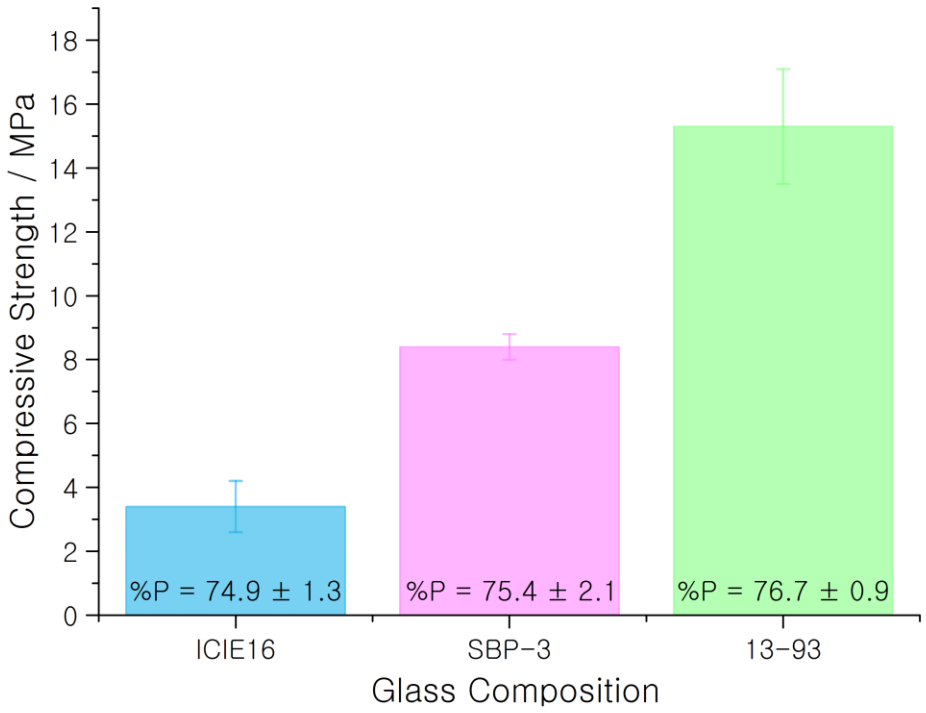


Figure 4.19: Compressive strength of gel-cast scaffolds of ICIE16, SBP-3, and 13-93 compositions and their associate percentage porosity.

Table 4.3: Mechanical properties of ICIE16, SBP-3 and 13-93 manufactured and sintered to their optimised process

Glass	Surfactant Concentration /ml	Sintering profile	Modal Interconnect Size /µm	Percentage Porosity /%	Max Compressive Strength /MPa
ICIE16	0.3	680°C 1.5 h	107.9 ± 8.6	74.9 ± 1.3	3.4 ± 0.3
13-93	0.4	700°C 1 h	132.4 ± 9.3	75.4 ± 2.1	15.3 ± 1.8
SBP-3	0.4 [130]	690°C 5 h	124.8 ± 12.4	76.7 ± 0.9	8.4 ± 0.8

ICIE16 had the lowest compressive strength of the scaffolds tested (3.4 ± 0.3 MPa), even though it had the lowest porosity (74.9 ± 1.3 %) and smallest interconnect diameter (107.9 ± 8.6 µm). This could be due to variability in

sinterability without crystallisation (Figure 4.20) but the primary reason is due to chemical composition. ICIE16 has the lowest network connectivity of the 3 glasses at 2.13, this means the ratio of network modifiers to the network former was highest. This results in a highly disrupted backbone of network formers, the more broken the network the less homogenous, the weaker the glass becomes [20]. This combination results in a highly bioactive glass at the expensive of mechanical properties.

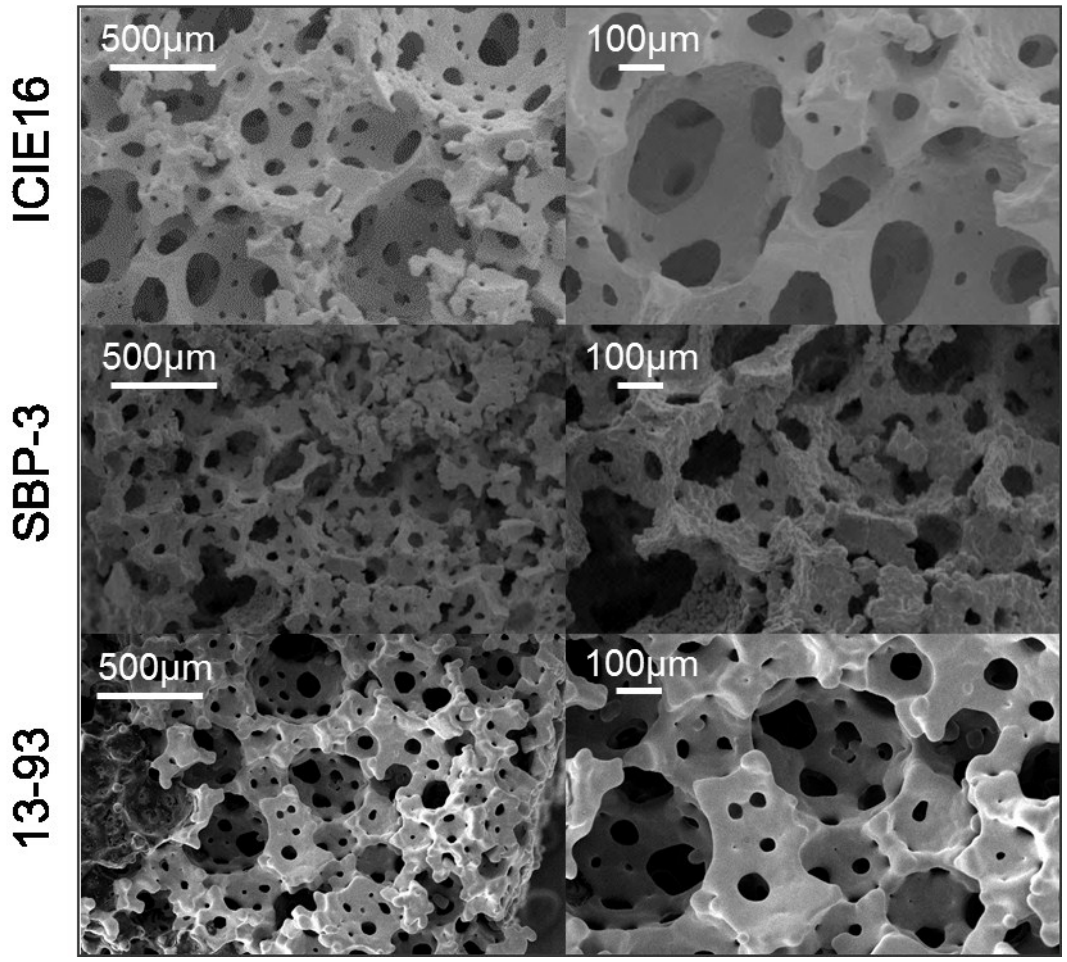


Figure 4.20: SEM images of ICIE16, SBP-3 and 13-93 gel cast foam scaffolds post sintering

The mechanical performance of SBP-3 and 13-93 followed the same trend relating to their specific network connectivity. Their network connectivities were 2.84 and 3.01 and compressive strengths of 8.4 ± 0.8 MPa and 15.3 ± 1.8 MPa respectively. The improved performance of 13-93 is due to its highly continuous network due to its low quantities of network modifiers within the

system, the yields a greater sintering window enabling sintering without crystallisation. This forms continuous struts during sintering, with less flaws, and homogenous surfaces via viscous flow within the scaffold (as shown in Figure 4.20).

As 13-93 is a well-documented composition in literature [34, 35, 37, 41, 121, 127, 156, 183], comparison between the gel-casting process and the foam replica method can be made. Both these processing method created porous scaffolds formation of for bone repair. Fu *et al.* [34] reported scaffolds manufactured via the foam replica method with porosities of 85 ± 2% and with comparable pore sizes and interconnect diameter to these scaffolds to have compressive strengths of 11 ± 1 MPa. The scaffolds reported here, even though they have slightly lower porosities have greater mechanical strengths, of 15.3 ± 1.8. This is likely to be due to the foam template leaving hollow struts, reducing the mechanical properties, a problem eliminated in the gel cast foaming process.

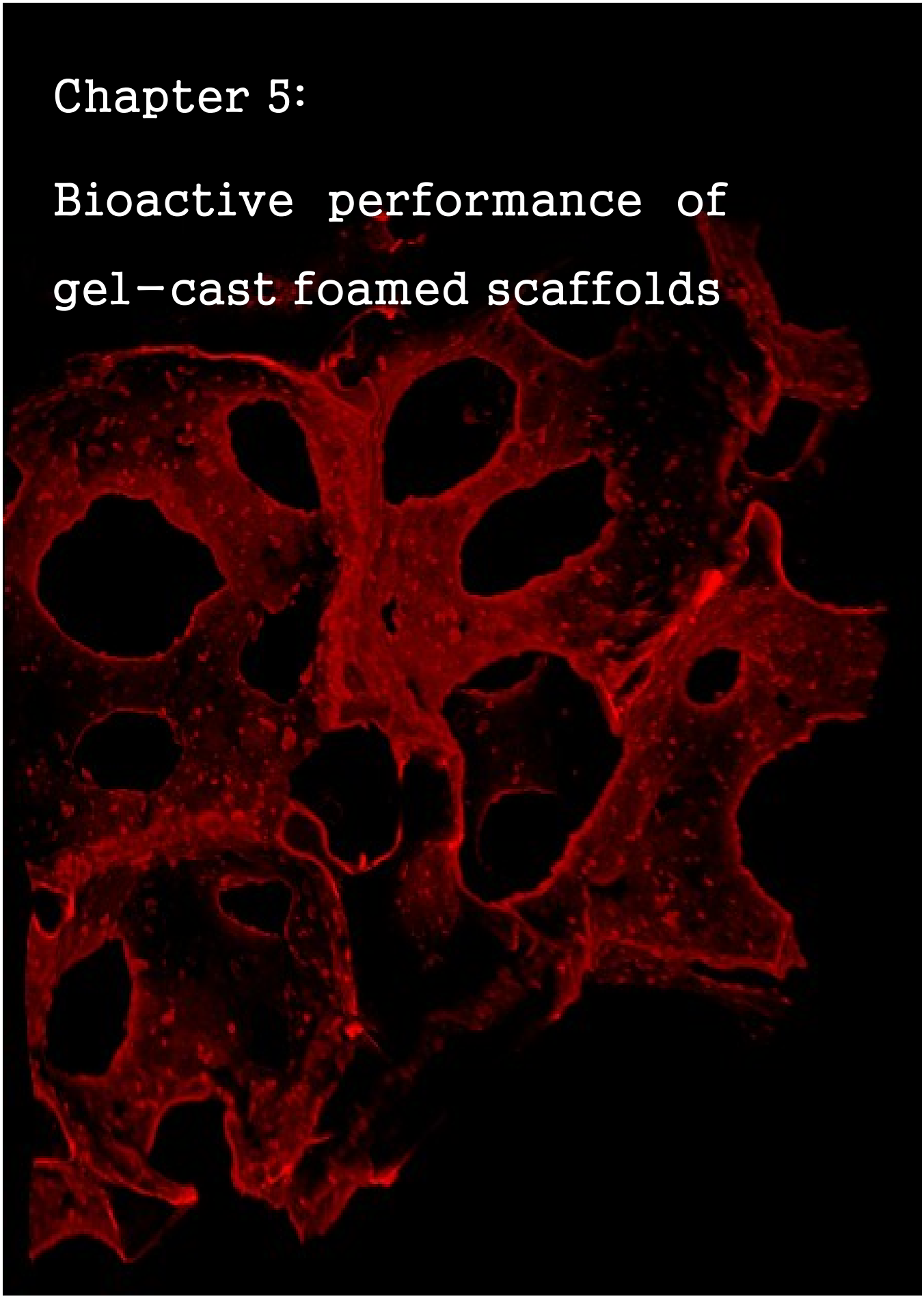
4.7 CONCLUSIONS

Bioactive glass scaffolds can be produced via the adapted gel-cast foaming route, with suitable interconnects and pore size for bone ingrowth. This technique is able to be adapted for use with 3 different glasses, ICIE16, SBP-3 and 13-93 all with different chemical compositions, and network connectivites. In order to produce scaffolds of similar porosity, the gel-cast foaming variables had to be modified for each composition.

The optimised scaffolds had 75% porosity, and a modal interconnect diameter between 100-150 μm and remained mainly amorphous post processing. All scaffolds had compressive strengths within the range of cancellous bone [182]. Compressive strengths of 13-93 gel cast foam scaffolds were slightly higher than similar foam scaffolds produced by foam templating.

Chapter 5:

Bioactive performance of gel-cast foamed scaffolds



5 BIOACTIVE PERFORMANCE OF GEL-CAST FOAMED SCAFFOLDS

5.1 INTRODUCTION

The dissolution behaviour of the scaffolds and rate of formation of the HCA surface layer in simulated body fluid (SBF) solution was investigated. Testing of bioactive glasses via SBF has been widely debated in literature, as previously discussed in section 2.4.1. The concern is that formation of a HCA layer in SBF does not mean that the glass or scaffold will bond to bone *in vivo.* However, the stages of glass dissolution that lead to HCA formation are generally agreed [184], discussed in section 2.1.2, consequently the rate at which HCA formation occurs in SBF is a useful comparison between new devices.

A pilot *in vivo* study was then completed to compare gel-cast scaffolds manufactured from ICIE16 and SBP-3. To understand if the morphology of the scaffolds produced via the adapted gel-cast foaming process enabled bone ingrowth, and if either glass gained better bone remodelling and ingrowth over a 12 week time point in a femoral head defect of a rabbit.

5.2 METHODOLOGY

5.2.1 SBF preparation

The protocol for this test method was taken from Maçon *et al.* [38], which arose from an international project to determine a standardised SBF testing protocol for bioactive glasses, which would allow comparison between different glasses. In order to prepare 1 L of solution media, ionic additions, shown in Table 5.1 were added, in the order shown, while the solution was stirred at 37 °C.

The pH of the solution was adjusted to 7.4 using 1 M HCl. Once all additions were made the solution volume was increased to 1 L by adding di-ionised water, using a volumetric flask. Stock solution was kept at 37°C rotating at 120 RPM throughout the length of the study, but for no longer than one month.

Table 5.1: Reagents used for preparing SBF solution.

Order	Reagent	Quantity /gL^{-1}	CAS number
1	NaCl	8.035	7647-14-5
2	$NaHCO_3$	0.355	144-55-8
3	KCl	0.225	7447-40-7
4	$K_2HPO_43H_2O$	0.231	16788-57-1
5	$MgCl_26H_2O$	0.311	7791-18-6
6	HCl 1M	38 ml	7647-01-0
7	$CaCl_22H_2O$	0.386	10035-04-8
8	$8Na_2SO_4$	0.072	7757-82-6
9	$(HOCH_2)_3CNH_2$	6.118	77-86-1

5.2.2 Dissolution protocol for bioactive glass scaffolds

150 mg of scaffolds of equivalent porosity, 72-75% and interconnect size 120-140 μm were immersed in 100 ml of SBF in a polypropylene container. The container was placed in an orbital shaker at 37°C, rotating at 120 rpm. The same protocol was applied to a SBF only sample as a control. Time points were taken at: 1, 2, 4, 8, 24, 48, 72 h and 7, 14, 21 and 28 days. At each time point, three containers were removed per glass composition, the pH of the solution was measured and 1 ml of the supernatant was removed to analyse the ionic concentration (Section 3.3.1). The scaffolds were rinsed in acetone, to terminate the reaction, and placed in a 40°C oven to dry. Surface analysis was then completed using FTIR, XRD and SEM.

5.2.3 Ion concentration profiles

Elemental concentrations in solution were measured using a Thermo Scientific iCAP 6300 Duo Inductively Coupled Plasma Optical Emission Spectrometer (ICP-OES) equipped with an auto sampler. Solutions were prepared by diluting the dissolution product supernatant by a factor of 10 with analytical grade 2 M nitric acid. Standards of the applicable elements; silicon, phosphorus, calcium, sodium, magnesium, strontium and potassium were prepared at 0, 5, 10, 20 and 40 μg ml^{-1} to gain a calibration curve. Calibration was carried out at the beginning of each sequence. Silicon and phosphorus were measured in the axial direction of the plasma flame whereas calcium, magnesium, strontium, sodium and potassium were measured in the radial direction.

5.2.4 Surface analysis

Fourier transformed infrared spectroscopy

Once samples were dried, they were ground by hand into a fine powder and characterised in Attenuated Total Reflection (ATR) using a Nicolet iS10 FTIR fitted with a Specac MK11 Golden Gate Single Reflection ATR module over wavenumbers from 4000 to 650 cm^{-1} across 64 scans.

X-Ray diffraction

Powdered samples were placed on an amorphous silicon disk, to give a zero background. The diffraction was measured with a Bruker D2 desktop XRD between 5° and 80° 2Θ, with a 0.03° step size and a total counting time of 20 min. The radiation source was a Ni filtered CuKα.

5.3 *SBF* TESTING RESULTS

5.3.1 pH change

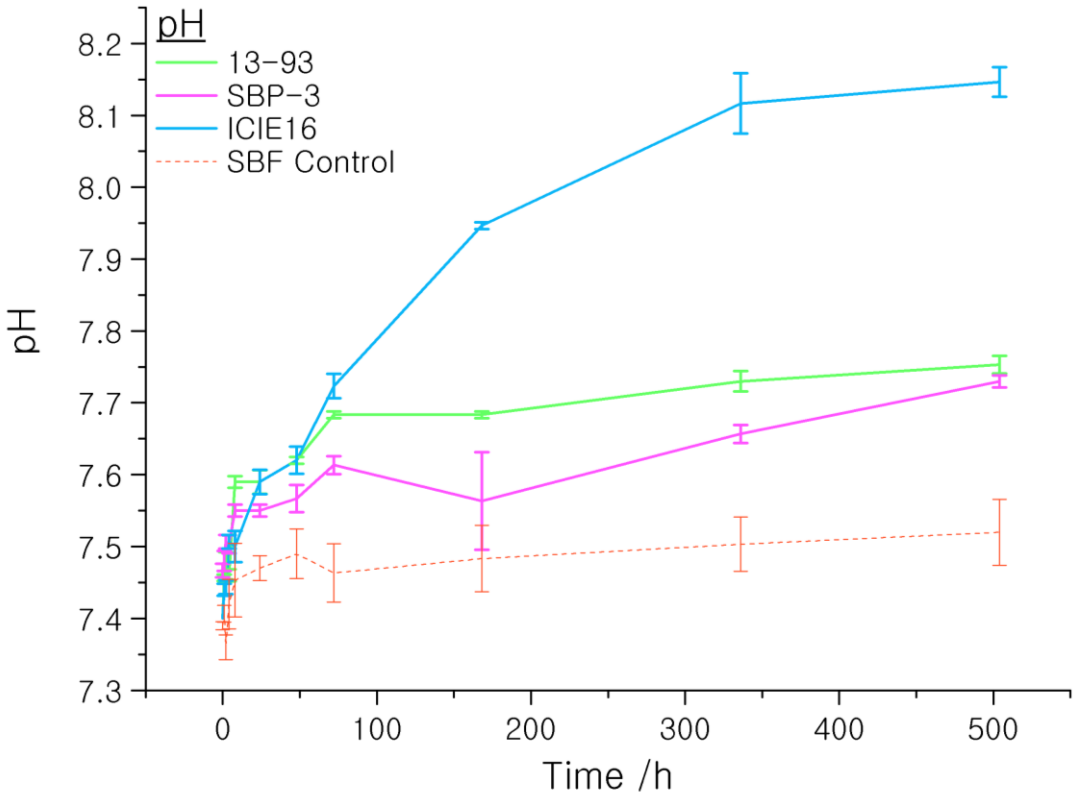


Figure 5.1: pH change across 500 h immersion in SBF for scaffolds made by gel-cast foaming from 13-93, SBP-3 and ICIE16 compositions.

Figure 5.1 summarises the pH change after immersion of gel-cast foam scaffolds in SBF. pH increase was synonymous with the release of cations into solution from the glass, through the exchange of H^+. The pH of the SBF control was stable at around 7.4 throughout the length of the study, whereas the pH of the solution containing glass scaffolds rose due to cation exchange. ICIE16 caused the highest pH increase, peaking at 8.1 after 500 h of immersion. The increase in pH caused by SBP-3 and 13-93, to 7.73 and 7.75 respectively by 500 h, was less than that of ICIE16 due to a lower level of cation exchange with the solution. ICIE16 network connectivity was the lowest of the three glasses tested, due to its higher ratio of modifying to glass forming ions, resulting in the

most discontinuous network. A lower network connectivity should result in the greatest dissolution rate consequently giving the high pH rise observed.

The pH of the SBF containing SBP-3 and 13-93 scaffolds rose at a similar rate for the first 24 h. After 24 h, both glasses caused a continued rise in pH, but the increase caused by SBP-3 was slower than that of 13-93 scaffolds. The solution containing 13-93 pH reached 7.7 by 72 h, where it remained throughout the rest of the study, whereas SBP-3 did not reach this point, until the end of the study.

For ease of reference, Table 5.2 summarises the glass compositions used within this study, as well as the compositional ratios of modifiers: formers: intermediates. 13-93 network connectivity was much higher than that of SBP-3, (3.1 compared to 2.84), therefore its cation exchange rate was expected to be much slower. This was contradictory to the results seen in Figure 5.1. This pH result cannot conclude whether this is due to 13-93 dissolving faster, or SBP-3 dissolving slower than expected. It is perhaps more likely that the SBP-3 composition degraded slower than predicted, perhaps due to some of the cations behaving as network intermediates, which was not taken into account by the network connectivity calculation.

Table 5.2: Glass compositions, including the ratios of network formers to modifiers within the compositions, all in mol%

		Oxide	45S5	ICIE16	13-93	SBP-3
		SiO_2	46.13	49.46	54.60	44.50
		CaO	26.91	36.60	22.40	17.80
		Na_2O	24.35	6.60	6.00	4.00
		P_2O_5	2.60	1.07	1.70	4.50
		K_2O		6.60	7.90	4.00
		MgO			7.70	7.50
		SrO				17.80
Total amount /mol %	Network formers		48.73	50.53	56.30	49.0
	Network modifiers		51.26	49.47	43.70	51.0
	Possible Network intermediates				7.70	7.50
	Modified Network Connectivity (NC')		2.10	2.13	3.01	2.84

5.3.2 ICP-OES results

Figure 5.2 to Figure 5.7 summarise the ionic dissolution results for each element of 13-93, SBP-3 and ICIE16 gel-cast scaffolds over 500 h immersion. Figure 5.2 shows the silica release.

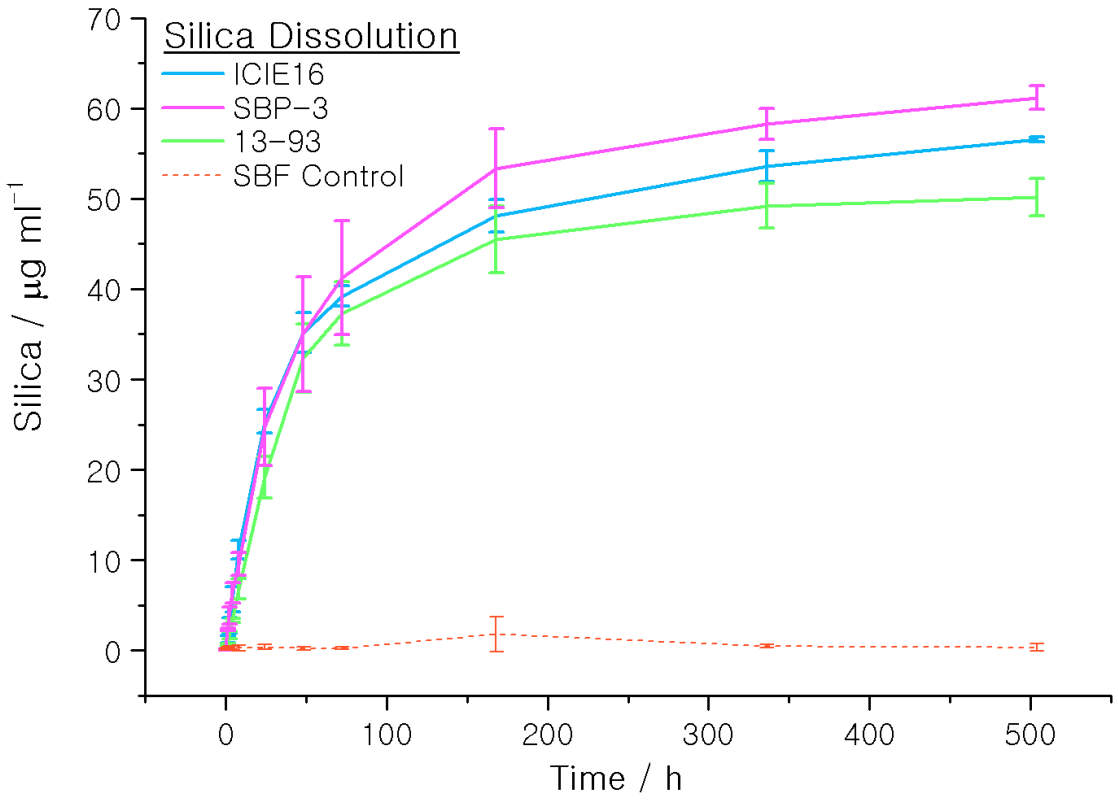


Figure 5.2: Silica dissolution profiles for 13-93, ICIE16 and SBP-3 gel cast foam scaffolds in SBF up to 500 h.

Silica release for all 3 glasses over 72 h was similar regardless of their composition or network connectivity. All three glasses followed the same trend with a steep release in the first 7 days followed by a plateau. After 7 days, Si content in SBF was nearing zero compared with 52.8 ± 1.3 µg ml^{-1} for ICIE16, 57.6 ± 2.5 µg ml^{-1} for SBP-3, and 48.3 ± 2.7 µg ml^{-1} for 13-93.

13-93 had the most silica and phosphorus within its composition acting as network formers (56.3 mol %), in addition to the magnesium being expected to act as a network intermediate [30], meaning a proportion of the Mg can act as a network former in the glass network. This results in it having the highest network connectivity of the three glasses tested within this study, and corroborates the ICP-OES result by having the slowest silica release.

SBP-3 has the lowest amount of silica within its network, 44.5 mol%, when compared with the other glasses tested, and 51 mol % of network modifiers. As

with the 13-93, it has some magnesium within its composition, which is expected to act as an intermediate. In addition to this, SBP-3 has the highest mol% of phosphorus within its composition at 4.5 mol%. Phosphate forms its own orthophospate phase which is charge balanced by modifying ions such as Ca^{2+}, removing them from some of the silicate network, which can indirectly cause an increase in network connectivity of the silica [30].

SBP-3 and ICIE16 both have similar ratios of network formers to modifying ions. However, SBP-3 has lower silica content, a difference of 4.96 mol% when compared with ICIE16, resulting in the highest silica release tested. This suggests that the role of intermediates with SBP-3 network is less than expected, reinforcing magnesium's behaviour to be compositional dependent [30].

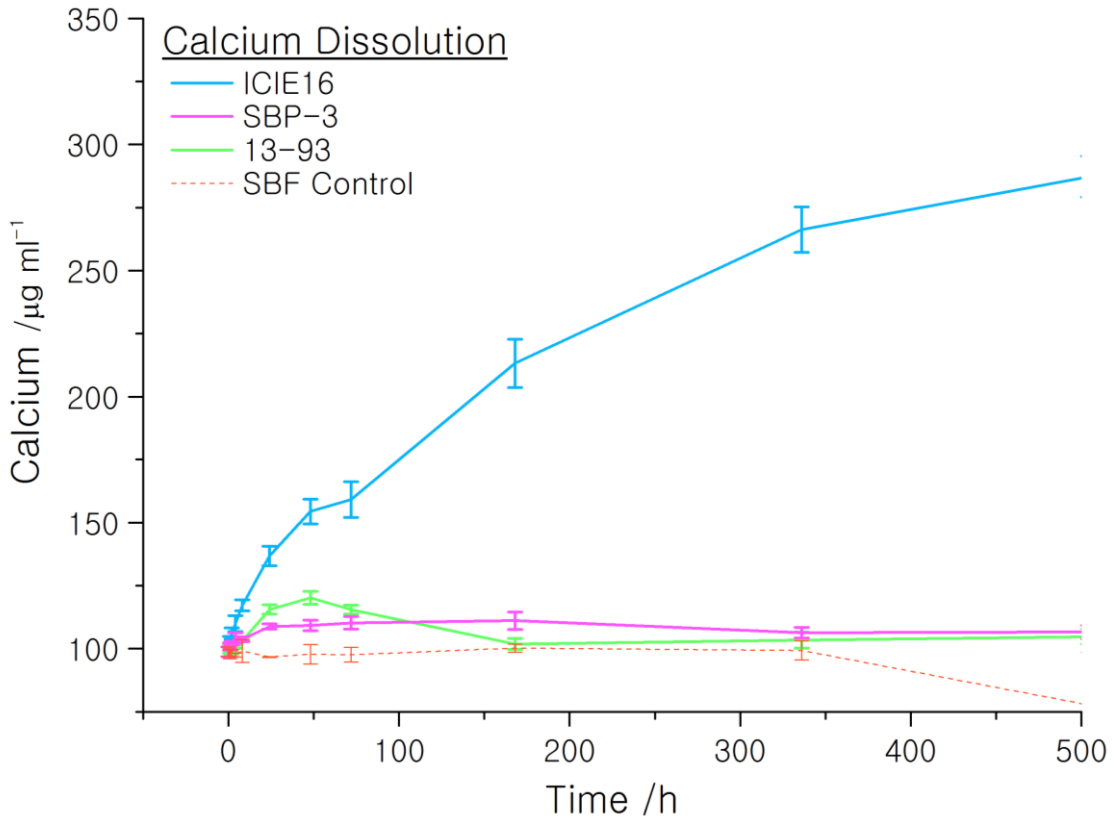


Figure 5.3: Calcium dissolution profiles in SBF following immersion of gel-cast foams of 13-93, ICIE16 and SBP-3 compositions, up to 500 h.

Figure 5.3 shows the calcium dissolution over 500 h in SBF. Calcium profiles in SBF are often difficult to interpret as the calcium released from the glass can combine with phosphate available in the solution to precipitate as calcium phosphate depending upon the pH. When comparing the three glasses, the calcium release profile within the SBF containing ICIE16 scaffolds was much greater than that of SBP-3 or 13-93. By 72 h, the concentration of calcium in the SBF reached 159.1 ± 7.1 μg ml^{-1} for ICIE16, compared to 110.3 ± 2.5 μg ml^{-1} for SBP-3 and 115.6 ± 1.7 μg ml^{-1} for 13-93. After this point, the calcium release from ICIE16 continued to increase to 287.2 ± 8.1 μg ml^{-1} at 500 h. However, the calcium content of the SBF containing 13-93 reduced gradually after 72 h to 104.8 ± 3.0 μg ml^{-1} by the end of the study. SBP-3 followed a similar strength to 13-93 with its calcium release reaching its peak at 72 h, after which it gradually decreased back to level of the SBF control (99.3 ± 0.2 μg ml^{-1}).

Calcium released into solution is known to drive pH increase, due to the H^+ depleting in the SBF during the ion exchange, therefore changes can be compared with the pH profiles in Figure 5.1. By 72 h, the pH increase of SBP-3 had also stabilised at 7.73, matching the calcium trend. The ICIE16 composition had much higher calcium content than 13-93 and SPB-3 (36.60 mol% versus 22.4 and 7.80 respectively). Combining the high concentration within the composition with its low network connectivity would result in the high calcium release and pH rise seen.

Reduction of phosphorus concentration from SBF is associated with the formation of a calcium phosphate rich layer upon the glass surface. The ICP-OES results for phosphorus are presented in Figure 5.4. Phosphorus reduction from the SBF was the fastest in the SBF containing ICIE16 scaffolds, reducing to 0.5 ± 0.2 μg ml^{-1} by 168 h. The ICIE16 scaffolds also caused the most rapid Ca release, and highest increase in pH. While increased calcium content into

SBF solution will encourage calcium phosphate precipitation, it is also preferential at elevated pH levels.

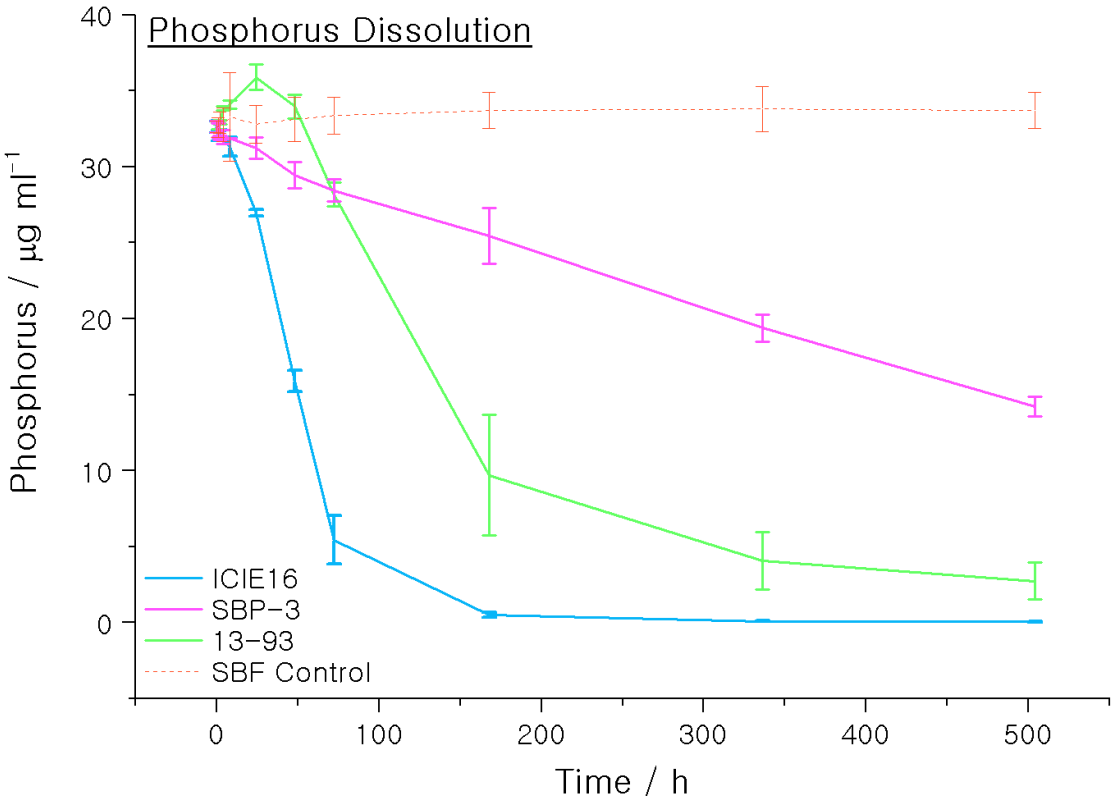


Figure 5.4: Phosphorous content in SBF after immersion of gel-cast foam scaffolds made from 13-93, ICIE16 and SBP-3 bioactive glass compositions, up to 500 h.

The phosphorus content of SBF containing 13-93 increased for the first 24 h of immersion to 35.9 ± 0.8 µg ml^{-1}, after which it reduced to 2.73 ± 1.2 µg ml^{-1} by 500 h. Phosphorus concentration of the SBF containing SBP-3 remained stable at 31.87 µg ml^{-1} over the first 24 h, with a standard deviation of 0.4 µg ml^{-1}, and after 24 h it reduced to 14.2 ± 0.6 µg ml^{-1} after 500 h.

SBP-3 had the highest amount of phosphate in its composition (4.5 mol%), nearly 4 times greater than both ICIE16 and 13-93, this resulted in a more sustained phosphorus release throughout the study. Watts *et al.* [30] stated that solid state ^{31}P and ^{29}Si NMR showed that calcium and sodium preferentially bond with the orthophosphate phase, over silica therefore, phosphate may have

tandem effects on their dissolution. Figure 5.3 shows that SBP-3 calcium release was slower than that of the other glasses, although it had the least calcium available within its composition, it could also be as a result of the higher phosphate concentration within its composition.

The maximum calcium release from 13-93 and SBP-3 was 20.2 ± 2.5 μg ml^{-1} and 9.4 ± 2.5 μg ml^{-1} respectively. HA, $Ca_5(PO_4)_3(OH)$, needs enough calcium and phosphate available in solution for precipitation. If there is not enough calcium available, substitution for Ca^{2+} has been known to occur with other ions of similar atomic size and charge, for example Sr^{2+} [33, 73, 79, 83, 185]. If alternatives are not available the rate of precipitation will be reduced.

Phosphorus levels in SBF containing 13-93 increased initially within the solution, instead of the reduction seen in SBF containing ICIE16. By 168 h, the amount of calcium available within the 13-93 study was equal to the level of calcium available within the SBF control, however, the amount of phosphorous continued to decrease after this point. This could suggest that, not only its network connectivity, but also the level of calcium available within the composition for dissolution was a limiting factor for calcium phosphate precipitation.

Potassium release is shown in Figure 5.5. Within 24 h, the initial release from all three glasses was comparable. However, over the length of the study this release rate changed. Potassium release from SBP-3 did not increase beyond 24 h, staying at approximately 243.2 ± 4.3 μg ml^{-1}. This could be due to the SBP-3 composition containing less potassium that the other two glasses. The potassium content of ICIE16 and 13-93 compositions were similar but potassium release from these two glasses increased at different rates after 24 h of immersion. ICIE16 produced the greatest potassium release reaching 342.4 ± 6.7 μg ml^{-1} at 500 h compared to 294.9 ± 3.6 μg ml^{-1} for 13-93. The lower network connectivity of ICIE16 compared to 13-93 could be responsible for the difference.

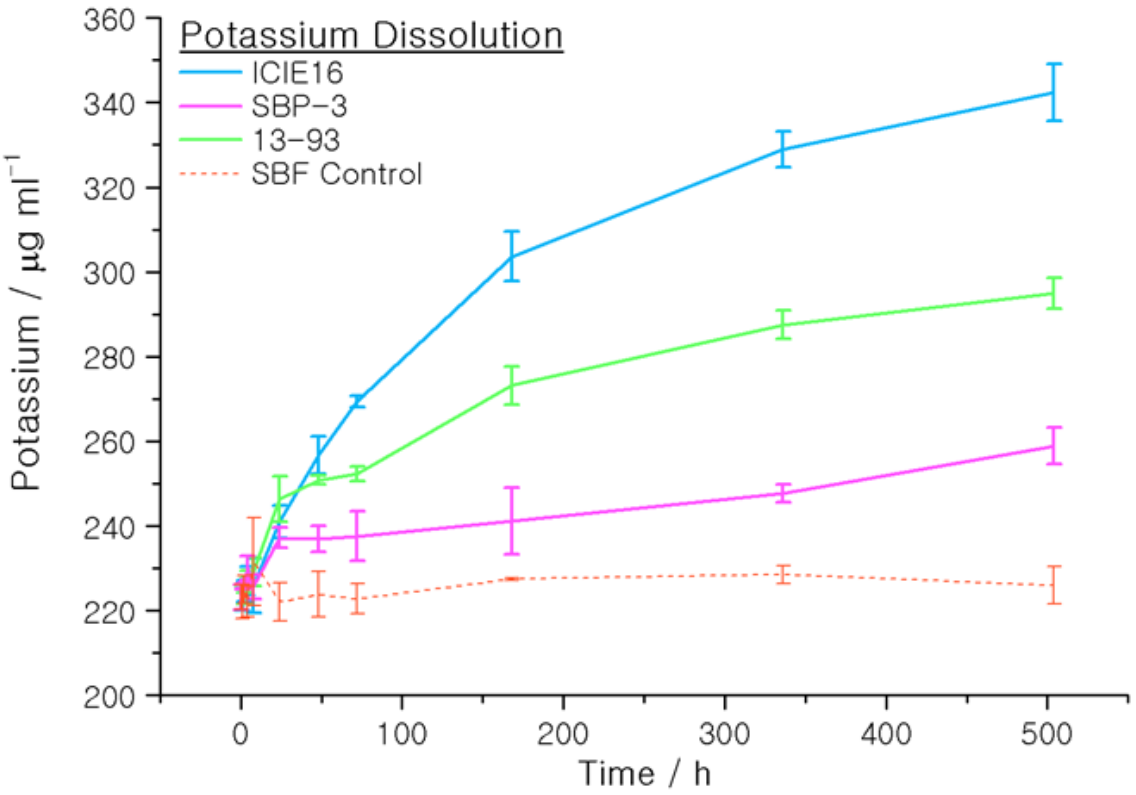


Figure 5.5: Potassium dissolution profiles in SBF containing gel-cast foam bioactive glass scaffolds of 13-93, ICIE16 and SBP-3 composition up to 500 h.

The magnesium dissolution of SBP-3 and 13-93 is summarised in Figure 5.6. Both glasses have similar molar quantities of magnesium of 7.50 and 7.70 mol % respectively. Magnesium is known to act as a network intermediate, with the amount which enters the glass network, or acts as a modifier dependent upon the glass composition [30]. By 72 h, the amount released by the two glasses was similar within 1.9 µg ml^{-1}, the end of the study 13-93 released 2.8 µg ml^{-1} more reaching 52.1 ± 1.2 µg ml^{-1} compared to 49.3 ± 0.8 µg ml^{-1} from SBP-3.

The only glass to contain strontium from this study was SBP-3, its dissolution profile is shown in Figure 5.7. The scaffold released 67.3 ± 10.0 µg ml^{-1}, nearly half of the total released, within the first 72 h. The rate of release then reduced, but continued throughout the length of the study, reaching a maximum concentration of 119.0 ± 5.1 µg ml^{-1}.

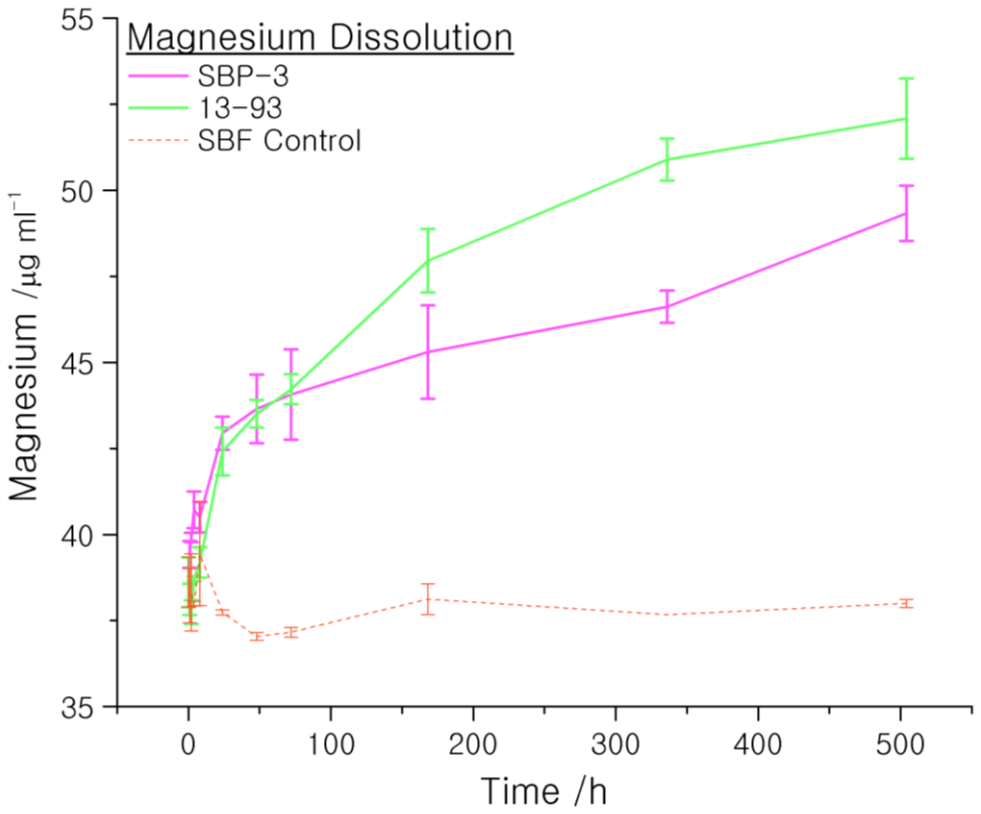


Figure 5.6: Magnesium dissolution from gel-cast foam scaffolds of the SBP-3 and 13-93 bioactive glass compositions over 500 h in SBF.

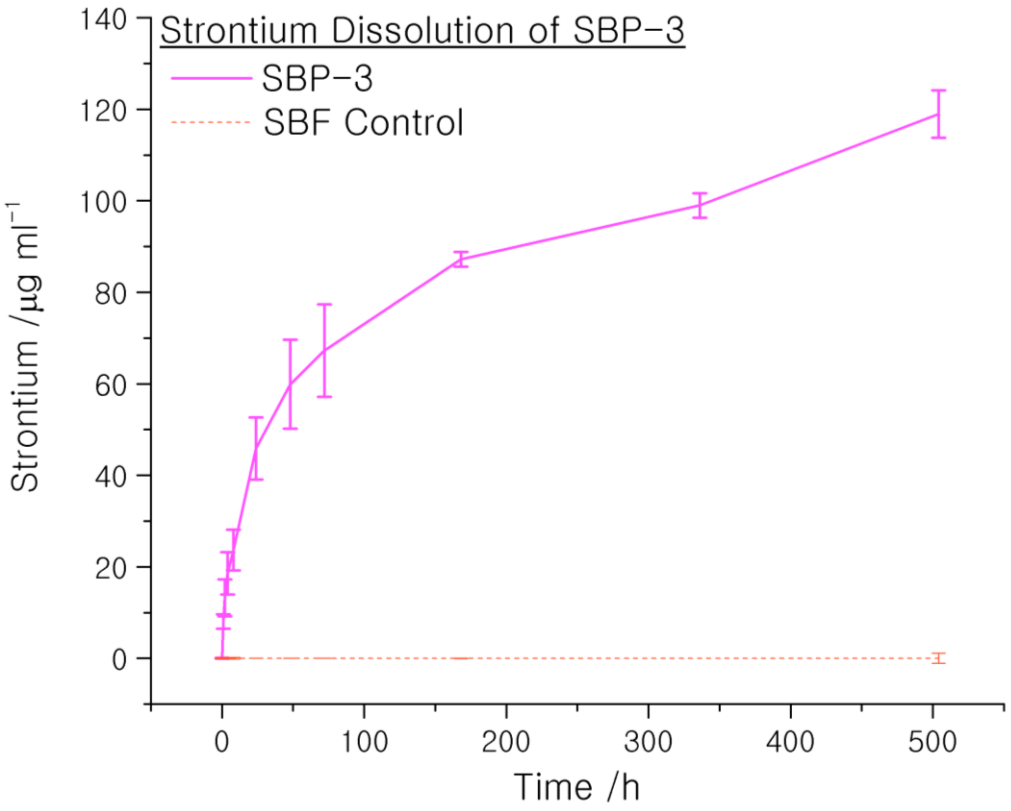


Figure 5.7: Strontium dissolution from gel-cast foam scaffolds of the SBP-3 bioactive glass composition over 500 h in SBF.

5.3.3 Surface analysis

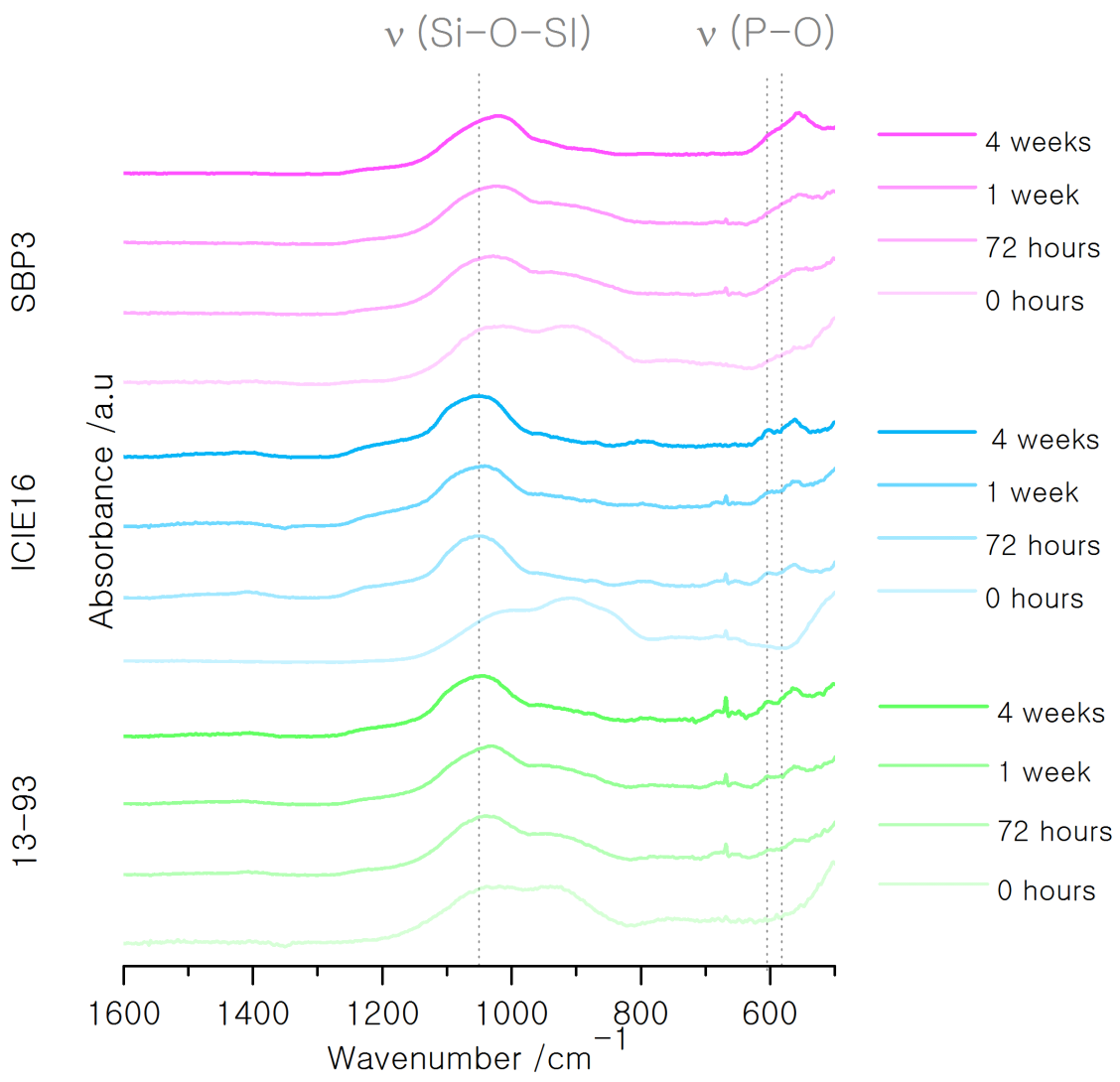


Figure 5.8: FTIR spectra collected from gel-cast foam scaffolds of three glass compositions at after 0, 72 h, 1 week and 4 weeks immersion in SBF.

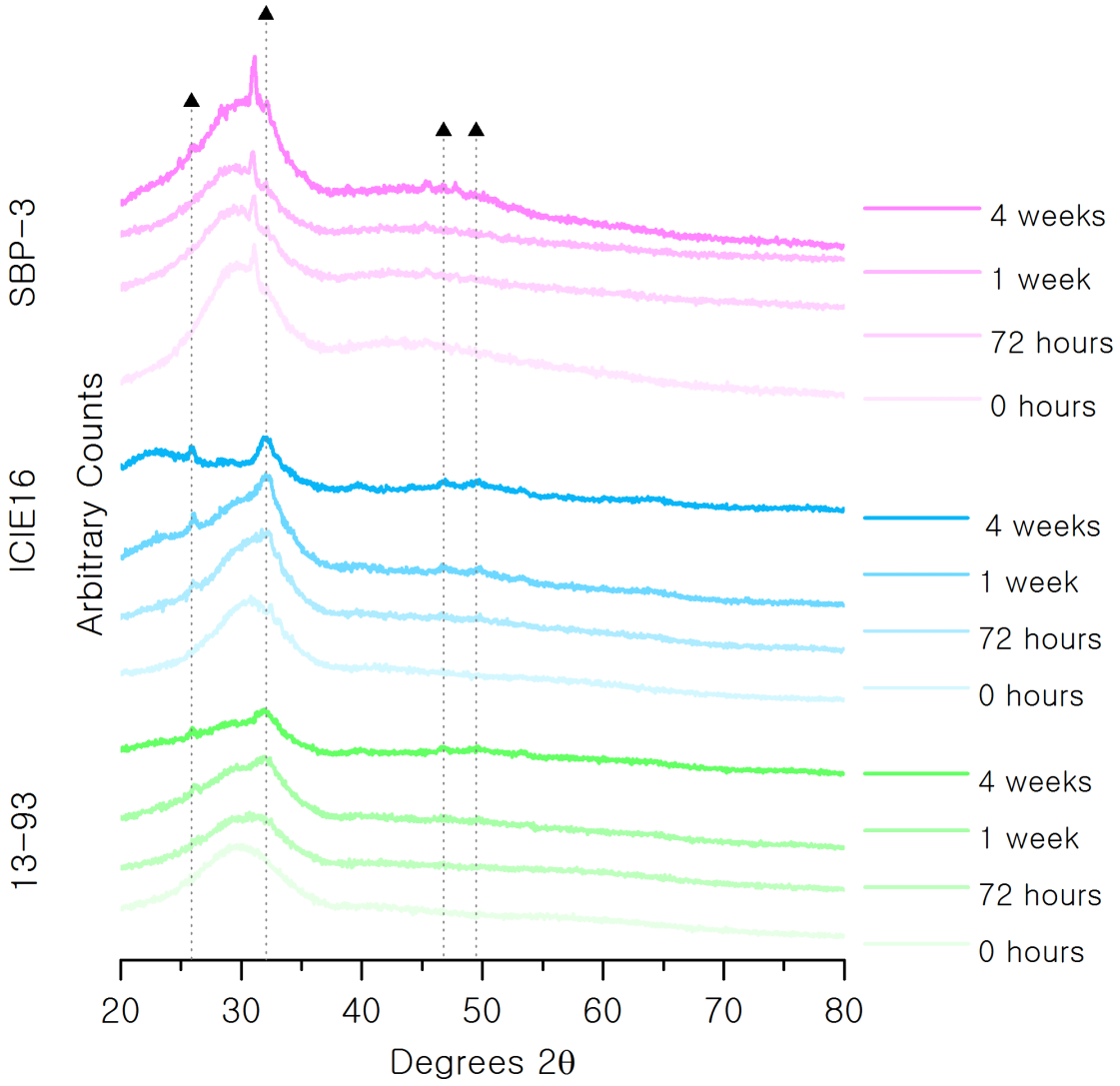


Figure 5.9: XRD patterns collected from gel-cast foam scaffolds of three glass compositions at after 0, 72 h, 1 week and 4 weeks immersion in SBF. Dotted grey lines represent the peaks for HCA reference (ICSD 01-084-199).

FTIR and XRD results at 0, 72 h, 1 week and 4 weeks are summarised in Figure 5.8 and Figure 5.9. By 72 h, ICIE16 shows the development of dual bands at 571 cm^{-1} and 605 cm^{-1} vibration, this corresponds to P-O bending vibrations than can be due to HCA formation [186], but are representative of presence of any orthophosphate. XRD patterns (Figure 5.9) show a change in the shape of the amorphous halo with time and a broad peak developing at 32° 2θ (211) which is indicative of HCA, and a secondary peak at 26° 2θ (002) [184]. The broad nature of this peak suggests the formation of either an amorphous calcium phosphate, or nanocrystalline HCA as opposed to crystalline HCA.

FTIR results for 13-93 were very similar to that of ICIE16 however, the vibration of the P-O bond, at 605 cm^{-1}, was seen to form at a slower rate than ICIE16 forming by 1 week. The XRD showed again a subtle change in the shape of the amorphous halo around the predominant HA peaks of 26° and 32° 2θ.

FTIR spectra of SBP-3 did not show the double vibrations of the P-O bending bands at 571 cm^{-1} and 605 cm^{-1} seen within ICIE16 and 13-93. SBP-3 results instead showed a broader shape change. The XRD patterns showed a subtle change over the length of the study with HCA peaks developing at 26°, 32°, 46° and 49° 2θ however, these are masked by a predominant peak at 31° 2θ which was formed during processing.

SEM images were collected at all-time points throughout dissolution. 0 and 72 h, 2 and 4 weeks are summarised for all three glass compositions in Figure 5.10. All three scaffolds, regardless of composition, started with similar bulk surface finishes and topography. Small post sintering defects were present upon the surface, which were analysed via EDS but did not differ from the bulk glass composition.

By 72 h, ICIE16 and 13-93 had the formation of a similar morphology across the surface. ICIE16 had a coating which was more homogeneous compared with that of 13-93. The surface of SBP-3 had notable changes in surface morphology compared to 0 h. However, the morphology was irregular compared to the continuity of ICIE16 and 13-93 and it appeared as if the smaller crystallites were of a different texture than that of the other two glasses.

By 2 weeks, all three glasses had continuous coverage across the scaffold surfaces. Again ICIE16 and 13-93 morphology was comparable with flower like formations consistent with HCA [187]. SBP-3 surfaces were markedly different with a much bumpier morphology and finer surface details. These formations continued to grow until four weeks, when the study was completed.

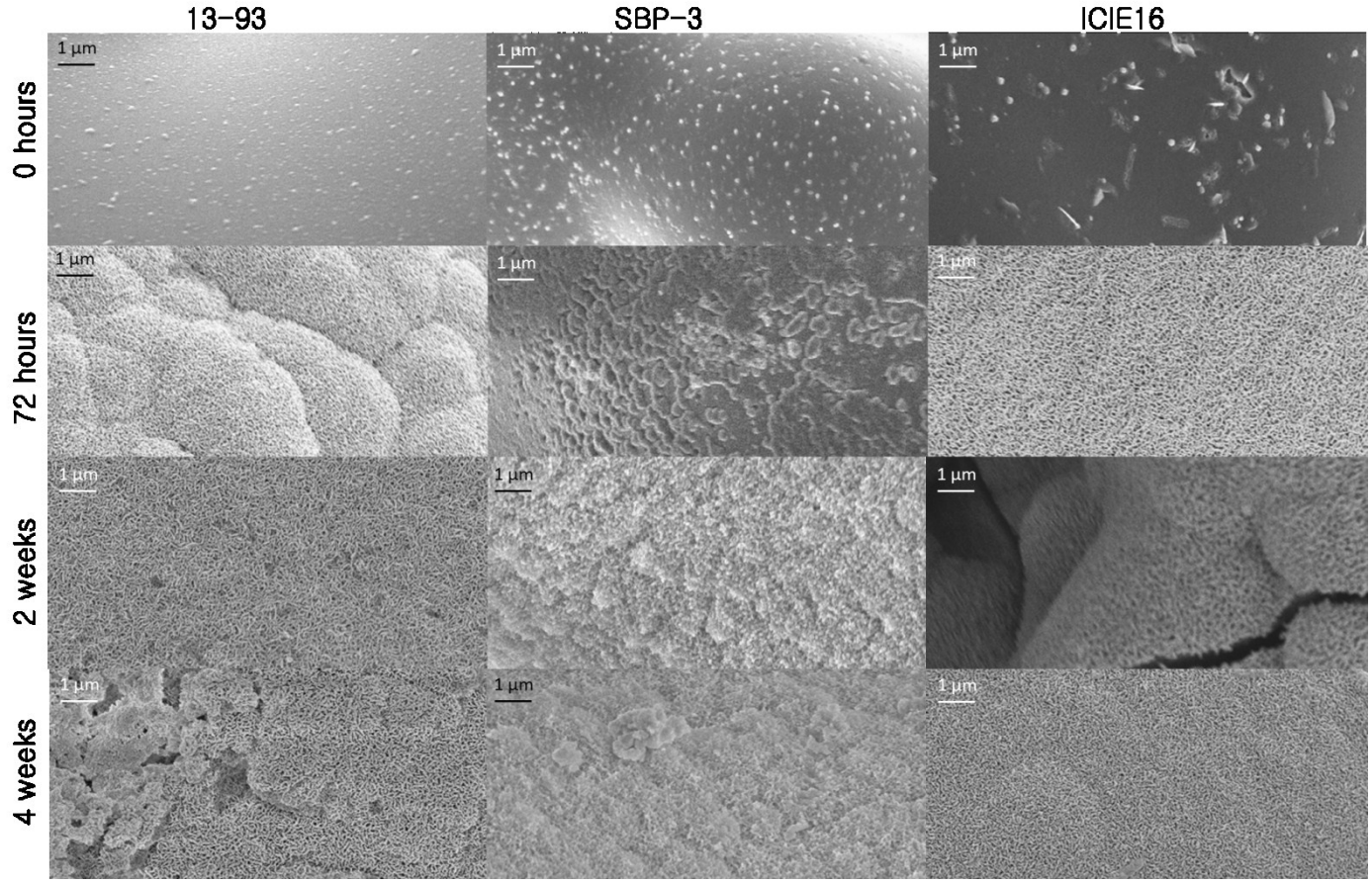


Figure 5.10: SEM images collected of scaffold surface of ICIE16, 13-93 and SBP-3 at various time points up to 4 weeks of SBF testing.

FTIR and XRD of SBP-3 and ICP-OES of the SBF does suggest the formation of a phosphate-rich phase. However, the morphology shown by SEM suggests that it is not the same as that which deposited upon the surface of 13-93 or ICIE16. This could be due to the added strontium available from the glass composition. There are mixed reports on the role of strontium in literature regarding its role in HCA formation. Fredholm *et al.* [84] suggested that Sr substitution for calcium within a glass system results in more rapid HCA formation due to a weaker silicate network, caused by the lower charge to size ratio of Sr^{2+} compared to Ca^{2+}. In contrast, Hoppe *et al.* [185] reported the inverse relationship for strontium substituted 13-93 nanoparticles. Theoretical studies performed via *ab initio* calculations by Zeglinski *et al.* [188] suggested

that strontium can be substituted from both Ca-1 and 2 sites within the HCA lattice, which could support the change in morphology seen at the surface when compared to 13-93 and ICIE16.

By four weeks, small variations could be seen between the morphology formed between 13-93 and ICIE16. Consequently, EDS analysis was conducted on the surface at 4 weeks to see if any variation could be seen between the three glass compositions, Figure 5.11 (within the data no peaks were seen above 10 keV so the data is not plotted). The EDS spectrum for ICIE16 and 13-93, showed that the layer formed was rich in calcium and phosphate. A small peak was also present inline with the k_{α} of silica and magnesium for 13-93. Both these elements are present within the glass compositions. This suggests that either these ions have been incorporated into the HCA layer, or that the thickness of the precipitate layer was less than that of the interaction volume of the technique.

The EDS results for SBP-3 showed inclusion peaks of strontium and magnesium within the calcium phosphate phase, supporting the difference in morphology seen within the SEM images compared with ICIE16 and 13-93. These inclusions have been reported previously in literature [33, 79, 84, 185].

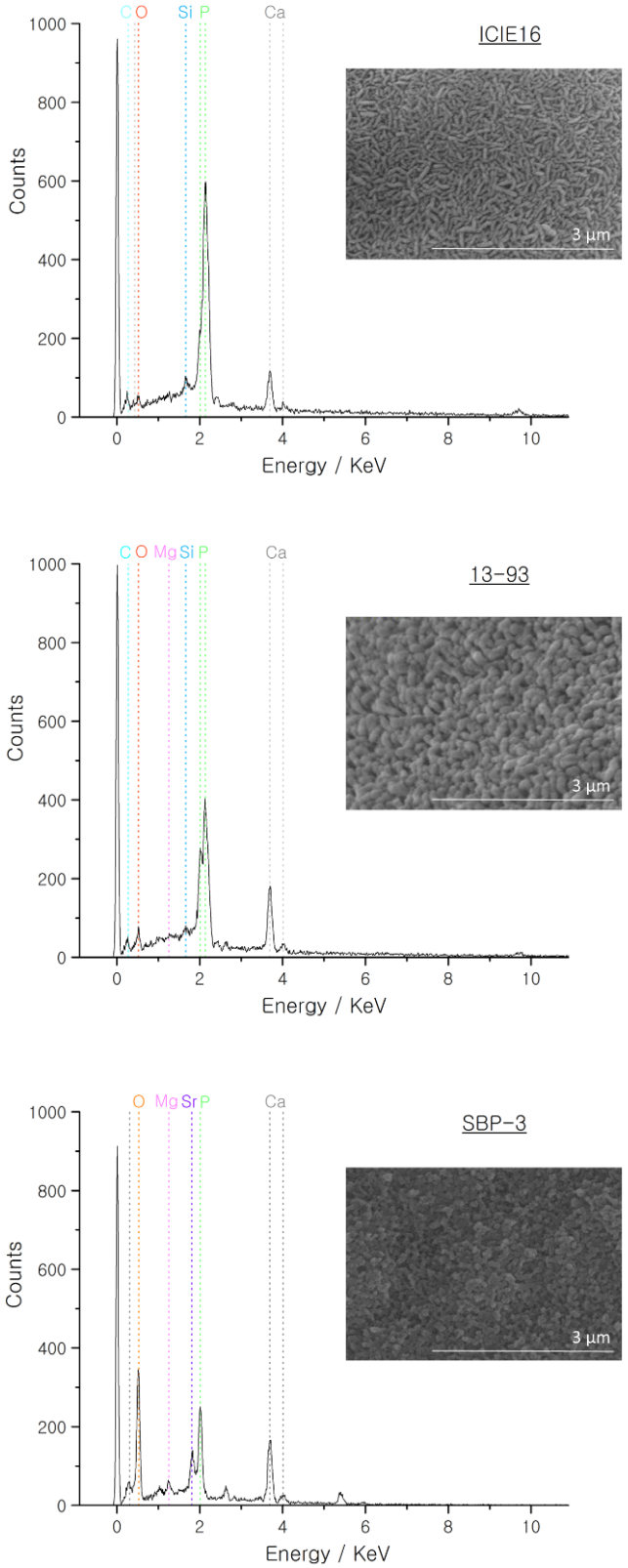


Figure 5.11: EDS spectra collected from the SEM images (insets) of surfaces of the three bioactive glasses, after 4 weeks in SBF. Dotted lines mark the corresponding K_α energies for each element.

5.3.4 Conclusions of the dissolution study

All three glass scaffolds resulted in the precipitation of a calcium phosphate rich phase upon the surface of the scaffolds within 4 weeks in SBF. As expected, variation was seen within the rate of precipitation. Following the modified network connectivity theory, it was expected that ICIE16 would be the most bioactive glass studied, suggesting its dissolution would be greater than that of the other two glasses tested and would form HCA at the greatest rate. ICP-OES results showed that cation exchange in ICIE16 was faster than the other glasses tested, shown by a large pH rise, combined with potassium and calcium release, and an obvious drop in phosphorous with calcium by 200 h. 13-93 had the highest network connectivity of the three glasses and its release profiles followed the same trend as ICIE16 but at slower rate of dissolution. Therefore, these two glasses fit the modified network connectivity model suggested by Hill *et al.* [26].

In contrast, SBP-3 had the highest silica release when compared to the three glasses tested however, its release of the other cations into the solution was the lowest. This supports the suggestion that cations took the role of intermediate ions within the glass network and have additional more complicated compositional dependent effects which effect the glasses bioactivity performance which is not characterised by the network connectivity equation.

5.4 *IN VIVO* TESTING

In vivo testing was completed by our collaborator Professor Christopher Mitchell at the University of Ulster.

Gel-cast scaffolds manufactured from SBP-3 and ICIE16 were tested *in vivo* in a rabbit femoral condyle model, with a critical sized 6.5 mm diameter defect within a rabbit model. The sample details are summarised in Table 5.3. The defect site was chosen as a previous study upon a tibia defect within a rat tibia,

not presented within this thesis, was found to be pushed out of the defect site before healing could start. Therefore, it was deemed this defect site would be more appropriate to maintain the sample location as well as allowing the use of a larger sample size for testing.

Table 5.3: Summary of the porosity and dimensions of the samples used within the rabbit in vivo study

Glass	Porosity /%	Diameter /mm	Thickness /mm	Modal Interconnect Diameter /μm
SBP3	88.82 ± 1.83	6.54 ±0.09	1.53 ±0.06	111.3 ± 12.2
ICIE16	85.76 ± 2.96	6.44 ±0.20	1.49 ±0.09	109.2 ± 4.5

5.4.1 Methodology

All animal procedures were approved and conducted in accordance with institutional (University of Ulster) animal care committee and National (UK Home Office) guidelines. A total of 4 female New Zealand half-lop rabbits (2.1 -2.8 kg) were used in this study. General anaesthesia was induced by subcutaneous injection of ketaset and xylapam (in sterile saline) as assessed by testing of loss of pedal reflex. Palliative pain relief was ensured by subcutaneous injection of Metacam. Subsequently, an appropriately plane of anaesthesia was maintained by inhalation of a Fluothane/air mixture.

The surgical site was initially prepared by mechanical clipping of fur, application of a depilatory cream and 3 successive washes with chlorhexidine followed by isopropanol. The rabbits were then placed on their sides and a 3cm incision over the lateral aspect of the knee joint made with a scalpel. The tissue overlying the lateral aspect of the knee was then cleared and muscle tissue retracted from the underlying bone. A 6.5 mm critical-sized circular defect was drilled down to the marrow cavity (with liberal application of sterile saline to prevent heat-induced osteo-necrosis) and bleeding minimised by application of pressure. The pre-sterilized ICIE16 (3 implants) or SBP3 scaffolds (3

implants) were then press fitted into the lesion until they were level with the edge of the remaining bony tissue. Muscle tissue was closed with 6:0 suture (Ethilon) and the skin was closed with 4:0 suture. After successful implant on one leg, the procedure was performed on the contra-lateral leg. Two sites in separate rabbits contained no implant and served as controls.

After surgery animals received prophylactic topical antibiotics on the surgical site as well as oral antibiotics. Pain relief was also administered for 3 days post-surgery in the form of oral Metacam. Animals were sacrificed by an overdose of pentobarbitone sodium solution at 7 and 12 weeks after surgery and the knee joints removed for subsequent XMT examination and histological processing.

5.4.2 Results

Example XMT images from the 7 and 12 week time points from this study are summarised in Figure 5.12. Part (a) and (b) show the location of the defect site and its relative size in ratio to the femoral condyle, as reference. Both the ICIE16 and SBP-3 gel-cast scaffolds stimulated bone growth.

By the 7 week time point, XMT results suggest that SBP-3 has stimulated more bone growth than ICI16. By 12 weeks, the inverse is seen, the bone growth stimulated by the ICIE16 scaffold outperforms that of SBP-3 in terms of new bone growth and the continuity of the bone structure which is formed. The structure within the ICIE16 defect site is more representative of the initial structure seen within the femoral head suggesting that remodelling is taking place.

SBP-3 enhanced performance within the first 7 weeks could be related to the strontium within its composition. As previously discussed (section 2.2.1) strontium is known to have a positive effect on the formation and proliferation of osteoblasts. Therefore, its initial release at the defect site, may have enabled the enhance bone formation seen over ICIE16 by the earlier time point. In

contrast ICIE16 lower modified network connectivity, (2.13) may have enabled greater and sustained released over the length of the study compared to that of SBP-3 (2.84), as seen within the ICP-OES results (discussed in 5.3.2), creating enhanced bone formation over the 12 weeks.

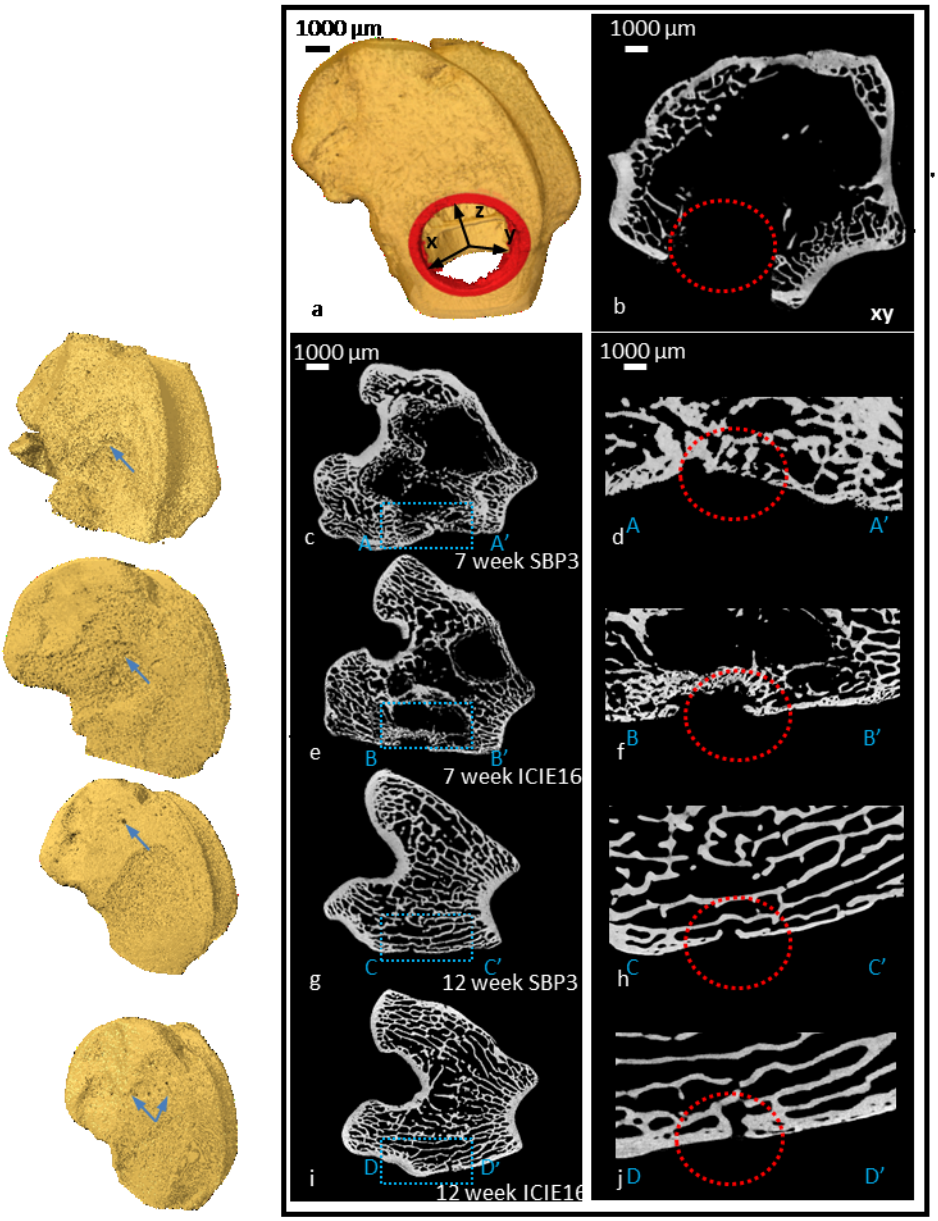


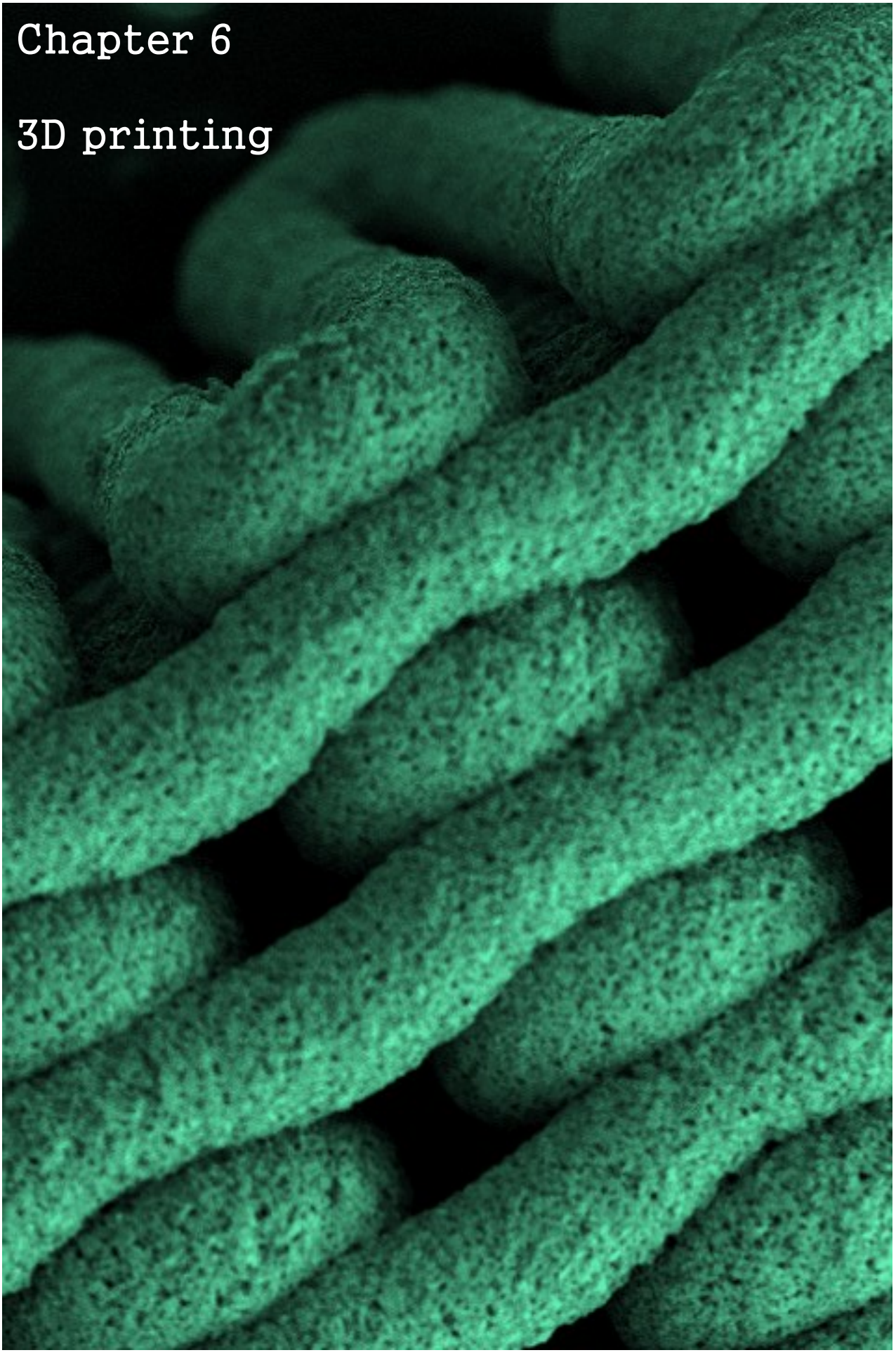
Figure 5.12: XMT evaluation of bone regeneration in rabbits femur condyle defect (a, b) implanted with ICIE16 and SBP-3 scaffold (c,d,e,f) at 7 weeks, (g,h,I,j) at 12 weeks post-operation. A reticulated trabecular bone is observed at 7 weeks followed by growth and development of bone. The morphology of the cortical region restored its pattern at 12 weeks post-operation. Image and analysis provide by Hua Geng.

5.4.3 Conclusions

The adapted gel-casting processing method creates scaffolds suitable for bone ingrowth. This *in vivo* study shows that the foamed morphology supports and sustains bone growth across the length of 12 weeks in a femoral head defect within a rabbit model. ICIE16 outperforms SBP-3 by the completion of this study showing greater growth and regeneration of the original bone structure. Histology work is needed to confirm the *in vivo* observations.

Chapter 6

3D printing



6 3D PRINTING

6.1 INTRODUCTION

The aim of this work was to optimise the 3D printing technique 'robocasting', for the manufacture of bioactive glass scaffolds from ICIE16 and SBP-3. As discussed in section 2.3.4, 13-93 has been widely 3D printed by various research groups [37, 49, 127, 140, 156], using various ink and printer combinations; therefore, 13-93 was also printed as a reference to literature.

Robocasting is an additive manufacturing technique where an ink is extruded through a nozzle, these extruded filaments can form 3D objects by layering under computer control. Within this context, polymeric binders are used and mixed with glass particles to form inks suitable for printing. The main processing parameters that control the robocasting process are the rheology of the ink that is used, the size of the particles and their distribution and the ratio of ink to powder that is used as discussed in Section 2.3.4.

Once a suitable ink has been found with suitable properties, scaffold parameters can be optimised to decide strut spacing, and filament diameter. These choices ultimately affect the scaffolds surface area and porosity which in turn affect its dissolution characteristic and consequent bioactivity.

The following body of work describes the optimisation process and outcomes achieved. The overall aim was to be able to form 3D grid like constructs with aligned struts to maximise compressive strength.

6.2 FINDING A SUITABLE INK: DESIGN CRITERIA

Considering our laboratory set-up and idealised aims a suitable ink must:

- Be non-toxic and able to be printed without fume hood extraction;
- Be able to be mixed safely within a lab environment;

- Be able to incorporate large volumes fractions of glass powder homogenously;
- Be non-aqueous, so that the glass does not degrade during processing;
- Exhibit suitable rheological properties to enable printing;
- Have a strength able to hold its own weight, when loaded with glass, without deformation to be able to print multiple layers;
- Be organic and burn out completely in air below the glass transition of the glass used;
- Allow fusion between multiple filaments at their contact points, so that mechanically strong green bodies can be formed.

In 2013, researchers had worked with two carriers, Pluronic F-127 and Ethyl cellulose [37, 52, 135, 140]. Therefore this work focussed on the adaptation of these inks with the glasses of choice within this project ICIE16 and SBP-3. Ethyl cellulose was first investigated followed by F-127. Other carrier inks have since been published, such as Carboxymethyl cellulose (CMC) [137], and Polyvinyl alcohol (PVA) [189] (discussed in Section 2.3.4).

6.2.1 Ethyl cellulose

Ethyl cellulose, when combined with poly(ethylene glycol), PEG, was reported to form a suitable ink for printing. Deliormanlı *et al.* [52] focussed upon the glass composition 13-93. Their ink composition is summarised in Table 6.1, which was modified for use with ICIE16 due to variations in glass densities. To gain the appropriate viscosity of ethyl cellulose, it was initially dissolved in a ratio of toluene to ethanol of 20:80.

Table 6.1: Ethyl cellulose ink composition defined by Deliormanlı et al. [52] and adapted for use with ICIE16

At 25 °C	Deliormanlı *et al.* [52] ink composition	
	Volume /%	Density /g.cm^{-3}
13-93	45	2.5
Ethyl cellulose	20.1	1.14
PEG	6.8	1.13
Ethanol	28.1	0.79

6.2.2 Pluronic F-127

Pluronic F-127 poly(ethylene oxide) (PEO)-poly(propylene oxide) is an aqueous triblock co-polymer with reversible thermal properties. At low temperatures (~5°C) it is a low viscosity solution, enabling easy mixing, and at ~40°C it reversibly gels and forms a self-supporting network, as discussed in Section 2.3.4. As temperature increases, the hydrophobic PPO segments release the water molecules which were adsorbed to them. This enables the formation of a self-supporting gel, due to the association of these polymeric groups forming a network. It has been used by various groups [37, 135, 140] as an ink for robocasting for this reason.

6.2.3 Ink Comparison

Mixing

When mixing the ethyl cellulose based ink, with high volume fractions of glass powder, it was difficult to keep the temperature low enough to stop solvent evaporation, which in turn changed the solution viscosity. Also, as toluene was needed to dissolve the ethyl cellulose, for safety reasons, it was deemed that an alternative ink would be preferable as the 3D printer was not housed within a fume hood.

Pluronic F-127's thermally dependent viscosity change made mixing easier than using the ethyl cellulose based ink. However, the mixing process resulted in the sample being heated over time, changing the viscosity. This made it difficult to incorporate ink loadings above 40 vol% of glass. It also made it difficult to produce consistently homogenous inks as the amount of evaporation would change between samples.

Even though Pluronic F-127 is a water based ink, which means there is a risk of the glass degrading in the ink, the glass particles only stayed within the aqueous environment for the mixing period and within the printing syringe. Once printed, the inks dried within an hour. So the 'wet' processing window was shorter than that of gel-cast foaming process, which did not show to have any adverse effects of premature crystallisation on the glass compositions used.

Thermal Properties

The thermal degradation of each ink was analysed via DSC/TGA and summarised in Figure 6.1. TGA showed that, under flowing air conditions, Pluronic F-127 burned out at less than 200°C, well below the sintering temperatures of the three glass compositions used. The ethyl cellulose ink had a two phase burn out, due to the two polymers phases (ethyl cellulose and PEG). The burn out range of this ink was much greater than that of Pluronic F-127, taking until nearly 500°C for complete burn out to occur.

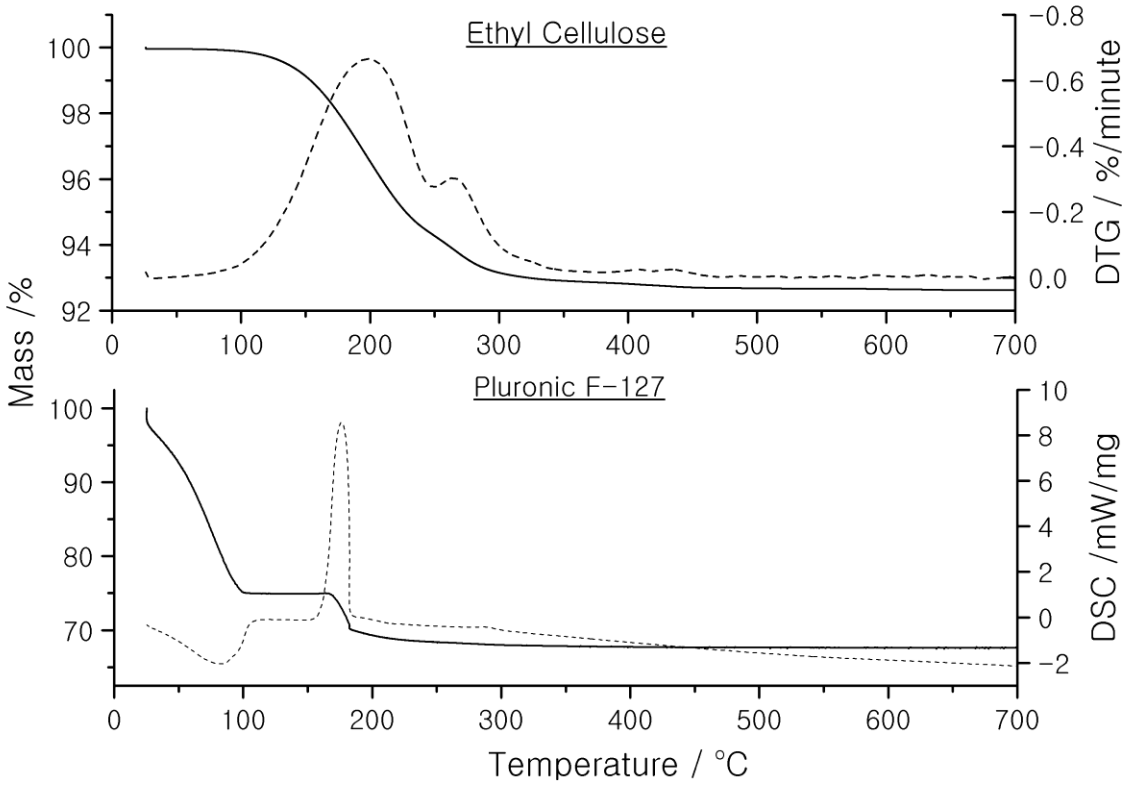


Figure 6.1: DSC/TGA data of ethyl cellulous and Pluronic F-127 inks.

6.2.4 Conclusions on carrier selection

Both the ethyl cellulose based ink and Pluronic F-127 were able to form suitable carrier inks for use with ICIE16 and SBP-3. Both inks were analysed against the initial aims defined in Section 6.2. Due to the lower thermal degradation, ease of processing and non-toxicity, Pluronic F-127 was chosen as the preferred ink for use within this system. Therefore, all consequent work completed upon robocasting within this thesis will be based upon using Pluronic F-127 as the carrier ink.

6.3 NOZZLE SHAPE

The 3D printer was compatible with printing tips manufactured by Nordson EFD®. Tips are available in a wide variety of geometries, nozzle diameters and materials, including stainless steel, polytetrafluoroethylene (PTFE), or polyethylene. Due to the abrasive nature of the glass particles, polyethylene tips

were chosen, as the sintering profile should burn out any residual polyethylene which may become incorporated into the scaffolds.

Franco *et al.* [140] showed that the force required to enable extrusion of inks within a syringe controlled 3D printer can be modelled using compression of a syringe. This method can be used to understand the variation in force needed to extrude inks with different printing variables, e.g. tip geometries, glass powder loading and ink formulations. Figure 6.2 summarises the testing set up used.

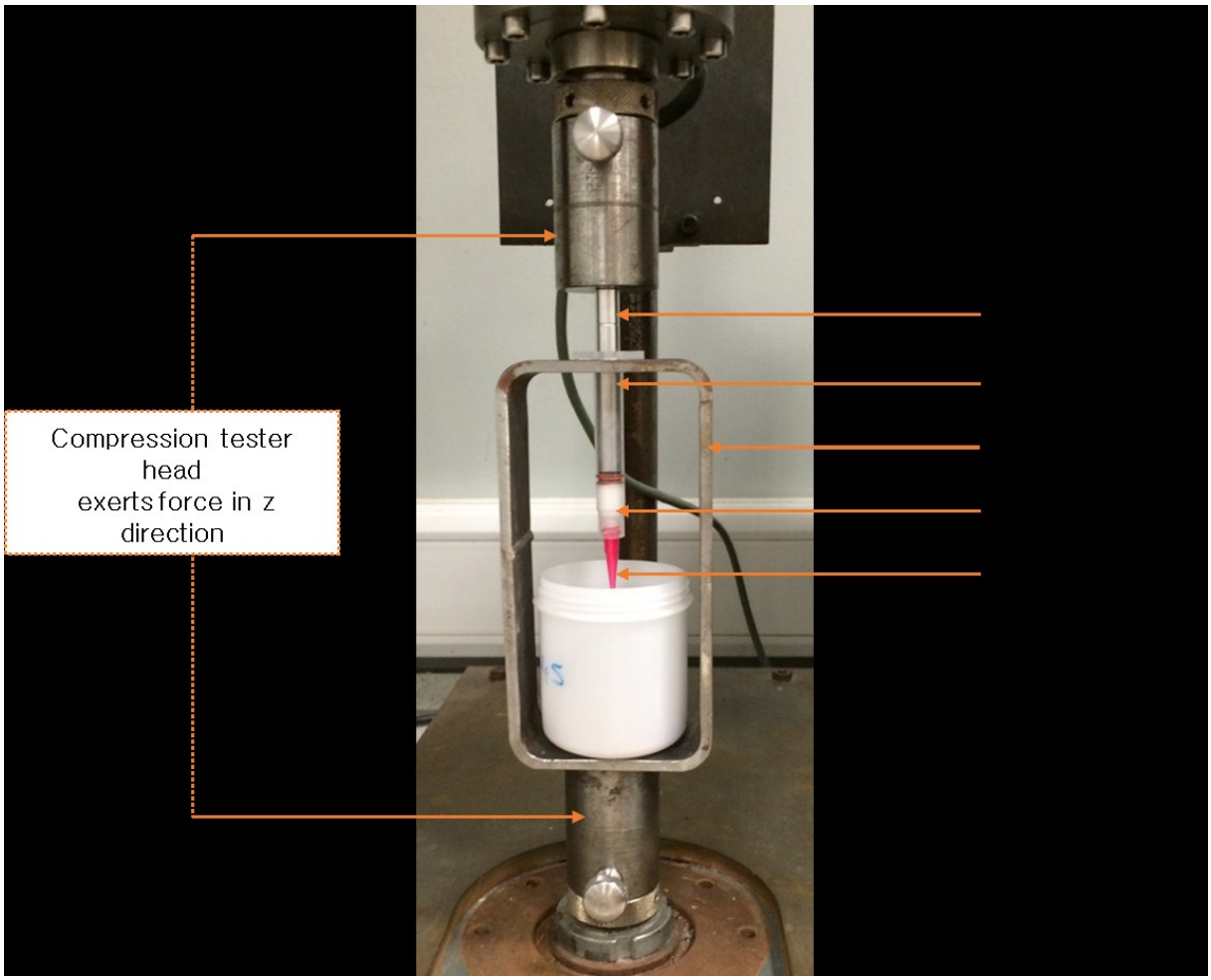


Figure 6.2: Compression testing aparatus to mimic the force dynamics during robocasting.

The force was measured at a constant displacement rate for the syringe piston (v_p). The equivalent printing velocity (v_w) was calculated assuming constant flow from the syringe chamber and a fixed ratio between the tip (Φ_t) and the

syringe diameter (Φ_s). This can be defined by the following equation, known as the extrusion ratio (equation 6.1).

$$\nu_p = (\frac{\Phi_t}{\Phi_s})^2 . \nu_w \qquad 6.1$$

Inks were tested to understand the stabilisation time, i.e. the time needed to obtain continuous flow, at various vol%, nozzle diameters and printing speeds. Figure 6.3 shows the effects of different nozzle geometries on extrusion forces.

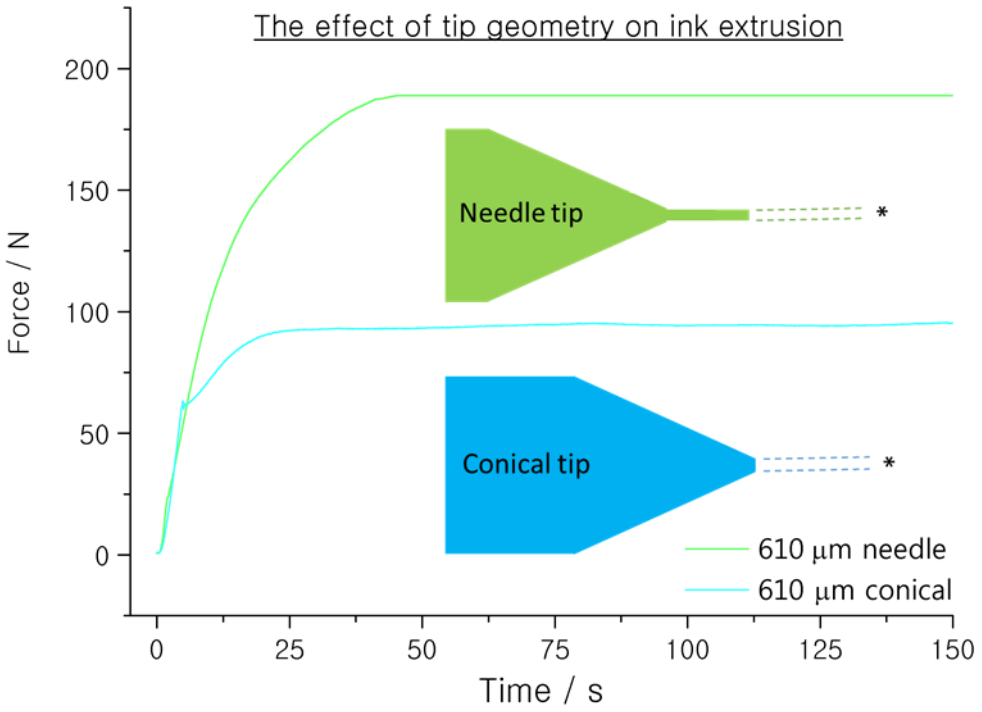


Figure 6.3: Compression testing of tips with diameters of 610 µm with needle and conical profiles.

Both nozzle geometries depicted a similar force/time relationship, with the graphs reaching a plateau once the stabilisation force was reached. This is the point where the force needed for shear thinning has been overcome, known as the yield point, and continuous steady state flow is achieved; this suggests that Pluronic F−127 acts pseudoplastically. For all nozzle diameters tested, the force needed to stabilise and extrude out of a needle nozzle was approximately double that of the conical nozzle, 95 versus 198 N. The decrease in force needed is thought to be linked with the reduction of flow dead zones within the

nozzle, easing flow. A three zone profile is thought to form when shear-thinning loaded inks are forced to flow through a conical nozzle [52, 190-192]. At the walls of the nozzle, a thin slip layer forms that does not contain any particles. In the centre of the nozzle, a gel core extrudes at constant velocity flows. Between these two layers a fluid shell of laminar flow extrudes. This does not exist within the needle shaped nozzle, therefore it is harder to resolve dead zones, increasing the forces needed for extrusion. This creates greater emphasis on the importance of particle size and its distribution within the ink [192, 193]. Due to the relationship between crystallisation and particle size, and the difficulty in processing bioactive glasses to different and discrete small particle sizes, from this point forward only conical nozzles were chosen and used within the printing process to minimise the load needed to continuously print.

6.4 PLURONIC F-127 INK RHEOLOGY

Understanding the rheological behaviour of glass loaded inks for robocasting is incredibly important. The rheological properties of the ink and the interaction between the particles and the carrier determine the quality of the green body produced, the subsequent manufacturing capability of the system and the strength of the scaffolds produced. The ink behaviour and inter-particle forces are dependent upon the concentration, shape, distribution and size of the particles themselves. To get an understanding of how the rheology varied with glass loading, various rheology studies have been completed.

6.4.1 Understanding Pluronic F-127

Previous studies that employed Pluronic F-127 [135] as a carrier in ink for robocasting used concentrations between 20-30 wt% dissolved in deionised water. 10% was shown to be too low to be able to create enough network to establish the reversible thermal reaction, which is needed for an ink to be printable and self-supporting. The effects of Pluronic F-127 concentration on

gelation temperature and viscosity were investigated using rheometry of non-particle loaded inks.

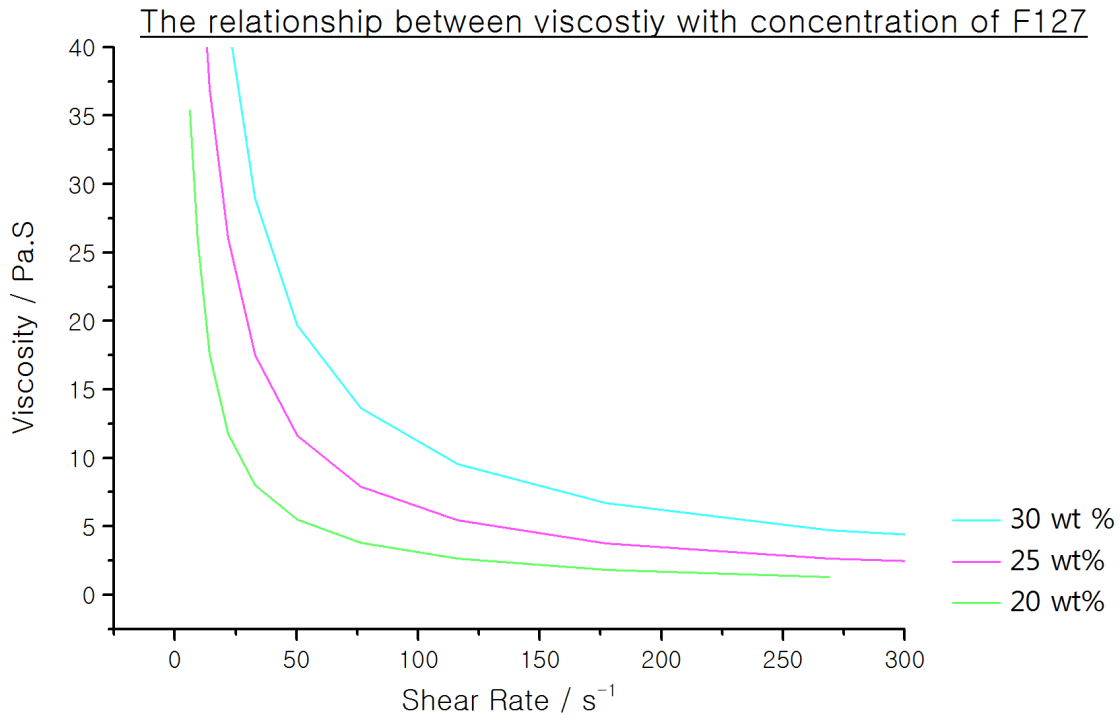


Figure 6.4: Rheological properties of Pluronic F-127 at various wt%: viscosity as a function of shear rate,

Shear thinning behaviour is desirable for an ink for robocasting, as when under force, the ink should flow through the nozzle, but once the force is removed the viscosity should increase enabling the ink to retain the shape printed. All inks exhibited shear thinning, or psuedoplastic behaviour as shown by Figure 6.4, characterised by the apparent viscosity η being highest at low shear rates and the viscosity reducing as the ink was subject to load. This was simulated here by increasing the shear rate. It is thought that the shear rate through the nozzle can be approximated as 50 s^{-1} [194]. With increasing wt% of Pluronic, F-127 viscosity increased, between 5 and 20 Pa s at a shear rate of 50 s^{-1}.

The relationship between gelation tempearture with concentration of F127

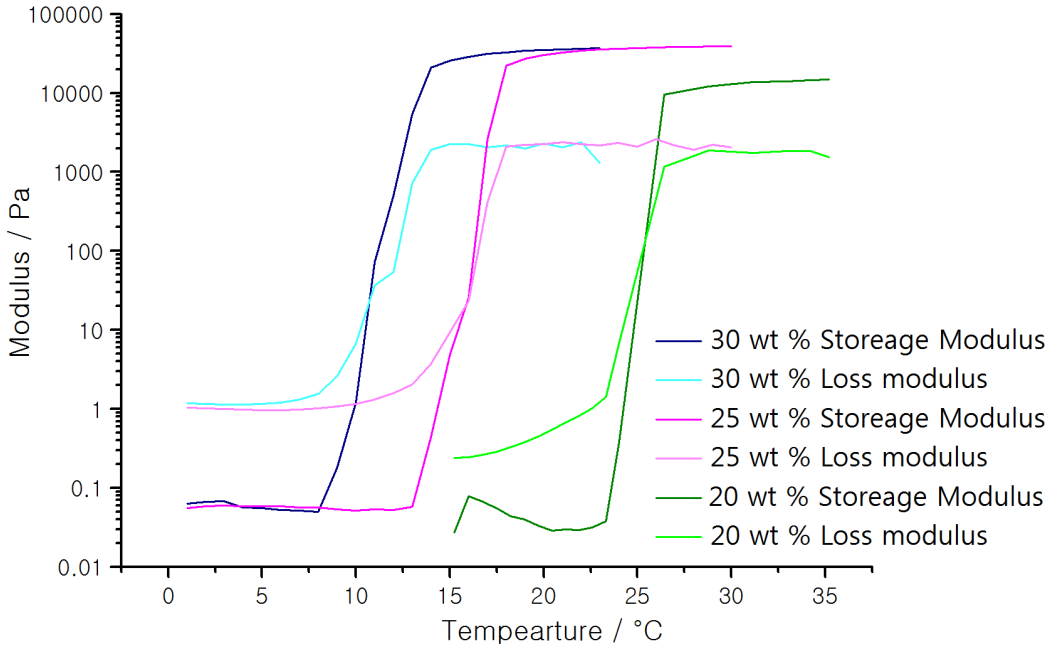


Figure 6.5: Rheological properties of Pluronic F-127: modulus as a function of temperature.

Figure 6.5 shows how the inks modulus changed with Pluronic F-127 concentration and temperature. Where the storage and loss modulus intersect is known as the gelling point of the ink. The temperature at which the ink gelled reduced as Pluronic F-127 concentration increased. This is due to less water available within the system, resulting in less energy needed for gelation.

The gelation temperature affects the processing parameters for a variety of reasons. When mixing particle loaded inks, the samples experienced some heating due to mechanical mixing. To obtain a thoroughly homogenous ink and enable inclusion of all the glass powder, the ink would ideally remain at as low a viscosity as possible during the mixing cycle. The higher the gelation point, the more homogeneous the ink can become.

Oscillation sweeps can yield information regarding the elastic plastic transformation in a solution, by studying the ratio of G' to G'' [194]. An example of an oscillation sweep above the gelation temperature of 25 wt% Pluronic F-127 is shown in Figure 6.6. At low stresses, the storage modulus G' was much

greater than the loss modulus G", resulting in an unyielding network. As the oscillation stress increased, the ratio between them reduced, with the loss modulus rising and storage modulus reducing. This was indicative of F-127's ability to yield under force, showing elastic characteristics similar to a liquid. Where G'= G" is the yield point (τ_y) of the solution. This is where the plastic characteristics dominate over the elastic. Above τ_y the solution breaks down, resulting in a rapid reduction in modulus, as the network cannot yield to any more deformation. This behaviour was characteristic of shear thinning properties, corroborating the results shown in Figure 6.4.

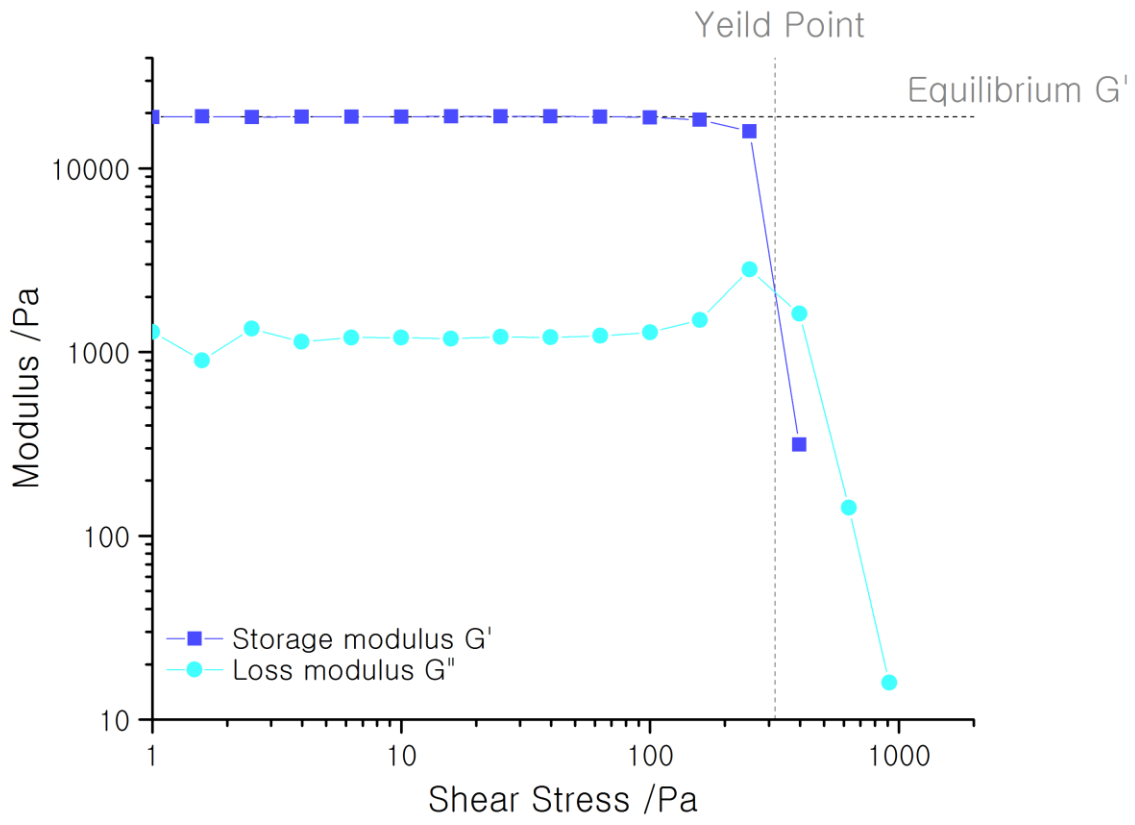


Figure 6.6: Oscillation sweep for a solution of 25 wt% F127 at 25°C, which is above its gelation temperature.

Table 6.2 summarises the yield strength and equilibrium storage modulus for Pluronic F-127 concentrations between 20 to 30 wt%. As Pluronic F-127 concentration increased, the yield strength and equilibrium storage modulus

increased, due to the polymer content increasing, which improved stiffness increasing the viscosity.

The solution containing 25 wt% of Pluronic F-127 had a suitable yield strength and a manageable gelation temperature to aid mixing of highly loaded glass inks. Therefore, from this point rheology studies focussed upon using 25 wt% Pluronic F-127.

Table 6.2: Summary of the variation in yield and storage modulus with Pluronic F-127 concentration between 20-30 wt%, all measured at 25°C.

Pluronic F-127 Concentration /wt%	Yield Strength /Pa	Equilibrium Storage Modulus /Pa
20	238	13372
25	318	19094
30	551	21044

6.4.2 Herschel-Bulkley model

The flow of particle loaded inks through the deposition nozzle can be modelled via the Herschel-Bulkley model (equation 6.2) [140, 178, 195, 196]. The model describes the behaviour of ideal non-Newtonian fluids which do not flow below a certain yield stress, and show shear-thinning behaviour at stresses above their yield.

$$\tau = \tau_y + K\dot{\gamma}^n \qquad 6.2$$

Where τ is the applied shear stress; τ_y is the yield stress; $\dot{\gamma}$ is the shear rate; n is the shear thinning exponent and K is the viscosity parameter. Inks loaded with 20-45 vol% of ICIE16 with 25 wt% Pluronic F-127 were analysed. The graphical interpretation and tabulated data is shown in Figure 6.7 and Table 6.3. For robocasting a low values of n and K are advantageous, as they aid mixing

and reduce extrusion forces. If n is less than 1, the ink is deemed to be psuedoplastic. The ICIE16 glass inks tested gave values of n between 0.04–0.27, which is within the psuedoplastic range. These values are within the same range as reported values by Fu *et al.* [135] for 13–93 and 13–93B glasses inks manufactured using Pluronic F–127.

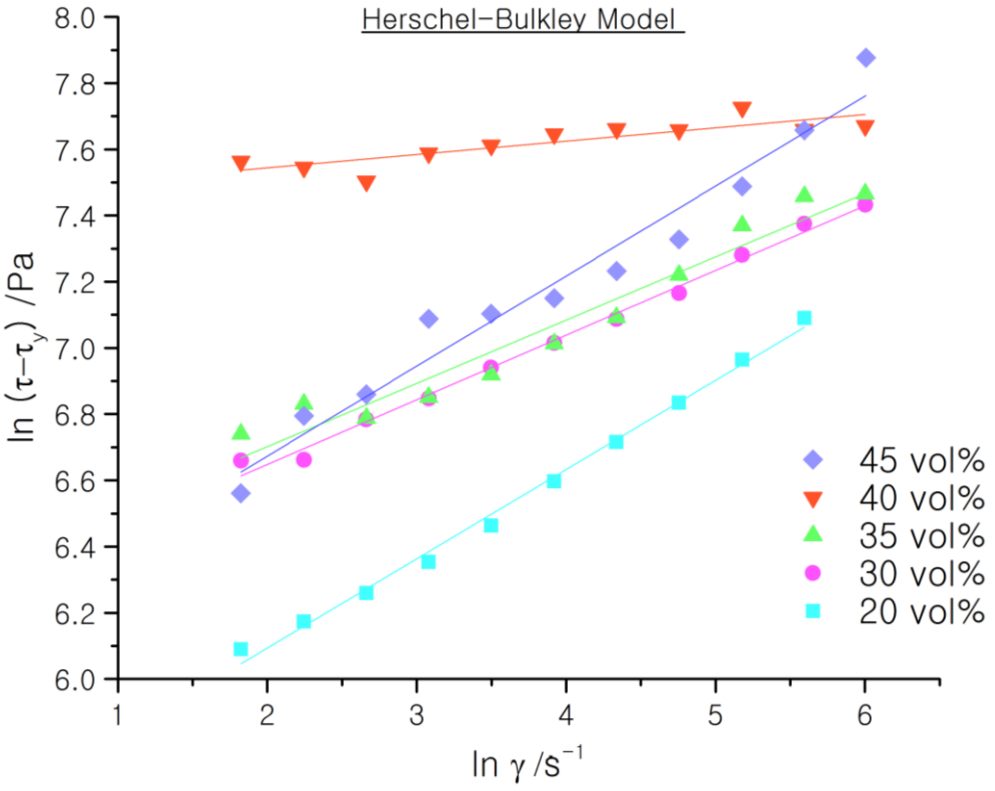


Figure 6.7: Rheometry data for 20–45 vol% of ICIE16 mixed with 25 wt% F127 fitted to the Herschel–Bulkley Model.

As concentrations of glass loading increased within the inks, the more challenging it became to produce repeatable, reliable data. This is due to high initial values of τ_y which overcame the force limit of the machine used.

Table 6.3: The Herschel-Bulkley Model parameters obtained from the gradients and intercepts of Figure 6.7.

Volume % of ICIE6 /%	$ln\,K$ /Pa.s^n	n
20	6.13	0.27
30	7.47	0.04
35	6.32	0.19
40	6.26	0.19
45	5.55	0.27

6.4.3 The effects of particle loading on gelation temperature

During the mixing of inks for robocasting, the solution temperature increased within the mixing vessel. If the temperature becomes greater than the gelation temperature, it becomes difficult to gain a homogenous ink and bubbles can become trapped within the ink. Understanding how the gelation temperature varied with glass loading enabled optimisation of the mixing cycle so that bubble free homogenous inks could be formulated.

The gelation temperature of 25 wt% F-127 Pluronic was studied for the three glass compositions at concentrations between 0-45 vol% of glass additions, and summarised in Figure 6.8. Data collected for ICIE16 and 13-93 was repeatable, however SBP-3 proved to be very challenging to gain repeatable data via rheology testing. This could be due to the force limit of the machine as previously discussed, due to variation in particle size and surface charge.

At low temperatures, the -OH groups within the solution can bond to the surface of the glass particles through Van der Waals interactions or hydrogen bonding, creating a stable low viscosity ink by steric repulsion. The solution of 25 wt% of Pluronic F-127 gelled at 17°C. Increasing particle loading, up to 45 vol%, caused the gelation temperature to decrease to 6°C, perhaps due to the increasing level of disruption created within the network with increasing glass

loading. Pluronic F-127 gels due to the release of water molecules from the PPO groups. Premature gelation suggests that the glass preferentially bonds the water molecules, taking up the water before it is energetically favourable to be released. Consequently, speeding up the gelation process by allowing the PPO groups to hydrophobically associate at lower temperatures. As glass concentration increased, this happened more readily.

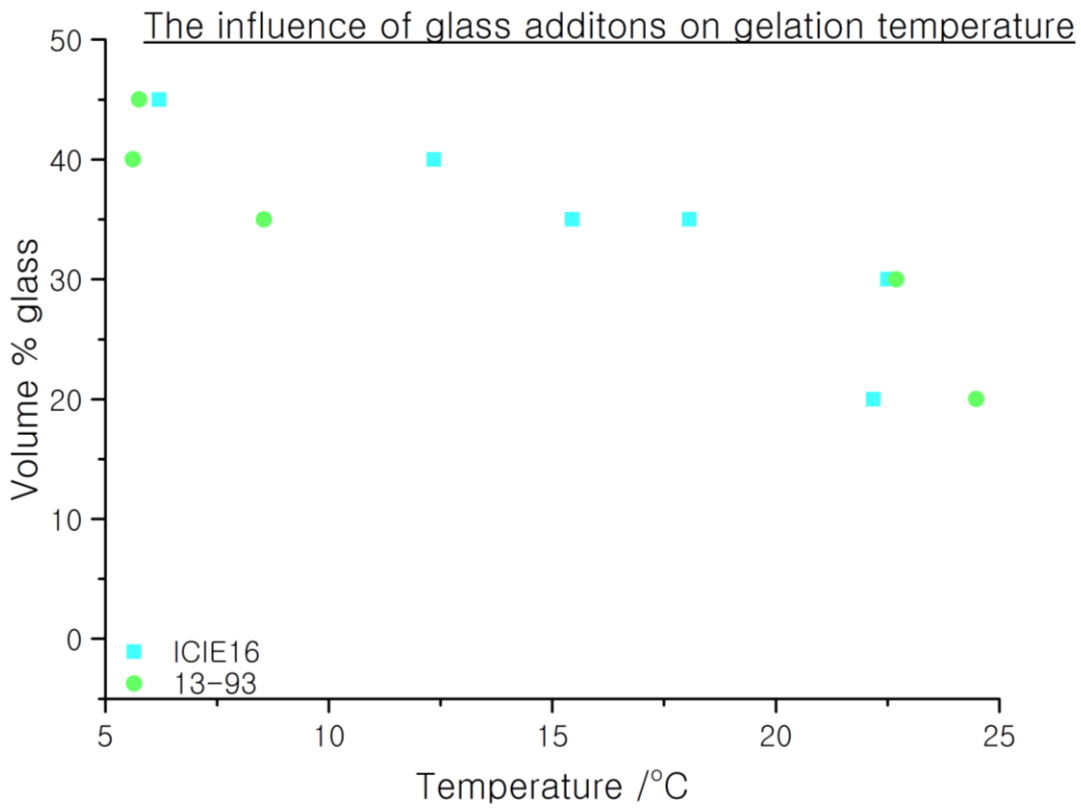


Figure 6.8: Relationship between the gelation temperature of 25 wt% of Pluronic F-127 loaded with 0-45 vol% of ICIE16 or 13-93 particles, the values are derived from oscillation sweeps shown in Figure 6.6

6.4.4 The effects of particle loading on viscosity

An understanding of how the concentration of glass affects the ink viscosity is useful when deciding upon a composition for printing. The viscosity needs to be high enough to be able to formulate an ink that can sustain its own structure when printed, but not too high that it cannot be extruded.

As previously discussed in section 6.4.1, literature suggests that the shear through a printing nozzle can be estimated to being equal to 50 s^{-1} [178, 194]. To analyse the viscosity of the solution at this point, studies were completed at shear rates between 0–200 s^{-1}. All tests were completed at 25°C to simulate room temperature printing, and the viscosity was measured when the shear rate was equal to that of 50 s^{-1}. Figure 6.9 shows that all three compositions followed a similar trend: viscosity increased as glass loading increased. The ICIE16 data set was the easiest to obtain with repeatable measures being taken at all loading values. The 13-93 and SBP-3 measurements were more difficult, suggesting that the viscosity of their inks overcame the maximum threshold for the rheometer at loadings greater than 45 vol%.

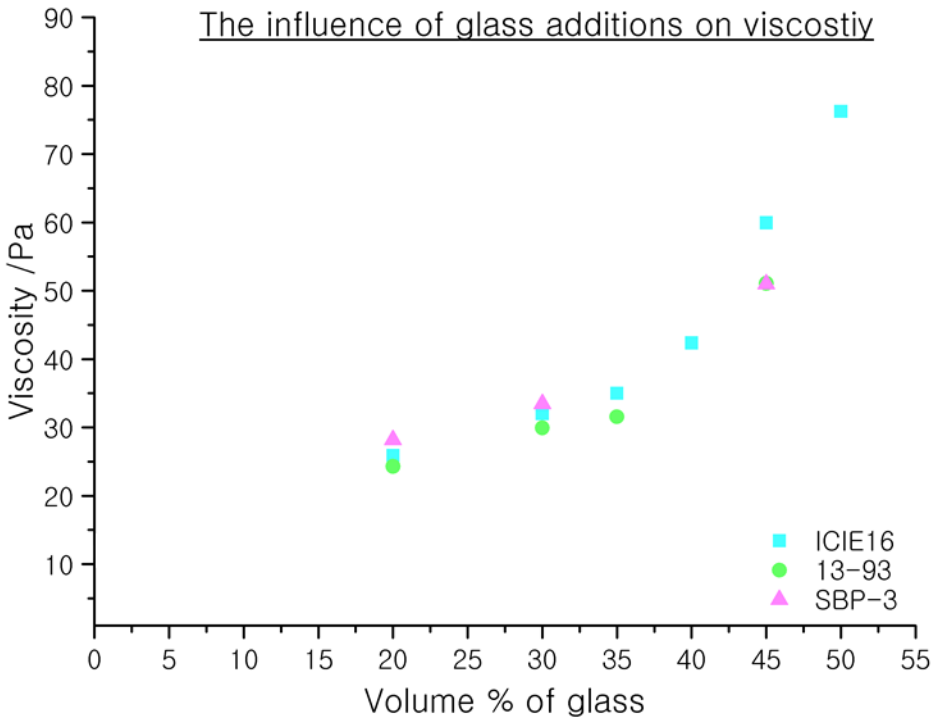


Figure 6.9: The influence of particle size on viscosity, values taken from the equivalent viscosity at a shear rate of 50 s^{-1}.

Literature associates the effect of viscosity on glass loading with the Kreiger–Dougherty Model (Equation 6.3) [135]; where η_r is the relative viscosity related to volume fraction φ, max theoretical volume fraction φ_m, and measured viscosity η.

$$\eta_r = \left(1 - \frac{\varphi}{\varphi_m}\right)^{-[\eta]\varphi_m} \qquad 6.3$$

This model shows that above a critical glass loading value, the viscosity becomes infinite. Allowing users to estimate the maximum theoretical particle loading that their ink can incorporate before processing becomes too difficult. The trend within this data is not as extreme as those reported in literature [135]. This could be due to differences in particle size altering the interparticle forces, as these particle sizes are over a factor of 10 greater than that of those used within the compared study (discussed further in Section 6.5.1).

The relationship between viscosity and printing is a complex one, there is no consensus about what works and what does not, as systems are composition and set-up dependent. Although Figure 6.9 does suggest a trend within the data set, the reality is that mixing of these inks varied from this test, as summarised in Table 6.4.

Combining the results from Figure 6.9 and Table 6.4, highlights the difference between theoretical and physical data. In inks containing 13-93 and SBP-3, the viscosity did not reach an infinite value suggesting that, from Kreiger-Dougherty Model, the maximum glass loading was not reached within these ink glass combinations. In reality, loading above 45 vol % for these compositions were difficult to produce reliably and the inks were difficult to extrude.

Table 6.4: Summarising the abilities of glasses to mix at various volume fractions of powder in a solution of 25wt % of Pluronic F-127.

Volume fraction of glass	Glass	
	ICIE16	SBP-3 and 13-93
20	All mixed	All mixed
30		
35		
40		
45		Very difficult to incorporate all powder, took multiple cooling cycles to gain a homogenous ink
50		
55	Powder residue left	Does not mix

6.4.5 The effects of particle loading on mechanical properties of inks

As viscosity changed with particle loading, it also created changes to the ink mechanical properties. As discussed in section 6.4.1, rheological data can enable the measurement of the yield strength and storage modulus at equilibrium for particle loaded inks. Yield strength of the solution is the stress where the loss modulus is equal to that of the storage modulus. These values are of interest as yield strength can be thought of as a measure of an ink's 'strength' and storage modulus a measure of its 'stiffness'. Figure 6.10 shows the relationship between yield strength and storage modulus with vol% additions of glass. As expected the storage modulus and yield point of the inks increased with increasing glass loading.

Within this data set, each glass behaved differently. For SBP-3 and ICIE16, the yield strength and modulus of the inks increased as volume loading of glass increased. Whereas, for inks containing 13-93, the yield strength was stable across the loadings tested, but the storage modulus did increase. The ink modulus and yield strength were expected to increase with glass loading as

there is a higher glass to polymer ratio, and it is the glass portion which would increase these properties.

The values reported for SBP-3 increased the most compared to the other glass compositions tested. Between 20 and 40 vol% loading, SBP-3 yield point increased by 326 Pa, and the modulus by 56011 Pa. This could be the reason why it is difficult to obtain rheological data for this glass composition without overloading the force unit on the rheometer. This suggests that something unique to this glass composition affects the relationship between the glass and the binder, which does not occur in the others.

Although nominal values can be determined via rheological measures, it is difficult to understand the meaning of these values without physically printing the inks. With increasing yield strength and modulus, inks should be able to span greater distances unsupported when manufactured into 'wood-pile' geometry scaffolds, which would enable greater scaffold design capability. However, a compromise needs to be found between highly loaded inks to gain good rheological properties and a low enough viscosity for processability. Increases in these values also increases viscosity, which results in inks which need more force to be extruded.

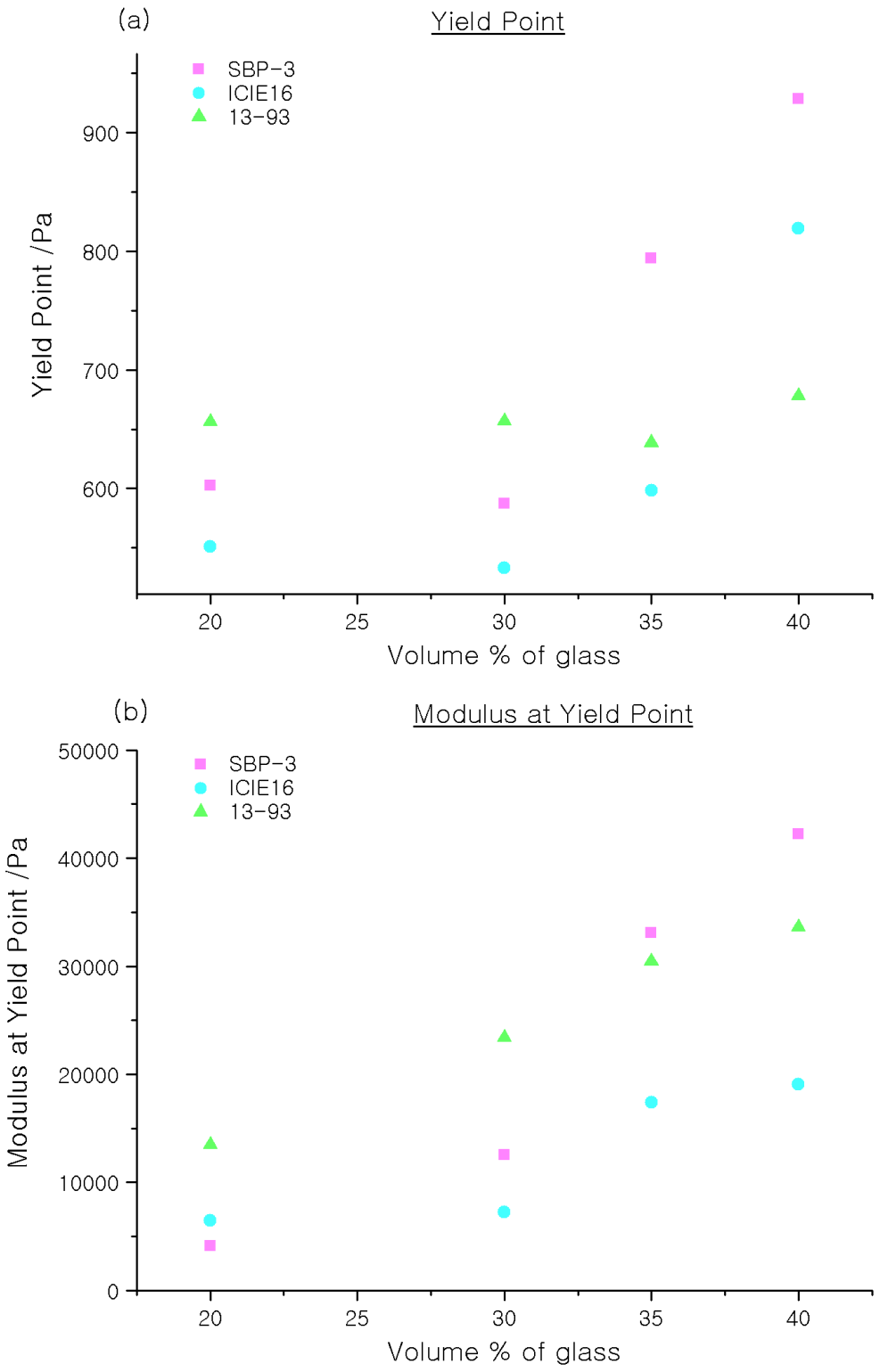


Figure 6.10: a) Yield point and b) Modulus at yield point as a function of vol% glass for inks of ICIE16, SBP-3 and 13-93 in solutions of 25 wt% F-127, tested at 25°C.

6.5 SIMULATING PRINTING

As discussed in section 6.3, compression testing can be used to simulate the robocasting process (Figure 6.2). To analyse and compare the 'printability' of the inks, compression tests were completed on inks of 20 and 30 wt% of Pluronic F−127 with 45 and 50 vol% of glass for all three glass compositions. Higher concentrations of powder are preferential as it enhances sintering due to higher particle packing density in the green body, theoretically resulting in higher mechanical strengths. Initial tests were completed at a standardised printing speed of 10 mms^{-1}.

The results were characterised by studying the time and force it took to reach steady state flow. An example of the results collected is shown in Figure 6.11. The following factors were analysed; the effect of volume fraction; tip diameter; particle size and extrusion speed.

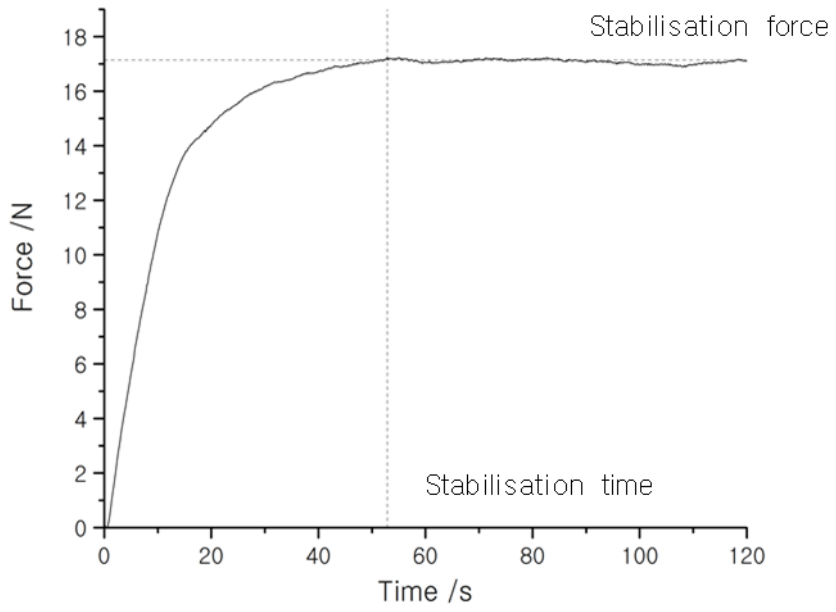


Figure 6.11: An example of the compression data created from ink testing: stabilisation force and time were compared and contrast between different ink concentrations, glass compositions and nozzle sizes.

6.5.1 The effect of particle size

The relationship between tip diameter and ink composition

All the inks tested followed the same trend as shown in Figure 6.11, with an increase in force until a plateau was reached. The time to reach this plateau, or stabilisation force, and the value of the force was analysed for each Pluronic F-127 concentration, glass composition, and tip diameter combination were recorded. The results are shown in Figure 6.12.

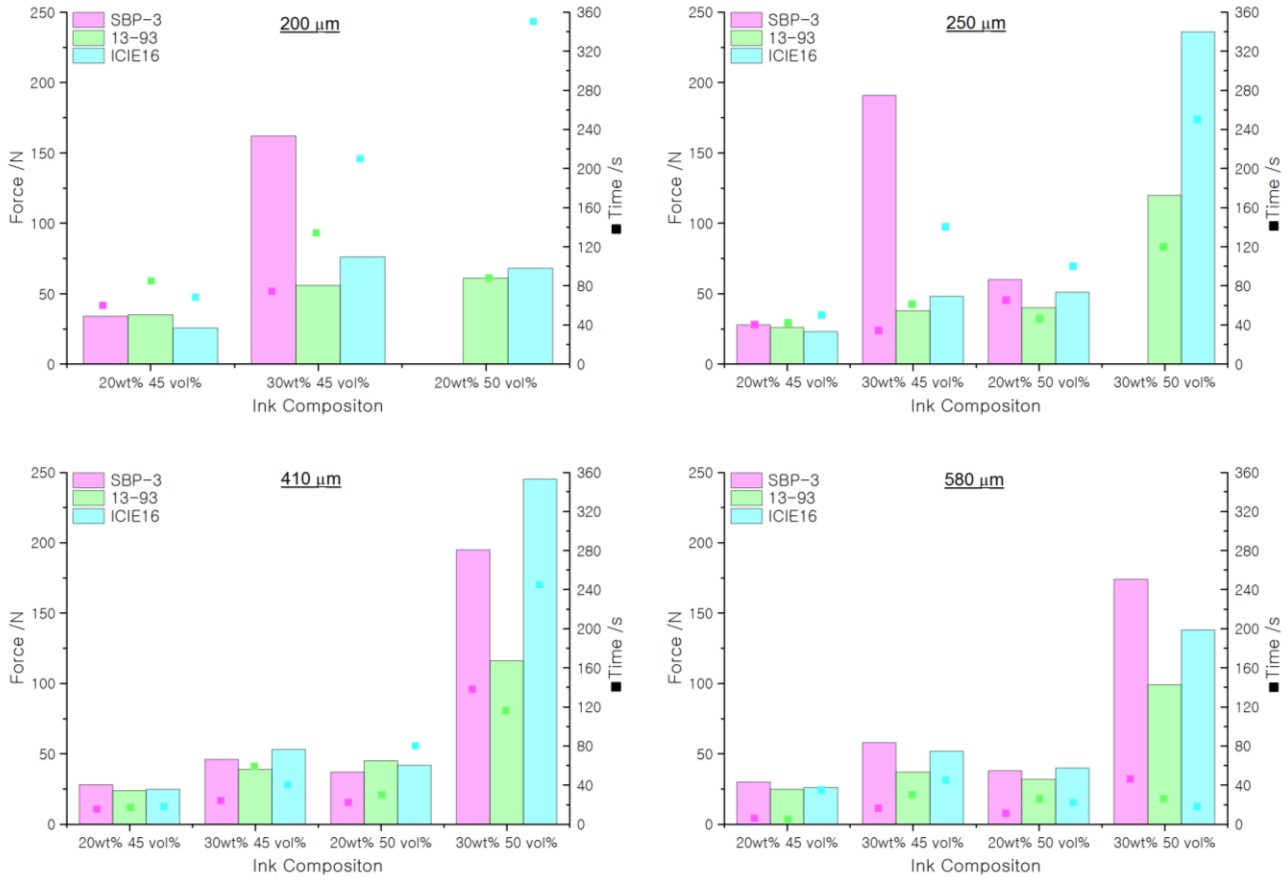


Figure 6.12: Data collected via compression testing to simulate the force and time needed to reach stabilisation of ink at various ink compositions through nozzles diameters of 200, 250, 410 and 580 µm. The bars represent force, and the points represent time. Wt% refers to the concentration of Pluronic in solution, before the vol% of glass was added.

The general trend was that as the nozzle diameter decreased, greater forces were needed to extrude the ink and a longer time was needed to reach stabilisation. When the glass loading and the concentration of Pluronic F-127

were increased within the inks the same trend, of greater forces and longer time to reach stabilisation, was shown.

At concentrations of 30 wt% of Pluronic F-127, the time and force needed to reach stability were consistently greater than that of the ink containing 20 wt% glass for all glass compositions, with percentage increases in time varying between 60-527%, depending on glass composition (Table 6.5). This is consistent with the rheological data collected (section 6.4.4) in that the viscosity of the higher glass loading was much greater than that of the lower, resulting in much greater forces needed to extrude the solution, by up to 483%.

Table 6.5: % increases in time and force required for extrusion, collected via compression testing through a 410μm nozzle from Figure 6.12.

Ink composition	SBP-3		13-93		ICIE16	
	Time /s	Force /N	Time /s	Force /N	Time /s	Force /N
20wt% 45 vol%	15	28	17	24	18	25
30wt% 45 vol%	24	46	59	39	40	53
% increase	60	64	247	63	122	112
20wt% 50 vol%	22	37	30	45	80	42
30wt% 50 vol%	138	195	65	116	205	245
% increase	527	427	117	158	156	483

When testing ink concentrations through the 200 μm nozzle, all of the compositions with the ratio of 30 wt% Pluronic F-127 to 50 vol% of glass broke the syringe during testing. The relationship between particle size and distribution is key when formulating inks for robocasting. Comparable work by Fu *et al.* [135] and Deliormanli *et al.* [52] extruded bioactive glass particles through 210 μm and finer nozzle diameters with modal glass particle sizes of 2 μm. The particle size used within this study is summarised in Table 6.6. The modal size of ICIE16, SBP-3, and 13-93, were 15.8 ± 0.1 μm, 12.5 ± 0.3 μm, and 10.8 ± 0.3 μm respectively. The larger particle size resulted in much higher forces needed to extrude the inks compared with the published works, especially through the smaller nozzle diameters.

Table 6.6: Particle size of ball milled glasses used within the printing inks all in μm.

Glass	$D_{[4,3]}$ volume weighted mean	D_{10}	D_{50}	D_{90}
13-93	14.3 ± 0.1	3.3 ± 0.1	10.8 ± 0.1	30.5 ± 0.2
ICIE16	18.9 ± 0.2	3.3 ± 0.1	15.8 ± 0.3	39.5 ± 0.7
SPB-3	17.1 ± 0.2	3.1 ± 0.1	12.5 ± 0.3	35.0 ± 0.9

Inks containing 50 vol% of SBP-3 were unable to be extruded through the 200 or the 250 μm nozzle at 30 wt% of Pluronic F-127, or through the 200 μm nozzle when mixed with 20 wt% of Pluronic F-127. However, at 45 vol% of glass loading, extrusion was possible. Throughout the majority of the study, SBP-3 needed much higher forces than the other glasses to be extruded. SBP-3 particle size was very similar to that of ICIE6, however, it was much more challenging to mix into homogenous inks and, as reported, to complete rheology studies. This suggests that there is something unique to the SBP-3 composition that alters the ink chemistry, making processing, printing and analysis more challenging.

Of the three glasses tested, 13-93 had the smallest modal particle size, and D_{90} of 10.82 μm and 30.52 μm respectively. The high network connectivity of 13-93 resulted in harder glasses therefore, during grinding produced a smaller particle sizes. When translated to printing, the viscosity of the compositions, the forces and times for stabilisation were less for 13-93 than that of the other glass compositions used.

Particle size variation

The reduction in force needed to extrude the inks and the stabilisation time for the ink containing 13-93 was attributed to its smaller particle size. Analysis was completed to understand the effect of different particle sizes and distributions on reaching the force and time needed for steady state printing. Literature

reports particle sizes used with robocasting technology to be between 1–5 μm, with a D_{50} of 2 μm [37, 52, 135, 140]. Two batches of ICIE16 were manufactured, one via ball milling and one via jet milling. Their particle size and distribution are summarised in Table 6.7 and Figure 6.13. Jet milling uses air pressure to hit the glass particles together, which are then filtered by a classifier wheel set at a specific rate per minute. This technique yields a much smaller particle size and narrower distribution than ball milling due to the opportunity to set the classifier speed within the system such that it only allows smaller particles to be collected, compared with generic sieving used with the ball milled glasses. The jet milled particles are within the range that is used within other printing literature [52, 135], with a modal size of 2.0 μm, compared with 15.8 μm for the ball milled glasses.

Table 6.7: ICIE16 particle size and distribution when produced via jet and ball milling, all in μm.

ICIE16	$D_{[4,3]}$ volume weighted mean	D_{10}	D_{50}	D_{90}
Ball Mill	18.9 ± 0.2	3.3 ± 0.1	15.8 ± 0.3	39.5 ± 0.7
Jet Mill	2.1 ± 0.3	1.4 ± 0.2	2.0 ± 0.1	3.8 ± 0.3

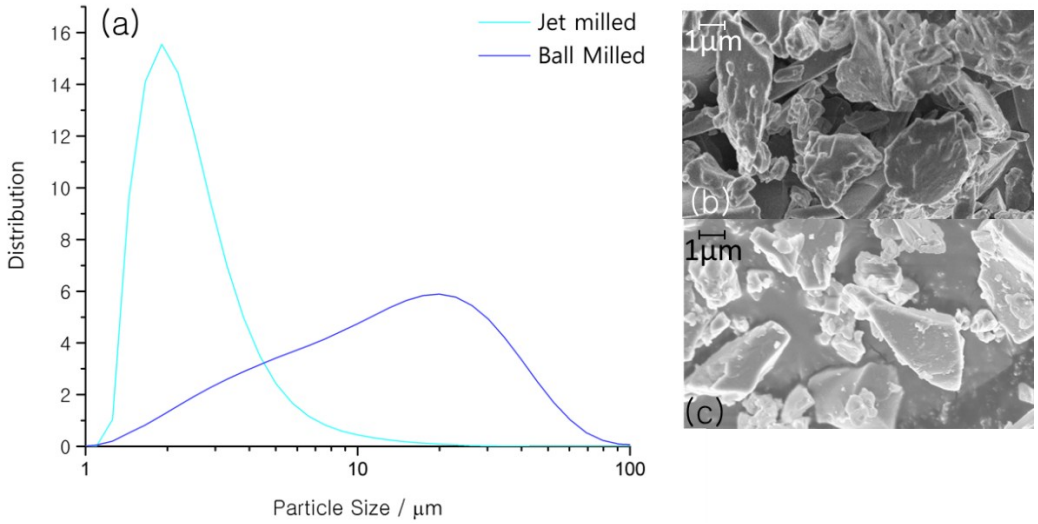


Figure 6.13: (a) Particle size distribution of ICIE16 when milled via jet and ball milling; SEM images of (b) jet milled glass; (c) ball milled glass.

To study the effect of particle size on printability the inks were analysed via compression testing. Inks were made with 20 wt% Pluronic F-127, with 45 and 50 vol% of ICIE16 ground via jet or ball milling. The results are shown in Figure 6.14.

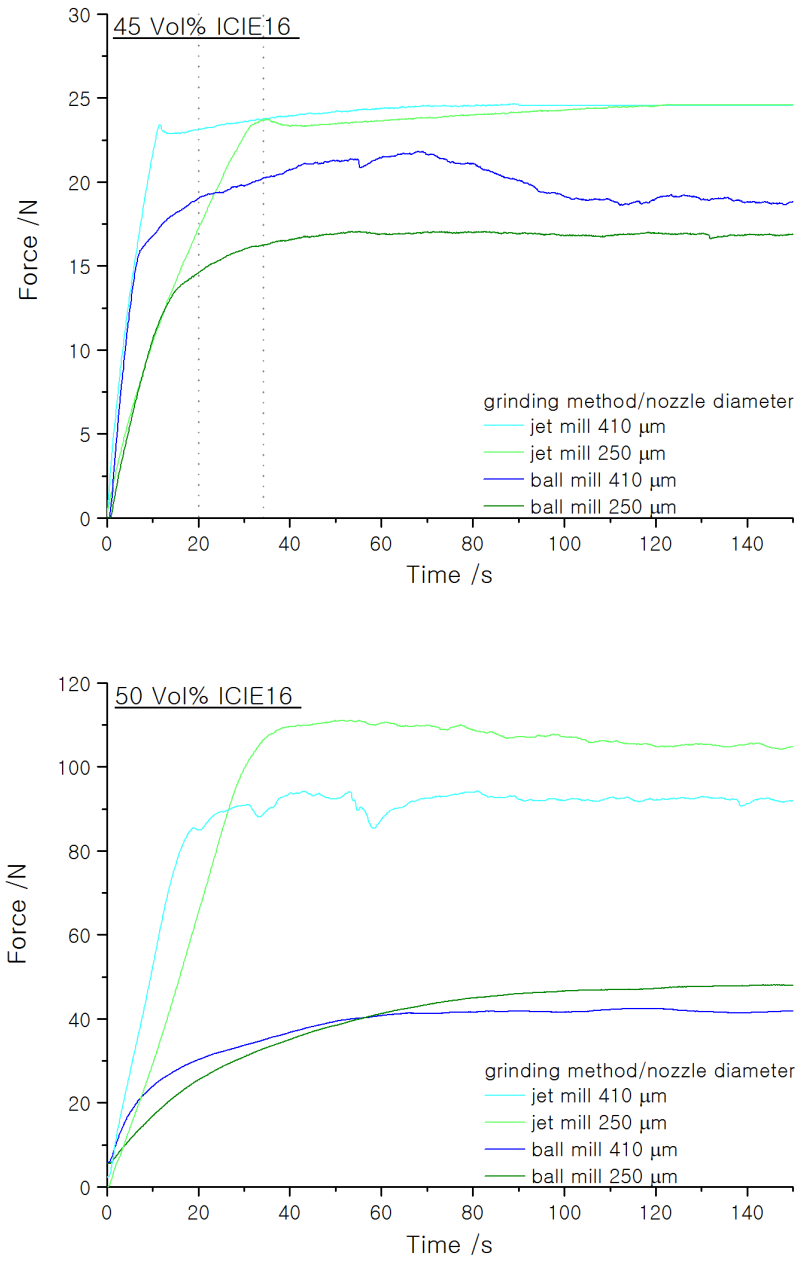


Figure 6.14: The effects of particle size on the force and time needed to reach stabilisation during simulated robocasting via compression testing of inks.

The inks formulated with a glass loading of 45 vol% behaved very differently to inks with 50 vol% glass. At 45 vol%, both the jet milled and ball milled inks reached their stabilisation force at comparable times, highlighted by the grey dashed lines. Even though they had a smaller particle size, the jet milled inks needed greater forces to be extruded through the same nozzle diameters. This suggests that the distribution of the jet milled glasses was too narrow to allow intimate packing within the nozzle, preventing slipping and rearrangement [52,

190-192]. This hypothesis is supported in Figure 6.13 and Table 6.7, which showed that the particle distribution of the ball milled glasses was much greater than the jet milled sample.

When the glass loading within the inks was increased to 50 vol%, the forces needed to extrude the ink containing jet milled glass was over double that of inks containing 45 vol% of glass. This suggests that the distribution of the particles had a greater effect than the particle size itself on ink formation and printability. The larger particle size and wider distribution created via ball milling produced inks that were easier to print but take longer to reach a stabilised printing force. The opposite was seen with the smaller sized jet milled particles.

6.5.2 The effect of printing speed

Another variable within the printing process is the rate in which the inks are extruded from the nozzle. When robocasting, this can be controlled by the plunger speed. When printing sharp corners, or when dimensions are paramount, the printing speed can be reduced so that accuracy can be increased. 40 vol % of ICIE16 was mixed with 30 wt % of Pluronic F-127 and the effect of printing speed on stabilisation was studied. The results are shown in Figure 6.15 Increasing printing speed reduced the time needed to reach equilibrium, but the force required for printing increased. The difference between a print speed of 4 and 10 mms^{-1}, was a force of 12 N and time of 63 seconds.

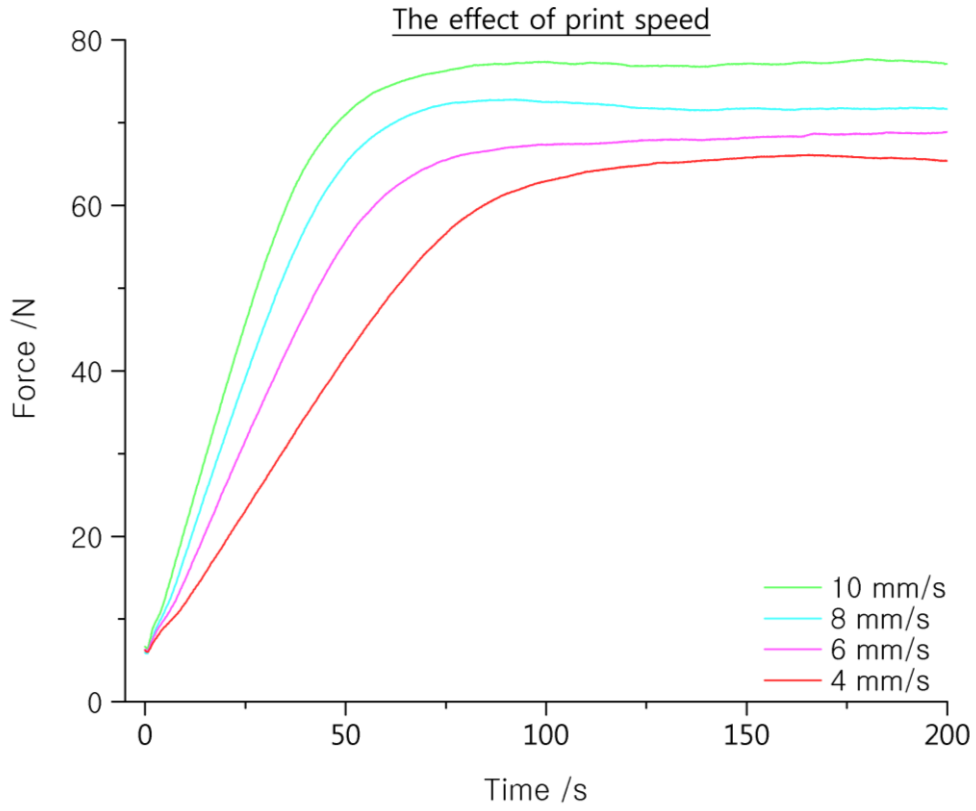


Figure 6.15: The effect of printing speed on stabilisation and force required to stabilise an ink, made of 25 wt% Pluronic with 40 vol% of ICIE16, through a 250 µm nozzle.

This highlighted the time dependent response in which these inks behave. Analysing the time and stabilisation force data (Figure 6.15), the length of extruded solution can be calculated for different printing speeds (Table 6.8). The results showed that regardless of the speed printed, the length of material that needed to be extruded before reaching steady state flow was 730 ± 12 mm for this ink composition.

Table 6.8: Analysis of the time taken to reach stabilisation at different extrusion speeds

Extrusion	Stabilisation	Stabilisation	Length extruded to reach

Speed /mms^{-1}	Time /s	Force /N	stabilisation /mm
4	180	65	720
6	123	68	738
8	93	72	744
10	72	77	720

When designing scaffolds for printing, a 'lead in' distance can be added before the scaffold is printed. This allows the ink to reach the required equilibrium conditions to achieve steady state flow prior to scaffold building. The difference in these values and their relationship with printing speeds needs to be taken into account when optimising 'lead in' lengths during scaffold design.

This analysis helped understand the loads exhibited during robocasting, and translates to the practical processing by understanding the time and lead in length needed to gain continuous steady state printing. It helps to build a better understanding of how the inks behave and perform within the robocasting environment. It moves beyond the theoretical values produces via rheometry testing and allows the printing to be modelled in an understandable and accessible way.

However, the limitations are that no two inks are the same, how the particles arrange within the nozzle is unique to the ink and loading profile at the time. Therefore, these results give an idea of the overall trends that can be seen between glass compositions and the effect of different compositional ratios on extrusion parameters but do not create a complete picture.

6.6 PROCESS OPTIMISATION

6.6.1 Ink formulation

Problems associated with ink formulation

One of the greatest challenges with optimising inks for robocasting is creating homogenous inks via mixing. The inks need to be self-supporting, therefore their high viscosities are not conducive with mixing. To be able to print continuously, the inks needed to be homogenous, with even particle distribution throughout, and without air bubbles.

Figure 6.16 highlights the effects of air bubbles and particle blockages on the flow of inks during ink compression testing. The blue circles highlight the effect of air bubbles upon printing forces observed through compression testing. Air bubbles entrapped in the solution become pressurised when the solution was put under force to extrude. When the bubbles are forced through the nozzle, any local ink was sprayed and printing temporarily stops. If bubbles were present during robocasting of scaffolds, scaffolds were left with breaks within the struts where bubbles have been forced out instead of ink, resulting in non-reproducible mechanically weakened scaffolds.

The green dotted circle in Figure 6.16 shows the increase in force needed to extrude during printing when particles block the nozzle. Nozzle blocking can be created by poor particle alignment and packing which can result in a blockage and consequent build-up in pressure. If the pressure becomes too high, the nozzle can be forced off the end of the syringe or the syringe can split. When blockages occur, a two phase solution can be extruded, where the liquid phase becomes separated from the glass particles through force. This reinforces the importance of particle size distribution and the resultant packing achieved within the nozzle during extrusion.

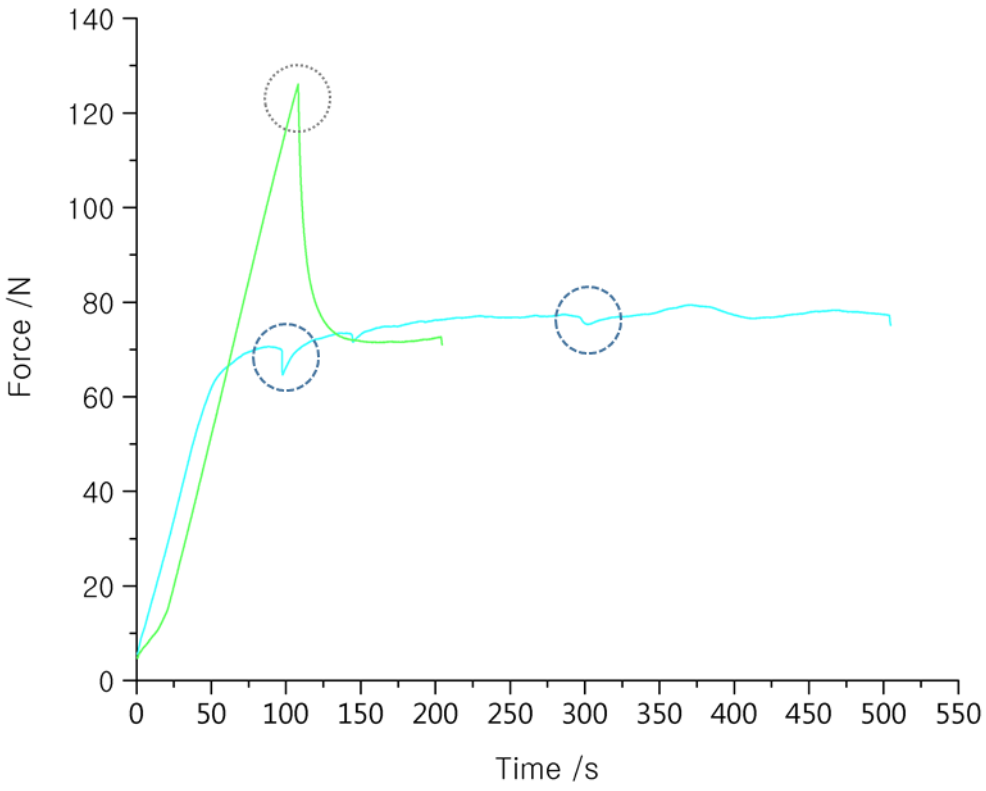


Figure 6.16: Force as a function of time for inks that contained air bubbles (blue) or by printing with nozzle blockages (green).

Poor mixing and poor transfer into the printing syringes resulted in air bubbles trapped within the solution which affected the extrusion rate and the strut density. Figure 6.17 (A) shows an example of the air bubbles that can be present in poorly manufactured inks. If not removed prior to printing, the air bubbles can be transferred to the green body. The sintering protocol is designed to create viscous flow of particle to agglomerate and densify. If large pores, or directional channels, exist within the struts then sintering is incomplete. This resulted in mechanically weak scaffolds, as the pores can act as crack nucleation sites [21] as highlighted by Figure 6.17 (B). This figure highlights a fracture surface of a printed strut, where air bubbles were present within the ink which led to inherent strut porosity.

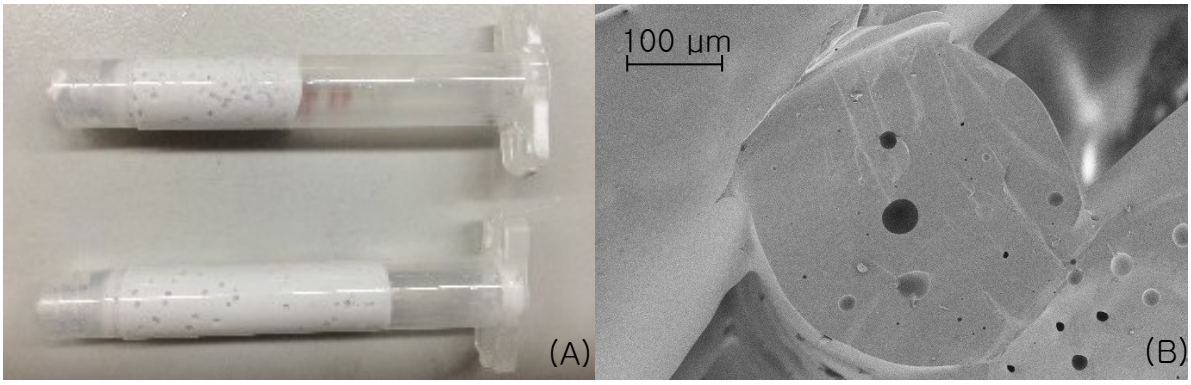


Figure 6.17: Issues associated with air bubbles induced during mixing and syringe transfer on robocast scaffolds. A) air bubbles coagulating within the ink after it has been stored in a fridge for 24 h; B) a fracture surface of a scaffold strut containing air bubbles.

Optimised ink mixing protocol

Other researchers have also published issues surrounding the inclusion of bubbles within their robocasting inks and consequent struts [135, 140, 155]. Franco *et al.* [140] added 1 wt% of Octanol-1 into their inks to help reduce this issue. The octanol-1 acts as a non-ionic surfactant, coalescing the bubbles and consequently reducing their prevalence. Therefore, the following protocol was designed to create homogenous inks and reduce air bubble inclusion:

1. F-127 solutions were prepared prior to use and kept in a fridge at 5 °C;
2. Small batches were mixed in individual pots, using a planetary centrifugal mixer (Thinky mixer ARE-310 USA) to reduce mixing time and overheating;
3. Glass additions were made step wise, inks were mixed on the 'mixing' setting for 4 minutes at 2000 RPM, then 'degassed' for 2 minutes at 1800 RPM;
4. Once mixed, inks were cooled, in a 5°C fridge for 15 minutes, before more glass was added and remixed. This was repeated until all glass was incorporated;
5. Prior to the final mix 1 wt% of octanol-1 was added;
6. Inks were the cooled and transferred to printing syringes, which were sealed and run on a 2 minute 'degass' prior to use to force any remaining bubbles to the top of the syringe.

6.6.2 Green bodies

Pluronic was mixed following literature protocol stated in Section 6.6.1, at Pluronic F-127 loadings of 20, 25 and 30 wt% [140]. Glass powder was then added between 20-55 vol%. Increasing Pluronic F-127 concentration increased the strength and stability of the gel, enabling self-supporting properties at lower glass concentrations. However, as seen in Section 6.4.4, with increased ink strength came an increase in the force needed to extrude the material.

As found during rheology and compression testing of the inks, ICIE16 and 13-93 particles could be mixed to higher concentrations than SBP-3. Maximum SBP-3 loading within an ink of 30 wt% of Pluronic F-127 was 47.5 vol%, compared with a maximum loading of 50 vol% for ICIE16 and 13-93 particles. Inks of 30 wt% Pluronic F-127 produced green bodies that were easier to handle than comparative inks with 20 wt% Pluronic F-127. When handling the green bodies, inks made with 13-93 and ICIE16 were mechanically strong, at all glass loadings, regardless of which tip size was used to manufacture them. Whereas when SBP-3 was printed it was difficult to transfer without disintegrating prior to sintering. Figure 6.18 shows SEM images of green bodies after drying of all three glass compositions produced using the same ratio of 30 wt% of Pluronic F-127 and 47.5 vol% of glass.

Figure 6.18 shows that 13-93 and ICIE16 scaffolds had the most uniform struts and the strut diameters are less deformed, staying cylindrical after drying when compared with SBP-3, which flattened in one direction. When studying the cross section of the struts at higher magnification (the bottom row of images), the packing and consequent porosity between the three glass compositions was different. The ICIE16 and 13-93 particles were better packed and more tightly arranged, compared with SBP-3. SBP-3 struts had more open structure, with obvious pores formed within the struts themselves. It is commonly remarked that the quality of the green body dictates the quality of the sintered product [21]. When working with bioactivity glasses, due to the limited

temperature that can be used during sintering, and the requirement to limit viscous flow to maintain the scaffolds morphology, porosity seen within these struts will transfer through to the final scaffold reducing its mechanical properties. Pores in brittle materials are sites of stress concentration and crack nucleation.

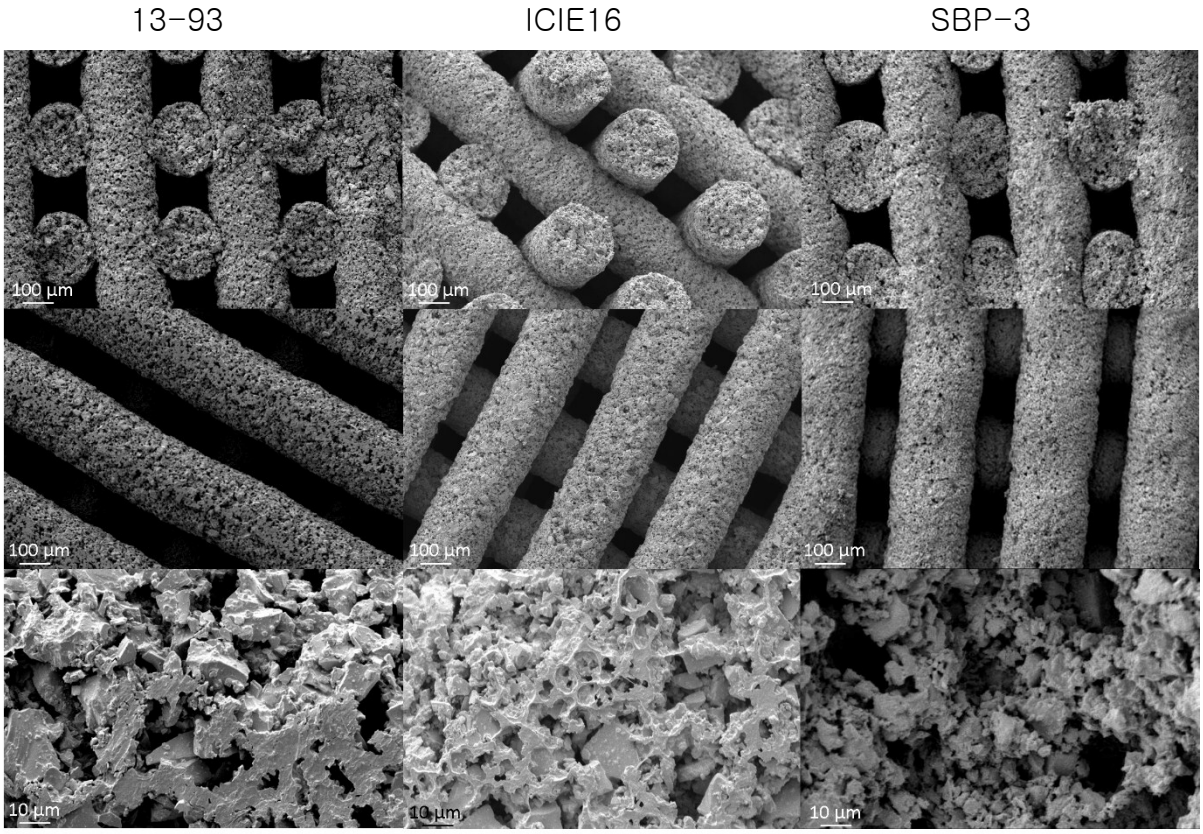


Figure 6.18: SEM images of z, and x,y struts of 13-93, ICIE16 and SBP-3 robocast green bodies 3D printed in inks of 30 wt% of Pluronic F-127 and 47.5 vol% of glass. The bottom row shows cross sections of the struts at higher magnification.

6.6.3 Sintering robocast scaffolds

The first use of Pluronic F-127 for robocasting a bioactive glass was published by Fu *et al.* printing 6P53B glass [135]. When sintering their scaffolds, they used a one-step sintering protocol without a dwell for burn out of the binder. To optimise sintering for these glasses and specific particle sizes, ICIE16 was printed and sintered using both the Fu *et al.* [135] one-step approach and the two step profile used previously for the gel-cast foam scaffold, see Table 4.3.

The two methods were subsequently compared. Both profiles resulted in XRD patterns with amorphous halos post-sinter, however, introducing the dwell in the sintering protocol decreased the surface roughness according to SEM images (Figure 6.19) and increased the compressive strength from 7.34 ± 1.82 MPa to 15.38 ± 2.97 MPa (Table 6.9 and Figure 6.20). TGA results presented in 6.2.2 show that Pluronic F-127 burn out temperature was below 300°C, suggesting that by 500°C none should remain.

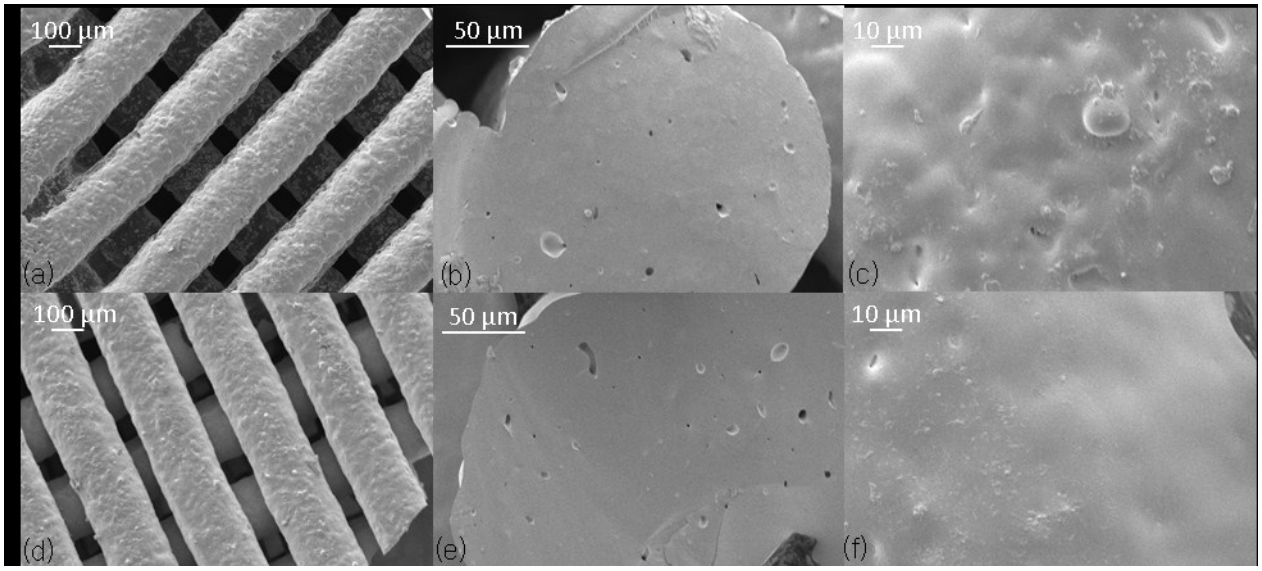


Figure 6.19: 3D printed ICIE16 scaffolds sintered with and without a dwell period for binder removal. (a-c) single step 1 h at 690 °C, (d-f) initial dwell at 500°C for 1 h followed by 690°C for 1 h.

Scaffolds sintered using a 1 h burn out dwell period at 500°C, followed by the second sintering step at 690°C for 1 h, resulted in more homogeneous struts, as shown by Figure 6.19. However, porosity still remained in the struts post sintering. This porosity was very difficult to remove, even after optimising the mixing protocol (Section 6.6.1). This porosity reduces the overall mechanical strength of the scaffolds, as summarised in Table 6.9. An example of the data collected is shown in Figure 6.20. The failure mechanism is via multiple struts fracturing, suggesting that the scaffolds can maintain load even if primary struts fail. From this point onwards all glasses were be sintered using the two step protocol, optimised by glass composition in Chapter 4.

Table 6.9: Tabulated summary of sintering outcomes

Sinter profile (all rates at 3°C/minute)	Compressive Strength /MPa	Porosity /%
One step ramp to 690°C for 1.5 h	7.34 ± 1.82	42.1% ± 0.4
Two step, dwell at 500°C for 1 h, ramp to 690°C for 1.5 h	15.38 ± 2.97	42.8% ± 0.3

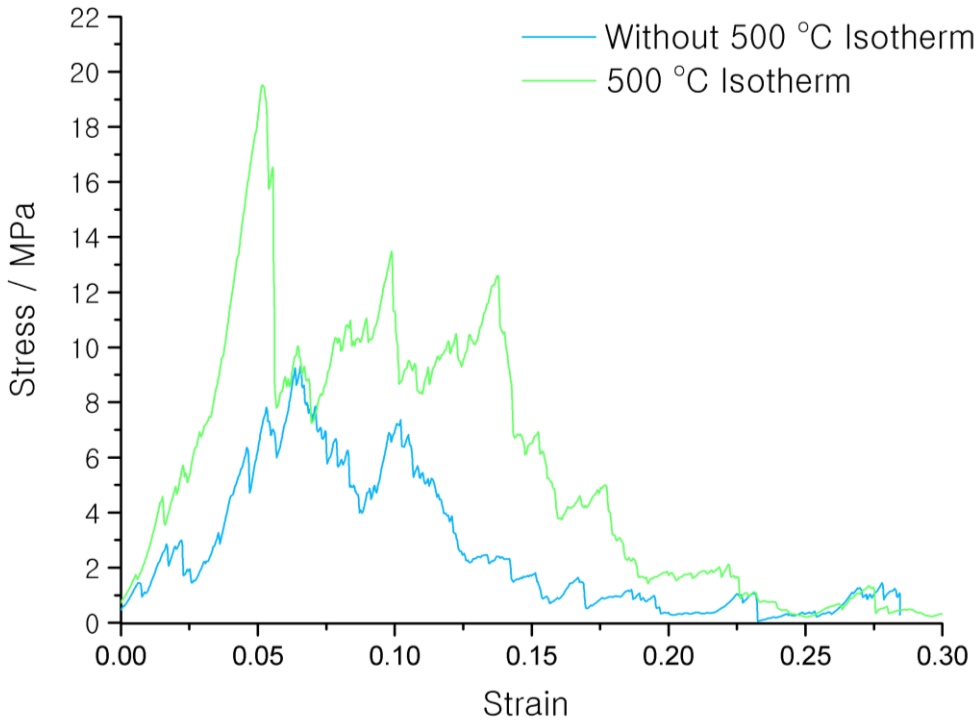


Figure 6.20: Typical stress-strain curves for ICIE16 scaffolds of similar porosity, printed with 47.5 vol% of glass and 30wt% pluronic, sintered using different protocols.

Figure 6.21 shows sintered robocast scaffolds made from ICIE16, SBP-3 and 13-93 using 47.5 vol% of glass using 30 wt% of Pluronic F-127. Each glass composition contained some strut porosity. These images suggest that 13-93 had the least porosity, followed by ICIE16 and SBP-3. This could be due to 13-93 enhanced sintering window allowing greater densification during sintering.

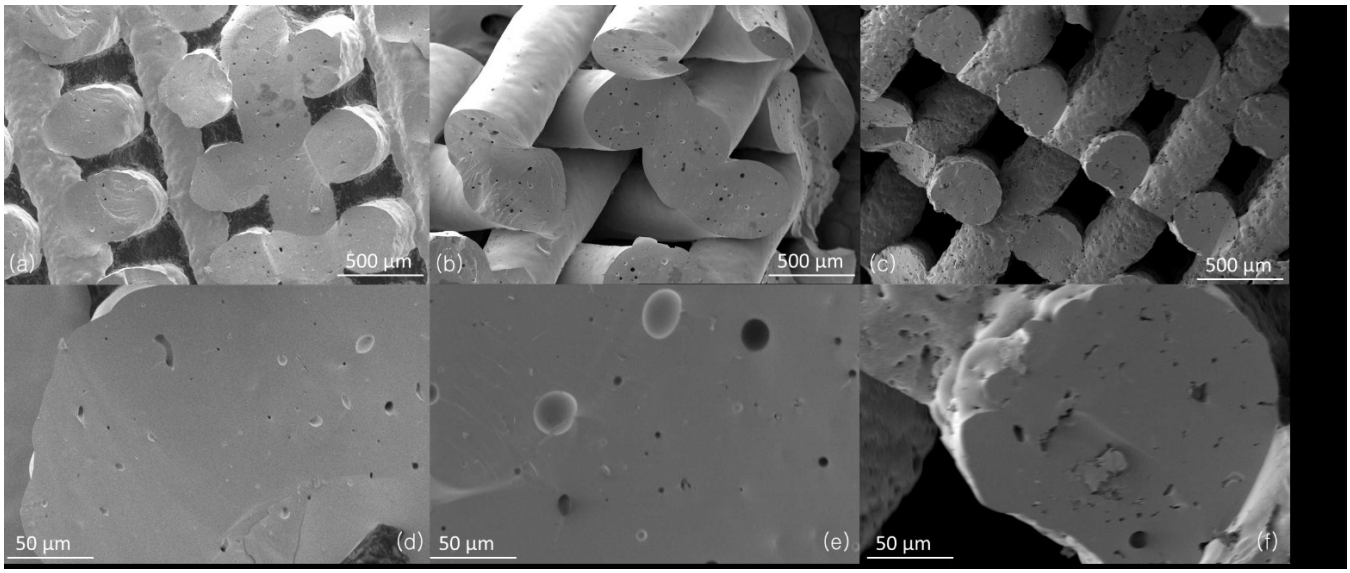


Figure 6.21: SEM images of fracture surfaces of struts, (a) and (d) ICIE16, (b) and (e) SBP-3 and (c) and (f) 13-93.

6.6.4 Reducing strut porosity

Some inherent strut porosity was found within the 3D printed scaffolds regardless of the glass used or its glass/binder ratio. Attempts were made to remove this by adding Octanol-1 surfactant (discussed previously in section 6.6) and altering the mixing protocol, to repeatedly cool the solution tip reduce the viscosity, to remove the bubbles.

Previous printing of bioactive glasses in literature used a modal particle size of between 1-2 µm [52, 140, 144]. It is thought that by reducing the particle size allowed for better packing within the ink, which therefore reduced porosity. Particle size distribution of the glass for robocasting is extremely important, (as shown in section 6.5.1) if the particle size distribution is too narrow, nozzles can become clogged and continuous extrusion will not be achieved. A broad distribution, with a high volume fraction of smaller particles, allows particles to slip past each other and re-arrange themselves under extrusion to create continuous flow at lower forces. This was seen during the simulated compression testing discussed previously where much higher forces were needed to extrude comparable solutions with narrower particle distributions.

To see if strut porosity could be reduced by reducing the particle size used within the inks the three glasses used within this project were jet milled and ball milled to creating different particle sizes. Their particle size and its distribution was measured, as summarised in Table 6.10. For all compositions the jet milled particle sizes and distributions were smaller than that of their ball milled equivalents. Trial scaffolds were printed mixed using 40 vol% of glass with 30 wt% Pluronic F-127, and sintered using the two stage protocol described previously (Section 6.6.3). Figure 6.22 shows the XRD results post-sinter.

Table 6.10: Particle size data of ICIE16, SBP-3 and 13-93 glasses when ground via ball or jet milling, all errors were below ± 0.3 µm.

Glass Composition	Ball Milled $D_{10}/D_{50}/D_{90}$ /µm	Jet Milled $D_{10}/D_{50}/D_{90}$ /µm
13-93	3.3/10.8/30.5	1.4/1.9/3.7
ICIE16	3.2/15.8/39.5	1.5/3.6/12.1
SBP-3	3.1/12.5 /35.0	2.8/10.5/27.2

ICIE16 jet milled glasses when sintered for 1 or 1.5 h at 690°C showed significant crystallisation compared with the ball milled glasses, with peaks appearing at 32° and 33° 2Θ. Crystallisation is an energy controlled process, with mass transfer of a solute from a liquid phase. For smaller particles, less energy is needed for this process to take place and therefore the greater the risk of crystallisation occurring, as supported by the XRD data collected. The same trend was seen within the SBP-3 glass composition with the jet milled glass crystallising more than that of the ball milled equivalents. 13-93 however, did not crystallise even at the lower particle size obtained via jet milling. 13-93 as discussed previously within this work has excellent thermal processing properties with the trade-off of reduced bioactivity. As the primary goal of this

work was to manufacture scaffolds maintaining the glasses amorphous structure only ball milled glasses were worked with.

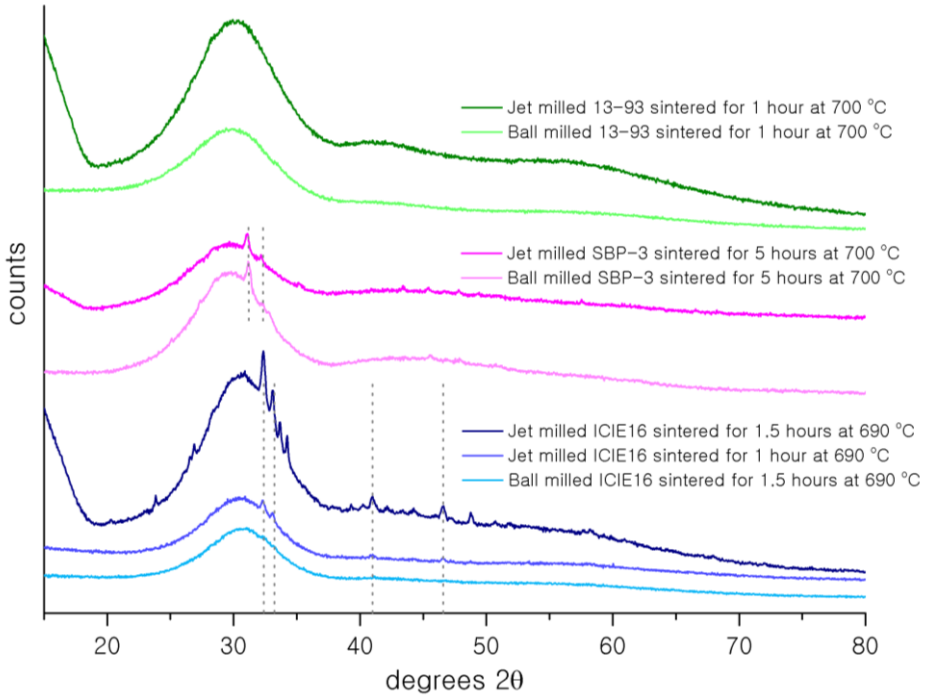


Figure 6.22: XRD patterns of ICIE16, SBP-3 and 13-93 glasses, post-sintering, with changing particle size due to the different grinding methods.

6.6.5 Drying

Scaffolds were characterised via XMT, which showed that within some layers cracking occurred within the struts, which remained present post-sintering, as shown by Figure 6.23.

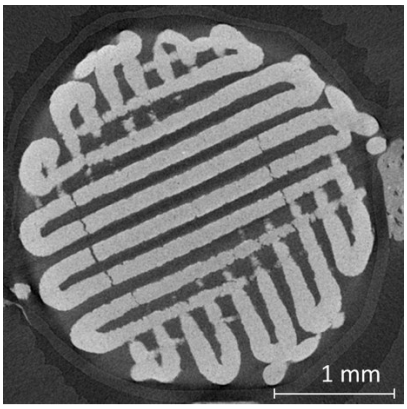


Figure 6.23: XMT image of ICIE16 scaffold with inherent cracking within the struts. Image provided by Xiaomeng Shi.

This cracking could be a result of large air bubbles within the inks, resulting in breakages within the ink flow during printing, or could be a result of the drying stages. Due to the cracks within the tomography scan being in similar areas, it suggests they were formed due to varying shrinkage gradients across the scaffolds during drying. To rectify this issue, ICIE16 scaffolds were printed and underwent one of the following drying stages:

- Dried in air as a reference;
- Printed into an oil reservoir, which was then drained, and left to dry in air for 24 h prior to sintering, (protocol taken from Franco *et al.* [140]);
- Printed as normal but surrounded by a water bath, keeping the humidity at 60% for 24 h prior to sinter;
- Printed and immediately rinsed in ethanol.

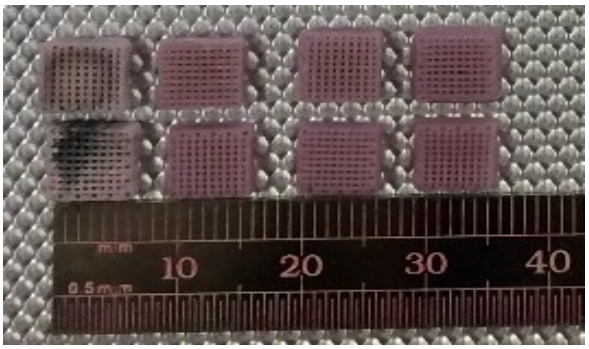


Figure 6.24: Photograph of sintered scaffolds after drying in different environments. From left to right: printed into oil, air dried, water bath, ethanol.

Figure 6.24 shows the variation in outcomes after subjecting the scaffolds to the same sintering protocol under the varying drying regimes stated above. The scaffolds that were printed directly into oil failed to sinter thoroughly as binder remained within the scaffolds, leaving a black residue. SEM (Figure 6.25) showed that in the corresponding black regions of the scaffold, the particles failed to sinter forming continuous struts and stayed as discrete particles. The two scaffolds that were died in air and those dried in a humid environment looked very similar, however under SEM they had very different morphologies of the struts. The samples kept within the water bath did not sinter as well as

those in air, with an obvious particle morphology remaining on the surface. This could be due to a premature reaction happening upon the glass surface while they were kept in the humidity, resulting in a change in the surface layer, prohibiting sintering. The scaffolds that were printed and rinsed within ethanol were geometrically distorted, forming pyramidal shapes where the binder had flowed due to a reaction with the solvent prior to sintering.

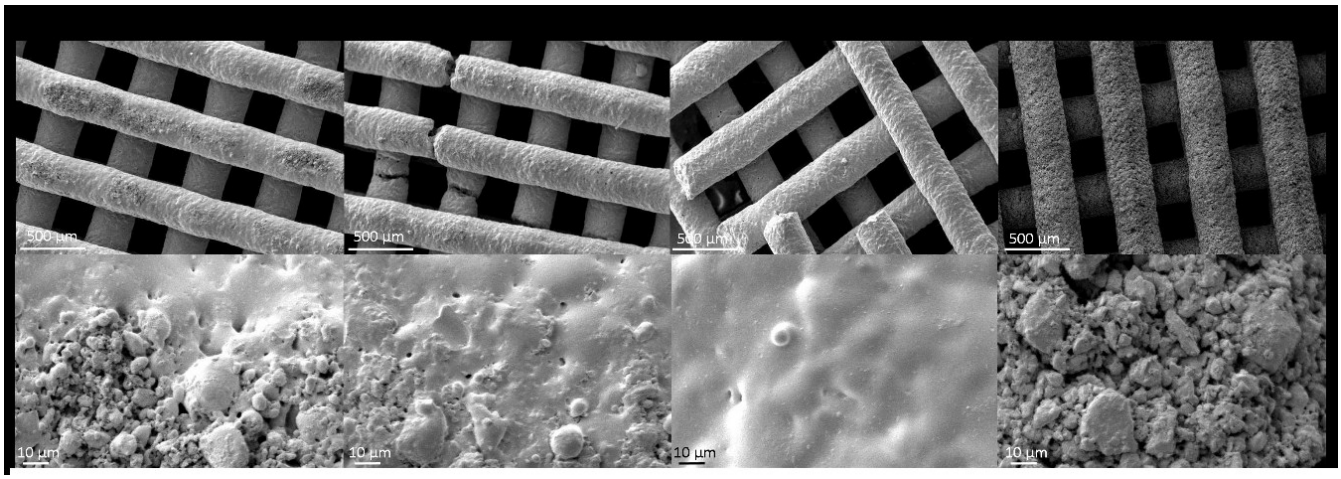


Figure 6.25: SEM images of the effects of different drying protocols on sintered ICIE16 scaffolds.

Compression testing was conducted on the samples which were air dried and dried in humidity to see if any variation in strength was induced, as summarised in Table 6.11. The scaffolds that were dried in air had the greatest mechanical strengths of 17.66 ± 4.09 compared with 12.79 ± 1.87 for the water bath equivalents.

Table 6.11: Variation in porosity and compressive strength with drying protocol.

Drying Method	Compressive Strength /MPa	Porosity /%
Air Dried	17.66 ± 4.09	43.8 % ± 0.01
Water Bath	12.79 ± 1.87	45.2 % ± 0.01

6.7 COMPARISONS OF ROBOCAST SCAFFOLDS MANUFACTURED FROM 3 GLASS COMPOSITIONS

6.7.1 Shrinkage

Scaffolds were printed from all three glasses with the same ratio of glass volume to binder. The shrinkage between green bodies to sintered construct was then compared when printed through a 410 μm nozzle, as summarised in Table 6.12.

Table 6.12: Shrinkage of printed scaffolds in x, y and z dimensions.

Direction	13-93 /%	SBP-3 /%	ICIE16 /%
x	26.71 ± 0.05	23.38 ± 0.02	28.54 ± 0.02
y	27.57 ± 0.06	23.76 ± 0.03	26.72 ± 0.03
z	21.31 ± 0.04	18.02 ± 0.06	18.84 ± 0.05

Shrinkage in x and y was homogeneous for all glass compositions, with ICIE16 shrinking the most followed by 13-93 and then SBP-3. Interestingly all shrinkage in the z direction was less than that of x and y, which is surprising, as during printing the z direction is under the load of the scaffold, and x and y are not. SBP-3 and ICIE16 shrinkage in the z direction was comparable, between 18-19%, which was less than 13-93's shrinkage of 21.3%. When looking at these results with the SEM images presented in Figure 6.21, the 13-93 struts shrank more in z direction, reducing the porosity compared to ICIE16 and SBP-3.

Work by Liu *et al.* [37] and Deliormanlı *et al.* [52] both report shrinkages of 13-93 through a 410 μm nozzle between 24-26 %, which is within the same range seen within this work.

6.7.2 Does glass chemistry affect rheology?

Of the three glasses tested, ICIE16 was the easiest to prepare and the most repeatable and reliable to print. SBP-3 was difficult to mix in high concentrations and challenging to print due to blockages and poor layer adhesion. To try and understand why they would behave differently particle size, and zeta potential analysis was completed. Particle size previously reported in Table 6.10 did not yield any suggestion as to why the glasses would behave differently within this protocol.

Zeta potential measurements (Table 6.13) conducted in water, reported stable suspensions with similar negative charges for all composition, suggesting that surface charge was also not the reason for the variation seen.

Table 6.13. Zeta potential results for the three glasses in water.

Glass Composition	Zeta Potential /mV	Standard Deviation
13-93	-38.6	8.07
ICIE16	-34.5	5.35
SBP-3	-29.4	5.23

The variation could be due to ionic leaching of the glasses in the aqueous environment due to their bioactive nature. However, ICIE16 would have the greatest pH change and dissolution of the three glasses worked with, and it was the easiest manufacture. Reported literature [37, 52] uses smaller particle sizes of 13-93 than those used within this work, and reduction in particle size is known to increase surface area and consequent ionic release, therefore, issues regarding glass degradation and mixing would be expected to reported within these works if this was the reason.

SBP-3 is the first bioactive glass to be robocast which contains strontium within its composition. The difficulties in processing could therefore be related

to its inclusion within the glass composition. However, no direct conclusions as to why have been made.

6.7.3 Compression testing

Effect of strut diameter on strength

All three glasses were printed at the same glass to ink ratio of 47.5 vol% of glass, using 30 wt% Pluronic F-127. This was the highest glass ratio that all three glasses could be homogeneously mixed. Scaffolds were printed using nozzle diameters, 410 and 610 µm forming scaffolds with the same volume. Scaffolds were designed so that the pore size in x y and z was equal. The results are summarised in Figure 6.26. Percentage porosity was similar at 48-50% using the 610 µm nozzle and 41-45% using the 410 µm nozzle.

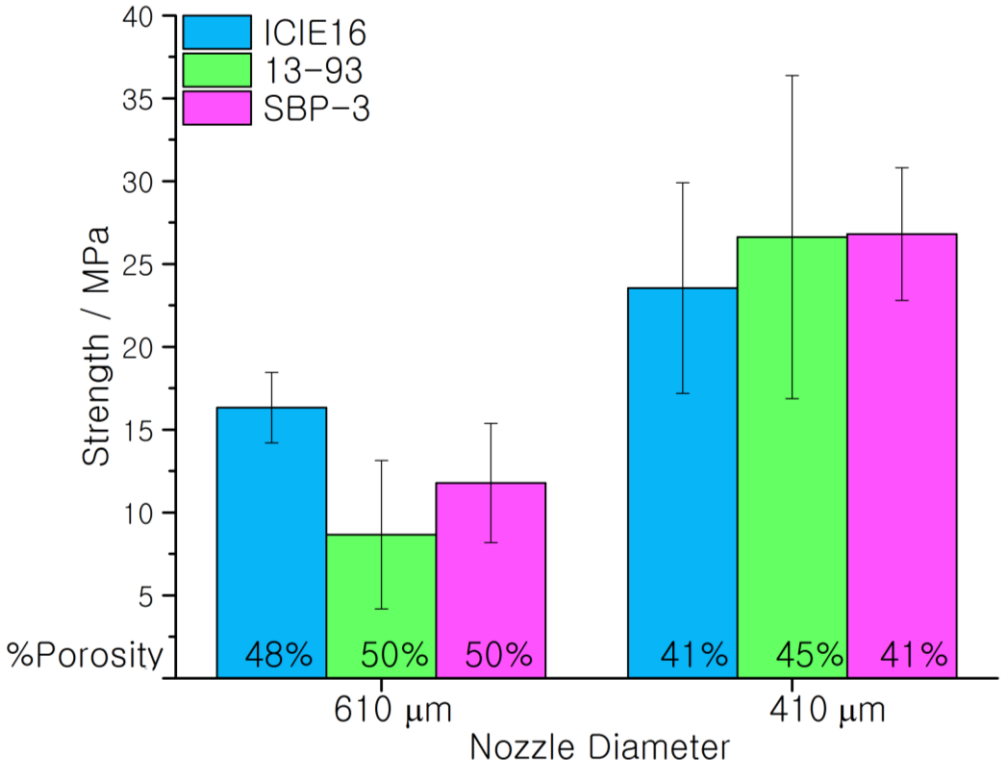


Figure 6.26: Summary of compression testing results of comparable scaffold printed hrough 410 and 610 µm diameter nozzles from ICIE16, SBP-3 and 13-93, porosity of the scaffolds is marked in % within the bars.

The trend seen within the adapted gel-cast scaffolds was that 13-93 produced the strong scaffolds, followed by SBP-3 and then ICIE16. Within the results

presented in Figure 6.26 this same trend is not seen. Brittle materials are only as strong as their biggest flaw. Porosity within the struts can act as crack nucleation sites, reducing scaffolds overall strength due to the random nature of the porosity this may have resulted in the differences seen as well as the variability within the results. Figure 6.26 shows that with reducing nozzle size an increase in compressive strength was seen, however the reduced nozzle size also gave a reduction in the porosity of the scaffolds so differences may not be significant.

13-93 was printed as a reference to compared with other literature within this field. Two researchers have published work using different binders with 13-93. Their reported strengths and experimental parameters are summarised in Table 6.14. All scaffolds were sintered for 1 h at 700 °C, and printed through a 410 µm nozzle diameter.

Table 6.14: Comparison of compressive strengths of ICIE16 scaffolds printed with a 410 µm nozzle diameter compared with published literature.

		Liu *et al.* [37]	Deliormanli *et al.* [52]	This work
Binder Chemistry		F-127	Ethyl cellulose	F-127
Particle Size D_{50}	/µm	1	2	10.8
Volume fraction of glass	/% vol	40	45	47.5
Sample Test Size	/mm	6 x 6 x 6	7.5 x 7.5 x 7.5	6 x 6 x 6
Testing Speed	/mm.minute^{-1}	0.5	0.5	1
Strut spacing	/µm	300	420 ± 30	320 ± 12
Filament Diameter	/µm	330	300 ± 20um	320 ± 10
Porosity	/%	47	48 ± 3	45 ± 1.2
Compressive Strength	/MPa	86 ± 9	142 ± 20	26.6 ± 9.7

The compressive strengths achieved in this study were far lower than those reported within literature. The sintering protocol used within the two studies reported above used a slower ramp rate of 0.1°C per minute, compared to 3°C per minute used within this work. The slower sintering rate, combined with the

reduced particle size could be the reasons such higher strengths are reported as they would reduce any strut porosity within the scaffolds.

6.8 SCAFFOLD COMPARISON: ROBOCASTING VERSES GEL-CAST FOAMING

Scaffolds were printed from ICIE16 with comparable interconnects to scaffolds manufactured via the adapted gel casting process. Figure 6.27 shows XMT images of scaffolds manufactured via the two processing methods and the difference in morphology achieved.

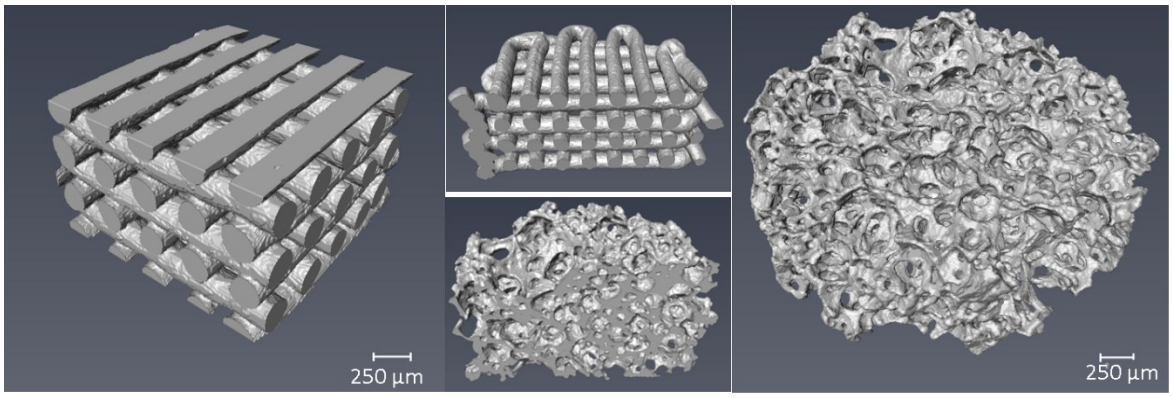


Figure 6.27: XMT images (provided by Xiaomeng Shi) of equivalent robocast and gel-cast scaffolds

Table 6.15 quantifies the differences between the two scaffolds. The robocast scaffolds were designed so that post-sintering they would have comparable pore interconnect diameters with the gel-cast foams. This resulted in a variation in the overall scaffold porosity, surface area and consequent compressive strength.

Table 6.15: Robocast scaffolds compared with adapted gel-cast foams rom ICIE16 with comparable pore interconnects.

		Robocast	Adapted Gel-Casting
Porosity	/%	53 ± 0.02	83 ± 0.02
Modal Interconnect Diameter	/µm	144.4 ± 3.6	146.3 ± 10.6
Compressive Strength	/MPa	18.3 ± 2.2	3.44 ± 0.3

The strengths of the robocast scaffolds manufactured from ICIE16 are greater than those created by the adapted gel casting process; 18.3 ± 2.2 MPa versus 3.44 ± 0.3 MPa. However, the porosity for the gel-cast scaffolds was 25% higher. The customisability of the robocast process yields a versatility which is not possible with the adapted gel-casting technique. However, the high porosity achievable with adapted gel-casting is not as easy to achieve via robocasting. Therefore, both processing methods have their unique advantages over the other.

6.9 CONCLUSIONS

Within this chapter Pluronic F-127 was been used for the first time as a binder to print highly bioactive glass compositions which remain amorphous post sintering. This work shows the versatility of the robocasting process; showing that scaffolds can be manufactured into a variety of pore geometries from different glass compositions, maintaining their bioactivity.

Using rheological measurements can be used as a tool to understand fundamental changes within ink compositions, but its values do not translate to the physical art of printing. The forces created during the robocasting process are dependent upon the nozzle profile and its diameter. However, it is also linked the particle size of the glass within the ink and particle distribution in the ink. To be able to produce inks that are suitable for continuous printing, and consequently scale up, mixing is key. The production of homogeneous inks with no air bubbles and even glass distribution facilitates good scaffold production.

As with all highly bioactive compositions the results of this work reinforce that there is a trade-off needed between highly bioactive scaffolds and mechanical strength. To be able to use robocasting to manufacture amorphous scaffolds from these compositions larger particle sizes were needed to be used. This

work comments upon the challenges associated with removing porosity from larger particle sized inks, from compositions that are subject to limited sintering temperatures due to crystallisation. A limitations of this work, is the lack of quantification of the internal strut porosity within the robocast scaffolds, which negates the ability to reduce or quantify the level of porosity obtained.

Although robocasting yields many advantages as a processing method, in terms of its potential ability for scale up; its reliability in scaffold production, and geometric control; the fragility of the green bodies produced; the dependence on particle size and the processing challenges associated with airless ink production makes this processing method and its associated optimisation a challenging one.

When comparing scaffolds manufactured via robocasting and those manufactured via the adapted gel-casting process with comparable sized interconnect diameters. Although a difference in porosity is seen, the robocast scaffolds produce much higher mechanical strength than the foamed equivalents. This is due to the orientation of the struts within the printed scaffolds allowing greater mechanical load to be sustained.

7 Conclusions

This body of work aimed to optimise two manufacturing techniques for potentially highly bioactive glass compositions, to produce suitable scaffolds for bone repair.

First, scaffolds were produced via the adapted gel-casting processing route, to form porous constructs with suitable interconnects and pore size for bone ingrowth. This technique proved to be able to be adapted for use with all 3 glass compositions, ICIE16, SBP-3 and 13-93; by varying the concentration addition of surfactant between 0.3 ml for ICIE16, and 0.4 ml for SBP-3 and 13-93

The optimised scaffolds had 75% porosity, a modal interconnect diameter between 100-150 μm while remaining amorphous post processing. The scaffolds produced had compressive strengths of 3.4 ± 0.3 MPa, 8.4 ± 0.8 MPa, 15.3 ± 1.8 MPa for ICIE16, SBP-3 and 13-93 respectively at 75.6 ± 2.6% porosity. These results are within the range of cancellous bone of 2-12 MPa at 50-90% porosity [182].

The gel-cast foam scaffolds were subjected to bioactivity testing in SBF. Each glass used has a different modified network connectivity, 2.13, 2.84 and 3.01 for ICIE16, SBP-3 and 13-93 respectively. For all three compositions a calcium-phosphate rich phase precipitated upon the surface of the scaffolds within 4 weeks. An expected variation was seen within the rate of precipitation between compositions. Following the modified network connectivity theory, ICIE16 was expected to form an HCA layer more rapidly than the other two compositions, which it did forming HCA within 8 h. 13-93 had the highest network connectivity of the three glasses tested and its release profiles followed the same trend as ICIE16 just at slower rate of dissolution. Therefore, these two glasses fit the network connectivity model.

In contrast, SBP-3 had the highest silica release when compared to the other glasses however, its release of other cations into the solution was the lowest. This supports the suggestion that intermediate ions within the glass network have additional, more complicated compositional affects that effect the bioactive performance which is not characterised within the NC' model.

The *in vivo* results presented within this work showed that scaffolds produced via the adapted gel-casting process are suitable for bone ingrowth within a rabbit femoral head model. Bone ingrowth was evident by 7 weeks, with the strontium rich SBP-3 outperforming ICIE16. By 12 weeks ICIE16 sample yielded greater bone regeneration and formulation of the natural bone structure present.

This project then looked to produce scaffolds via robocasting of the three glass compositions of interest. Pluronic F-127 was used, for the first time, to print highly bioactive glass compositions which remained amorphous post sintering. It was found that a compromise had to be made between glass loading and the printability of inks, and consequently 47.5 vol% of ball milled glass combined with 30 wt% of Pluronic F-127 was used with all three glass compositions. This ratio enabled inks which were able to be continuously printed through a 250 μm nozzle. This work highlights the versatility of the robocasting manufacturing process, and Pluronic F-127 as a binder. The results showed that scaffolds can be manufactured into a variety of pore geometries from different glass chemistries, with larger particle size distributions than currently reported in literature.

The thesis reports upon the challenges associated with removing porosity from inks containing large particle sizes, from compositions that are subject to limited sintering temperature due to crystallisation. A limitation of this work is the lack of quantification of the internal strut porosity within the robocast scaffolds, which negates the ability to measure the level of porosity seen.

The compressive strengths achieved from the robocast scaffolds compared with literature suggest that there is a trade-off needed between highly bioactive scaffolds and compressive strength; due to the aforementioned limitations associated with sintering and particle size.

Scaffolds with comparable interconnect sizes to the adapted gel-cast foams were able to be printed via the robocasting process from ICIE16. Although a difference in porosity was a consequence, interconnects between the foams and prints were 144.4 ± 3.6 μm and 146.3 ± 10.6 μm respectively. The robocast scaffolds, with reduced porosity, produce much higher mechanical strength of 18.3 ± 2.2 MPa than their foamed equivalents, 3.44 ± 0.3 MPa. This is due to the orientation of the struts within the printed scaffolds allowing greater mechanical load to be sustained.

Although this work shows that highly bioactive glass scaffolds can be produced via robocasting with enhanced mechanical strengths, the general limitation of bioactive glasses as a material for bone repair still remains. Their inability to absorb the cyclic loading experienced within the human body continues to remain an issue. Work by researchers to form hybrids of inorganic-organic composites which maintain the bioactive nature of the glass as well as improving the material toughness are a promising approach to solving this issue. Further work to improve the toughness of glass materials within this application needs to continue to yield a promising and viable alternative to autograft bone repair.

8 FURTHER WORK

This work has shown that scaffolds can be manufactured via the robocasting process from highly bioactive glasses using Pluronic F-127 as a binder. However, the current protocol allows the inclusion of air bubbles into the inks which limits the mechanical strengths of the scaffolds produced. Further work to investigate other ink chemistries and glass composition to reduce said porosity, enabling the formation of stronger scaffolds while maintaining their bioactivity should be completed to maximise the potential of this processing method.

At the end of this project an *in vivo* study was started, to compare and contrast the bone bonding, and ability to stimulate bone ingrowth, of ICIE16 scaffolds produced via the adapted gel-casting process and robocasting with comparable pore interconnect diameter as detailed in Section 6.8. Preliminary XMT results, show bone integration of the robocast scaffold at 12 weeks within a femoral head defect within a rabbit model.

Further work of this project is to compare via histology and XMT the bone in growth into the scaffolds to determine whether local topography has an impact on bone growth across 12 weeks. As well to discover if robocast scaffold's regularly geometry is attractive to cells over the random tortuosity created by the foamed scaffold architecture.

9 REFERENCES

1. Hench, L.L., et al., *Bonding mechanism at the interface of ceramics prosthetic materials.* Journal of Biomedical Materials Research, 1971. **5**(6): p. 117-141.
2. Xynos, I.D., et al., *Ionic Products of Bioactive Glass Dissolution Increase Proliferation of Human Osteoblasts and Induce Insulin-like Growth Factor II mRNA Expression and Protein Synthesis.* Biochemical and Biophysical Research Communications, 2000. **276**(2): p. 461-465.
3. Hench, L.L., *Bioactive Materials for Gene Control*, in *New Materials and Technologies for Healthcare*. World Scientific: Singapore. p. 25-48.
4. Jones, J.R., *Review of bioactive glass: From Hench to hybrids.* Acta Biomaterialia, 2013. **9**(1): p. 4457-4486.
5. Wang, Z., et al., *Evaluation of an osteostimulative putty in the sheep spine.* Journal of Materials Science: Materials in Medicine, 2011. **22**(1): p. 185-191.
6. Wu, Z.Y., et al., *Melt-derived bioactive glass scaffolds produced by a gel-cast foaming technique.* Acta Biomaterialia, 2011. **7**(4): p. 1807-1816.
7. Magallanes-Perdomo, M., et al., *Bioactivity modulation of Bioglass® powder by thermal treatment.* Journal of the European Ceramic Society, 2012. **32**(11): p. 2765-2775.
8. Plewinski, M., et al., *The effect of crystallization of bioactive bioglass 45S5 on apatite formation and degradation.* Dental Materials, 2013. **29**(12): p. 256-1264.
9. Filho, O.P., G.P. La Torre, and L.L. Hench, *Effect of crystallization on apatite-layer formation of bioactive glass 45S5.* Journal of Biomedical Materials Research, 1996. **30**(4): p. 509-514.
10. Hench, L.L., *Bioceramics: From Concept to Clinic.* Journal of the American Ceramic Society, 1991. **74**(7): p. 1487-1510.
11. Lefebvre, L., et al., *Sintering behaviour of 45S5 bioactive glass.* Acta Biomaterialia, 2008. **4**(6): p. 1894-903.
12. Clupper, D.C. and L.L. Hench, *Bioactive response of Ag-doped tape cast Bioglass 45S5 following heat treatment.* Journal of Materials Science: Materials in Medicine, 2001. **12**(10-12): p. 917-21.
13. Li, P., et al., *The effect of residual glassy phase in a bioactive glass-ceramic on the formation of its surface apatite layerin vitro.* Journal of Materials Science: Materials in Medicine, 1992. **3**(6): p. 452-456.
14. Shirtliff, V.J. and L.L. Hench, *Bioactive materials for tissue engineering, regeneration and repair.* Journal of Materials Science, 2003. **38**(23): p. 4697-4707.
15. Elgayar, I., et al., *Structural analysis of bioactive glasses.* Journal of Non-Crystalline Solids, 2005. **351**(2): p. 173-183.
16. Boccaccini, A.R., L.A.H. Durand, and A.A. Gorustovich, *Bioactive Glasses and Angiogenesis*, in *New Materials and Technologies for Healthcare*. p. 65-76.
17. Brauer, D.S., *Phosphate Glasses*, in *Bio-Glasses*. 2012, John Wiley & Sons, Ltd. p. 45-64.
18. Fagerlund, S., et al., *T-T-T behaviour of bioactive glasses 1-98 and 13-93.* Journal of the European Ceramic Society, 2012. **32**(11): p. 2731-2738.

19. Jones, J.R., L.M. Ehrenfried, and L.L. Hench, *Optimising bioactive glass scaffolds for bone tissue engineering.* Biomaterials, 2006. **27**(7): p. 964-73.
20. Shelby, J.E., *Introduction to Glass Science and Tenchology*. 2nd ed. 2005: The Royal Society of Chemistry.
21. Richerson, D.W., *Modern Ceramic Engineering*. 3rd ed. 2006, USA: Taylor and Francis.
22. Cormack, A.N., *The Structure of Bioactive Glasses and Their Surfaces*, in *Bio-Glasses*. 2012, John Wiley & Sons, Ltd. p. 65-74.
23. Hench, L.L. and J. Wilson, *Introduction*, in *An Introduction to Bioceramics*. 1993, World Scientific London. p. 1-24.
24. Holliday, L., *The connection number of polymers with particualr reference to carbon polymers.* Journal of applied polymer science, 1968. **12**: p. 333-336.
25. Hill, R., *An alternative view of the degradation of bioglass.* Journal of Materials Science Letters, 1996. **15**(13): p. 1122-1125.
26. Hill, R.G. and D.S. Brauer, *Predicting the bioactivity of glasses using the network connectivity or split network models.* Journal of Non-Crystalline Solids, 2011. **357**(24): p. 3884-3887.
27. Hill, R.G. and D.S. Brauer, *Predicting the glass transition temperature of bioactive glasses from their molecular chemical composition.* Acta Biomaterialia 2011. **7**(10): p. 3601-5.
28. O'Donnell, M.D., *Melt-Derived Bioactive Glass*, in *Bio-Glasses*. 2012, John Wiley & Sons, Ltd. p. 13-27.
29. Mercier, C., et al., *Influence of P2O5 content on the structure of SiO2-Na2O-CaO-P2O5 bioglasses by 29Si and 31P MAS-NMR.* Journal of Non-Crystalline Solids, 2011. **357**(24): p. 3901-3909.
30. Watts, S.J., et al., *Influence of magnesia on the structure and properties of bioactive glasses.* Journal of Non-Crystalline Solids, 2010. **356**(9-10): p. 517-524.
31. Lockyer, M.W.G., D. Holland, and R. Dupree, *NMR investigation of the structure of some bioactive and related glasses.* Journal of Non-Crystalline Solids, 1995. **188**(3): p. 207-219.
32. Fagerlund, S., et al., *Phase composition and in vitro bioactivity of porous implants made of bioactive glass S53P4.* Acta Biomaterialia 2012. **8**(6): p. 2331-9.
33. Fredholm, Y.C., et al., *Influence of strontium for calcium substitution in bioactive glasses on degradation, ion release and apatite formation.* Journal of the Royal Society Interface, 2012. **9**(70): p. 880-889.
34. Fu, Q., et al., *Mechanical and in vitro performance of 13-93 bioactive glass scaffolds prepared by a polymer foam replication technique.* Acta Biomaterialia, 2008. **4**(6): p. 1854-64.
35. Liu, X., M.N. Rahaman, and Q. Fu, *Oriented bioactive glass (13-93) scaffolds with controllable pore size by unidirectional freezing of camphene-based suspensions: Microstructure and mechanical response.* Acta Biomaterialia, 2011. **7**(1): p. 406-16.
36. Liu, X., et al., *Porous and strong bioactive glass (13-93) scaffolds prepared by unidirectional freezing of camphene-based suspensions.* Acta Biomaterialia, 2012. **8**(1): p. 415-23.

37. Liu, X., et al., *Mechanical properties of bioactive glass (13-93) scaffolds fabricated by robotic deposition for structural bone repair.* Acta Biomaterialia, 2013. **9**(6): p. 7025-34.
38. Maçon, A.L.B., et al., *A unified in vitro evaluation for apatite-forming ability of bioactive glasses and their variants.* Journal of Materials Science: Materials in Medicine, 2015. **26**(2): p. 1-10.
39. Salman, S.M., S.N. Salama, and H.A. Abo-Mosallam, *The role of strontium and potassium on crystallization and bioactivity of Na2O-CaO-P2O5-SiO2 glasses.* Ceramics International, 2012. **38**(1): p. 55-63.
40. Kolan, K.C., et al., *Effect of material, process parameters, and simulated body fluids on mechanical properties of 13-93 bioactive glass porous constructs made by selective laser sintering.* Journal of the Mechanical Behavior of Biomedical Materials 2012. **13**: p. 14-24.
41. Fu, Q., et al., *Preparation and bioactive characteristics of a porous 13-93 glass, and fabrication into the articulating surface of a proximal tibia.* Journal of Biomedical Materials Research Part A, 2007. **82**(1): p. 222-9.
42. Andersson, O. and L.L. Hench, *Bioactive Glasses*, in *An Introduction to Bioceramics*. 1993, World Scientific. p. 41-62.
43. Tylkowski, M. and D.S. Brauer, *Mixed alkali effects in Bioglass® 45S5.* Journal of Non-Crystalline Solids, 2013. **376**(0): p. 175-181.
44. Arcos, D., D.C. Greenspan, and M. Vallet-Regí, *A new quantitative method to evaluate the in vitro bioactivity of melt and sol-gel-derived silicate glasses.* Journal of Biomedical Materials Research Part A, 2003. **65A**(3): p. 344-351.
45. Wallace, K.E., et al., *Influence of sodium oxide content on bioactive glass properties.* Journal of Materials Science: Materials in Medicine, 1999. **10**(12): p. 697-701.
46. Hoppe, A., N.S. Guldal, and A.R. Boccaccini, *A review of the biological response to ionic dissolution products from bioactive glasses and glass-ceramics.* Biomaterials, 2011. **32**(11): p. 2757-74.
47. Sen, C.K., et al., *Copper-induced vascular endothelial growth factor expression and wound healing.* Am J Physiol Heart Circ Physiol, 2002. **282**(5): p. 1821-7.
48. Modglin, V.C., et al., *In vitro performance of 13-93 bioactive glass fiber and trabecular scaffolds with MLO-A5 osteogenic cells.* Journal of Biomedical Materials Research Part A, 2012. **100A**(10): p. 2593-2601.
49. Liu, X., et al., *Enhanced bone regeneration in rat calvarial defects implanted with surface-modified and BMP-loaded bioactive glass (13-93) scaffolds.* Acta Biomaterialia, 2013. **9**(7): p. 7506-7517.
50. Hupa, L. and A. Yli-Urpo, *Dental Applications of Glasses*, in *Bio-Glasses*. 2012, John Wiley & Sons, Ltd. p. 159-175.
51. Gu, Y., et al., *Bone regeneration in rat calvarial defects implanted with fibrous scaffolds composed of a mixture of silicate and borate bioactive glasses.* Acta Biomaterialia, 2013. **9**(11).
52. Deliormanlı, A.M. and M.N. Rahaman, *Direct-write assembly of silicate and borate bioactive glass scaffolds for bone repair.* Journal of the European Ceramic Society, 2012. **32**(14): p. 3637-3646.
53. Bi, L., et al., *Effect of bioactive borate glass microstructure on bone regeneration, angiogenesis, and hydroxyapatite conversion in a rat calvarial defect model.* Acta Biomaterialia, 2013. **9**(8): p. 8015-8026.

54. Deliormanlı, A.M., X. Liu, and M.N. Rahaman, *Evaluation of borate bioactive glass scaffolds with different pore sizes in a rat subcutaneous implantation model.* Journal of Biomaterials Applications, 2014. **28**(5): p. 643-653.
55. Bi, L., et al., *Healing of critical-size segmental defects in rat femora using strong porous bioactive glass scaffolds.* Materials Science and Engineering: C. **42**(1).
56. Liu, X., M.N. Rahaman, and D.E. Day, *In Vitro Degradation and Conversion of Melt-Derived Microfibrous Borate (13-93B3) Bioactive Glass Doped with Metal Ions.* Journal of the American Ceramic Society, 2014. **97**(11): p. 3501-3509.
57. Huang, W., et al., *Kinetics and mechanisms of the conversion of silicate (45S5), borate, and borosilicate glasses to hydroxyapatite in dilute phosphate solutions.* Journal of materials science. Materials in medicine, 2006. **17**(7): p. 583-96.
58. Deliormanlı, A.M., *Size-dependent degradation and bioactivity of borate bioactive glass.* Ceramics International, 2013. **39**(7): p. 8087-8095.
59. Jung, S.B., *Bioactive Borate Glasses*, in *Bio-Glasses*. 2012, John Wiley & Sons, Ltd. p. 75-95.
60. Dzondo-Gadet, M., et al., *Action of boron at the molecular level: Effects on transcription and translation in an acellular system.* Biological Trace Element Research, 2002. **85**(1): p. 23-33.
61. Yao, A., et al., *In Vitro Bioactive Characteristics of Borate-Based Glasses with Controllable Degradation Behavior.* Journal of the American Ceramic Society, 2007. **90**(1): p. 303-306.
62. Fu, Q., et al., *Silicate, borosilicate, and borate bioactive glass scaffolds with controllable degradation rate for bone tissue engineering applications. I. Preparation and in vitro degradation.* Journal of Biomedical Materials Research Part A, 2010. **95A**(1): p. 164-171.
63. Midha, S., et al., *Preconditioned 70S30C bioactive glass foams promote osteogenesis in vivo.* Acta Biomaterialia, 2013. **9**(11): p. 9169-9182.
64. Azevedo, M.M., et al., *Hypoxia inducible factor-stabilizing bioactive glasses for directing mesenchymal stem cell behavior.* Tissue Eng Part A, 2015. **21**(1-2): p. 382-9.
65. Azevedo, M.M., et al., *Synthesis and characterization of hypoxia-mimicking bioactive glasses for skeletal regeneration.* Journal of Materials Chemistry, 2010. **20**(40): p. 8854-8864.
66. Quinlan, E., et al., *Hypoxia-mimicking bioactive glass/collagen glycosaminoglycan composite scaffolds to enhance angiogenesis and bone repair.* Biomaterials, 2015. **52**: p. 358-66.
67. Shima, D.T., U. Deutsch, and P.A. D'Amore, *Hypoxic induction of vascular endothelial growth factor (VEGF) in human epithelial cells is mediated by increases in mRNA stability.* FEBS Letters, 1995. **370**(3): p. 203-208.
68. Smith, J.M., et al., *Structural characterisation of hypoxia-mimicking bioactive glasses.* Journal of Materials Chemistry B, 2013. **1**(9): p. 1296-1303.
69. Wu, C., et al., *Hypoxia-mimicking mesoporous bioactive glass scaffolds with controllable cobalt ion release for bone tissue engineering.* Biomaterials, 2012. **33**(7): p. 2076-85.
70. Lee, I.H., et al., *Development, characterisation and biocompatibility testing of a cobalt-containing titanium phosphate-based glass for engineering of*

vascularized hard tissues. Mater Sci Eng C Mater Biol Appl, 2013. **33**(4): p. 2104-12.
71. Hoppe, A., et al., *Cobalt-releasing 1393 bioactive glass-derived scaffolds for bone tissue engineering applications.* American Ceramics Society Applied Materials and Interfaces, 2014. **6**(4): p. 2865-77.
72. Gorustovich, A.A., J.A. Roether, and A.R. Boccaccini, *Effect of bioactive glasses on angiogenesis: a review of in vitro and in vivo evidences.* Tissue Eng Part B Rev, 2010. **16**(2): p. 199-207.
73. Rabiee, S.M., et al., *Effect of ion substitution on properties of bioactive glasses: A review.* Ceramics International, 2015. **41**(6): p. 7241-7251.
74. Zreiqat, H., et al., *Mechanisms of magnesium-stimulated adhesion of osteoblastic cells to commonly used orthopaedic implants.* Journal of Biomedical Materials Research, 2002. **62**(2): p. 175-184.
75. Ma, J., et al., *Effect of magnesia on the degradability and bioactivity of sol-gel derived SiO2-CaO-MgO-P2O5 system glasses.* Colloids Surf B Biointerfaces, 2010. **81**(1): p. 87-95.
76. Vallet-Regi, M., et al., *Effect of magnesium content on the in vitro bioactivity of CaO-MgO-SiO2-P2O5 sol-gel glasses.* Journal of Materials Chemistry, 1999. **9**(2): p. 515-518.
77. Pereira, D., et al., *Surface behaviour of high MgO-containing glasses of the Si-Ca-P-Mg system in a synthetic physiological fluid.* Journal of the European Ceramic Society, 2004. **24**(15-16): p. 3693-3701.
78. Wornham, D.P., et al., *Strontium potently inhibits mineralisation in bone-forming primary rat osteoblast cultures and reduces numbers of osteoclasts in mouse marrow cultures.* Osteoporosis International, 2014. **25**(10): p. 2477-2484.
79. Gentleman, E., et al., *The effects of strontium-substituted bioactive glasses on osteoblasts and osteoclasts in vitro.* Biomaterials, 2010. **31**(14): p. 3949-3956.
80. Marie, P.J., et al., *Mechanisms of Action and Therapeutic Potential of Strontium in Bone.* Calcified Tissue International, 2001. **69**(3): p. 121-129.
81. Autefage, H., et al., *Sparse feature selection methods identify unexpected global cellular response to strontium-containing materials.* Proc Natl Acad Sci U S A, 2015. **112**(14): p. 4280-5.
82. Santocildes-Romero, M.E., et al., *The osteogenic response of mesenchymal stromal cells to strontium-substituted bioactive glasses.* Journal of Tissue Engineering and Regenerative Medicine, 2015. **9**(5): p. 619-631.
83. Massera, J. and L. Hupa, *Influence of SrO substitution for CaO on the properties of bioactive glass S53P4.* Journal of Materials Science: Materials in Medicine, 2014. **25**(3): p. 657-668.
84. Fredholm, Y.C., et al., *Strontium containing bioactive glasses: Glass structure and physical properties.* Journal of Non-Crystalline Solids, 2010. **356**(44-49): p. 2546-2551.
85. Massera, J., et al., *The influence of SrO and CaO in silicate and phosphate bioactive glasses on human gingival fibroblasts.* Journal of Materials Science: Materials in Medicine, 2015. **26**(6): p. 1-9.
86. Massera, J., et al., *Thermal properties and surface reactivity in simulated body fluid of new strontium ion-containing phosphate glasses.* Journal of Materials Science. Materials in Medicine, 2013. **24**(6): p. 1407-16.

87. O'Donnell, M.D. and R.G. Hill, *Influence of strontium and the importance of glass chemistry and structure when designing bioactive glasses for bone regeneration.* Acta Biomaterialia, 2010. **6**(7): p. 2382-2385.
88. Lao, J., J.M. Nedelec, and E. Jallot, *New strontium-based bioactive glasses: physicochemical reactivity and delivering capability of biologically active dissolution products.* Journal of Materials Chemistry, 2009. **19**(19): p. 2940-2949.
89. Groh, D., F. Dohler, and D.S. Brauer, *Bioactive glasses with improved processing. Part 1. Thermal properties, ion release and apatite formation.* Acta Biomaterialia, 2014. **10**(10): p. 4465-73.
90. Aina, V., et al., *Zinc-containing bioactive glasses: surface reactivity and behaviour towards endothelial cells.* Acta biomaterialia, 2009. **5**(4): p. 1211-22.
91. Fielding, G. and S. Bose, *SiO2 and ZnO Dopants in 3D Printed TCP Scaffolds Enhances Osteogenesis and Angiogenesis in vivo.* Acta Biomaterialia. **9**(11).
92. Oki, A., et al., *Preparation and in vitro bioactivity of zinc containing sol-gel-derived bioglass materials.* Journal of biomedical materials research. Part A, 2004. **69**(2): p. 216-21.
93. Oudadesse, H., et al., *Apatite forming ability and cytocompatibility of pure and Zn-doped bioactive glasses.* Biomedical materials, 2011. **6**(3): p. 35-44.
94. Yamaguchi, M., *Role of zinc in bone formation and bone resorption.* The Journal of Trace Elements in Experimental Medicine, 1998. **11**(2-3): p. 119-135.
95. Zhang, J., et al., *Effects of bioactive cements incorporating zinc-bioglass nanoparticles on odontogenic and angiogenic potential of human dental pulp cells.* Journal of biomaterials applications, 2015. **29**(7): p. 954-64.
96. Wang, H., et al., *Three-dimensional zinc incorporated borosilicate bioactive glass scaffolds for rodent critical-sized calvarial defects repair and regeneration.* Colloids and Surfaces B: Biointerfaces, 2015. **130**: p. 149-156.
97. Jaroch, D.B. and D.C. Clupper, *Modulation of zinc release from bioactive sol-gel derived SiO 2-CaO-ZnO glasses and ceramics.* Journal of Biomedical Materials Research - Part A, 2007. **82**(3): p. 575-588.
98. Goh, Y.-F., et al., *In vitro study of nano-sized zinc doped bioactive glass.* Materials Chemistry and Physics, 2013. **137**(3): p. 1031-1038.
99. Du, R.L., et al., *Characterization and in vitro Bioactivity of Zinc-containing Bioactive Glass and Glass-ceramics.* Journal of Biomaterials Applications, 2006. **20**(4): p. 341-360.
100. Zhang, F., et al., *Spark plasma sintering of macroporous calcium phosphate scaffolds from nanocrystalline powders.* Journal of the European Ceramic Society, 2008. **28**(3): p. 539-545.
101. Wang, Y.Y., et al., *Biological and bactericidal properties of Ag-doped bioactive glass in a natural extracellular matrix hydrogel with potential application in dentistry.* European cells and materials, 2015. **29**: p. 342-55.
102. Newby, P.J., et al., *Ag-doped 45S5 Bioglass®-based bone scaffolds by molten salt ion exchange: processing and characterisation.* Journal of Materials Science: Materials in Medicine, 2011. **22**(3): p. 557-569.
103. Blaker, J.J., et al., *Mechanical properties of highly porous PDLLA/Bioglass composite foams as scaffolds for bone tissue engineering.* Acta biomaterialia, 2005. **1**(6): p. 643-52.

104. Bellantone, M., H.D. Williams, and L.L. Hench, *Broad-spectrum bactericidal activity of Ag(2)O-doped bioactive glass.* Antimicrobial agents and chemotherapy, 2002. **46**(6): p. 1940-5.
105. Chen, W., et al., *In vitro anti-bacterial and biological properties of magnetron co-sputtered silver-containing hydroxyapatite coating.* Biomaterials, 2006. **27**(32): p. 5512-7.
106. Ruparelia, J.P., et al., *Strain specificity in antimicrobial activity of silver and copper nanoparticles.* Acta Biomater, 2008. **4**(3): p. 707-16.
107. El-Kady, A.M., et al., *Synthesis, characterization and microbiological response of silver doped bioactive glass nanoparticles.* Ceramics International, 2012. **38**(1): p. 177-188.
108. Finney, L., et al., *Copper and angiogenesis: unravelling a relationship key to cancer progression.* Clinical and experimental pharmacology & physiology, 2009. **36**(1): p. 88-94.
109. Barbucci, R., et al., *Role of the Hyal-Cu (II) complex on bovine aortic and lymphatic endothelial cells behavior on microstructured surfaces.* Biomacromolecules, 2005. **6**(1): p. 212-9.
110. Gorter, R.W., M. Butorac, and E.P. Cobian, *Examination of the cutaneous absorption of copper after the use of copper-containing ointments.* American journal of therapeutics, 2004. **11**(6): p. 453-8.
111. Hu, G., *Copper stimulates proliferation of human endothelial cells under culture.* Journal of Cellular Biochemistry, 1998. **69**(3): p. 326-335.
112. Zhao, S., et al., *Wound dressings composed of copper-doped borate bioactive glass microfibers stimulate angiogenesis and heal full-thickness skin defects in a rodent model.* Biomaterials, 2015. **53**: p. 379-391.
113. Zhao, S., et al., *Copper-doped borosilicate bioactive glass scaffolds with improved angiogenic and osteogenic capacity for repairing osseous defects.* Acta Biomaterialia, 2015. **14**: p. 185-196.
114. Stähli, C., et al., *Effect of ion release from Cu-doped 45S5 Bioglass® on 3D endothelial cell morphogenesis.* Acta Biomaterialia, 2015. **19**(0): p. 15-22.
115. Lin, Y., et al., *Angiogenic effects of borate glass microfibers in a rodent model.* Journal of biomedical materials research. Part A, 2014. **102**(12): p. 4491-9.
116. Hung, Y.H., A.I. Bush, and R.A. Cherny, *Copper in the brain and Alzheimer's disease.* Journal of biological inorganic chemistry : a publication of the Society of Biological Inorganic Chemistry, 2010. **15**(1): p. 61-76.
117. Gaetke, L.M. and C.K. Chow, *Copper toxicity, oxidative stress, and antioxidant nutrients.* Toxicology, 2003. **189**(1-2): p. 147-163.
118. Stahli, C., N. Muja, and S.N. Nazhat, *Controlled copper ion release from phosphate-based glasses improves human umbilical vein endothelial cell survival in a reduced nutrient environment.* Tissue engineering. Part A, 2013. **19**(3-4): p. 548-57.
119. Rath, S.N., et al., *Bioactive Copper-Doped Glass Scaffolds Can Stimulate Endothelial Cells in Co-Culture in Combination with Mesenchymal Stem Cells.* PLoS ONE, 2014. **9**(12).
120. Milkovic, L., et al., *Effects of Cu-doped 45S5 bioactive glass on the lipid peroxidation-associated growth of human osteoblast-like cells in vitro.* Journal of biomedical materials research. Part A, 2014. **102**(10): p. 3556-61.

121. Liu, X., M.N. Rahaman, and Q. Fu, *Bone regeneration in strong porous bioactive glass (13-93) scaffolds with an oriented microstructure implanted in rat calvarial defects.* Acta biomaterialia, 2013. **9**(1): p. 4889-98.
122. Grasso, S., et al., *Low temperature spark plasma sintering of 45S5 Bioglass®.* Journal of Non-Crystalline Solids, 2013. **362**(0): p. 25-29.
123. Tokita, M., *Mechanism of Spark Plasma Sintering.* Material Science Forum, 1999. **83**: p. 308-311.
124. Feng, P., et al., *Liquid phase sintered ceramic bone scaffolds by combined laser and furnace.* International journal of molecular sciences, 2014. **15**(8): p. 14574-90.
125. O'Flynn, K.P. and K.T. Stanton, *Laser sintering and crystallization of a bioactive glass-ceramic.* Journal of Non-Crystalline Solids, 2013. **360**: p. 49-56.
126. Sudarmadji, N., et al., *Investigation of the mechanical properties and porosity relationships in selective laser-sintered polyhedral for functionally graded scaffolds.* Acta Biomaterialia, 2011. **7**(2): p. 530-537.
127. Velez, M., et al., *In Vivo Evaluation of 13-93 Bioactive Glass Scaffolds Made by Selective Laser Sintering (SLS)*, in *Biomaterials Science: Processing, Properties and Applications II*. 2012, John Wiley & Sons, Inc. p. 91-99.
128. Gu, Y., et al., *Biodegradable borosilicate bioactive glass scaffolds with a trabecular microstructure for bone repair.* Materials Science and Engineering: C, (0).
129. Sepulveda, P. and J. Binner, *Processing of cellular ceramics by foaming and in-situ polymerisation of organic monomers.* Journal of the European Ceramic Society, 1999. **19**(12): p. 2059-2066.
130. Tang. H, *PhD Thesis: Bioactive glass scaffolds produced by the gel cast foaming process*, in *Department of Materials*. 2013, Imperial College: London.
131. Cesarano Iii, J., R. Segalman, and P. Calvert, *Robocasting provides moldless fabrication from slurry deposition.* Ceramic Industry, 1998. **148**(4): p. 94.
132. Dellinger, J.G., A.M. Wojtowicz, and R.D. Jamison, *Effects of degradation and porosity on the load bearing properties of model hydroxyapatite bone scaffolds.* Journal of Biomedical Materials Research Part A, 2006. **77A**(3): p. 563-571.
133. Fu, Q., E. Saiz, and A.P. Tomsia, *Bioinspired Strong and Highly Porous Glass Scaffolds.* Advanced Functional Materials, 2011. **21**(6): p. 1058-1063.
134. Butscher, A., et al., *Structural and material approaches to bone tissue engineering in powder-based three-dimensional printing.* Acta biomaterialia, 2011. **7**(3): p. 907-20.
135. Fu, Q., E. Saiz, and A.P. Tomsia, *Direct ink writing of highly porous and strong glass scaffolds for load-bearing bone defects repair and regeneration.* Acta biomaterialia, 2011. **7**(10): p. 3547-54.
136. Wu, C., et al., *Three-dimensional printing of hierarchical and tough mesoporous bioactive glass scaffolds with a controllable pore architecture, excellent mechanical strength and mineralization ability.* Acta biomaterialia, 2011. **7**(6): p. 2644-50.
137. Eqtesadi, S., et al., *Robocasting of 45S5 bioactive glass scaffolds for bone tissue engineering.* Journal of the European Ceramic Society, 2014. **34**(1): p. 107-118.
138. Eqtesadi, S., et al., *Influence of sintering temperature on the mechanical properties of ϵ-PCL-impregnated 45S5 bioglass-derived scaffolds fabricated*

by robocasting. Journal of the European Ceramic Society, 2015. **35**(14): p. 3985-3993.
139. Cesarano, J., *Robocasting: Direct fabrication of ceramics from colloidal suspensions.* Proceedings of Solid Freeform Fabrication Symposium, 1997: p. 25-36.
140. Franco, J., et al., *Direct write assembly of calcium phosphate scaffolds using a water-based hydrogel.* Acta Biomaterialia, 2010. **6**(1): p. 218-228.
141. Cohn, D., A. Sosnik, and S. Garty, *Smart Hydrogels for in Situ Generated Implants†.* Biomacromolecules, 2005. **6**(3): p. 1168-1175.
142. Lenaerts, V., et al., *Temperature-dependent rheological behavior of Pluronic F-127 aqueous solutions.* International Journal of Pharmaceutics, 1987. **39**(1-2): p. 121-127.
143. Vadnere, M., et al., *Thermodynamic studies on the gel-sol transition of some pluronic polyols.* International Journal of Pharmaceutics, 1984. **22**(2-3): p. 207-218.
144. Eqtesadi, S., et al., *A simple recipe for direct writing complex 45S5 Bioglass® 3D scaffolds.* Materials Letters, 2013. **93**(0): p. 68-71.
145. Chen, Q.Z., et al., *Surface functionalization of Bioglass-derived porous scaffolds.* Acta biomaterialia, 2007. **3**(4): p. 551-62.
146. Grimal, Q., et al., *Assessment of cortical bone elasticity and strength: Mechanical testing and ultrasound provide complementary data.* Medical Engineering & Physics, 2009. **31**(9): p. 1140-1147.
147. Fung, Y.C., *Biomechanics: mechanical properties of living tissues*. 1993, Springer: New York. p. 500-538.
148. Rho, J.Y., L. Kuhn-Spearing, and P. Zioupos, *Mechanical properties and the hierarchical structure of bone.* Med Eng Phys, 1998. **20**(2): p. 92-102.
149. Røhl, L., et al., *Tensile and compressive properties of cancellous bone.* Journal of Biomechanics, 1991. **24**(12): p. 1143-1149.
150. Rho, J.Y., M.C. Hobatho, and R.B. Ashman, *Relations of mechanical properties to density and CT numbers in human bone.* Medical Engineering and Physics, 1995. **17**(5): p. 347-355.
151. Fu, Q., et al., *Bioactive glass scaffolds for bone tissue engineering: state of the art and future perspectives.* Materials science & engineering. C, Materials for biological applications, 2011. **31**(7): p. 1245-1256.
152. Oyen, M.L., *The materials science of bone: Lessons from nature for biomimetic materials synthesis.* MRS Bulletin, 2008. **33**(1): p. 49-55.
153. Deliormanlı, A.M., *Preparation, in vitro mineralization and osteoblast cell response of electrospun 13-93 bioactive glass nanofibers.* Materials Science and Engineering: C, 2015. **53**(0): p. 262-271.
154. Doiphode, N., et al., *Freeze extrusion fabrication of 13-93 bioactive glass scaffolds for bone repair.* Journal of Materials Science: Materials in Medicine, 2011. **22**(3): p. 515-523.
155. Eqtesadi, S., et al., *Effect of milling media on processing and performance of 13-93 bioactive glass scaffolds fabricated by robocasting.* Ceramics International. **41**(4): p. 1379-1389.
156. Fu, Q., et al., *In vivo evaluation of 13-93 bioactive glass scaffolds with trabecular and oriented microstructures in a subcutaneous rat implantation*

model. Journal of Biomedical Materials Research Part A, 2010. **95A**(1): p. 235-244.
157. Bohner, M. and J. Lemaitre, *Can bioactivity be tested in vitro with SBF solution?* Biomaterials, 2009. **30**(12): p. 2175-2179.
158. Deliormanlı, A.M., *Preparation and in vitro characterization of electrospun 45S5 bioactive glass nanofibers.* Ceramics International Part A, 2015. **41**(1): p. 417-425.
159. Liu, X., M.N. Rahaman, and D.E. Day, *Conversion of melt-derived microfibrous borate (13-93B3) and silicate (45S5) bioactive glass in a simulated body fluid.* Journal of materials science. Materials in medicine, 2013. **24**(3): p. 583-95.
160. Miola, M., et al., *In vitro study of manganese-doped bioactive glasses for bone regeneration.* Materials Science and Engineering: C, 2014. **38**(1): p. 107-118.
161. Yun, H.S., et al., *Effect of the pore structure of bioactive glass balls on biocompatibility in vitro and in vivo.* Acta biomaterialia, 2011. **7**(6): p. 2651-60.
162. Kokubo, T. and H. Takadama, *How useful is SBF in predicting in vivo bone bioactivity?* Biomaterials, 2006. **27**(15): p. 2907-2915.
163. Kokubo, T. and H. Takadama, *Simulated Body Fluid (SBF) as a Standard Tool to Test the Bioactivity of Implants*, in *Handbook of Biomineralization*. 2008, Wiley-VCH Verlag GmbH. p. 97-109.
164. Oyane, A., et al., *Preparation and assessment of revised simulated body fluids.* Journal of biomedical materials research. Part A, 2003. **65**(2): p. 188-95.
165. Pan, H., et al., *Apatite-formation ability - Predictor of "bioactivity"?* Acta Biomaterialia, 2010. **6**(11): p. 4181-4188.
166. Nandi, S.K., et al., *The repair of segmental bone defects with porous bioglass: An experimental study in goat.* Research in Veterinary Science, 2009. **86**(1): p. 162-173.
167. Feng, B., et al., *The effect of pore size on tissue ingrowth and neovascularization in porous bioceramics of controlled architecture in vivo.* Biomed Mater, 2011. **6**(1): p. 015007.
168. Oonishi, H., et al., *Comparative bone growth behavior in granules of bioceramic materials of various sizes.* Journal of Biomedical Materials Research, 1999. **44**(1): p. 31-43.
169. Lin, Y., et al., *Long-term bone regeneration, mineralization and angiogenesis in rat calvarial defects implanted with strong porous bioactive glass (13-93) scaffolds.* Journal of Non-Crystalline Solids.
170. Pearce, A.I., et al., *Animal models for implant biomaterial research in bone: a review.* European cells and materials, 2007. **13**: p. 1-10.
171. Mapara, M., B.S. Thomas, and K.M. Bhat, *Rabbit as an animal model for experimental research.* Dental Research Journal, 2012. **9**(1): p. 111-118.
172. Mills, L.A. and A.H. Simpson, *In vivo models of bone repair.* The Journal of Bone and Joint Surgery: British Volume, 2012. **94**(7): p. 865-74.
173. *Malvern Instruments Worldwide: A Basic Guide to Particle Characterization*. 2012, Malvern Instruments Limited.
174. Cullity, B.C., *Elements of X-ray diffraction*. 2nd ed. 1978, United States of America: Addison-Wesley Publishing Company
175. Suryanarayan, C. and M. Grant Norton, *X-Ray Diffraction: A practical approach*. 1998, United States: Plenum Pres.

176. Callister, W.D. and D.G. Rethwisch, *Materials Science and Engineering: An Introduction*. 8th ed. 2009, USA: Wiley.
177. Giesche, H., *Mercury Porosimetry: A General (Practical) Overview.* Particle & Particle Systems Characterization, 2006. **23**(1): p. 9-19.
178. Smay, J.E., J. Cesarano, and J.A. Lewis, *Colloidal Inks for Directed Assembly of 3-D Periodic Structures.* Langmuir, 2002. **18**(14): p. 5429-5437.
179. Kim, T.B., et al., *Additive manufactured porous titanium structures: Through-process quantification of pore and strut networks.* Journal of Materials Processing Technology, 2014. **214**(11): p. 2706-2715.
180. Rosen, M.J. and J.T. Kunjappu, *Characteristic Features of Surfactants*, in *Surfactants and Interfacial Phenomena*. 2012, John Wiley & Sons, Inc. p. 1-38.
181. O'Donnell, M.D., *Predicting bioactive glass properties from the molecular chemical composition: glass transition temperature.* Acta Biomaterialia, 2011. **7**(5): p. 2264-9.
182. Carter, D. and W. Hayes, *Bone compressive strength: the influence of density and strain rate.* Science, 1976. **194**(4270): p. 1174-1176.
183. Gu, Y., et al., *Biodegradable borosilicate bioactive glass scaffolds with a trabecular microstructure for bone repair.* Materials Science and Engineering: C, 2014. **36**(0): p. 294-300.
184. Hench, L.L., N. Roki, and M.B. Fenn, *Bioactive glasses: importance of structure and properties in bone regeneration.* Journal of Molecular Structure, (0).
185. Hoppe, A., et al., *In vitro reactivity of Sr-containing bioactive glass (type 1393) nanoparticles.* Journal of Non-Crystalline Solids, 2014. **387**: p. 41-46.
186. Filgueiras, M.R., G. La Torre, and L.L. Hench, *Solution effects on the surface reactions of a bioactive glass.* Journal of Biomedical Materials Research, 1993. **27**(4): p. 445-453.
187. Deliormanlı, A.M., *In vitro assessment of degradation and bioactivity of robocast bioactive glass scaffolds in simulated body fluid.* Ceramics International, 2012. **38**(8): p. 6435-6444.
188. Zeglinski, J., et al., *Unravelling the specific site preference in doping of calcium hydroxyapatite with strontium from ab initio investigations and Rietveld analyses.* Physical Chemistry Chemical Physics, 2012. **14**(10): p. 3435-3443.
189. Kolan, K.C.R., et al., *Fabrication of 13-93 bioactive glass scaffolds for bone tissue engineering using indirect selective laser sintering.* Biofabrication, 2011. **3**(2): p. 025004.
190. Kalyon, D.M., et al., *Rheological behavior of a concentrated suspension: A solid rocket fuel simulant.* Journal of Rheology (1978-present), 1993. **37**(1): p. 35-53.
191. Buscall, R., J.I. McGowan, and A.J. Morton-Jones, *The rheology of concentrated dispersions of weakly attracting colloidal particles with and without wall slip.* Journal of Rheology (1978-present), 1993. **37**(4): p. 621-641.
192. Chen, Z., et al., *Effect of particle packing on extrusion behavior of pastes.* Journal of Materials Science, 2000. **35**(21): p. 5301-5307.
193. Benbow, J.J., *The dependence of output rate on die shape during catalyst extrusion.* Chemical Engineering Science, 1971. **26**(9): p. 1467-1473.
194. Conrad, J.C. and J.A. Lewis, *Structure of colloidal gels during microchannel flow.* Langmuir, 2008. **24**(15): p. 7628-7634.
195. Smay, J.E., et al., *Directed colloidal assembly of 3D periodic structures.* Advanced Materials, 2002. **14**(18): p. 1279-1283.

196. Lewis, J.A., *Direct-write assembly of ceramics from colloidal inks.* Current Opinion in Solid State and Materials Science, 2002. 6(3): p. 245-250.